FACTORS AFFECTING THE PERFORMANCE OF HYDRAULIC IMPULSE TURBINES

by

JAMES WEBSTER

A thesis submitted to the

UNIVERSITY OF GLASGOW

for the degree of

Doctor of Philosophy

September 1968.

SUMMARY

It has been apparent that the Turgo wheel, since its introduction at the end of the First World War, has been substantially less efficient than a Pelton wheel of comparable size. This investigation was undertaken principally to establish the reason for the lower efficiency.

The condition of the fluid discharging from a jet type impulse turbine appears never to have been accurately assessed. With a knowledge of outlet flow distribution, velocity and direction at the optimum speed ratio, the leaving loss can be calculated. Since power input and output, and mechanical and nozzle losses can be found by conventional methods, friction losses can then be obtained by subtraction.

Since the state of the discharging fluid was irregular the method adopted was to divide the area generated at outlet into a grid composed of a series of equiangular radial lines and a series of concentric circles. Devices were developed to measure the flow density, velocity and direction at each grid intersection.

Enough information was now available to construct velocity diagrams for the discharge from each intersection. The way in which the pattern of flow altered became clear and the changing degree in which the energy of the fluid was utilised across the wheel, was also apparent.

Using a graphical step-by-step method mean trajectories were constructed for an ideal fluid. It was at once evident that the paths followed

by particles of real fluid across the bucket surface were much further removed from the centre of rotation than the corresponding ideal trajectories.

Further study of entry conditions occasioned a graphical method which revealed the variation in relative energy across the jet. It was clear that the changing relative velocity across the jet caused a mixing effect and an outward turning moment on the fluid. It was shown that the difference in relative energy was proportional to the jet : wheel diameter ratio. The mixing effect thus increased with increasing specific speed.

A one-dimensional theory was developed on a non-dimensional basis. The extent to which certain factors influence the relative performance of tangential and inclined jet turbines was demonstrated by varying the parameters in turn. Emphasis throughout was laid on the importance of firstly, the variation of relative energy across the jet, and secondly, the mean value of the relative energy which, when friction losses are included, remains constant across the bucket.

A study of the form of velocity diagrams showed the inadequacy of the existing bucket design, particularly with regard to the true relative angle of discharge of the fluid. It could be seen that an increase in turning angle of the order of ten degrees was possible at outlet and would lead to a worthwhile gain in efficiency for the Turgo wheel.

Separate tests were inaugurated in order to study the basic factors contributing to the spread of water across static vanes of two different forms, one curved in two dimensions, the other in three. Using jets of different cross-sections, the jet profile and the variation in angle of spread and velocity were measured at outlet. A computer program based on an ideal jet of fluid of rectangular cross-section, indicated the effects of friction when a comparison was made with the experimental results. Amongst other findings, the tests revealed that there was an optimum shape for the rectangular jet, important in determining the bucket pitch of a Turgo wheel. Also the wave pattern was shown to be independent of head.

In general it was concluded that the Turgo wheel was inherently less efficient than the Pelton. The tests also showed how minor improvements in design could be achieved, possibly leading to an efficiency sufficiently increased to ensure that this basically simple turbine remained competitive with other types.

Preface

As suggested by the title this thesis deals with the whole field of jet type impulse turbines, but the experimental work is devoted principally to a study of the inclined jet turbine or Turgo wheel. The conclusions reached are equally applicable to the Pelton wheel except where specifically stated.

Prior to the present series of tests, the general apparatus had been installed at the University of Strathclyde and preliminary tests performed using the flow measuring device. All other aspects of the investigation are the work of the writer.

The author claims as original firstly, the ideas and devices developed for measuring the velocity and direction of the water discharging from the Turgo wheel and secondly, the design of the equipment connected with tests on the static vanes.

James Webster.

CONTENTS

Appendices

Diagrams

Graphs

Graphs (Auxiliary tests)

Charts

Colour code

Notation

V	absolute velocity
v	relative velocity
u	tangential velocity of wheel
w	tangential component of absolute velocity
f	meridional component of absolute velocity
θ	absolute angle
ϕ	relative angle
d	jet diameter
D	wheel diameter
r	grid station radius
z	elevation
p	pressure
ρ	fluid density
γ	fluid specific weight
C_d	coefficient of discharge
C_v	coefficient of velocity
H	overall head
H_o	useful head
h	head
Q	flowrate
q	flowrate from grid station
N	rotational speed
N_s	specific speed

N_u	unit speed
P_u	unit power
Δ	speed ratio
m	radius ratio
K	friction factor
P_1	input power
P	shaft power
P_o	wheel power
P_m	mechanical power loss
P_b	hydraulic power loss
P_e	power loss due to kinetic energy at discharge
P_n	nozzle power loss
E_o	wheel power/unit weight flow
E_{rel}	relative energy
T	shaft torque
T_o	wheel torque
T_m	mechanical resisting torque
η	overall efficiency
η_b	hydraulic efficiency
η_w	wheel efficiency
η_m	mechanical efficiency

<u>Subscripts</u>

1	inlet

0	outlet
3	outlet (meridional)

See diagrams D.1 and D.2 for additional definitions.

Additional notation (Appendix 7)

M	hydraulic mean depth
R	radius of curvature of vane
θ	turning angle of vane
F	force
B, b	jet width
H, h	jet depth
$\dot{m}$	mass flowrate

See graph GA.0 for additional guide to notation.

1. INTRODUCTION

1.1 Definition

In a hydraulic IMPULSE turbine, all the energy of the fluid is converted to kinetic energy within one or more stationary nozzles. Rotating wheel vanes are designed to run only partially full, thus ensuring that the pressure on the free surface of the water remains unchanged across the vanes. As the pressure is uniform throughout the turbine casing, partial admission may be used. The term "impulse" has little justification in this connection, but has become established by long usage.

1.2 Historical survey

In interesting descriptive papers Doble and Durand (1,2) trace the development of the impulse turbine in the U.S.A. from the simple water-wheel, the origin of which is lost in antiquity, to the Pelton wheel, as it appeared at the end of last century.

Until about 1850 there had been no serious demands for large power or high efficiency. Over the next thirty years progress in turbine design was directed mainly towards the performance of mechanical work, then advances in electrical engineering made it possible to transmit energy economically over large distances and provided an impetus to the development of hydraulic prime movers.

During the previous century the foundations of turbine theory had been laid by Borda and Euler. In America, Jearum Atkins applied for a patent in 1853 and was probably one of the first to design an impulse type water turbine incorporating the basic requirements for the efficient utilisation of the energy contained in the fluid. His design fulfilled the following conditions, viz. that the water should be applied tangentially to the vanes, that the peripheral velocity of the wheel should be half that of the jet, that the direction of flow should be fully reversed and that the absolute velocity at exit should be substantially zero. However his design was not put into practice at once in America, perhaps because it was not based on the familiar "hurdy-gurdy" water-wheel, but employed a volute type casing to guide water to the runner.

Instead progress in this field centred on the development by Knight of the water-wheel, driven by a jet of water emanating from a nozzle and directed tangentially on to the wheel periphery, to which was fitted a series of cup-shaped buckets to reverse the flow. The central wedge or "splitter", developed simultaneously by Pelton and others during the same period, considerably reduced the turbulence within the bucket without introducing axial thrust.

The removal of the cross formed by the central wedge and bucket periphery was patented in 1899 and further progress was made in changing the shape of the buckets from a simple curve in two dimensions with flat ends to an ellipsoid, substantially the form in which the Pelton bucket appears today.

At the close of the century, there was a growing need to find some means of maintaining optimum speed in the face of varying power demands and this was achieved by changing the flowrate. The next ten years saw the development of various devices which performed basically the same function, viz. an immediate diversion of part of the jet away from the runner until gradual movement of a spear or needle valve within the nozzle adjusted the jet size to the new conditions of load, this sequence of events being necessary to avoid water hammer in the supply line. This type of device was incorporated relatively easily into the supply arrangements of the Pelton wheel.

In Europe, parallel development of impulse machines produced the Girard type of turbine, in which the flow could be either axial or radially outward with full or partial admission. These turbines had a series of fixed guide vanes in which the energy of the water was wholly transformed into kinetic energy. The free jets so formed at outlet then impinged tangentially on to moving runner vanes curved backwards to reverse the flow. The efficiency at that time was comparable to that of the Pelton wheel.

The Girard turbine proved very versatile owing to the wide range of specific speeds made possible by adjusting the degree of admission. For regulation a plate sliding over the guide nozzles at inlet could be controlled either manually or by a governor, but this device proved complicated and clumsy. The superiority of the Pelton wheel regulator marked the demise of the Girard wheel.

1.3 Review of progress

Early in the twentieth century development of the Pelton wheel was

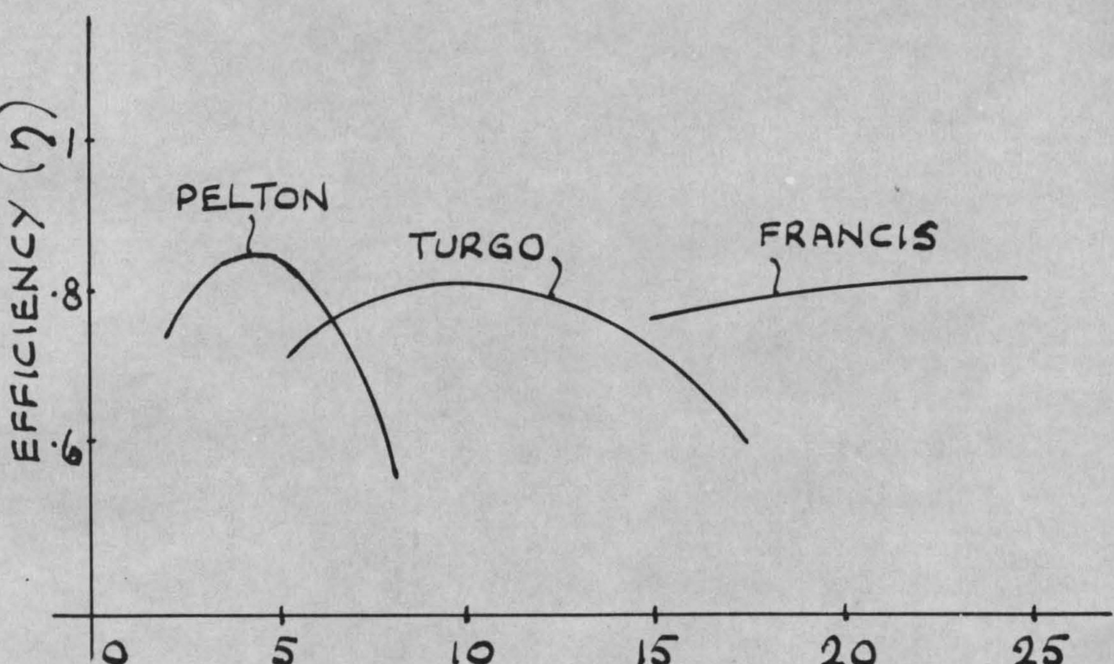
EFFICIENCY (η)
1
·8
·6
PELTON
TURGO
FRANCIS
0
5
10
15
20
25
SPECIFIC SPEED (N_S)

FIG. 1

fostered in Europe until it has become the main form of impulse machine used today. Nevertheless the elimination of the Girard turbine has left a gap in the range of performance between Pelton and Francis turbines which it has not been easy to fill. (Fig. 1). Partial admission and the absence of pressure change across the runner, make the Pelton wheel suitable for small flowrates and high heads; consequently, it is characterised by a low specific speed. Appendix 1 shows that the specific speed, $N_s \propto \left(\frac{d}{D}\right) \cdot \left(\frac{u}{V_1}\right) \cdot \left(\eta\right)^{\frac{1}{2}}$ for impulse turbines of this type. Of these parameters, $\left(\frac{d}{D}\right)$ is the dominant factor in deciding the value of the specific speed. For optimum efficiency this ratio is about $\frac{1}{10}$ when the specific speed is 5. Increase in specific speed implies an increase in the jet size in relation to the wheel diameter, but the condition at inlet to each bucket departs progressively further from the ideal causing a fall in efficiency, and bucket connections are subjected to increasing stresses.

Taking the lower limit of specific speed for the Francis turbine as 15, the intervening range has been accommodated by the use of multi-jet Pelton wheels, and much development work has been done on this principle. Such arrangements suffer from certain disadvantages e.g. interference of jet action, high capital cost, etc.

Soon after the first world war, Gilbert Gilkes and Gordon developed a new type of impulse turbine which they called the TURGO wheel. As described by Crewdson (3) this turbine comprised a Pelton wheel jet and a Girard type runner. Advantages claimed for this new design were the higher specific speed of the Girard wheel combined with the simple and reliable

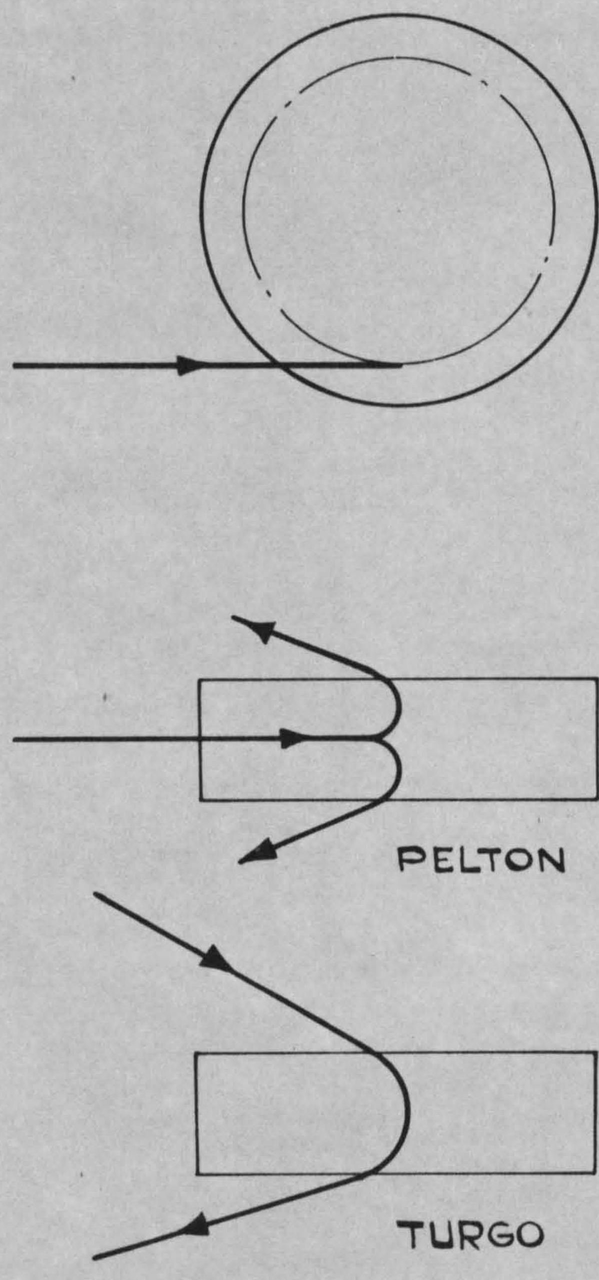

FIG. 2.

regulating arrangement of the Pelton wheel. At the outset the runner was basically similar to the Girard wheel insofar as the vanes were curved in two dimensions only, but after some years of development an ellipsoidal shape was adopted somewhat similar to the Pelton bucket.

As can be seen in Fig.2 the Turgo wheel is essentially an inclined jet turbine whilst the Pelton wheel jet acts tangentially. The geometrical layout of the Turgo wheel at inlet is such that it permits the use of a much larger jet relative to the wheel diameter. This implies that for the same wheel diameter, the flow capacity of the Turgo wheel is greater. Alternatively, if the jet diameter is maintained, the Turgo wheel is smaller in diameter and therefore runs at a higher speed; or again, to operate at the same speed as the Pelton wheel, the head on the Turgo wheel has to be reduced. In short, the specific speed of the Turgo wheel is higher and for optimum efficiency is about twice that of the Pelton wheel, corresponding to a jet : wheel diameter ratio of the order of 1 : 5.

Although inclined entry entails axial thrust and a reduced turning angle, it might have been expected that, with a smaller relative windage loss, the Turgo wheel would have been at least as efficient as the Pelton wheel at the appropriate specific speed, but in spite of design improvements the efficiency has remained decidedly lower. Hence despite a simpler layout, it remains questionable whether the Turgo wheel is more economical than the multi-jet Pelton wheel for the range of specific speed under review.

1.4 Review of published literature

Prior to 1938, it seems that very little research work was done on the impulse turbine; certainly most of the publications were of a descriptive nature. Firstly Doble (1) and then Durand (2) dealt adequately with the evolution of the Pelton wheel in America. Crewdson (3) traced the origin of the Turgo wheel soon after its appearance and discussed some basic features of bucket design. In 1938, in a notable exception to this type of paper, Eilken (4) gave a description of tests carried out to determine the optimum angular setting of a Pelton bucket relative to the wheel.

Lowy (5) was one of the first to attempt to analyse the passage of fluid across a bucket surface. He argued the case for direct tests on a static Pelton bucket on the basis that the variation in peripheral velocity with radius was small. Progressively less justification can be found for this assumption as the jet : wheel diameter ratio increases. Lowy also performed tests with a jet impinging on the edge of a flat plate at varying inclinations. His paper is widely quoted by those now attempting more advanced work.

Where a bend is required in the supply pipe, e.g. in a multi-jet Pelton wheel layout, resulting in secondary flow and increased turbulence, the water jet diffuses quickly after leaving the nozzle. The development of suitable flow straighteners was described by Quick (6) but this problem was investigated in greater depth both theoretically and experimentally by Oguey et al. (7) a few years later.

In Russia research in this field now appears to be established on an organised basis. During the nineteen fifties Kwiatkowski and Shipulin devoted several papers to an analysis of the inclined jet turbine or Turgo wheel. Shipulin (8) discusses at some length the effects of numerous factors on the performance of these turbines and his comments result from tests on several wheels of different specific speeds. In a subsequent article (9) produced from the same experimental work, Shipulin presents a detailed evaluation of the division of jet energy but his appreciation of major losses is based on a simple one-dimensional estimate of discharge conditions. Nonetheless the tests provide a practical basis for the design of a range of Turgo wheels in the appropriate field of application.

More recently, Edel has published a book (10) and several articles in sequel, devoted to the design of the Pelton wheel, in which he not only covers the standard methods of design but also describes some experimental work carried out at a research institute. In a recent article (11) he attempts to analyse friction losses across the bucket surface and deduces an associated theory using simplifying assumptions. Complementary tests on a static vane with straight sides, constraining the fluid to a predetermined path, provide a practical basis of comparison.

It will be seen from the above survey that no attempt appears to have been published dealing with the condition of the fluid at outlet from a moving wheel. Without this information no estimate of kinetic energy at discharge can be considered accurate and no realistic assessment can be made of the paths of fluid particles across the bucket.

1.5 Object of investigation and general approach

This series of studies and tests has been undertaken to assess the performance of the Turgo impulse turbine and to determine to what extent the efficiency may be improved.

The investigations have been based on a wheel speed corresponding to optimum efficiency, and the methods adopted can be divided conveniently into two main parts. In the first part, the condition of flow has been analysed at inlet with the aid of simple graphical methods, but at outlet, the state of the fluid is much more complex and an experimental approach has been used to make a full assessment. It has thus been possible to estimate to a reasonable degree of accuracy the kinetic energy at discharge, and to formulate an energy balance. Also knowledge of inlet and outlet conditions has facilitated an understanding of the paths of the filaments of fluid across the bucket surface.

Secondly, in an attempt to analyse the changing condition of the fluid as it moves across the vane, a series of auxiliary tests has been performed on static vanes curved in either two or three dimensions. This part appears in Appendix 7.

2. IMPULSE TURBINE THEORY AND CHARACTERISTICS

It is useful to compare the actual flow through an impulse turbine with an idealised, simplified case. Concepts as they are used in this study are defined as follows:-

One-dimensional flow

It will be assumed that the fluid is concentrated at the centre line of the jet as it impinges on the vane under optimum conditions and traces a linear path across it. The state of the fluid at entry is thus simplified and the complication of lateral spread can be overcome by the use of a numerical coefficient. As can be seen from photographs P.10 and P.11, the Turgo wheel, when running at uniform speed, discharges water through a surface generated by the outlet edges of the buckets at non-uniform rates of flow and velocity. In consequence, a one-dimensional theory cannot be wholly accurate but at best will serve as an approximation to the mean condition.

Ideal fluid

For the purposes of this study, an ideal fluid is defined as homogeneous, incompressible and inviscid.

Real fluid

Due to the viscosity of water which is invariably used as the flow medium, friction effects arise as a result of the relative motion of fluid particles. This causes an increase in thermal energy which will be considered an energy loss as it cannot be harnessed.

2.1 Mechanical Work done by the fluid

The momentum principle may be used to prove that, for a flowrate of 1 lbf of fluid per second, the work done per second by the fluid on the wheel,

$$E_o = {}^{P_o}/_{lbf} = \frac{w_1 u_1 - w_o u_o}{g} \qquad \dots (1)$$

This expression also represents the power output by the wheel.

2.2 Energy equations

For one-dimensional flow the energy interchanges between the inlet and outlet of a turbine may be given either on an absolute basis or relative to the motion of the wheel. In absolute terms, the equation may be written,

$$z_1 + \frac{p_1}{\gamma} + \frac{V_1^2}{2g} = z_o + \frac{p_o}{\gamma} + \frac{V_o^2}{2g} + E_o + h_L \qquad \dots (2)$$

where h_L represents the head loss due to friction.

From velocity diagrams, Fig.7, p.33,

$$V_1^2 = f_1^2 + \left[(w_1 - u_1) + u_1\right]^2$$

$$= f_1^2 + (w_1 - u_1)^2 + 2 w_1 u_1 - 2u_1^2 + u_1^2$$

$$\therefore \quad V_1^2 = v_1^2 - u_1^2 + 2w_1 u_1 \qquad \dots (3)$$

and similarly

$$V_o^2 = v_o^2 - u_o^2 + 2w_o u_o \qquad \dots (4)$$

If the term "relative energy", E_{rel} is used to describe $(v^2 - u^2)$, it can be generally stated that <u>kinetic energy = relative energy + work component</u>

Substituting for V_1^2 and V_o^2 in equation (2), the equation of <u>relative</u> motion emerges,

$$z_1 + \frac{p_1}{\gamma} + \frac{v_1^2 - u_1^2}{2g} = z_o + \frac{p_o}{\gamma} + \frac{v_o^2 - u_o^2}{2g} + h_L \quad \ldots (5)$$

In this expression, the mechanical work term does not appear explicitly.

As impulse turbines are suitable for medium to high heads, the difference in elevation between inlet and outlet, $z_1 - z_o$, is usually very small. In addition, $p_1 = p_o$, by definition.

$$\therefore\ v_1^2 - u_1^2 = v_o^2 - u_o^2 + h_L \quad \ldots (6)$$

where h_L represents the energy loss in appropriate units.

If the actual flow of a real fluid across the vane were visualised, then neglecting for the moment the effect of changing peripheral velocity, it would be seen that the reduction of v_o could be ascribed to two factors:-

(a) a real reduction in mean relative velocity due to the effect of friction.

(b) the spreading action of the jet where only the velocity components of the discharging jet normal to the bucket edge, contribute to the mean relative velocity.

For the purposes of one-dimensional flow, h_L may be regarded as including the effects of both these factors. In each case the head loss is proportional to the square of velocity and it is assumed that the combined effect may be expressed as $h_L = c v_o^2$. Then in equation (6),

$$v_1^2 - u_1^2 = (1 + c) v_o^2 - u_o^2, \text{ or}$$

$$v_1^2 - u_1^2 = K^2 v_o^2 - u_o^2 \qquad \ldots (7)$$

where $K^2 = 1 + c$

It is also of interest to note that combining equations (4) and (6) leads to

$$V_o^2 + h_L = (v_1^2 - u_1^2) + 2 w_o u_o \qquad \ldots (8)$$

2.3. General one-dimensional theory.

The assumptions made in evolving a general theory as as follows:-

(a) friction and spread are included in a single factor, K.

(b) the fluid may enter and leave the vane at different mean radii such that the radius ratio, $m = \frac{r_o}{r_1}$.

Peripheral velocity of the wheel, $u = \omega r$

$$\therefore \quad m = \frac{r_o}{r_1} = \frac{u_o}{u_1} \quad \text{and} \quad u_o = m u_1$$

From equation (7),

$$v_o = \frac{1}{K}\sqrt{v_1^2 - u_1^2 + u_o^2}$$

$$= \frac{1}{K}\sqrt{v_1^2 - u_1^2 + m^2 u_1^2}$$

but $\quad v_1^2 = f_1^2 + (w_1 - u_1)^2$ in Fig.7, p.33.

$$\therefore \quad v_1^2 = V_1^2 + u_1^2 - 2w_1u_1$$

$$\therefore \quad v_o = \frac{1}{K}\sqrt{V_1^2 + m^2u_1^2 - 2w_1u_1}$$

Also $\quad w_o = u_o - v_o \cos \varnothing_o$

$$= mu_1 - \frac{\cos \varnothing_o}{K}\sqrt{V_1^2 + m^2u_1^2 - 2w_1u_1}$$

From equation (1), the work done/lbf,

$$E_o = \frac{1}{g}\left[w_1u_1 - mu_1\left(mu_1 - \frac{\cos \varnothing_o}{K}\sqrt{V_1^2 + m^2u_1^2 - 2w_1u_1}\right)\right]$$

$$= \frac{1}{g}\left[w_1u_1 - m^2u_1^2 + mu_1\frac{\cos \varnothing_o}{K}\sqrt{V_1^2 + m^2u_1^2 - 2w_1u_1}\right]$$

or since $w_1 = V_1 \cos \theta_1$,

$$E_o = \frac{1}{g}\left[V_1 \cos \theta_1 . u_1 - m^2u_1^2 + mu_1\frac{\cos \varnothing_o}{K}\sqrt{V_1^2 + m^2u_1^2 - 2V_1 \cos\theta_1 . u_1}\right]$$

The speed ratio, $\Delta = \dfrac{u_1}{V_1}$

The power input/lbf to the wheel $= \dfrac{V_1^2}{2g}$

$\therefore$ Wheel efficiency, $\eta_w = \dfrac{2g . E_o}{V_1^2}$

Substituting for E_o,

$$\eta_w = 2\left[\frac{u_1}{V_1}\cos \theta_1 - m^2\frac{u_1^2}{V_1^2} + m\frac{u_1}{V_1}\frac{\cos \varnothing_o}{K}\sqrt{1 + m^2\frac{u_1^2}{V_1^2} - 2\cos\theta_1\frac{u_1}{V_1}}\right]$$

$$\eta_w = 2\left[\Delta\cos\Theta_1 - \Delta^2 m^2 + \frac{\Delta m\cos\phi_o}{K}\sqrt{1+\Delta^2 m^2 - 2\Delta\cos\Theta_1}\right] \quad \ldots (9)$$

Differentiating equation (9) with respect to Δ leads to

$$\frac{\partial\eta_w}{\partial\Delta} = 2\left[\cos\Theta_1 - 2\Delta m^2 + \frac{m\cos\phi_o}{K}\,\frac{(1+2\Delta^2 m^2 - 3\Delta\cos\Theta_1)}{\sqrt{(1+\Delta^2 m^2 - 2\Delta\cos\Theta_1)}}\right] \quad \ldots (10)$$

$$= 2\ S$$

The value of Δ at maximum power can thus be obtained by equating equation (10) to zero.

In spite of the limitations of this approach, it is interesting to assign typical values to the various parameters and to compare the resultant trends. Although the theory is perfectly general in its application, it will be restricted in this study to comparing turbines of the axial flow type, viz. the Pelton wheel, where the jet is tangential to the pitch circle of the buckets, and the Turgo wheel, where the jet is inclined to the plane of the wheel.

The following cases will be considered in turn:-

I. Tangential jet.
   (a) ideal case.
   (b) effect of inclined outlet and friction.

II. Inclined jet.
   (a) ideal case.
   (b) effect of inclined outlet.
   (c) further effect of increasing mean radius at outlet.
   (d) further effect of friction.

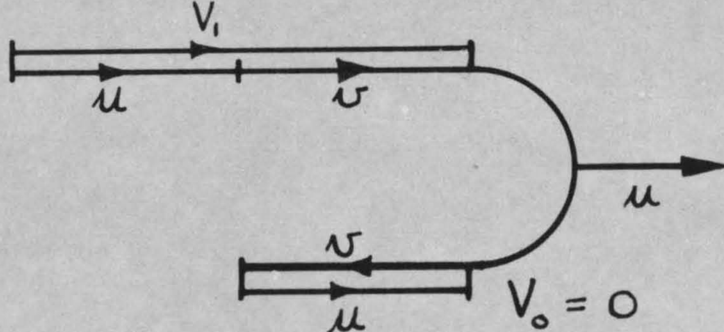

FIG. 3.

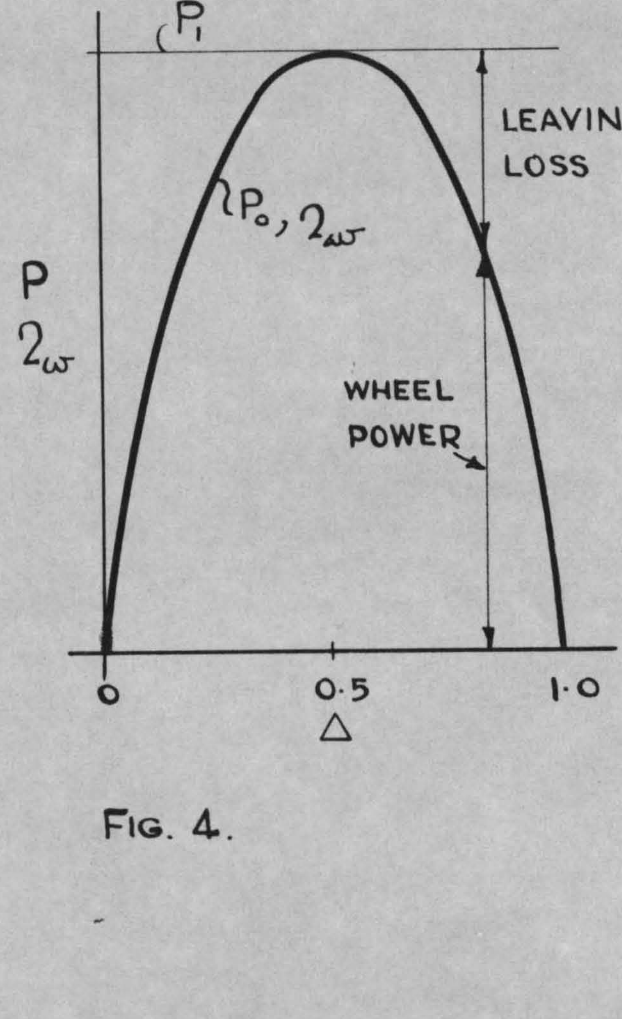

FIG. 4.

I. Tangential jet

In general, when $\theta_1 = 0$ and $m = 1$, in equation (10) the value of S becomes $(1 - 2\Delta)(1 + \frac{\cos \phi_o}{K})$. As is well known, $\Delta = 0.5$ for maximum efficiency, the speed ratio being independent of ϕ_o and K.

I(a) ideal case, Fig.3.

$$\theta_1 = 0, \quad \phi_o = 0, \quad m = 1, \quad K = 1$$

In equation (9), substitution leads to

$$\eta_w = 4\Delta(1 - \Delta)$$

When $\Delta = 0.5$, max $\eta_w = 1.0$

Notes. Fig.4.

1. η_w varies parabolically with Δ.
2. At max η_w, $\Delta = 0.5$, $v = u$ and $E_{rel} = 0$.
3. For any other value of Δ, $E_{rel} \neq 0$, efficiency falls and the total energy rejected appears as kinetic energy at discharge from the buckets. This is sometimes termed the "leaving loss".
4. Both in this case and the ideal case II(a) for max η_w it can be seen that m does not have to be unity as there is no leaving loss when ϕ_o is zero.

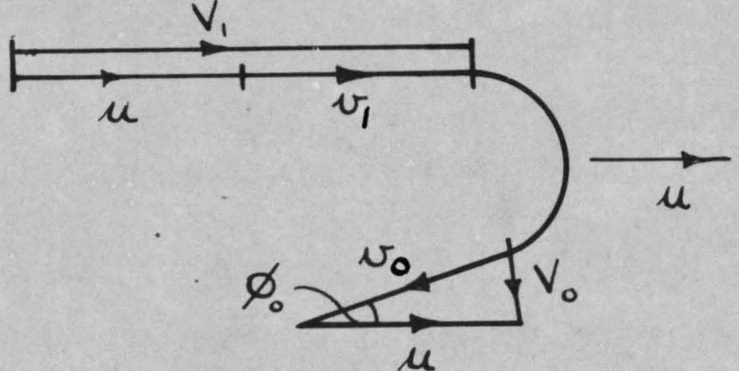

FIG. 5.

I(b), effect of inclined outlet and friction, Fig.5.

In practice V_o, and hence also ϕ_o, must have some magnitude in order that the fluid may leave the wheel without impinging on the following vane.

$$\theta_1 = 0, \quad \phi_o \neq 0, \quad m = 1, \quad K \neq 1$$

In equation (9),

$$\eta_w = 2\left(\Delta - \Delta^2 + \frac{\cos\phi_o}{K}\,\Delta\,(1-\Delta)\right)$$

$$= 2\Delta(1-\Delta)\left(1 + \frac{\cos\phi_o}{K}\right)$$

When $\Delta = 0.5$, max $\eta_w = \frac{1}{2}\left(1 + \frac{\cos\phi_o}{K}\right) < 1.0$

Notes

1. Optimum speed ratio is independent of ϕ_o and K.
2. Maximum η_w is less than the ideal case, I(a).
3. At max η_w, $E_{rel} = 0$.

II. Inclined jet.

Differentiating equation (9) with respect to θ_1 leads to

$$\frac{\partial\eta_w}{\partial\theta_1} = 2\,\Delta\,\sin\theta_1 \left[\frac{\Delta\, m\cos\phi_o}{K\sqrt{\left(1 + \Delta^2 m^2 - 2\,\Delta\,\cos\theta_1\right)}} - 1\right]$$

When equated to zero this gives the condition for maximum efficiency for values of θ_1.

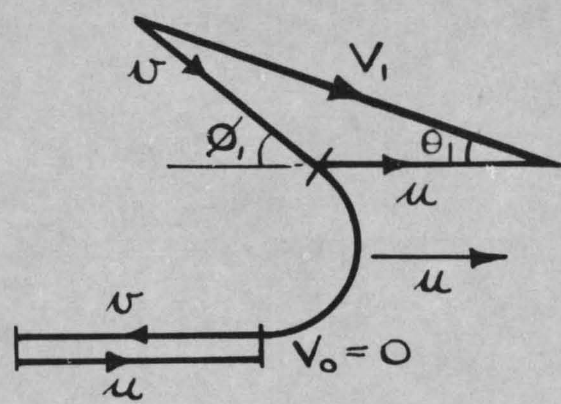

FIG. 6.

Then <u>either</u> $\theta_1 = 0$, representing the tangential jet, <u>or</u>

$$2\Delta \cos\theta_1 = 1 + \Delta^2 m^2 \left(1 - \frac{\cos^2 \phi_o}{K^2}\right) \qquad \ldots (11)$$

representing the inclined jet.

<u>II(a) ideal case,</u> Fig.6.

$\theta_1 \neq 0, \quad \phi_o = 0, \quad m = 1, \quad K = 1$

Substituting in equation (11), η_w is a maximum when $\Delta \cos\theta_1 = \frac{1}{2}$.

Then max $\eta_w = 2(0.5 - \Delta^2 + \Delta\sqrt{1 + \Delta^2} - 1) = 1.0$

For these conditions, in the inlet diagram, Fig.6,

$$u_1 = \frac{V_1}{2\cos\theta_1}$$

$$\therefore \quad v_1^2 = f_1^2 + (w_1 - u_1)^2$$

$$= f_1^2 + w_1^2 - 2w_1u_1 + u_1^2$$

$$= V_1^2 - 2V_1\cos\theta_1 \cdot \frac{V_1}{2\cos\theta_1} + u_1^2$$

i.e. $\quad v_1^2 = u_1^2$

$\therefore \quad \underline{v_1 = u_1} \quad$ and $\quad E_{rel} = 0$

Also $\quad \phi_1 = 2\theta_1$

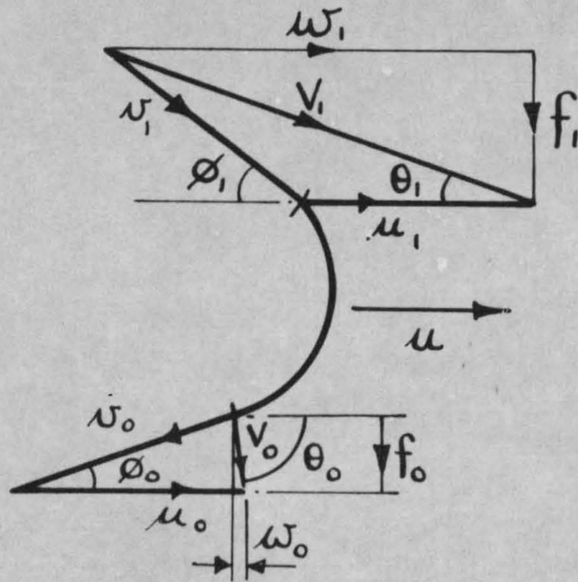

FIG. 7.

For the Turgo wheel on test, $\theta_1 = 20^\circ$ and the optimum speed ratio in the ideal case, $\Delta_{opt} = 0.532$.

Notes

1. The optimum speed ratio, $\Delta_{opt} > 0.5$ and its value is such that $E_{rel} = 0$ at both inlet and outlet.

In the following cases where the number of variables is increasing, equation (10) becomes more complex. Numerical values typical of the turbine under test have therefore been chosen for the variables and the equation solved graphically as shown in graph G.10.

II(b) effect of inclined outlet, Fig.7.

$\theta_1 = 20^\circ$, $\phi_o = 15^\circ$, $m = 1$, $K = 1$

In graph G.10, $\Delta_{opt} = 0.531$ and max $\eta_w = 0.98$.

Notes.

1. Introducing an outlet angle slightly reduces the optimum speed ratio and maximum efficiency. v_1 is slightly greater than u_1 and there is a small amount of relative energy.

2. For a condition of maximum efficiency, as the inlet angle is further increased the speed ratio rises; but as the outlet angle is further increased the speed ratio falls. In both cases the relative energy gains in value and the wheel efficiency decreases.

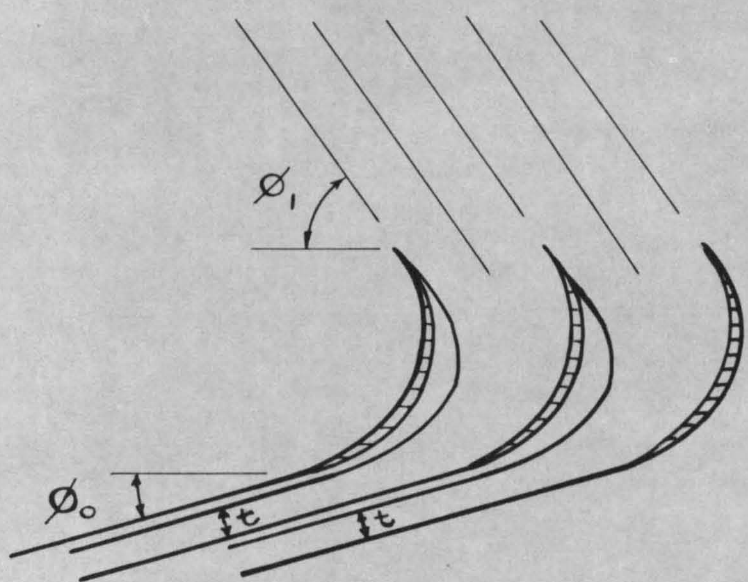

FIG. 8.

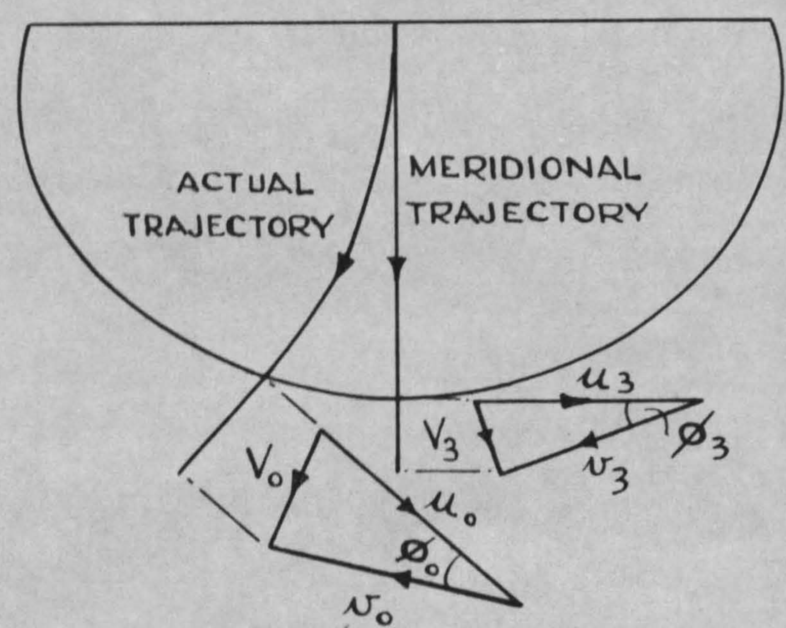
ACTUAL
TRAJECTORY
MERIDIONAL
TRAJECTORY
u_3
V_3
ϕ_3
v_3
V_0
u_0
ϕ_0
v_0

FIG. 9.

3. It is necessary for the fluid to maintain a free surface during its passage across the vanes and this is normally ensured by allowing the fluid to spread naturally in a lateral direction. However, it can be seen in Fig.8 that for a given film thickness the vane outlet angle has a lower critical valve. A typical u
average value for the vane outlet angle is 15°.

II(c) further effect of increasing mean radius at outlet.

Although the particles of fluid striking a turbine bucket all behave differently, the mean radius at outlet from a Turgo wheel is greater than the mean radius at inlet. Thus instead of discharging meridionally from the bucket, the fluid has in addition a radial velocity component which decreases the effective turning angle of the bucket as shown in Fig.9, i.e. $\phi_o > \phi_3$.

For this and other reasons, instead of following the blade angle, the fluid discharges at varying angles ranging from 15° to 40°. For the purposes of calculation, a mean value of 30° was chosen for ϕ_o.

For reasons to be given the minor axis of the jet ellipse at inlet was offset from the centre line of the wheel. Thus although the inclination of the jet to the plane of the wheel was 20°, mean values have been selected corresponding to the true centre of the jet, and on this basis $\theta_1 = 26^{\circ}$ and the mean radius ratio, $m = 1.3$.

Thus when $\theta_1 = 26^{\circ}$, $\phi_o = 30^{\circ}$, $m = 1.3$, $K = 1$,
in graph G.10, $\Delta_{opt} = 0.49$ and max $\eta_w = 0.87$.

Notes.

1. The increases in effective entry and exit angles, and in radius ratio, all contribute to a fall in speed ratio to the detriment of efficiency.

2. In the outlet velocity diagram when V_o is normal to u_o, relative energy = kinetic energy at discharge. This is not a necessary condition for maximum efficiency which is subject to the interaction of several factors, but the trend is towards this configuration. Increasing the value of $\emptyset_o$ implies a larger leaving loss, a lower maximum efficiency and an increasing amount of relative energy.

II(d) further effect of friction.

Data from the Turgo wheel under test gives an optimum speed ratio, $\Delta_{opt} = 0.455$, where u_1 is the peripheral speed of the centre of the jet ellipse at inlet and V_1 the mean absolute velocity. Using the same values for other variables, viz. $\theta_1 = 26^\circ$, $\emptyset_o = 30^\circ$, $m = 1.3$ substitution in equation (10) gives $K = 1.135$. Using these values equation (9) yields a maximum wheel efficiency of 0.78. This value should be compared with the test result shown in graph G.3 where max $\eta_w = 0.794$.

Notes

1. A further large drop in efficiency results from the effect of friction and spread.

2. Energy loss due to fluid friction entails a reduction in relative velocity below the ideal. Thus the condition of maximum efficiency requires an increase in relative velocity at inlet with a consequent increase in relative energy.

3. A graphical comparison of cases II(c) and II(d) is given in Appendix 2.

2.4 Interim Findings.

The major findings emerging from a study of one-dimensional flow may now be assessed.

1. The types of turbine under review attain their maximum efficiency in the ideal case when the relative energy of the fluid is zero.

2. For a tangential jet turbine the optimum speed ratio is independent of outlet angle and friction effects. In the case of the inclined jet turbine, increasing the outlet angle diminishes the optimum speed ratio and increases the relative energy. On this basis alone the inclined jet turbine is inherently less efficient than the tangential.

3. The incidence of relative energy has an unfavourable effect on the wheel efficiency. In the region of best efficiency, the velocity configuration at outlet is such that the relative energy at outlet is totally discarded in the form of kinetic energy.

4. The deleterious effect of raising the radius ratio, m above unity

is evident. An increase in peripheral velocity is accompanied by a corresponding increase in relative velocity and this incurs higher friction losses. The outward motion of the fluid and its further consequences are accounted for in the following section.

5. A computational survey could be performed on the basis of the one-dimensional theory by varying the parameters. However since so little is known of the parameters and their interaction, and because they represent only the mean condition of the fluid, such an exercise could give misleading results.

2.5 Analysis of the fluid at inlet.

2.5.1 General method.

This analysis was carried out graphically using the physical dimensions of the test apparatus as shown in photograph P.1, but the method is generally applicable. Diagram D.6 shows the geometrical layout of the wheel and jet at inlet and the graphical method employed.

The circular jet from the nozzle is shown impinging on the Turgo wheel at an inclination of 20° thus forming an ellipse in the inlet plane of the wheel. The centre of impact of the jet is offset from the wheel centre as shown.

To investigate the range of relative and peripheral velocities across the jet a series of points has been chosen, points 1 and 9 where the lip of the bucket enters and leaves the ellipse and points 2 to 8 equally spaced on the major axis. The bucket inlet profile is shown at point 1, and 2, 2' and 2" for example show points across the ellipse in such positions that all particles bearing this number enter the bucket at the same instant. A', A", B' and B" are additional points. The radius to each point on the major axis has been drawn and the peripheral velocity of the wheel at each point is normal to its respective radius.

It is appreciated that the total head of water is relatively small ($6\frac{1}{2}$ ft) and that the variation in head over the jet ellipse is about 4%. For the sake of simplicity a mean absolute inlet velocity has been assumed to apply at all points of the ellipse and this involves an error of about $\pm$ 1%.

The velocity diagram shows the components of the absolute velocity in the plane of the wheel (x'z') and normal to it (y'). In the plane of the wheel the peripheral velocities of all points on the major axis of the jet ellipse have been drawn and the components of relative velocity in this plane thus obtained. It will be seen that the velocity diagrams in the plane form an ellipse similar to that in the space diagram.

The effect of entry conditions is immediately apparent. On the inner boundary of the ellipse i.e. nearer the wheel centre, the peripheral velocity falls and the relative velocity rises, whereas on the outer boundary of the ellipse, the reverse occurs. Thus it is clear that the relative energy $(v_1^2 - u_1^2)$ varies across the minor axis of the ellipse, or in other words that a relative energy gradient has been established. Due to shearing stresses, this progressive change in relative velocities gives rise to a mixing effect as the fluid crosses the bucket surface tending to reduce the energy difference across the stream;

since higher relative velocities are nearer to the wheel centre, an outward turning moment is impressed on the fluid.

Moreover as the jet : wheel diameter ratio increases it can be seen that the overall difference in relative energy also increases. Hence the difference in relative energy grows larger with increasing specific speed.

In equation (3), $V_1^2 = v_1^2 - u_1^2 + 2V_1 u_1$ for tangential entry

$$\therefore \quad \frac{v_1^2 - u_1^2}{V_1^2} = 1 - \frac{2u_1}{V_1}$$

Taking (a) and (b) as the paths of jet particles respectively nearest to and furthest from the wheel centre, the relative energy differential may be defined as

$$\frac{v_a^2 - u_a^2}{V_1^2} - \frac{v_b^2 - u_b^2}{V_1^2}$$

$$= \left(1 - \frac{2u_a}{V_1}\right) - \left(1 - \frac{2u_b}{V_1}\right)$$

$$= \frac{2}{V_1} (u_b - u_a)$$

$$= \frac{2}{V_1} \left[\pi (D + d) N - \pi (D - d) N \right]$$

$$= \frac{4}{V_1} \cdot \pi dN$$

$$= 4 . \frac{\pi DN}{V_1} \cdot \frac{d}{D}$$

$$= 4 \left(\frac{u}{V_1}\right)\left(\frac{d}{D}\right) \propto N_s$$

It can also be shown that a similar relationship exists when the jet is inclined.

Relative energy differential is thus defined as a non-dimensional quantity which is independent of head but varies with specific speed.

Relative energy gradient may now be defined as

$$\frac{\text{relative energy differential}}{\text{jet diameter}} .$$

2.5.2 Jet position.

In jet type impulse turbines it is normally found that the turbine operates more efficiently if the mean point of application of the jet at inlet is offset along the major axis of the jet ellipse as shown in diagram D.6.

Several trajectories across the bucket surface have been drawn for ideal fluid particles entering the bucket at various positions (see section 2.6). As shown in diagram D.9 the trajectory of point 7 has a considerable radially outward component. This has no connection with the mixing effect of a relative energy gradient, since shearing effects are absent in the ideal fluid, but is due to the relative motion of the bucket during the time that the particle takes to cross the surface, and to the curvature of the bucket surface.

Comparing this with the ideal trajectory of point 5, the velocity diagram of the latter at inlet shows that the relative velocity has a radially inward component and the particle emerges at a smaller radius than at entry. The further a particle is removed from the centre line at entry along the major axis, the greater will be this radial component and in a real fluid this helps in resisting outward motion.

This advantageous characteristic however is accompanied by an increase in the magnitude of the relative velocity, an undesirable feature as friction increases in proportion to the square of this quantity. There is evidently an optimum position for the mean point of impact, where a balance is reached between these two main features.

2.5.3 Effect of jet position on relative energy.

Consider a typical velocity diagram. Referring to point 5 in diagram D.6, the relative energy at inlet = $v_1^2 - u_1^2$

$$= v_{y'}^2 + v_{x'z'}^2 - u^2 \qquad l_2^2 \quad l_1^2$$

$$= v_{y'}^2 + (l_2^2 + c^2) - (l_1^2 + c^2)$$

where c is a common distance.

$$= \text{const} + l_2^2 - l_1^2$$

But this applies to all points on the major axis of the ellipse. Hence the relative energy is the same for all points on the major axis of the jet ellipse. Similarly the relative energy will have a different but common value along any axis parallel to the major axis.

This means that the relative energy of a jet will not change due to any movement of the jet along the major axis. By the same token it is clear

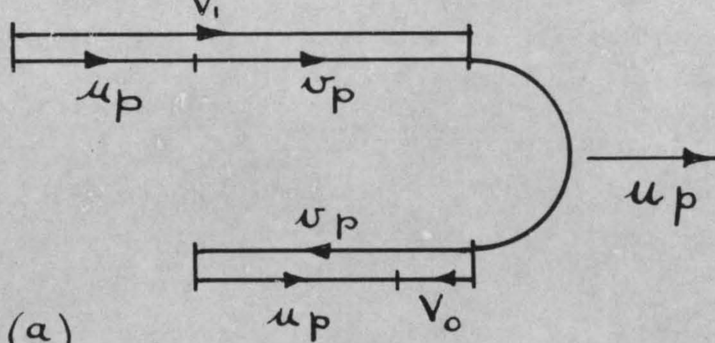

V₁
up
vp
up
vp
up
Vo

(a)

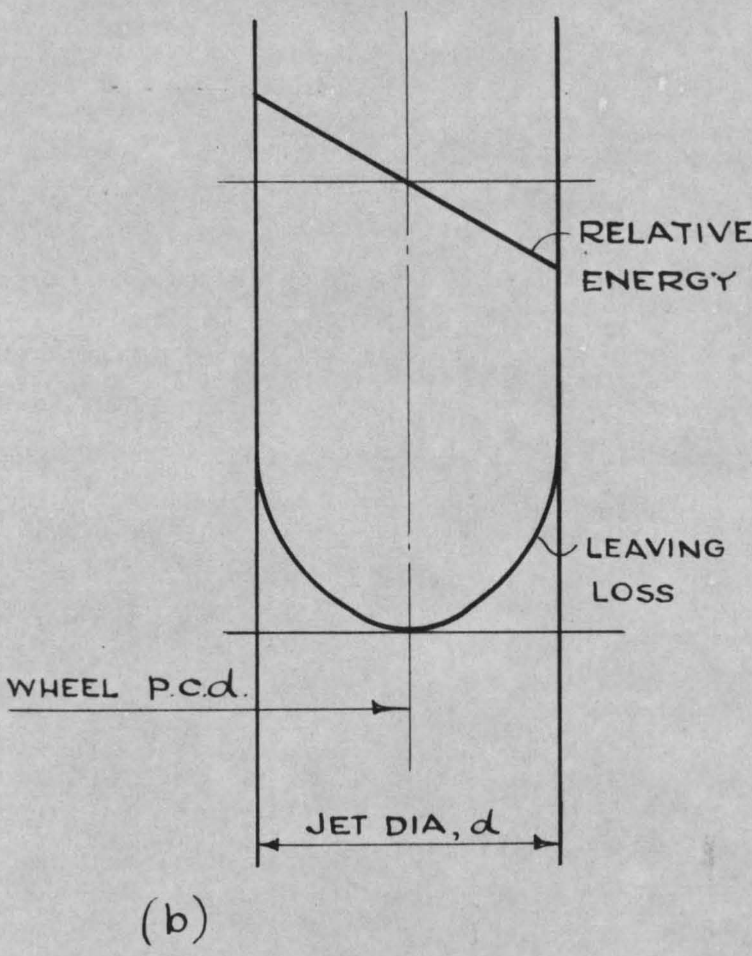

RELATIVE ENERGY
LEAVING LOSS
WHEEL P.C.d.
JET DIA, d

(b)

FIG. 10.

that no reduction in relative energy can be effected by attempting to reduce the length of the major axis of the jet ellipse, for instance by increasing the inlet angle, θ_1.

2.5.4 Relative energy differential

Apart from its effect on the radius ratio, m, no variation of relative energy across the jet has been taken into account in the analysis of one-dimensional flow. Consider again a jet of ideal fluid applied tangentially to a turbine runner. Retaining a one-dimensional basis and assuming that the motion of the centroid of the jet represents the condition of best efficiency, consider the action of any other particle entering the vane at the same instant at a different radius but on a parallel path, assuming that no spreading takes place. Let the motion of this particle be described by suffix p. Fig.10(a) shows the relevant velocity diagrams. In equation (3),

$$V_1^2 = (v_p^2 - u_p^2) + 2 V_1 u_p$$

$$\therefore \quad \frac{v_p^2 - u_p^2}{V_1^2} = 1 - \frac{2u_p}{V_1}$$

$\therefore \quad E_{rel,p} = V_1^2 (1 - 2\Delta_p)$, where Δ_p is the speed ratio of the particle. Then, since $\Delta_p \propto r_p$, E_{rel} varies linearly with radius.

Also, $V_o = v_p - u_p = V_1 - 2u_p$

$$\therefore \quad \frac{V_o}{V_1} = 1 - 2\Delta_p$$

$$\therefore \quad \frac{V_o^2}{V_1^2} = (1 - 2\Delta_p)^2$$

i.e. leaving loss varies parabolically with radius.

It can be seen in Fig.10(b) that even when the fluid is ideal, a relative energy differential has an adverse effect on the wheel output.

Reverting now to the use of a real fluid, graph G.8 shows the relative energy condition at inlet for the turbine under test. Owing to the high specific speed, the relative energy differential is large. In addition, taking into account other factors which have been discussed at some length, the mean relative energy at inlet is high. These two features are in large part responsible for the poor efficiency of a turbine of this type.

2.5.5 Effect of jet inclination.

Shipulin (8) deduces from a series of tests that 22.5° is the optimum value of the absolute inlet angle, θ_1. Increasing the angle above this value decreases the turning angle of the bucket thus reducing its energy potential. When the angle is reduced below this value Shipulin believes that decreasing efficiency is due to water striking the inside of the strengthening ring on the wheel. It appears however that a major factor influencing this trend is the increasing length of the jet ellipse, incurring higher relative velocities at the extremities and hence increased friction losses.

The wheel under test was designed for an entry angle of 20°, and this angle was maintained for all tests performed on the turbine.

2.6 Trajectory across a bucket surface.

Edel in his book on impulse water turbines (10) deals at some length with the path of a particle of ideal fluid, uninfluenced by external forces, across a curved surface. He deals firstly with the theory of motion across a static bucket of ellipsoidal shape then goes on to describe a part-analytical, part-graphical step-by-step method of approximating to the path across a bucket of irregular shape, taking the bucket motion into account. In this study, the latter approach has been used, but the method is entirely graphical.

When a jet of ideal fluid impinges tangentially on a vane curved in the direction of motion, it tends to spread laterally due to internal pressures within the fluid film. A pressure difference is experienced by all particles except those at the "centre of motion", and it is only to such particles that this construction can reasonably be applied. In addition, if the vane curvature is three-dimensional and irregular, the centre of motion of an ideal fluid will change during its passage across the vane surface. Despite these limitations, the method affords a basis on which a comparison between the real and ideal fluids may be made. The resulting paths bear a consistent relation to actual tests. Since there was no advantage to be gained by further repetition, the number of trajectories so produced was restricted to three, corresponding to positions 1, 5 and 7 of the inlet jet ellipse shown in diagram D.6.

2.6.1 Method of trajectory construction.

Assuming that the point selected represents the centre of motion of the portion of fluid being considered, the mean components of the relative velocity and the point of impingement at entry to the bucket, must be found. This has been done graphically in D.6 and the velocity components are listed together with the appropriate components of the relative inlet angle.

Diagram D.7 shows the geometrical details of the bucket design for this wheel. The plan view has been divided into a number of rectangles of suitable size and the sections dimensioned in relation to a datum x'y' plane. Hence a number of plane facets approximate to the curved surface of the bucket.

In the absence of shear effects the force exerted by the bucket surface on an ideal fluid will be normal to the surface curvature at any point, hence the trajectory will be orthogonal. In the same way the path of a particle across a rectangular plane element will be the line of intersection of a plane which is at once perpendicular to the element and in line with the relative velocity vector of the particle at the instant of impact. The trajectory across a plane element is thus found graphically by obtaining the true shape of the element and extending the projection of the velocity vector across it.

During the time required for the particle to cross the surface of the element, the bucket will have turned through an angle dependent on the

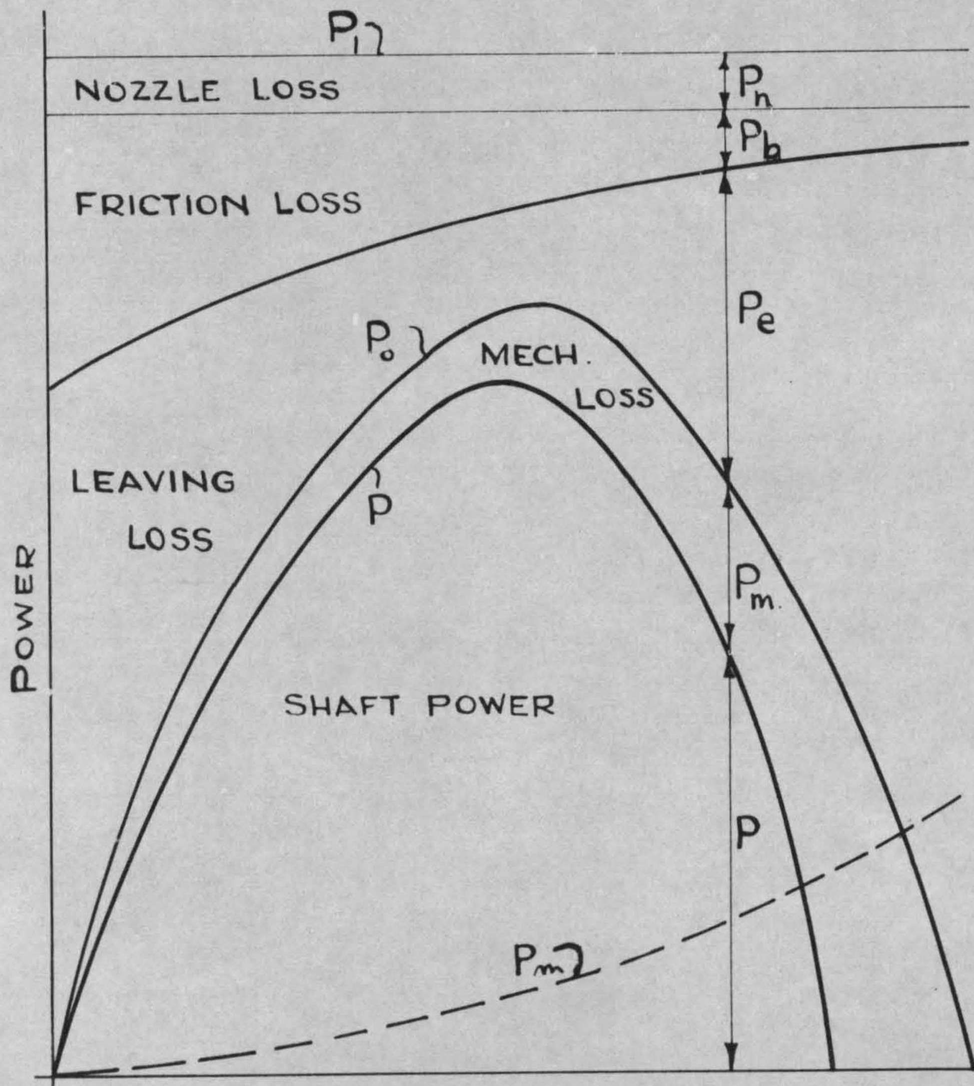

P_1
NOZZLE LOSS
P_n
P_b
FRICTION LOSS
P_e
P_o
MECH. LOSS
LEAVING LOSS
P
P_m
POWER
SHAFT POWER
P
P_m
Δ

FIG. 12.

speed of rotation and a correction has to be made to the direction of the vector before repeating the procedure on an adjacent element. In this way an allowance can be made for the wheel rotation during the passage of the fluid. The greater the number of facets the more accurate will be the result.

It has been shown that one effect of friction is to reduce the optimum speed ratio. If the mean trajectory of an ideal fluid is constructed using the optimum speed found in an actual test, it may be expected that the energy of the fluid at outlet will not have been fully utilised and the shape of the ideal outlet velocity diagrams bears this out.

A typical step in the construction is given in diagram D.8 and the trajectories so produced are shown together in D.9. Appendix 6 shows details of the construction.

2.7 Performance characteristics.

The distribution of power of a jet type impulse turbine may be assessed firstly, at constant head and flowrate but with varying speed; and secondly, at constant head and optimum speed, but with varying flow or load.

2.7.1 Effect of varying speed.

The first condition is illustrated in Fig.12. At a fixed nozzle opening the input power, P_1 and nozzle power loss, P_n remain constant. The wheel power curve is approximately parabolic in shape. The effect of

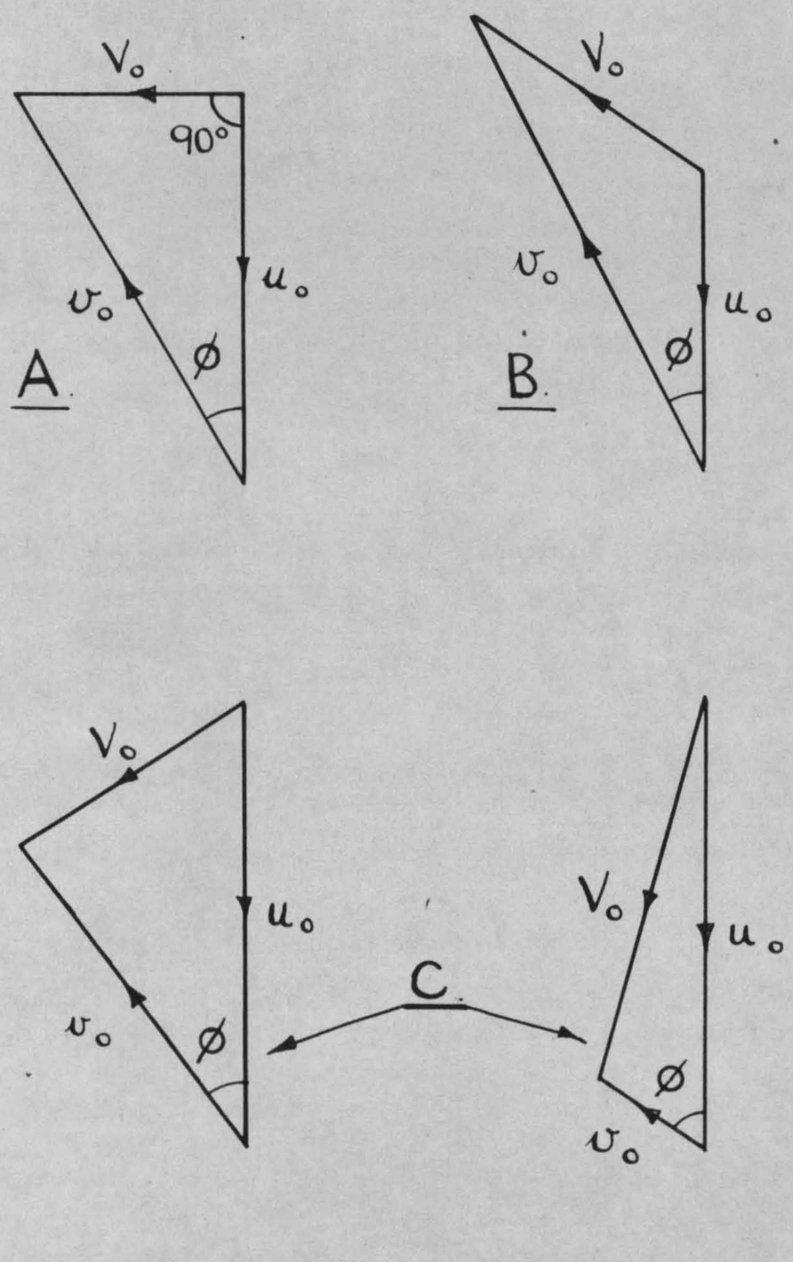

FIG. 13

mechanical power losses, which are discussed in section 2.7.3, is a further reduction in speed ratio for maximum shaft power and a reduction in "runaway" speed. Using an ideal fluid the remaining loss would appear as kinetic energy at discharge, but with a real fluid there is also a power loss due to friction. This latter is a maximum when the wheel is at rest and varies approximately parabolically as the wheel speed is increased, reaching a minimum at runaway speed.

For analysis it is convenient to divide the performance curve into three regions:-

A - region of maximum efficiency.

B - region of low values of speed ratio.

C - region of high values of speed ratio.

On a basis of one-dimensional flow, the velocity diagrams at outlet adopt the characteristic forms shown in Fig.13.

Region A. As the shape of the diagram is affected by several factors it is impossible to state categorically that V_o should be normal to u_o for optimum efficiency. In fact, for the one-dimensional study, the outlet diagram for case II(d) shows a tendancy to depart from this condition (see Appendix 2). Nonetheless the diagram is approximately of the form shown and the work component at outlet is small. When V_o is normal to u_o, at outlet the relative energy is equal to the kinetic energy.

Region B. This form of diagram may be considered a typical case of energy

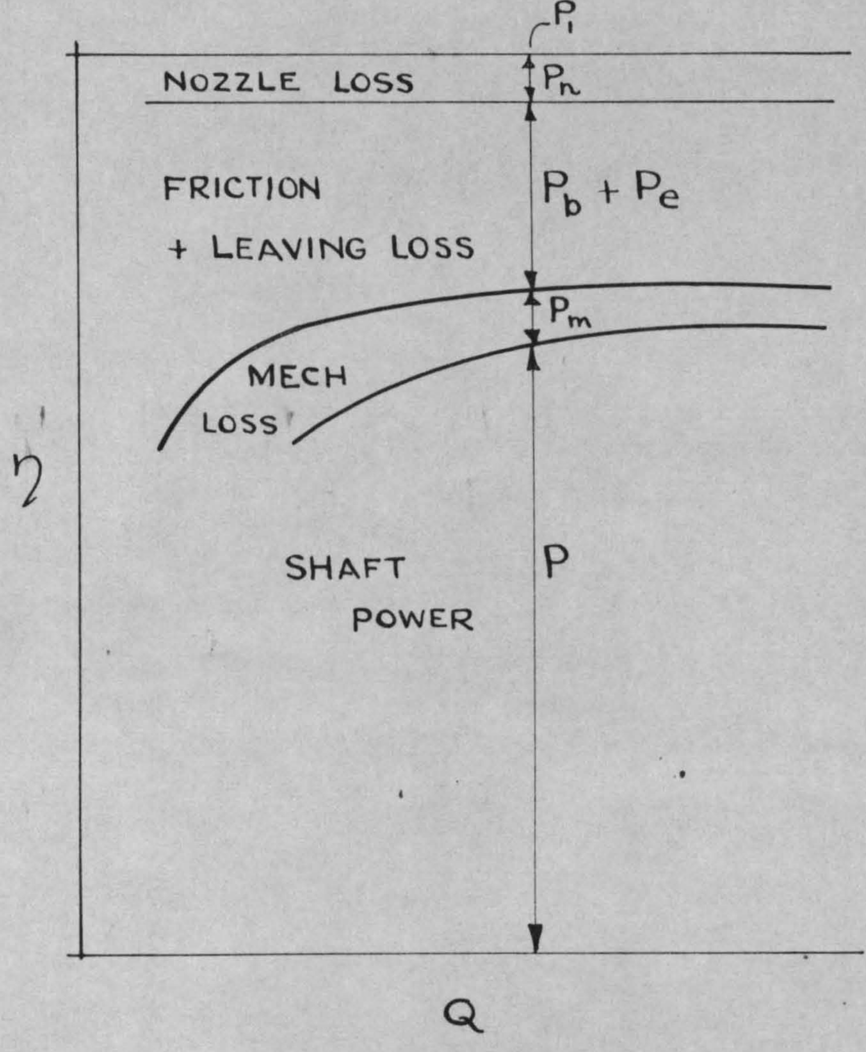

P_1
NOZZLE LOSS
P_n
FRICTION
+ LEAVING LOSS
$P_b + P_e$
P_m
MECH
LOSS
η
SHAFT
POWER
P
Q

FIG. 14.

under-utilised in the wheel. The relative velocity exceeds the peripheral and a considerable amount of relative energy is retained in the fluid.

Region C. In this case the diagram may be taken to represent energy over-utilised in the wheel. The relative velocity is less than the peripheral so that relative energy is again present. If the relative velocity of a particle becomes severely attenuated by friction then the absolute velocity at outlet increases and in the limit tends to the value of the peripheral velocity and power is absorbed into the fluid from the wheel.

2.7.2 Effect of varying flow.

The second basis of analysis is shown in Fig.14. In this case the optimum efficiency curve forms the envelope of maximum efficiencies at a number of different flowrates. A well-known characteristic of these turbines is that the overall efficiency is maintained near the maximum over a wide range of flow. As the speed ratio varies little over the flow range, the diagram may be taken to represent constant speed conditions. At this speed the mechanical losses may be considered nearly constant and so constitute a decreasing fraction of the input as the flow increases.

In constructing an energy balance, the shaft power, mechanical and nozzle losses can all be found by conventional means, but there are serious difficulties in determining either the friction or leaving loss by experiment. One of the cornerstones of this project is the use of an experimental method to assess the leaving loss over a range of flow embracing the condition of peak efficiency.

2.7.3 Analysis of mechanical losses.

It was no part of this project to subdivide the mechanical losses into component parts by experimental means. However, when evaluating the losses obtained at a low head from a turbine suitable for medium heads it is deemed advisable to consider the source of each part of the total loss.

The components of the external load imposed on the shaft bearings are the result of firstly, the weight of the runner and secondly, the hydrodynamic forces due to the pattern of flow through the runner. These forces cause a power loss due to friction in the bearings which is commonly assumed directly proportional to the shaft speed ratio.

The other power loss of a mechanical nature is due to friction when the runner disc and buckets spin in the air within the casing. This windage loss is proportional to the cube of the shaft speed.

Over the range of design heads it is probable that the pattern of mechanical losses relative to speed ratio will be preserved. However, when the head is very low, the weight of the runner exceeds the jet force and then the pattern is likely to be distorted. Thus the mechanical losses for the head used in these tests should not be regarded as typical for the turbine.

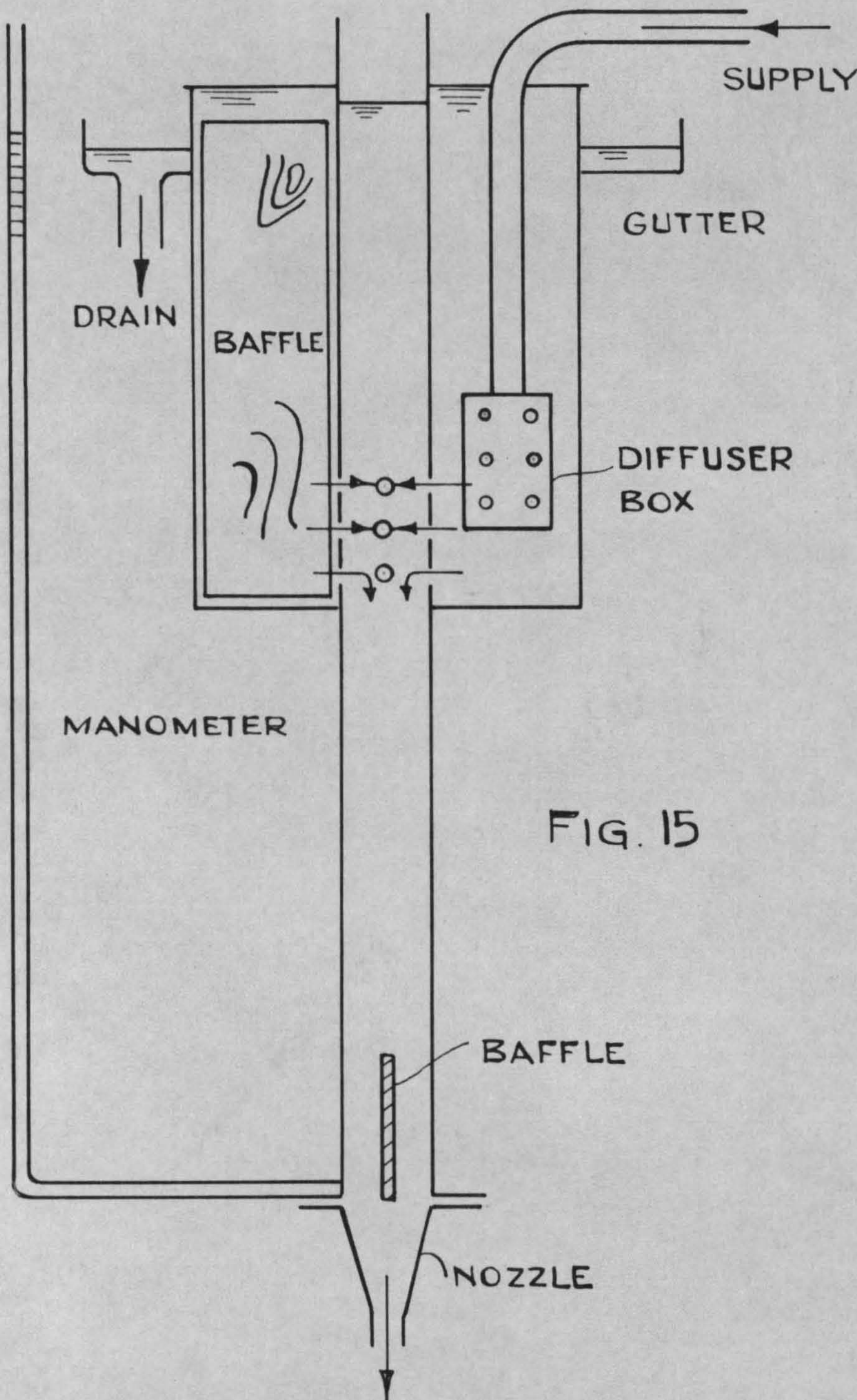
SUPPLY
GUTTER
DRAIN
BAFFLE
DIFFUSER
BOX
MANOMETER
BAFFLE
NOZZLE

FIG. 15

3. TEST EQUIPMENT

The installation was designed to provide a suitable range of flow of water at a low constant head for the purpose of performing tests on a standard 6 inch Turgo impulse wheel manufactured by Gilbert Gilkes and Gordon Ltd., Kendal. The wheel output was controlled by a variable speed electrical dynamometer. Individual parts of the apparatus are described in the following.

3.1 Water supply.

A low head of water was used (about $6\frac{1}{2}$ ft) since the fluid at discharge could thus fall to the sump without elaborate baffling arrangements and to ensure that experimental devices on the discharge side were not subjected to large hydrodynamic forces.

This head of water was provided by the arrangement in photograph P.1 which shows the header tank suspended by a frame secured to beams above. This method of mounting ensured free access to the discharge side of the runner as is well demonstrated in P.2.

Water was drawn from a large sump by a centrifugal pump and supplied through a 2 inch diameter pipe to the header tank. Fig.15 shows the baffles and diffusers designed to minimise turbulence and vortex effects which tend to distort the jet at outlet from the nozzle.

The head was maintained constant by allowing the water to flow over the top of the tank into a gutter around the periphery whence it drained back to the sump.

Water was led to the nozzle through a 4 inch diameter vertical pipe, and a simple manometer connected through the outlet flange indicated the pressure head upstream of the nozzle. Due to energy losses and velocity head this gauge reading varied slightly depending on the flow through the nozzle.

3.2 Flow control

The range of jet sizes suitable for the runner was spanned by the use of seven nozzles of different diameters graded to supply flowrates changing by equal increments under a constant head. These were cast in brass and as can be seen in photographs P.6 and P.7, were machined internally to give a smooth tapering profile, and externally to provide location.

The advantage of this arrangement was that, under the constant head, flowrates and coefficients of discharge could be determined accurately by a single calibration test, instead of recording the flow continuously.

Number 1 nozzle refers to the smallest nozzle in the range and the others are numbered in sequence with increasing diameter.

3.3 Runner

Photographs P.8 and P.9 show inlet and outlet views of the runner. Twenty buckets were cast in gunmetal integral with the hub and a rim provided support at the outer periphery. The jet was designed to impinge on the wheel at an absolute angle of 20° and since the nozzle was mounted vertically, the runner shaft was inclined at the appropriate angle as shown in P.3. The shaft was mounted in ball bearings in a frame with a flat horizontal base, the position of which could be adjusted in both axial and radial directions to obtain the correct setting of the runner relative to the nozzle. Such details can be distinguished in P.1.

3.4 Flow diverter.

It was frequently necessary to interrupt the flow of water from the nozzle on to the runner in order to change the position of some measuring device. To fulfil this purpose without stopping the pump a flow "diverter" was developed which could be swung on a hinge to intercept the jet just below the nozzle and lead the water to the sump. The flow diverter can be seen to the left of the runner in P.2.

3.5 Power measurement.

A variable speed electrical dynamometer was used for power testing and speed control. When absorbing power, the dynamometer was used as a generator but it could also be used as a motor irrespective of the power of the jet. This motoring facility was used not only to assess mechanical power losses but also when the energy contained in the jets was insufficient to drive the wheel at the required speeds.

As can be seen in photograph P.3 the belt drive enabled the

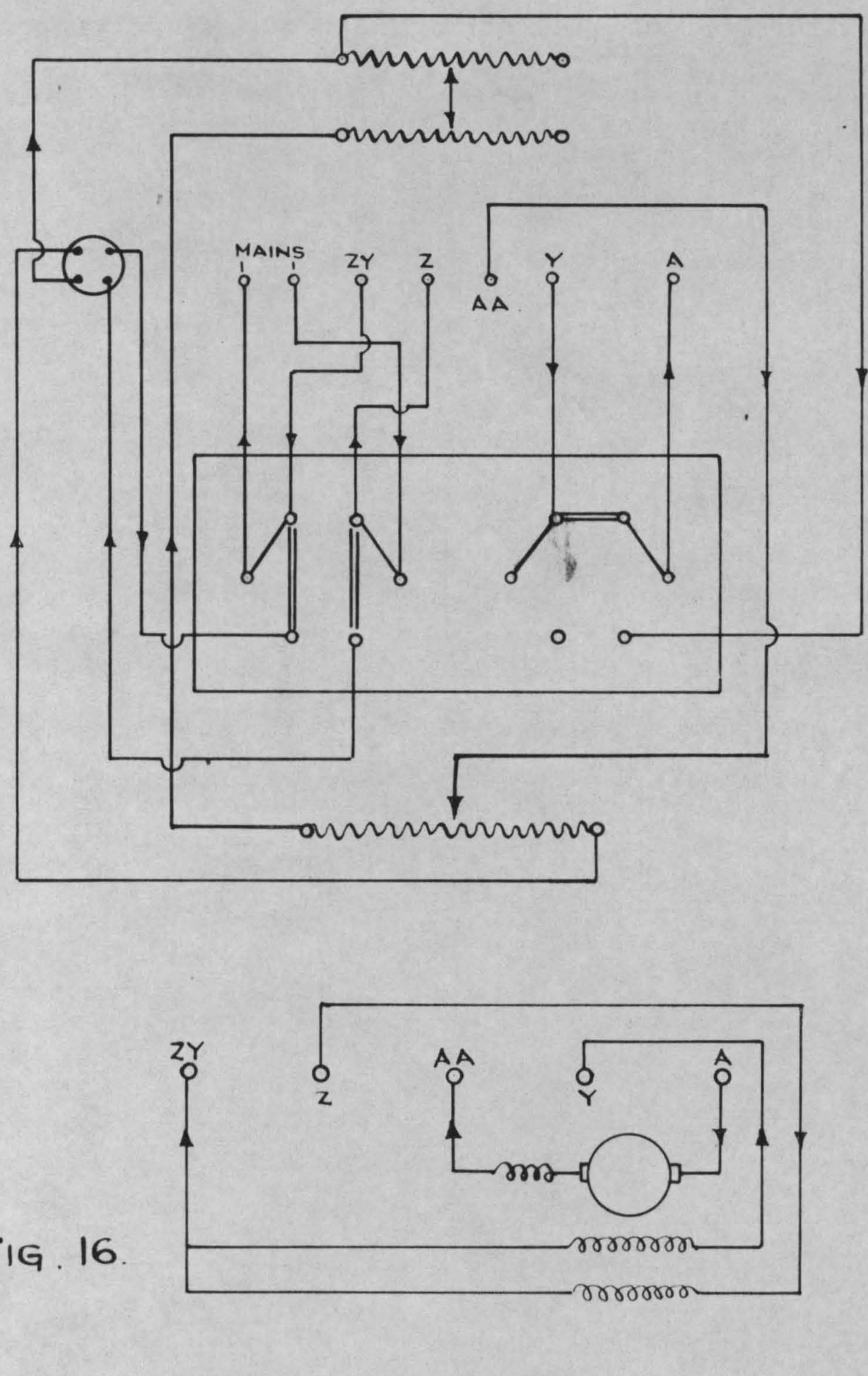

FIG. 16.

dynamometer and wheel shaft to be mounted as one unit, a useful feature for the purpose of lining-up. The dynamometer was a direct-current machine rated $1\frac{1}{2}$ h.p. The shaft was mounted in trunnion bearings and horizontal arms were fixed to the casing to measure the torque on the stator. The weights used to apply the resisting torque were suspended on carriers and transmitted to the torque arm through the pulley arrangement shown to ensure that the forces acted in the plane of rotation of the arm.

The speed of the runner was controlled by rheostats in the field and armature circuits of the dynamometer. The circuit diagram is shown in Fig.16.

3.6 Speed measurement

The rotational speed of the wheel was recorded by a digital frequency meter, which was connected to a magnetic transducer receiving impulses from a gear wheel with 60 teeth mounted on the wheel shaft. The speed was thus read directly in revolutions per minute. Details of the transducer and gear wheel are clearly depicted in photograph P.3.

4. DEVELOPMENT OF MEASURING DEVICES

Photographs P.10 - P.13 inclusive give pictures of the discharge from the Turgo wheel when using No.6 nozzle and running at the optimum speed. These represent views as seen firstly, by the eye and secondly, with the aid of a stroboscope. The irregular confines of the flow and the layering effect as the water is discharged from each bucket in turn, are immediately apparent. The mean conditions are steady to the extent that, at any point on the generated discharge surface, for identical bucket shapes, the absolute velocity, direction and rate of flow from any bucket will remain constant. Devices for measuring these three quantities at any point on this discharge surface had to be developed, since a knowledge of flow and velocity was necessary for the assessment of leaving loss. In addition, the direction of flow was required to construct the outlet velocity diagram.

4.1 Device for measuring flow

In the design of this appliance attention had to be paid to the following points. The water discharged in diverse directions with both axial and radial components. For the purpose of comparison, the flow at any point had to be directed through an aperture of constant cross-section, i.e. the flow per unit area or flow density was measured. Care had to be taken in the design of the collector or "separator" to ensure that the flow passing through the aperture was able to discharge freely downstream. In addition means were required to enable the separator to be positioned at any point in the discharge area.

The ultimate design is shown generally and in detail in photographs P.14 - P.17 inclusive. As shown in P.17 the aperture was rectangular in shape, measuring nominally $\frac{1}{2}$ in $\times$ $\frac{1}{4}$ in, but the longer edge could be reduced if required. The sides of the separator leading from the aperture were tapered outwards to ensure that the collected fluid was not reflected back into the main stream, but directed to one of two outlet ports. These ports were arranged at right angles so that, whatever the position of the separator relative to the wheel, water could discharge freely from one port through a large bore plastic tube and the other port was plugged. The flow was thus collected and transferred to measuring cylinders.

In order to change the position of the separator in a radial direction it was attached to a follower and mounted on a cam geometrically similar to the outlet edge of the buckets as shown in P.15. This cam had two guiding edges and the follower was fitted with two adjusting screws contacting the edges of the cam, so that a positive location could be retained when clamping the follower to the cam in any position. As the photograph shows there were nine positions marked as test stations at half-inch intervals along the outlet edge of the bucket and a corresponding mark for setting purposes along one edge of the aperture.

In order to traverse the discharge area circumferentially the cam was mounted on a bracket containing two bearings, one fitted to the wheel shaft and the other to a stub shaft on the runner locknut. The whole apparatus could thus be rotated about the centre of the runner. A pointed fitted to the bracket indicated the angular position on a large wooden protractor fitted to the header tank frame.

Care was taken to check the following features to ensure correct positioning and alignment of the apparatus. The bearings were lined up and located to the bracket in such a way that the aperture centre line traced a radial path relative to the runner as the separator moved along the cam. The protractor had to be secured at an angle of 20° in order to lie parallel to the plane of the wheel, and was aligned to the wheel in the vertical plane by the use of a plumbline. Also the pointer, mounted on the bracket parallel to the cam, had to be horizontal in the 90° position.

Finally the angular position of the bracket was controlled by two fine wires suspended over pulleys and fixed by clamps at convenient points remote from the discharge area. These wires can be detected in P.14.

4.2 Device for measuring absolute velocity.

Devices have been developed for measuring the velocity of pulsating flow. When the flow is also discontinuous, a visual method of measurement becomes possible, using the camera or stroboscope.

Photographs P.11 and P.13 show the layers of fluid cascading from the buckets. The first requirement made of any device is that it should allow the flow, at a desired position on the discharge side, to pass undisturbed and with its direction unchanged. Secondly, it should divert the surrounding flow away from the vicinity of the selected position. The ultimate solution was the metal cone shown in P.18. When a cone of this nature was placed close to the outlet side of the wheel in the stream, it was found that any movement of the cone about its apex had no effect on the direction of the discharge. Thus if the direction of the cone were adjusted until the fluid passing through the orifice adopted a central position, the cone would in addition give a means of measuring direction.

It will be seen that this original or "development" cone had a large orifice at the apex. Tests were performed to find the best size of orifice since, in regions of low flow density, drops which were too small quickly dispersed, and in regions of high flow density, drops which were too large tended to merge. These tests involved observing the discharge from various regions through a number of small auxiliary cones attached to the apex of the master cone. A hole size 9/32 inch diameter proved suitable for inspecting the discharge at any position.

An observer viewing the water discharging through the cone orifice with the aid of a stroboscope flashing once per revolution of the wheel would gain an impression shown typically in P.20. The row of drops represents the discharge from adjacent buckets. Provided the wheel speed and rate of flashing remain synchronised, the series of drops will appear at rest; moreover because of minor differences due to the casting process, each drop will retain an identity which renders it distinguishable from its neighbours. The drops elongate in the plane of the velocity diagram reflecting the range of variation in the angle of discharge as the tip of the bucket sweeps across the orifice.

As indicated by the arrow in P.18 a perspex tube of small bore was secured in a position coincident with the cone centre line by means of the bracket attached to the cone wall. A graduated scale of rectangular section was supported in such a way that it could revolve about the tube and also move along its own axis. Attached to this scale was a small fixed pin of adjustable length and a longer pin capable of moving relative to the scale. The way of using this device was to align the small fixed pin with a drop newly emerged from the cone orifice, taking care that the pin should not touch the drop, then to align the longer pin with another drop several pitches away and to measure the distance between the pins. As a rule the pitches were nearly equal and each pitch represented the distance travelled by a particle in the time for one bucket to move to the position occupied by its neighbour, thus providing a simple means of measuring the velocity of the particle.

Owing to inevitable inaccuracies in the runner casting, neither the shapes of the buckets nor their positions relative to the wheel centre were uniform and variations occurred between drops at any test station not only in velocity, but also in direction. Because of this it was difficult to obtain observations which would give valid average values, and refinements were sought which would improve both the method and results.

These refinements are described in the following. In the first place, due to minor changes in wheel speed it proved impossible to synchronise the flashing frequency with the wheel speed by hand control. This problem was surmounted by using a contactor fixed to the free end of the runner shaft to actuate the stroboscope. Secondly, the angular position or phase of the contact could be controlled by rotating the contactor head, and by this movement the row of drops could be made to appear to move either away from the orifice or towards it. An alternative method of measurement at once suggested itself. As shown in P.23 a protractor was attached to the contactor head which was rotated, and the angle of rotation corresponding to the movement of one drop between the two scale pins, was found relative to a fixed pointer. This angle was checked for the movement of several drops emanating from different buckets around the periphery to obtain average values of velocity for each position under test. Although this method was eventually chosen as a means of obtaining velocities, yet another approach was partially developed.

If the stroboscope flashes at a rate slightly lower than the rotational speed of the wheel the drops appear to advance. Then if this frequency ratio is known and the time is taken for a characteristic drop from a bucket to advance a known distance the velocity of the drop can be found. P.24 shows how this concept was initially developed. The contactor was attached to a lay shaft, belt driven from the main shaft, the driven wheel being made of wood to facilitate changes in diameter. For the optimum speed of the runner, a speed ratio of the order of 101 : 100 was found suitable. Had this method been used, gear wheels would have been necessary to maintain the correct ratio. In the event it was found that the measurement of the time interval was subject to too large an error, and in any case the first improved method was quicker and more flexible.

The cone used for test purposes was derived from the development cone with the following differences. The apex angle was reduced from 90° in the development cone to 70° to enable tests to be made closer to the shaft nut. The perspex bracket supporting the central tube was simplified to cause less visual interference in certain positions as is shown in the photographs P.25. The measuring pins were fixed 3 inches apart, a compromise between the minimum distance required to achieve some degree of accuracy and the maximum distance, for certain flowrates, prior to the dispersal of the drops. The design of the mounting bracket is shown clearly in P.19 whilst P.21 shows the bracket mounted on the shaft at the entry side of the runner, and also the method of securing the cone.

The cone could now be fixed in position by rotating the mounting bracket to the required angle and aligning the orifice to the required traverse mark on the bucket. The cone also had to be able to move about the orifice in any direction without shifting the position of the orifice. This was achieved by hinging the cone at two points in line with the orifice each giving angular motion in a plane normal to the other. The top hinge was attached to a single support on the cone, thus increasing the angular range of movement by setting the cone in the alternative positions shown in P.21 and P.22.

Care was taken in setting up this appliance to ensure that it was aligned with test stations identical to thos used by the flow measuring device.

4.3 Device for measuring direction.

After discharging from the runner the water fell to the sump under the floor through a large circular hole. It has been shown how the cone was used to determine the direction of flow at any position on the outlet side of the runner. The means of measuring this angle will now be described.

In photograph P.26 angle supports can be seen projecting from the base of the wheel frame. The angles were adjusted until they lay in the same horizontal plane and were parallel to each other and to the horizontal projection of the wheel shaft.

A large sheet of plywood, 36 in x 32 in x $\frac{1}{2}$ in thick, was varnished to seal it from water, then covered by a sheet of squared graph paper retained and sealed by a sheet of perspex 1/16 inch thick, fixed around the edges with waterproof tape. Machined wooden blocks were secured to the underside of the board and carefully aligned so that when the board was in position on the supports with the blocks along the edge of one angle, a grid was available with lines parallel and perpendicular to the vertical plane through the shaft centre line. (see P.26 and P.27).

A column was now made up with the base machined flat and square on all sides. The column was vertical and round in section with a locating keyway machined along its length. A horizontal protractor was located by this slot and was thus restricted to vertical motion.

A plastic bush to which was attached a horizontal pointer, was mounted above this protractor and was able to move in both angular and vertical directions. The angle in the vertical plane was determined with the aid of a protractor fitted with a spirit level and, as shown in P.27, with a hollow perspex tube aligned to that angle.

The method of measurement was then in the following sequence. The cone was set in the required position adjusted about its hinges until the line of flow of the drops lay along the cone centre line. This was done by eye and due to the effect of gravity, the centre line had to form a tangent to the flow trajectory at the orifice. The diverter was then used to interrupt the flow from the nozzle to the runner, the board was placed in position and the column set up as shown in P.26 with the base sitting squarely on the graph paper. Final alignment was achieved by inserting a slack fitting needle through the perspec tubes, on the cone and protractor, which were of the same bore, and clamping the bushes to the column before noting the required angles.

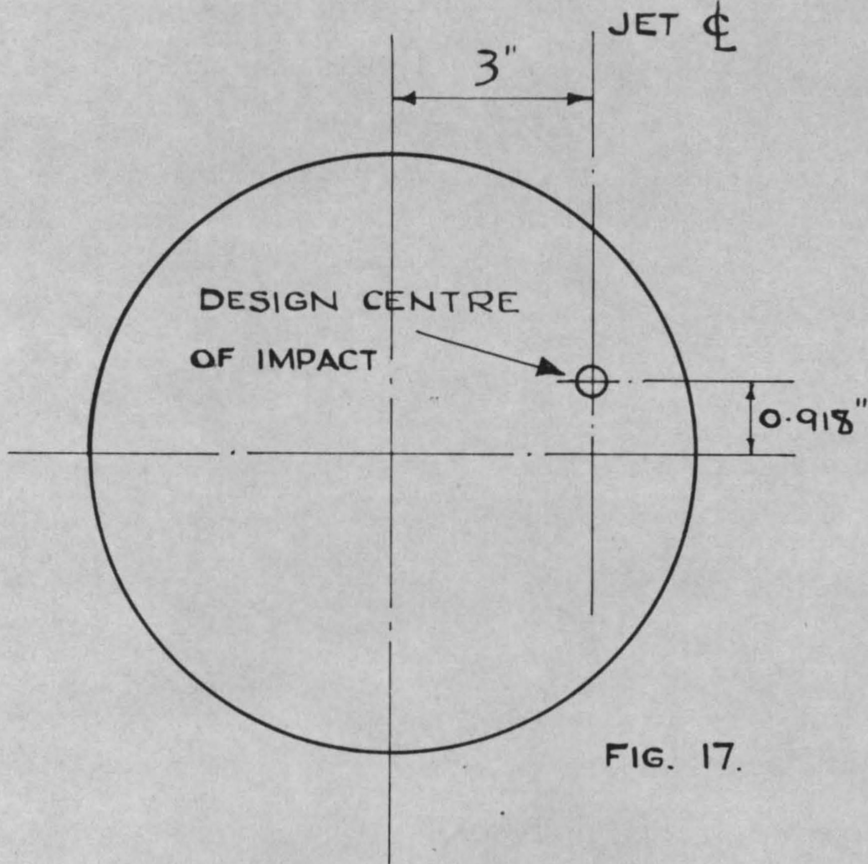

FIG. 17.

5. PROCEDURE.

5.1 Nozzle calibration.

During these tests, for each nozzle the head was maintained constant, hence it was possible to determine, by means of one test, the flowrate corresponding to this head and the coefficient of discharge in the event of a change in head.

The flowrate was measured by weighing the discharge over a period of time varying from 2 to 5 minutes depending on the tank capacity and nozzle size. This test was repeated several times under identical conditions and a mean rate obtained for each nozzle.

Photograph P.5 shows the apparatus used for this test. A large capacity tank was mounted on a weighbridge which was checked for accuracy with several weights of known value. With the runner removed a pipe of large bore with a bend at one end was suspended from wires so that it could be swung to intercept the jet.

The flowrates and coefficients of discharge are tabulated in Appendix 3 together with a specimen calculation.

5.2 Alignment of nozzle and runner.

As explained in section 2.5.2, there is an optimum position on the wheel inlet surface where the centre of the jet should impinge. Fig.17 shows the design position for the wheel under test. Power tests performed with small variations in the position of the jet showed in all cases a reduction in shaft output.

As the outside diameter of each nozzle at outlet had been machined concentric with the bore, this was used as a spigot for the nozzle centring jig illustrated in photograph P.4. A pin mounted in the centre of the jig could be adjusted vertically and secured by a screw.

Another jig mounted on the wheel shaft consisted of a centre-rule held in position against the shaft and a slide containing a distance gauge. With the rule held horizontally, and with the slide and distance gauge at appropriate settings, the position of the wheel was adjusted (see section 3.3) until the points of the distance gauge and the nozzle pin coincided with the inlet edge of any bucket.

5.3 Power tests.

5.3.1 Shaft power output.

Tests were run to obtain the power at the shaft for the range of flow covered by the seven nozzles. For each nozzle, readings were taken of output torque at intervals of 20 rev/min between 200 and 400 rev/min as it was known that the optimum speed, around which subsequent tests were centred, lay within this range.

In the case of the larger nozzles the power in the jets was sufficient not only to overcome mechanical losses but also to generate power over the required speed range. The two small jets however possessed insufficient energy at the higher speeds in the range, and the wheel shaft had to be motored to obtain the desired readings.

5.3.2 Mechanical power losses.

Tests were performed to evaluate the overall mechanical power loss by motoring the runner on its shaft, again between 200 and 400 rev/min. As the measuring equipment was somewhat insensitive to the small range of torque, readings were taken at increments of 40 rev/min.

As the head remained constant, ideally one test should have been sufficient to determine how mechanical losses varied with speed. Due to changes in temperature affecting the viscosity of the bearing lubricant, considerable variations were observed in these losses from tests performed at different times, but the wheel power curve remained unchanged. This factor increased in significance with decreasing output, and in consequence, this test was repeated in conjunction with each shaft power test.

5.3.3 Presentation of power tests.

Experimental results, calculations and graphs have been given in detail for No.6 nozzle only as the conditions produced by this nozzle were nearest to the point of best efficiency. Thus graph G.1 shows the variation of torque and power over the test speed range. It will be noted that the wheel torque, T_o has been obtained by adding the shaft output torque, T to the torque due to mechanical losses, T_m and the power curves have been constructed in the same way. The linear nature of the torque/speed relation can be observed, also that the effect of mechanical losses is a reduction in the speed ratio corresponding to maximum efficiency.

An indication of how the wheel torque and power vary with speed over the whole range of output is given in G.2. It will be seen that the speed corresponding to maximum output remains nearly constant at 330 rev/min for nozzles 3 to 7 inclusive.

Graph G.3 gives the non-dimensional variation of wheel efficiency against capacity coefficient. The efficiency remains high over a range of about 80% of the capacity of the turbine. The wheel efficiency is of interest in this study, as attention is mainly directed towards leaving and friction losses and to a much lesser extent towards nozzle and mechanical losses, etc.

Graph G.4, which shows the wheel characteristic, gives a commonly used basis of comparison with other types of turbine. Due to factors explained in sections 2.7.3 and 5.3.2 this characteristic is based on wheel output and shows that the point of optimum hydraulic efficiency would occur at a capacity somewhat greater than that given by No.6 nozzle. The low value of the maximum efficiency is at once apparent.

5.4 Condition of the fluid at outlet.

5.4.1 Method of presentation.

The marks at half inch intervals on the outlet side of one of the buckets, shown in photograph P.15, were numbered in sequence from 1 to 9 moving radially outwards. When the wheel was spun these marks traced out concentric circles and the measuring grid was formed when these circles were intersected by radial lines equally spaced at 5° intervals.

The results could have been presented graphically to a base of either the radial lines or the circles, but a far more comprehensive picture is obtained when they are given in the form of contours on a grid chart. The grid envelope is three-dimensional in form but this has been represented in a plane by developing the bucket edge, thus distorting the generated area particularly in the region of the outer radii.

5.4.2 Measurement of flow.

The apparatus described in section 4.1 was mounted on the wheel about the runner. The separator was moved round the cam until the mark on the collector box was in line with position No.1 on the edge of the bucket. When it had been adjusted as close as possible to the wheel without touching it as it rotated, the separator was clamped in position.

With one of the nozzles suitably mounted the turbine was set to generate power at the optimum speed of 330 rev/min and this speed was maintained throughout these tests. The separator bracket was secured in a selected angular position and when the discharge of water from the separator became uniform, it was collected over a period of one minute; this time interval gave a reasonable range of flow, adequate to ensure repeatability and was adopted as standard for all positions. The quantity thus collected was measured in graduated cylinders and an average of three readings was taken.

The bracket was now swung through 5° and the procedure repeated. In this way the surface was traversed for position 1 between the boundaries of flow at outlet. Similar traverses were performed for positions 2 to 9. The whole test was repeated for nozzles 3 to 7 inclusive, since nozzles 1 and 2 did not exhibit characteristic features as can be seen from the performance graphs. The flow density for nozzles 3 to 7 is presented in contour form in charts C.1 to C.5.

5.4.3 Conversion to flowrate.

Since the discharge over the outlet region was collected through an aperture of constant area, these flow readings have been categorised as "flow densities". To determine the total flowrate emanating from the wheel, a proportional share of the outlet area had to be allocated to each grid intersection point. The flowrate for each point was then determined by multiplying the flow density by the appropriate factor. A valuable check on the effectiveness of the apparatus was obtained by summing the individual flowrates and comparing the total with the flow from the nozzle. This summing process gave a total discharge within $2\frac{1}{2}$% of the flow at entry for nozzles 5, 6 and 7, but the error was 5% for nozzle 4 rising to 6.4% for nozzle 3. Thus the selected angular and linear grid intervals are justified for the larger nozzles but for greater accuracy would have to be decreased for the smaller nozzles.

5.4.4 Turbine head.

In practice the tail race level of an impulse turbine may be expected to vary, but for a high or medium supply head this variation is relatively small and the efficiency scarcely affected. However in the case of these tests where the supply head was very low, a tail race level had to be selected to give an overall head which would afford a valid comparison with practice. This condition would be fulfilled if the mean level of discharge were taken as the tail level. Accordingly the head at each grid intersection point was multiplied by the corresponding flowrate and the product divided by the total flowrate to obtain the mean head, i.e. $H = \dfrac{\Sigma(qh)}{\Sigma q}$

5.4.5 Measurement of absolute velocity and direction.

The cone was mounted on its bracket about the wheel shaft. An endless string wound several times round the contactor head gave a remote means of controlling the phase of the contact relative to the shaft. It can be seen in photograph P.3 that the protractor scale was marked off in twenty equal divisions, representing the number of buckets on the wheel.

The cone was set close to the discharge side of the wheel with the traverse mark on the bucket bisecting the orifice. For a selected test nozzle the wheel was set to generate power at the optimum speed and water spouted from the orifice, the rest of the discharge being swept away from the point of observation. The cone was now swivelled about its hinges until the spout lay tangent to the cone centre line. When the stroboscope was set flashing, the spout appeared as a series of static drops. A drop was selected for test and moved in line with the smaller pin by rotating the contactor head. The angle on the protractor was noted then the head again rotated until the drop moved into line with the larger pin. The corresponding angle was observed and the angular change of the wheel corresponded to a linear movement of 3" of the drop. This procedure was repeated for two other drops emerging from buckets selected around the wheel and hence a mean value of velocity was obtained. When this had been done the horizontal and vertical angles of discharge were measured in the manner explained in section 4.3. In this way velocities and directions were measured for all grid intersections where flow had been recorded, within the limitations of the apparatus.

There were two disadvantages to this method of measurement. The first was that when the flow was less than 50 in^3/min (cf. maximum 210 in^3/min), the drops were small and dispersed too rapidly to obtain a measure of velocity. Secondly, when the angle of discharge was less than half the cone angle, it was impossible to take readings. Fortunately, in the main, these features occurred together at the bottom of the discharge area. The flowrate in this region had been determined and the trend of the velocities was sufficiently clear to enable the leaving loss to be estimated. For example, for nozzle 6, the percentage flowrate in the region of unrecorded velocities was 13.8%, leading to an uncharted leaving loss of something less than 6%.

These tests were performed on nozzles 4 to 7, but as a trend was clearly established the test was not repeated for nozzle 3. The variation in absolute velocity is shown for each nozzle in contour form in charts C.6 to C.9.

5.5 Leaving loss and energy balance.

Knowing the flowrate and absolute velocity at each grid intersection on the discharge side, it was possible to calculate the leaving loss for each point and obtain the total by addition. These results are shown in detail for nozzle 6 and in contour form in chart C.14. The distribution of energy at the optimum speed on a quantitative and percentage basis are shown relative to the input power in graphs G.5 and G.6, the hydraulic loss being obtained as a difference. In order to compare the hydraulic loss with the leaving loss, a separate graph G.7 has been prepared. This shows that the leaving loss increases gradually to a maximum with increasing jet size. The hydraulic loss on the other hand decreases sharply to a minimum at about the best efficiency point then starts increasing again. The numerical values in the energy balance are shown in Appendix 3.

5.6 Outlet velocity diagrams.

With a knowledge of rotational speed and radius, absolute velocity and angle of discharge, enough information was available to draw an outlet velocity diagram for each outlet station. The method of drawing these diagrams involved changes in axes of reference and is described in Appendix 5. Using the data obtained for nozzles 5, 6 and 7, over two hundred diagrams were drawn, details from which have been presented in the form of charts. Diagram D.1 gives a pictorial guide to the notation used and D.2 shows the various forms of outlet diagram encountered, again with notation. D.3, D.4 and D.5 show the actual diagrams and the construction for various positions, representing types A, B and C as defined in section 2.7.1.

Direct from these velocity diagrams, for nozzles 5, 6 and 7, the variation in relative velocity is given in C.10, C.12 and C.13. C.16 to C.18 show the extent to which the various outlet regions fall into the categories A, B or C. C.19 to C.21 give an indication of how the fluid has spread over the bucket surface. C.22 to C.24 give other details pertaining to nozzle 6 and C.15 shows the state of the relative energy at outlet for nozzle 6.

6. DISCUSSION.

The object of the tests performed on this turbine was to analyse the condition of the fluid at the optimum speed ratio and to make recommendations in the light of the results. As No.6 nozzle gives a condition nearest to that of best efficiency, the first part of this discussion refers to the results obtained using that nozzle and is therefore based on constant head, flowrate and speed.

6.1 Trajectories of ideal fluid.

The trajectories of various particles of ideal fluid across a bucket surface, shown in diagram D.9, can be studied in conjunction with the flow chart C.2. From this it may be judged that, with the possible exception of the particle in position 1, the stations reached at the bucket outlet bear little resemblance to the destinations of corresponding particles of real fluid, which emerge at points much farther out on the wheel. The marked outward movement of the fluid may therefore be attributed to the properties of the real fluid as distinct from those of the ideal fluid.

It is also of interest to note that the angle of wheel rotation corresponding to the trajectory time shows little variation among the particles selected (34° - 35°). Taking account of the relative gain in elevation of the fluid as it traverses the bucket, which can be seen in diagram D.7, the discrepancy between ideal and actual discharge stations can be seen to increase from the top of the region downwards. This appears to be due to the increasing effect of friction on the relative velocity, thus extending the time of trajectory.

Another useful bye-product of this construction is that it enables a check to be made on the angle of entry to the bucket. For instance water at position 1 does not initially make contact with the surface of the bucket as the angle of incidence of the bucket is too steep.

6.2 Fluid characteristics at discharge.

On comparing charts C.2 and C.7 it can be seen that there is no direct connection between the distribution of flow and velocity, but equally the two effects cannot be entirely separated as they are governed by certain common factors. Before interpreting the nature of flow and velocity at discharge, a summary is given of the major factors which influence the fluid motion:-

(a) The mean relative energy at inlet has been shown to be large when the radius ratio, m and friction factor, K are high.

(b) The relative energy differential is large for a high specific speed configuration. The variation in relative velocity and relative energy at inlet are shown in C.11 and C.15 respectively. Graph G.9 shows the variation in the range of relative energy as the inlet edge of the bucket crosses the jet.

(c) The position of the jet ellipse (see diagram D.6). At the top of the ellipse there is a strong inward radial relative-velocity component; also relative velocity vectors across the ellipse may be seen to converge on impact with the bucket. As the bucket moves down the ellipse, the radial component weakens and finally changes sense, and the bundle of vectors tends to straighten and finally diverge.

(d) The bucket shape and spread of the fluid are intimately linked. These are investigated in Appendix 7.

6.2.1 Distribution of flow.

The flow chart may be conveniently divided into four distinct regions, each being associated with a certain portion of the jet ellipse.

(1) Top Region (100° in C.2)

The concentration of flow at the top of the discharge region comes from the top part of the jet ellipse, say between positions 1 and 3. In this portion the inward radial component of the relative velocity is large and this factor dominates the flow across the bucket. In addition the range of relative velocity is small, the vectors converge at impact and the bucket shaping tends to contain spread. These factors allow only a small outward deviation from the ideal trajectory and tend to concentrate the flow.

(2) Transition region (between 70° and 90° in C.2)

The flow in this region emanates roughly from that part of the jet ellipse bounded by positions 3 and 5. In this part the radial component of velocity is somewhat reduced and the range of relative velocity is increasing, thus strengthening the outward turning moment on the fluid. The water is traversing the flatter portion of the bucket hence the spreading effect is strong. No factor appears to predominate but towards the wheel centre the spreading and turning effects are in opposition and this tends to concentrate a body of the fluid around the station 2 - 75°. Away from the wheel centre, these effects support each other. The nett effect is to create a valley or separation of the fluid paths along No.3 traverse, a feature which can be seen to persist over the remainder of the discharge and is preserved in the flow pattern from other nozzles.

(3) Mid-region (60° in C.2)

This part of the flow is derived from the part of the jet ellipse approximately between points 5 and 7. Here the inward component is decreasing rapidly but the range of relative velocity reaches a maximum, hence the outward turning moment is strong and this is the dominant feature. The velocity vectors at inlet may be regarded as being parallel but the bucket curvature at outlet is sharp between stations 7 and 9 and this tends to concentrate the flow.

(4) Tail region.

At the bottom part of the jet ellipse the radial velocity component is here directed outwards, the velocity vectors are divergent on impact and the range of relative energy is decreasing. The residual flow comes mainly from this region, the elongated flow paths being due to the dissipation of relative velocity of the thin films as a result of the wide spreading action.

6.2.2 Distribution of absolute velocity.

An analogy may be drawn between the condition of the fluid discharging from any position on the measuring grid and one-dimensional flow through a turbine changing speed to give the corresponding condition. The forms of typical outlet diagrams in the speed range are described in section 2.7.1 and it can be seen from chart C.17 that the flow at discharge may be divided into the three different regions previously defined as A, B and C. (These correspond roughly to the regions (3), (1) and (4) respectively, used in the previous section, the transition region (2) being absorbed by regions A and B). Examples of actual diagrams in these regions are shown in D.3, D.4 and D.5. The limits of variation of β in region A are $\pm 6^{\circ}$; β increases negatively in region B and positively in region C.

Region A may be taken to represent an area of good efficiency, but it will be noted that the relative angle of discharge, ϕ is large and the absolute velocity, V_o high. Also since the discharge radii are all large, the relative velocities are correspondingly high. Thus although this is the region of optimum efficiency, both leaving loss and friction loss are high. A study of one-dimensional theory (section 2.3) has shown that a large value of the radius ratio, m entails a low speed ratio and high relative energy at inlet. Equation (8) shows that, for optimum efficiency, this relative energy is entirely lost in the combined form of friction and leaving losses.

In region B, from the upper reaches of the ellipse the fluid in general experiences a radially inward movement. As the energy of the fluid is under-utilised, the outlet velocity diagram adopts a peaked shape and both relative and absolute velocities are large. This condition is analogous to that of a turbine running at low speed.

Region C represents the area where the relative velocity is small due to friction effects. This condition is somewhat analogous to one-dimensional flow at high speed.

Chart C.7 shows the variation in absolute velocity at outlet. The two characteristic discharge regions, A and B are easily discernible as is the transition region where the velocity reaches a minimum. The leaving loss for this nozzle is charted in C.14 and serves to confirm some of the above suggestions.

The flow and velocity patterns are primarily determined by the condition of the jet at inlet but the bucket shape also has an important influence on the distribution of flow at outlet.

6.2.3 Distribution of other variables.

It is of interest to comment on charts of other variables produced for nozzle 6.

Relative velocities (C.12) This chart was prepared from velocity diagrams at outlet. In the region of good efficiency it shows the expected increase in relative velocity with radius. In addition velocities of the order of 14 ft/s can be seen to extend into the region of decreasing radius where the energy is underutilised. The steep velocity gradient at the inner lower boundary of the chart shows the severe dissipation of energy in that region. When it is borne in mind that the mean relative velocity at inlet amounts to 12.3 ft/s, this chart gives a graphic indication why the hydraulic losses are so high.

Relative energy (C.15) The relative energy at both inlet and outlet is shown. At inlet it can be seen that the relative energy does not change along the major axis but varies linearly across it. The mixing effect due to the variation in relative velocity results in the contour pattern illustrated at outlet. In the short distance across the bucket only a partial equalisation of energy is achieved. The energy peaks are clearly defined. The transition region is represented by a flatter profile, due firstly to the wide lateral spread of the fluid and secondly to the fact that the mean relative energy at inlet falls to a minimum as the bucket lip traverses the mid-section of the ellipse (see graph G.9)

Depth profiles (C.24) This chart confirms earlier findings in that the layers are thick in regions of heavy fluid density. In the transition region the thinning of the layer is evident where the fluid filaments tend to separate; where the layer is very thin this is accompanied by a severe reduction in relative velocity.

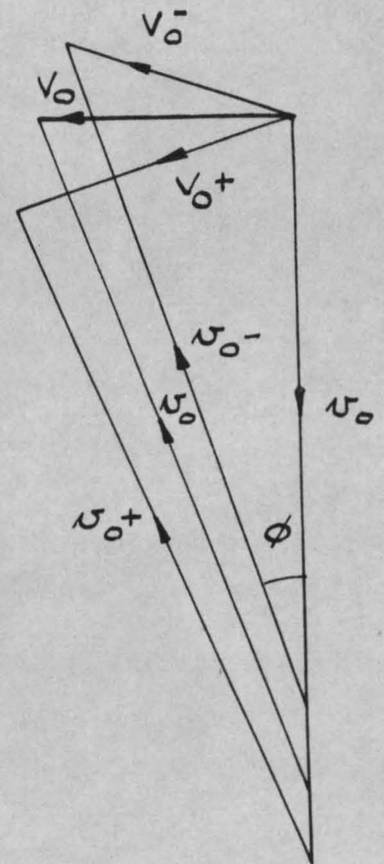

FIG. 21.

6.2.4 Effect of small changes in speed.

If reference is made to Fig.12 which shows the performance characteristics at varying speed when the flow is constant, it will be seen that the minimum leaving loss does not coincide with the minimum overall energy loss but occurs at a slightly lower speed. Tests run using nozzle 6 at 300 rev/min confirm this view and lead to a reduction in leaving loss of 1.5% but it is not claimed that this is the speed giving a minimum leaving loss. Any overall reduction in friction loss apart from being beneficial in itself would bring the speed of the minimum leaving loss nearer to the point of maximum efficiency.

The effect of small speed changes can be visualised in reference to diagram D.6. A reduction in speed causes a reduction in size of the velocity diagram ellipse and the outward moment on the fluid becomes smaller. As a whole the fluid can thus be expected to move in and up as it discharges from the wheel. On the other hand an increase in speed will produce an outward, downward movement. Such tendencies were apparent for the wheel on test and the effect on the velocities at outlet can be seen in Fig.21.

6.3 Effect of variation in flowrate.

Additional insight into the working of a turbine of this type is afforded by the effect of varying the flow. At constant head this entails varying the jet diameter and consequently the specific speed, and certain concepts must be clarified before making such comparisons.

It has been shown in section 2.5.1 that the relative energy differential is directly proportional to the jet : wheel diameter ratio, and would also be proportional to the specific speed if the efficiency were to remain constant. Thus for any selected geometrical configuration the relative energy differential has a fixed value, but as the size of the machine increases the jet size increases and the relative energy gradient diminishes. Deduction and experiment both point to the gradient as the factor controlling the flow pattern. If this were true, the larger the turbine the smaller would be the mixing effect. This would lead to a reduction in radius ratio, thus increasing the speed ratio, overall efficiency and specific speed. This trend is apparent from reference to the manufacturer's catalogue (12), which shows an increase of about 6% in efficiency over the range of geometrically similar machines at the same head.

6.3.1 Flow distribution.

The Turgo wheel under test is the smallest in a range. The jet diameter is small, the gradient steep and the efficiency very low. Varying the jet diameter implies a variation in specific speed, but it will be noted that as the wheel diameter does not change, the relative energy gradient remains constant. There is a basic similarity common to the charts C.1 to C.5, showing a mode of operation shared by all jet sizes and this supports the argument put forward in the previous section. Salient points are the concentrations of flow and the separation of flow paths in the transition region. As the jet ellipse increases in size so the flow extends both up and down the discharge side of the wheel; also the upper flow concentration shows a tendency to move inwards due to the strengthening of the inward velocity component while the energy gradient remains unaltered. A slight departure from the general pattern is apparent in the flow distribution from nozzle 7 where the lower peak on traverse 2 is the source of an outward moving ridge. This distribution may be the result of the wheel's flowing full in this region, thus creating pressures and flows atypical of the range.

6.3.2 Friction.

When an impulse turbine is designed to operate at a fixed specific speed, the number of buckets in the wheel may be determined from such considerations as are outlined in Appendix 7. If this wheel were now subjected to tests using varying jet diameters - as in these tests - since the optimum speed remains sensibly constant for all jet sizes, the bucket pitch relative to the oncoming jet would remain unchanged. Considering comparable near-rectangular sections of the jets cut off by adjacent buckets, the change in shape factor (defined as M/B in Appendix 7) is due only to a change in jet diameter. Also if the head of water were to remain constant, the boundary layer characteristics across the bucket surface would not change.

The smallest jet has the largest shape factor and spreads quickly across the bucket surface until it forms a wide thin film in which friction effects are at a maximum. Decreasing the shape factor means a reduction in spread and an increase in the film thickness so that the film is progressively less affected by the boundary layer. However as a decrease in shape factor entails an increase in jet diameter, the flow at entry extends over a larger number of vanes. Thus for a small jet the friction effect is large due to the spreading and thinning of the film, whereas for a large jet the friction effect is large due to the number of slices into which the jet is divided. At some intermediate jet diameter a balance may be found where the friction is at a minimum and this is demonstrated in graph G.7.

6.3.3 Velocity distribution.

As the jet is diminished in size, the centre of the jet ellipse remains at position 5 and for the mid-region no change is experienced either in the mean relative velocity or in the relative energy gradient. Thus in region A the effects of friction are similar for the jet sizes studied and little variation can be detected either in the velocity pattern or in the shape and orientation of velocity diagrams.

In the top part of the jet ellipse however a reduction in jet size leads to a drop in mean relative velocity while the relative energy gradient remains constant. Thus in region B, the relative velocity diminishes with reducing jet size. In company with this trend it appears that the outward turning moment on the fluid suffers an increasing reduction across the bucket, causing the angle α to become smaller. This change of trajectory is accompanied, at the bucket outlet, by a reduction in ϕ (see Fig.9), thus increasing the peaked appearance of the velocity diagrams and reducing the absolute velocity. Hence the reduction in relative velocity in this region is accompanied by a decrease in absolute velocity, also apparent in G.7. This effect is somewhat akin to a small reduction in speed below the optimum for a single jet as discussed in section 6.2.4.

Although it was not possible to assess fully the condition of the fluid in region C, it seems unlikely that a change in flow would alter the expected pattern.

6.4 Jet spread at outlet.

A study of the angles of emergence of the fluid reveals some significant features. Experimental results show that the absolute motion of part of the jet is in a vertical plane parallel to the wheel axis and this is faithfully reflected in chart C.20 as it occurs where the distortion of the grid is at a minimum. Between outlet stations 3 and 6 the radius of bucket curvature is large entailing wide spreading of the fluid across this part of the bucket. This is confirmed by the close proximity of the equiangular lines. Beyond station 6 however the radius of curvature is much sharper, reducing the spread of fluid and resulting in a concentration of flow. The flow concentration at the top of the discharge region can also be interpreted but a factor additional to the change of radius of curvature may be of significance. It can be seen in C.20 that the equiangular lines converge from top to bottom, thus inferring an overall tendancy for the spread to increase in that direction. In some part this may be due to the change in the relative directions of the velocity vectors at inlet, a feature discussed in section 6.2.1. Comparison with other flowrates shows that the pattern of spread is similar.

Chart C.22 which shows the deviation from the normal at points along the rim of the bucket at outlet, illustrates how the direction of flow is affected by bucket curvature. The large maximum deviation along traverse No.6 can be better appreciated in diagram D.11 in which the reversal of the angle of spread is also evident.

6.5 Miscellaneous features.

6.5.1 Effect of head.

From theoretical considerations, it has been shown that the spread of a jet across a stationary vane and the relative energy associated with the motion of the vane are unaffected by changes in head. Thus, apart from boundary layer effects, this evidence and the manufacturer's performance (12) figures suggest that the pattern of flow across a wheel moving with constant speed ratio will be independent of head.

6.5.2 Actual and one-dimensional flow.

The efficiency calculated on a basis of one-dimensional flow compares favourably with the experimental value. However in this case it was possible to evaluate the radius ratio and hence obtain the friction factor. It is clear that these two parameters are closely linked but without further research it cannot be established how they would vary with respect to each other, or to other variables such as bucket shaping, specific speed, turbine size etc.

It might be expected that the one-dimensional outlet velocity diagram for the optimum condition would bear comparison with a typical diagram in region A. In practice the optimum discharge condition occurs where the absolute velocity is at right angles to the peripheral. In the corresponding one-dimensional condition, shown in Fig.11, Appendix 2, the absolute angle is somewhat less than 90°.

Two factors may contribute towards this difference. Firstly, it was assumed for convenience that the factor K accounted for the effects of both spread and friction. As the reduction of force, due to spreading alone, results in a kinetic rather than a heat loss, it is likely that the outlet relative velocity found from theory would be lower than the actual mean value.

Secondly, it is probable that, due to the transfer of momentum, the fluid particles emerging in region A would show an energy gain during the trajectory, again leading to a higher relative velocity.

6.5.3 Bucket geometry at inlet.

The inlet edge of a bucket, owing to the thickness of metal, must present some angle, albeit small, to the approaching jet. This edge divides the jet into two parts, the "impinging" part which moves across the bucket surface, and the "deviated" part which moves on to strike the neighbouring bucket. Serious dispersion, distortion of shape and change of direction result from deviation of the jet.

Crewdson (3) indicated that in the design of the initial Turgo wheel

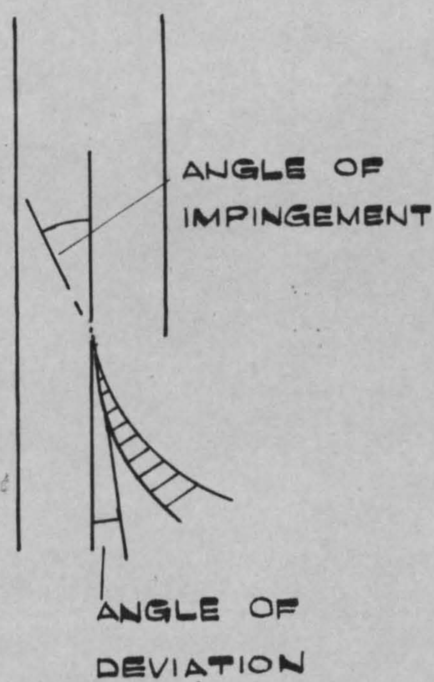

FIG. 22.

an attempt had been made to avoid these undesirable features by making the angle of deviation of the bucket negative. The angle of impingement thus became much larger than the ideal value as is shown in Fig.22. Diagram D.7 shows the entry angle at the design impact point to be 50° whereas the fluid strikes the vane at a relative angle of 35°. Any expected improvement in deviation is thus accompanied by a deterioration in the impingement condition. The disparity between bucket and fluid angles leads not only to a shock effect at inlet, with resulting energy loss, but also to an undesirable all-round spreading effect which can cause part of the jet to reverse its direction of flow. Extempore tests of a jet on a static vane showed that this back flow occurred almost immediately the jet departed from a direction tangential to the vane curvature at inlet.

Lowy (5) studied the nature of this deviation and carried out extensive tests using a circular jet striking the chamfered edge of a flat plate set at different angles. The relationship between deviation and distortion proved complex but the results of the tests appear more directly applicable to the Turgo wheel bucket than the Pelton. Further study could usefully be devoted to this aspect of bucket design in order to obtain the best compromise.

6.5.4 Jet shape at inlet.

On the discharge side the regions of lesser efficiency are well defined and can be reasonably identified with parts of the circular jet section at inlet. This suggests that a method of increasing efficiency might stem from changing the shape of cross-section of the jet, the object being to eliminate areas of poor energy utilisation.

To demonstrate the feasibility of this idea a test was run with a segment of the jet removed in the region of the higher relative velocities, reducing the flowrate by about 20% and increasing the efficiency by over 3%. Photographs of the flow pattern taken before and after the change of jet form, arranged in P.39, clearly illustrate the reduction of flow in region B.

The main objections to this course of action as a practical method of improving performance are that the power output, and consequently the specific speed, would be reduced, and that shaping the jet would involve problems of flow regulation.

6.6 General review.

If practical considerations were neglected it would be possible to design Pelton and Turgo wheels in the same range of jet : wheel diameter ratios. From theoretical considerations however it is evident that the inclined jet turbine is inherently less efficient than the tangential. Also in practice the Pelton wheel attains its maximum efficiency at the lower specific speeds whereas the field of operation of the Turgo wheel covers a range of higher specific speeds where energy differentials across the jet are larger. It can therefore be appreciated why the Turgo wheel performance is comparatively poor.

A conclusion reached from this study must therefore be that as the main losses in the Turgo wheel stem from the inlet conditions, a major improvement in efficiency cannot be achieved. Marginal improvements may however be made in ways which are outlined in the following sections.

6.6.1 First proposal.

Let it be assumed that the inlet conditions are the best obtainable and that no improvement is possible through changing the radius ratio or friction factor. Scope for improvement is then restricted to changing the shape of the bucket surface. It can be appreciated that the conventional design of the Pelton wheel requires a long straight central splitter and the ellipsoidal shape, patented by Doble at the turn of the century, was a logical development from the hitherto two-dimensional shaping. Little change in bucket design has appeared in published literature since that time.

In its simplest terms the ellipsoid may be represented by two radii of curvature, a large and a small. Such a configuration is basically unsuitable for flow direction. The large radius gives a surface little removed from the two-dimensional, thus incurring a wide spreading action; the small radius concentrates the flow and results locally in a deep profile leading to the risk of impingement on the back of the adjacent bucket.

In diagram D.11 it can be seen that a similar bucket shape has been adopted in the case of the Turgo wheel. A circular outline, chain-dotted, has been superimposed on this drawing, representing the proposed change to a spherical surface. In the first place the spread would be somewhat modified leading mainly to a redistribution of the flow peak in region A.

Secondly, the deviation from the normal, ψ in angles of discharge would be considerably improved. Chart C.23 shows the extent to which the relative outlet angle of the fluid, ϕ departs from the designed bucket angle of 15°. If the mean fluid outlet angle were reduced to say 20° from the present mean value of about 30°, then one-dimensional flow would predict a rise in efficiency of 6%. (see Appendix 2) This is rather optimistic as the change in ϕ would involve a rise in speed ratio, leading in turn to an increase in the size of the velocity ellipse in D.6. This would entail a steeper relative energy gradient and in consequence a greater degree of mixing. The value of the friction factor K in the one-dimensional formula would therefore increase, thus slightly reducing the predicted rise in efficiency.

6.6.2 Second proposal.

It has been shown that outward motion of the fluid is detrimental both to friction effects and to kinetic energy at discharge. An improvement has already been effected by offsetting the jet from the wheel centre thus introducing an inward velocity component. It might be possible to wrest an additional improvement by altering the bucket shape with a view to directing the fluid inwards in the region of optimum efficiency thus reducing the radius ratio. On the other hand, since the conditions at inlet are mainly responsible for dictating the pattern of losses, such a change would cause increased turbulence in the fluid, and a reduction in radius ratio would be matched by an increase in friction factor. This proposal could be the subject of further research.

7. CONCLUSIONS.

1. The performance of jet type impulse turbines is dictated largely by the condition of the flow at inlet.

2. The Turgo wheel is inherently less efficient than the Pelton wheel both by virtue of its geometrical configuration and the range of specific speeds for which each is suited.

3. The main source of energy loss is the relative energy differential across the jet at inlet which leads to a mixing effect and an outward turning moment on the fluid. The bulk of the fluid thus leaves the wheel at a radius greater than that at entry, entailing higher friction and leaving losses.

4. The relative energy differential is directly proportional to the jet : wheel diameter ratio. The flow pattern across the bucket however, appears to be determined by the relative energy gradient across the jet, hence for a constant jet : wheel diameter ratio the larger the machine the lower the gradient and the higher the efficiency.

5. The one-dimensional approach gives a reasonable estimate of efficiency and speed ratio provided the relationship between radius ratio and friction factor is known.

6. A marginal gain in the efficiency of the Turgo wheel could be attained by changing the bucket shape with a view to improving the angle of discharge and flow distribution. A spherical form of bucket would ensure a more even spread of fluid than the present ellipsoidal form, which has proved unsuitable for flow direction.

7. It is important to ensure that the number of buckets, the cross-section of the lip of the buckets at entry, the angle of jet inclination and the position of the jet relative to the wheel, are all designed to give maximum efficiency.

Acknowledgments

The author wishes to thank Professor A.S.T. Thomson for making facilities available in the Hydraulics Laboratory at the University of Strathclyde, Mr. D.B. Swinbanks for reading the manuscript and for his helpful suggestions, Mr. D. Rachman for his assistance in obtaining and translating references, Mr. W.J. Lowe and his staff for their help with test equipment and photography, and the staff of the drawing office.

Appendix 1.

Specific speed of a jet type impulse turbine.

For any type of turbine the specific speed is commonly given as,

$N_s = \dfrac{N\sqrt{P}}{H^{5/4}}$. For an impulse turbine of the jet type, the various quantities may be written in the following terms:-

$$u = \frac{\pi DN}{60}$$

where u is the linear wheel speed at the p.c.d.

$$\therefore \; N = \frac{60}{\pi} \times \frac{u}{D}$$

$$V_1 = C_v \sqrt{(2g\,H)}$$

where H is the head upstream from the nozzle.

$$\therefore \; H = \frac{1}{C_v^{\,2}} \cdot \frac{V_1^{\,2}}{2g}$$

$$P = \frac{\gamma QH}{550} \cdot \eta$$

where γ is the fluid specific weight

$$= \frac{\gamma}{550}\left(\frac{\pi}{4}\, d^2 V_1\right)\left(\frac{1}{C_v^{\,2}} \cdot \frac{V_1^{\,2}}{2g}\right)\eta$$

$$\therefore \; \sqrt{P} = \left(\frac{\gamma}{550} \cdot \frac{\pi}{4} \cdot \frac{1}{2g}\right)^{\frac{1}{2}} \times \frac{1}{C_v} \cdot d \cdot V_1^{\,3/2} \cdot \eta^{\frac{1}{2}}$$

$$\therefore \; N_s = \frac{\frac{60}{\pi}\left(\frac{\gamma}{550} \cdot \frac{\pi}{4} \cdot \frac{1}{2g}\right)^{\frac{1}{2}}}{\left(\frac{1}{2g}\right)^{5/4}} \times \frac{\frac{u}{D} \cdot \frac{1}{C_v} \cdot d \cdot V_1^{\,3/2} \cdot \eta^{\frac{1}{2}}}{\left(\frac{1}{C_v}\right)^{5/2} \cdot V_1^{\,5/2}}$$

For water, $\gamma = 62.4\ \text{lbf/ft}^3$,

$$\therefore\ N_s = 130\ .\ (C_v)^{3/2}\ .\ \left(\frac{d}{D}\right)\cdot\left(\frac{u}{V_1}\right)\cdot(\eta)^{\frac{1}{2}}$$

Specific speed for wheel on test.

The use of nozzle 6 gives an efficiency close to the optimum. For this nozzle,

$C_v = 0.979$, $d = 1.2$ in, $D = 6$ in, $u/V_1 = 0.435$, $\eta_b = 0.764$.

$$\therefore\ N_s = 130 \times (0.979)^{3/2} \times \frac{0.435}{5} \times (0.764)^{\frac{1}{2}}$$

$N_s = 9.6$

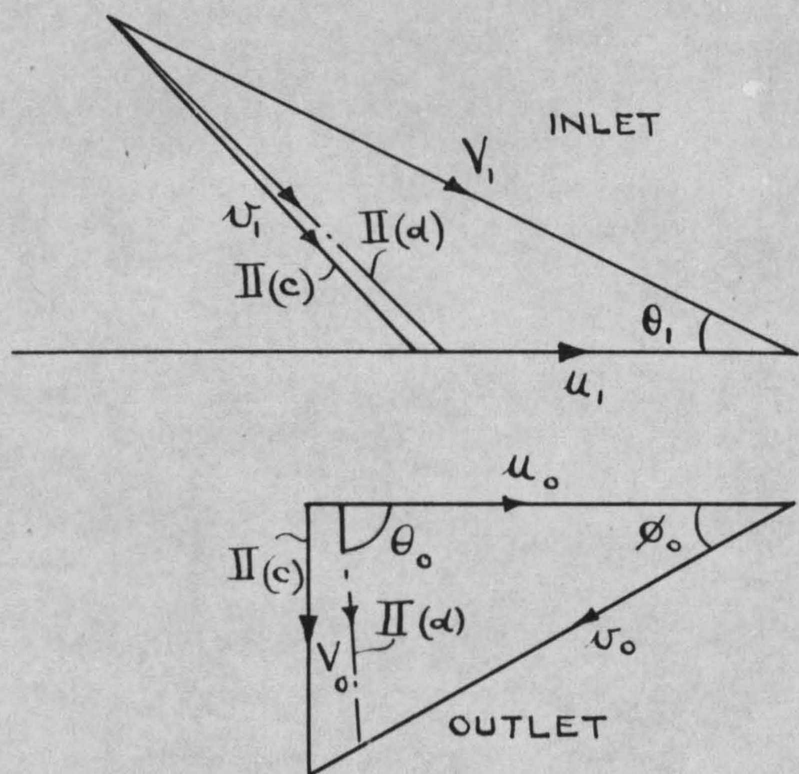

SCALE ; 10 cm = UNIT VELOCITY.

FIG. 11

Appendix 2.

Graphical representation of one-dimensional flow.

For mean values of angles, $\theta_1 = 26^\circ$, $\phi_o = 30^\circ$, the effects of radius ratio, m = 1.3 when K = 1 (case II(c)) and of friction, etc. K = 1.135 (case II(d)) are shown in the velocity diagrams drawn to scale in Fig.11.

Case II(c). $\Delta_{opt} = 0.49$, max $\eta_w = 0.87$

$$v_1 = 0.6, \quad v_1^2 = 0.36 \qquad (V_1 = 1)$$

$$u_1 = 0.49, \; u_1^2 = 0.24$$

$$\therefore \quad v_1^2 - u_1^2 \quad 0.12$$

$$u_o = 1.3 \times 0.49 = 0.638$$

$\therefore$ $u_o^2 = 0.407$, and in equation (7), since K = 1

$$v_o^2 = 0.12 + 0.407 = 0.527$$

$$\therefore \quad v_o = 0.726$$

From outlet diagram, $V_o = 0.36$, $\theta_o = 89^\circ$

Then $\eta_w = 1 - \dfrac{V_o^2}{V_1^2} = \dfrac{1 - 0.13}{1} = 0.87$

Case II(d). $\Delta_{opt} = 0.455$, max $\eta_w = 0.78$

$$v_1 = 0.625, \quad v_1^2 = 0.391 \qquad (V_1 = 1)$$

$$u_1 = 0.455, \quad v_1^2 = \underline{0.207}$$

$$\therefore v_1^2 - u_1^2 = \underline{0.184}$$

$$u_o = 1.3 \times 0.455 = 0.592$$

$\therefore$ $u_o^2 = 0.35$, and in equation (7), $K = 1.135$

$$\therefore \quad 1.285\, v_o^2 = 0.184 + 0.35 = 0.534$$

$$\therefore \quad v_o^2 = 0.416 \text{ and } v_o = 0.645$$

and $v_o^2 - u_o^2 = \underline{0.066}$

In equation (6), $h_L = (v_1^2 - u_1^2) - (v_o^2 - u_o^2)$

$\therefore$ $\underline{h_L = 0.118}$, % friction loss

From outlet diagram, $V_o = 0.32$, $\theta_o = 84^\circ$

$\therefore$ $\underline{V_o^2 = 0.102}$, % leaving loss

$\therefore$ Total loss $= V_o^2 + h_L = 0.22$

$$\therefore \quad \eta_w = \frac{1 - 0.22}{1} = 0.78$$

Notes.

1. $\left.\begin{array}{l}\text{Comparing with test results} \\ \text{on a basis of wheel power}\end{array}\right\}$, $\begin{array}{ll}\text{\% leaving loss} & = 0.1025 \\ \text{\% friction loss} & = 0.105\end{array}$

Case II(e).

Consider a case where ϕ_o is reduced.

$\theta_1 = 26^\circ$, $\phi_o = 20^\circ$, $m = 1.3$, $K = 1.135$.

From graph G.10, $\Delta_{opt} = 0.48$, max $\eta_w = 0.84$.

Compared with case II(d), if reducing the outlet angle were to leave the friction loss unaffected, any increase in efficiency would stem from a reduction in leaving loss.

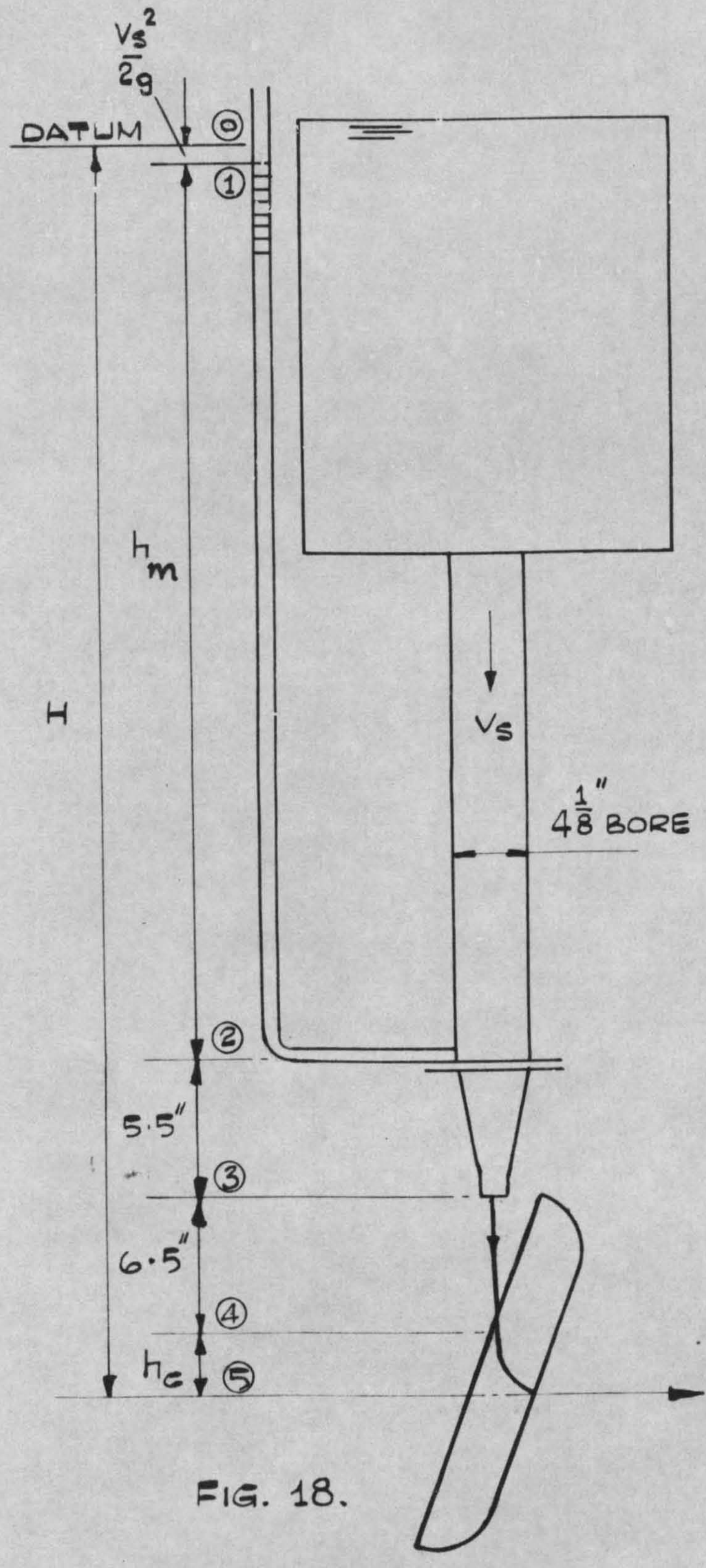

FIG. 18.

Appendix 3.

TABULATED RESULTS AND SPECIMEN CALCULATIONS.

A3.1 Coefficient of discharge of nozzles.

See section 5.1

Average weight collected in $2\frac{1}{2}$ minutes = 1416.4 lbf

$\therefore$ Actual rate of discharge = 566.55 lbf/min

or $Q = 0.1514\ \mathrm{ft^3/s}$

From fig.18, head available at nozzle inlet relative to nozzle outlet,

$$H_2 = h_m + \frac{5.5}{12} + \frac{V_s^2}{2g}.$$

For nozzle 6,

$$V_s = \frac{Q}{A_s} = \frac{0.1514}{\frac{\pi}{4} \times \frac{(4.125)^2}{144}} = 1.63\ \mathrm{ft/s}$$

$$\therefore \frac{V_s^2}{2g} = 0.041\ \mathrm{ft.}$$

$$\therefore H_2 = 5.134 + \frac{5.5}{12} + 0.041 = \underline{5.633}\ \mathrm{ft.}$$

Ideal rate of discharge = nozzle area $\times \sqrt{(2g\, H_2)}$

$$= 0.00813 \times \sqrt{(64.4 \times 5.633)}$$

$$\therefore Q' = 0.1548\ \mathrm{ft^3/s}$$

$$\therefore \text{ Coeff. of discharge, } C_d = \frac{Q}{Q'} = \frac{0.1514}{0.1548} = \underline{0.979}$$

As the nozzle bore was maintained for some distance upstream from the outlet, the coefficient of contraction, C_c has been taken as unity. Hence the coefficient of velocity, $C_v = C_d$.

Table 1 shows results for all nozzles.

Table 1. Coefficients of discharge

Nozzle	Bore in	Area ft^2	Ideal Disch, Q' ft^3/s	Actual Disch, Q ft^3/s	Coeff. of disch, C_d
1	0.377	0.00078	0.0149	0.0146	0.979
2	0.501	0.00137	0.0264	0.0259	0.981
3	0.752	0.00308	0.0593	0.0582	0.982
4	0.889	0.00431	0.0827	0.0813	0.983
5	1.063	0.00616	0.1179	0.1159	0.983
6	1.221	0.00813	0.1548	0.1514	0.979
7	1.377	0.01034	0.1952	0.1916	0.981

A3.2 Power tests.

Table 2. Mechanical power loss. Nozzle 6.

Speed, N rev/min	Torque, T_m lbf.ft	Power, P_m ft.lbf/s
400	0.08	3.35
362	0.07	2.65
318	0.07	2.33
279	0.06	1.75
239	0.06	1.50
203	0.05	1.06

$$P_m = 2\pi N T_m$$

Table 3. Shaft power output. Nozzle 6.

Speed, N rev/min	Torque, T lbf.ft	Power, P ft. lbf/s
198	1.82	37.74
222	1.72	39.99
243	1.62	41.22
260	1.56	42.47
281	1.47	43.26
301	1.39	43.81
321	1.31	44.04
339	1.24	44.02
361	1.14	43.10
382	1.05	42.00
399	0.98	40.95

$P = 2\pi NT$

A3.3 Estimation of head.

As can be seen in Fig. 18, friction and other losses upstream from the nozzle have not been considered in this study.

The overall head, H however includes nozzle losses, and the other variables are the manometer reading h_m, the standpipe velocity head and the head gained in passing through the wheel, h_c. This latter is calculated as indicated in section A3.7.2.

For nozzle 6, h_m = 5.134 ft

$V_s^2/2g$ = 0.041 ft

h_c = 0.253 ft

+ 1.0 ft

∴ Overall head, H = 6.428 ft

Useful head at (3) = $C_v^2 . H_2$

= $0.979^2 \times 5.633$

= 5.40 ft.

Useful head at (4) = 5.4 + 0.542

= 5.942 ft

Useful overall head at (5) = 5.942 + 0.253

$$H_o = 6.195 \text{ ft.}$$

As can be seen in diagram D.6 the filaments of fluid enter the wheel at different elevations and velocities, and there are complex interchanges of energy as the fluid passes through the wheel. A major simplification can be attained by assuming a mean velocity of entry to the wheel, which takes account of the gain in head across the wheel.

Thus for nozzle 6, let the velocity at entry have a mean value,

$$V_1 = \sqrt{(2g \times 6.195)} = 19.9 \text{ ft/s.}$$

It will also be noted in D.6 that the jet diameter at entry (1.2") allows for the gain in velocity of the jet between the nozzle and the wheel, but takes no account of diffusion due to turbulence.

A3.4 Efficiency calculations

For nozzle 6, overall head, $H = 6.428$ ft

$$\text{Input power, } P_1 = \gamma QH$$

$$= 62.4 \times 0.1514 \times 6.428$$

$$= 60.74 \text{ ft.lbf/s}$$

From graph G.1, maximum wheel power,

$$P_o = 46.4 \text{ ft.lbf/s}$$

$\therefore$ Hydraulic efficiency, $\eta_b = \frac{46.4}{60.74} = 0.764$

See table 4 for other flowrates.

Power input to the wheel,

$$P_w = \gamma Q H_o$$

$$= 62.4 \times 0.1514 \times 6.195$$

$$= 58.5 \text{ ft.lbf/s}$$

$\therefore$ Wheel efficiency, $\eta_w = \frac{46.4}{58.5} = 0.794$

See table 5 for other flowrates.

A3.5 Unit calculations.

Calculations for nozzle 6 are shown in sufficient detail in table 6. Unit values of speed and power for other nozzles are shown graphically in the performance characteristic, G.4.

Table 4. Hydraulic efficiency.

Nozzle		1	2	3	4	5	6	7
Mano. rdg, h_m	(ft)	5.318	5.308	5.286	5.263	5.214	5.134	5.021
Pipe vel. hd, $V_s^2/2g$	(ft)	0.0004	0.0012	0.006	0.012	0.024	0.041	0.067
Head gain, h_c	(ft)	0.255*	0.255*	0.255	0.261	0.255	0.253	0.257
Overall hd, H	(ft)	6.573	6.564	6.547	6.536	6.493	6.428	6.345
Flow rate, Q	(ft^3/s)	0.0146	0.0259	0.0582	0.0813	0.1159	0.1514	0.1916
Input power, P_1	(ft. lbf/s)	6.00	10.60	23.79	33.15	46.95	60.74	75.87
Max wheel power, P_o	(ft. lbf/s)	3.05	6.1	17.0	24.2	35.25	46.4	57.6
Hydraulic effy, η_b	$= P_o/P_1$	0.508	0.576	0.715	0.730	0.751	0.764	0.759

* estimated

Table 5. Wheel efficiency.

Nozzle	1	2	3	4	5	6	7
Nozzle hd, H_2 (ft)	5.776	5.767	5.750	5.733	5.696	5.633	5.546
Nozzle hd loss, $H_2(1 - C_v^2)$ (ft)	0.240	0.217	0.205	0.195	0.192	0.233	0.208
Useful hd at wheel, H_o (ft)	6.333	6.347	6.342	6.341	6.301	6.195	6.137
Power input to wheel, P_w (ft.lbf/s)	5.77	10.25	23.0	32.2	45.6	58.5	73.3
Wheel effy, $\eta_w = P_o/P_w$	0.528	0.595	0.74	0.752	0.772	0.794	0.785
Capacity coefficient, $\frac{Q}{\sqrt{(g H_o D^2)}}$	0.004	0.007	0.016	0.022	0.032	0.043	0.054

Table 6. Unit speed and power.

Nozzle No.6	$H = 6.428$ ft				$P_1 = 60.74$ ft. lbf/s				
Speed N (rev/min)	200	225	250	275	300	325	350	375	400
Unit speed, $Nu = N/H^{\frac{1}{2}} = N/2.535$	78.9	88.8	98.6	108.5	118.3	128.2	138.1	147.9	157.8
Wheel power, P_o (ft. lbf/s) (from G.2)	39.0	41.4	43.3	44.8	45.8	46.3	46.2	45.4	44.2
Unit power, $Pu = P_o/H^{3/2} = P_o/16.297$	2.39	2.54	2.66	2.75	2.81	2.84	2.835	2.79	2.71
Hydraulic efficiency, $\eta_b = P_o/P_1$	0.642	0.682	0.713	0.737	0.754	0.763	0.761	0.747	0.728

Table 7. Properties of measuring grid.

Angular interval, $\theta = 5^\circ \equiv 0.0873$ radians

Nominal radial length, $l = \frac{1}{2}$ in.

$$u = \frac{2\pi N}{60} \cdot r = \frac{2\pi \times 330}{60} \times \frac{r''}{12} = 2.88r \text{ ft/s}$$

Traverse	Radius r (in)	Circum length $r\theta$ (in)	Mean area $r\theta l$ (in^2)	Periph speed u_o (ft/s)	Link angle ϵ°
1	2.25	0.197	0.101	6.48	+ 30
2	2.70	0.236	0.120	7.77	+ 16
3	3.18	0.278	0.141	9.16	+ 2
4	3.68	0.322	0.162	10.60	- 6
5	4.17	0.364	0.183	12.00	- 14
6	4.63	0.404	0.203	13.35	- 25
7	5.02	0.439	0.220	14.45	- 43
8	5.30	0.463	0.232	15.26	- 68
9	5.38	0.469	0.235	15.50	-100

Aperture area of separator = 0.113 in^2

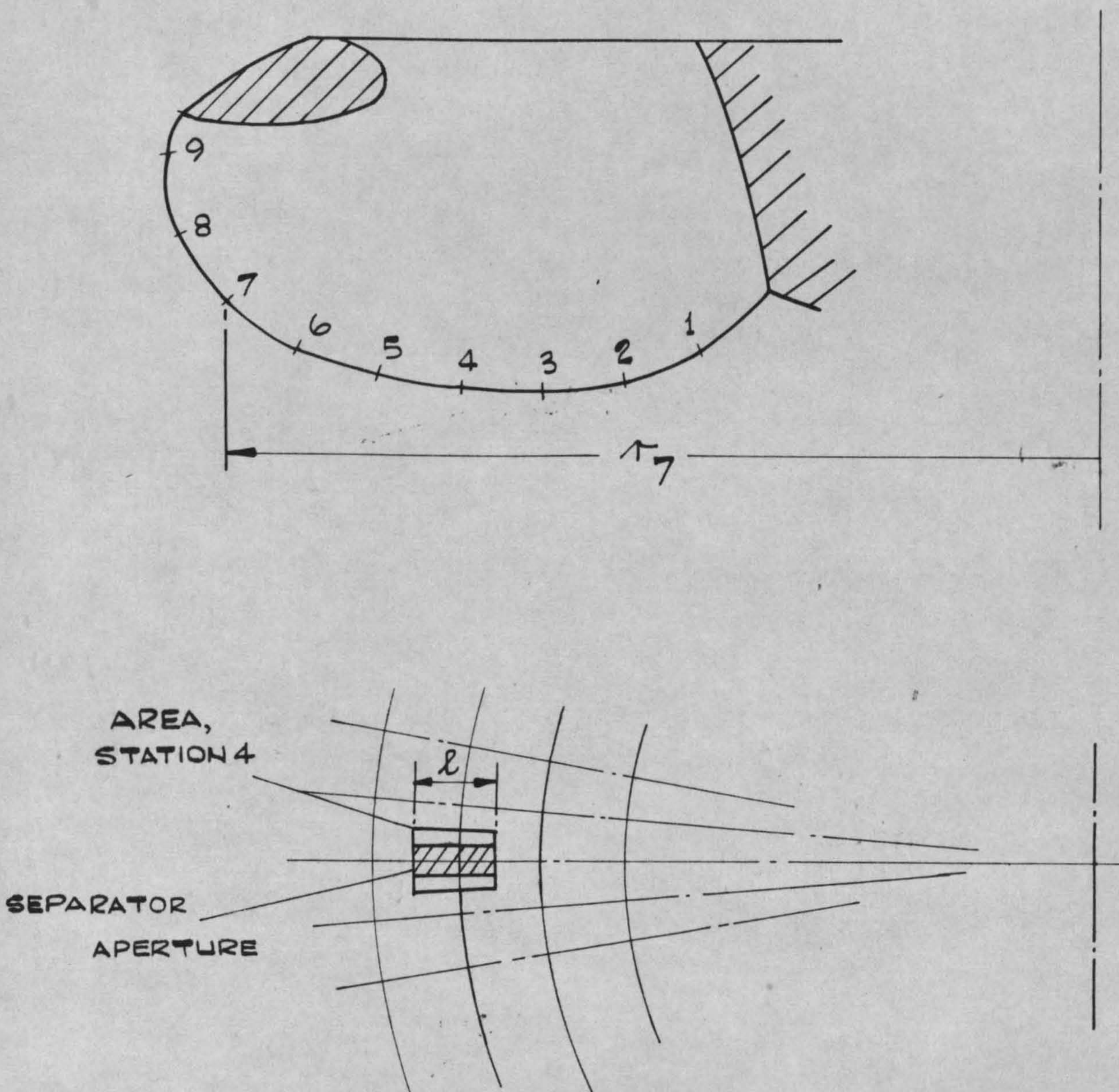

FIG. 19.

A3.6 Flow and velocity calculations.

The position on the measuring grid at the wheel outlet is given by the number of the traverse followed by the angle, e.g. $7 - 60^{\circ}$.

A3.6.1 Flow

At $7 - 60^{\circ}$, by measurement, the flow density $= 165\ \text{in}^3/\text{min}$.

Aperture area of separator $= 0.113\ \text{in}^2$

From table 7 and Fig.19 area associated with outlet station $= 0.220\ \text{in}^2$

$$\therefore \text{ Flowrate at } 7 - 60^{\circ} = \frac{0.220}{0.113} \times 165$$

$$q = 320\ \text{in}^3/\text{min}$$

A3.6.2 Velocity

At $7 - 60^{\circ}$, selected drops moving the standard distance of 3 in corresponded to the following phase angles:-

	Range of observations		
1st angle	9.0	20.9	18.2
2nd angle	5.6	17.6	14.7
Difference	3.4	3.3	3.5

mean angle of rotation, $n = 3.4$ bucket pitches

$$\text{Absolute velocity} = \frac{\text{distance moved by drop}}{\text{time for corres. angle of rotation}}$$

$$= \frac{\frac{3}{12}\ \text{ft (distance moved)}}{\frac{n}{20\ \text{(buckets per rev)}} \times \frac{60}{330\ \text{(test speed)}}}$$

$$= \frac{27.5}{n}$$

When $n = 3.4$, $V_o = \frac{27.5}{3.4} = 8.10$ ft/s.

A3.6.3 Kinetic energy at outlet or leaving loss

At $7 - 60^\circ$, leaving loss $= \frac{1}{2} \rho q V_o^2$

$$= \frac{1}{2} \times \frac{62.4}{32.2} \times \frac{320}{1728} \times (8.1)^2$$

$$= 11.77 \text{ ft.lbf/min.}$$

A3.6.4 Direction

The sign convention for angles measured in vertical and horizontal planes is given in Diagram D.10.

Table 8/1 Leaving loss. Nozzle 6. N = 330.

Posn.	Flow density in^3/min	Flowrate q in^3/min	Abs.vel. V_o ft/s	KE $\frac{1}{2}\rho q V_o^2$ ft.lbf/min	Angle V°	Angle H°
1-115	86.0	77.5	9.07	3.58	-17	-4
1-110	136.2	122.5	7.88	4.26	-14	-2
1-105	131.0	118.0	7.03	3.27	-13	0
1-100	135.0	121.4	6.05	2.49	- 8	0
1-95	134.8	121.0	5.62	2.14	- 8	4
1-90	127.5	114.7	3.76	0.91	- 7	1
1-85	122.5	110.0	2.97	0.54	- 3	0
1-80	108.1	97.5	2.73	0.41	7	-1
1-75	89.0	80.1	2.81	0.35	20	-5
1-70	68.3	61.5				
1-65	49.2	44.4		17.95		
1-60	35.2	31.7	182.2			
1-55	25.3	22.8				
1-50	15.6	14.0				
1-45	8.7	7.8				
		1145.0				

Table 8/2 Leaving loss. Nozzle 6. N = 330

Posn.	Flow density in^3/min	Flowrate q in^3/min	Abs. vel. V_o ft/s	KE $\frac{1}{2}\rho q V_o^2$ ft. lbf/min	Angle V^o	H^o
2-115	39.0	41.6			-24	8
2-110	124.2	132.5	8.27	5.08	-25	9
2-105	188.0	201.0	8.35	7.86	-23	11
2-100	199.0	212.0	7.84	7.30	-18	14
2-95	177.5	189.2	7.70	6.29	-12	12
2-90	114.0	111.0	7.26	3.28	-11	10
2-85	101.5	108.1	5.76	2.01	- 5	8
2-80	117.2	125.1	4.87	1.66	11	0
2-75	127.3	136.0	4.0	1.22	24	- 9
2-70	129.0	137.5	4.04	1.26	31	-16
2-65	118.3	126.2	3.24	0.74	33	-24
2-60	102.4	109.2	3.51	0.75	43	-29
2-55	85.5	91.2		37.45	44	-41
2-50	65.5	70.0				
2-45	47.8	51.0	295.8			
2-40	33.5	35.8				
2-35	23.1	24.7				
2-30	15.5	16.5				
2-25	6.2	6.6				
		1925.2				

Table 8/3 Leaving loss. Nozzle 6. N = 330

Posn.	Flow density in^3/min	Flowrate q in^3/min	Abs.vel. V_o ft/s	KE $\frac{1}{2}\rho q V_o^2$ ft.lbf/min	Angle V°	H°
3-110	19.7	24.5			-24	10
3-105	102.3	127.2	6.90	3.39	-23	12
3-100	148.0	184.0	7.20	5.35	-18	17
3-95	149.8	186.0	7.31	5.57	-15	23
3-90	136.5	170.0	7.37	5.18	-10	23
3-85	110.8	137.6	7.51	4.35	- 3	25
3-80	108.2	134.6	7.58	4.34	8	26
3-75	112.0	139.2	6.81	3.62	17	21
3-70	106.8	132.7	6.48	3.12	32	7
3-65	94.2	117.0	5.53	2.0	31	3
3-60	76.0	94.5	4.25	0.96	36	-10
3-55	65.2	81.2	4.20	0.80	36	-23
3-50	58.0	72.2	3.72	0.56	39	-43
3-45	52.6	65.5		39.24	41	-45
3-40	45.8	57.0				
3-35	37.6	46.8				
3-30	29.8	37.1	271.1			
3-25	22.5	28.0				
3-20	18.4	22.9				
3-15	11.1	13.8				
		1871.8				

Table 8/4 Leaving loss. Nozzle 6. N = 330

Posn.	Flow density in^3/min	Flowrate q in^3/min	Abs. vel. V_9 ft/s	KE $\frac{1}{2}\rho q V_9^2$ ft. lbf/min	Angle V°	H°
4-105	12.2	17.5				
4-100	64.6	92.8	5.50	1.57	-12	24
4-95	123.0	176.5	5.80	3.32	- 9	31
4-90	132.0	189.5	6.26	4.16	- 3	40
4-85	135.0	194.0	6.77	4.98	1	46
4-80	123.0	176.5	6.67	4.40	12	50
4-75	112.9	162.0	6.81	4.21	18	49
4-70	108.5	156.0	6.89	4.15	28	47
4-65	104.5	150.0	6.81	3.90	32	39
4-60	92.0	132.0	6.82	3.45	38	29
4-55	73.5	105.7	6.68	2.65	48	14
4-50	49.6	71.3	5.43	1.18	47	- 6
4-45	34.4	49.4	3.93	0.43	40	-44
4-40	25.7	36.9		38.40		
4-35	23.0	33.0				
4-30	23.6	33.9	194.5			
4-25	23.9	34.3				
4-20	22.0	31.6				
4-15	17.3	24.8				
		1867.7				

Table 8/5 Leaving loss. Nozzle 6. N = 330

Posn	Flow density in^3/min	Flowrate q in^3/min	Abs. vel. V_9 ft/s	KE $\frac{1}{2}\rho q V_9^2$ ft.lbf/min	Angle V^o	H^o
5-95	37.5	60.8	5.72	1.11	2	44
5-90	108.8	176.0	5.72	3.23	5	50
5-85	122.0	197.5	6.09	4.11	7	56
5-80	136.0	220.0	6.77	5.65	12	61
5-75	142.4	231.0	7.45	7.19	17	64
5-70	137.2	223.0	8.10	8.20	23	63
5-65	124.0	201.0	8.06	7.32	28	64
5-60	107.7	174.0	8.43	6.93	33	64
5-55	93.3	151.0	8.22	5.72	37	60
5-50	77.0	124.5	6.89	3.31	41	50
5-45	44.3	71.8	6.71	1.81	55	32
5-40	17.6	28.5		54.58	59	6
5-35	11.3	18.3				
5-30	10.1	16.4				
5-25	10.9	17.6				
5-20	15.0	24.3	188.1			
5-15	21.6	35.0				
5-10	22.0	35.6				
5-5	negligible	-				
5-0	7.7	12.4				
		2018.7				

Table 8/6 Leaving loss. Nozzle 6. N = 330

Posn.	Flow density in^3/min	Flow rate q in^3/min	Abs.vel. V_o ft/s	KE $\frac{1}{2}\rho q V_o^2$ ft.lbf/min	Angle V^o	H^o
6-90	15.6	28.0	4.02	0.25	14	53
6-85	84.5	152.0	6.48	3.58	17	61
6-80	127.5	229.0	5.66	4.11	18	69
6-75	134.0	241.0	6.93	6.49	22	75
6-70	147.0	264.0	7.41	8.13	24	78
6-65	150.4	270.0	7.89	9.42	26	79
6-60	135.0	243.0	8.42	9.65	32	80
6-55	103.9	186.5	8.36	7.30	37	81
6-50	77.6	139.5	8.28	5.37	41	75
6-45	59.3	106.5	7.85	3.67	52	70
6-40	36.0	64.7	4.66	0.79	64	25
6-35	13.2	23.7		58.76		
6-30, 25, 20		negligible				
6-15	8.5	15.3	145.2			
6-10	21.2	38.1				
6-5	25.8	46.4				
6-0	12.1	21.7				
		2069.4				

Table 8/7 Leaving loss. Nozzle 6. $N = 330$

Posn.	Flow density in^3/min	Flowrate q in^3/min	Abs.vel. V_o ft/s	KE $\frac{1}{2}\rho q V_o^2$ ft.lbf/min	Angle V^o	H^o
7-80	41.8	81.0	5.11	1.18	16	71
7-75	127.5	247.0	6.20	5.32	23	80
7-70	151.0	293.0	6.11	6.14	24	83
7-65	162.0	315.0	7.25	9.28	27	88
7-60	165.0	320.0	8.10	11.77	31	90
7-55	140.0	272.0	8.47	10.94	30	92
7-50	95.5	185.5	8.76	8.0	35	94
7-45	47.2	91.8	7.85	3.17	43	96
7-40	25.8	50.1		55.80	57	108
7-35	15.6	30.3				
7-30	9.3	18.05				
7-25, 20, 15		negligible	200.3			
7-10	9.5	18.45				
7-5	26.4	51.3				
7-0	16.5	32.0				
		2005.5				

Table 8/8 Leaving loss. Nozzle 6. N = 330

Posn.	Flow density in^3/min	Flowrate q in^3/min	Abs. vel. V_o ft/s	KE $\frac{1}{2}\rho q V_o^2$ ft. lbf/min	Angle V^o	H^o
8-70	65.0	133.0	4.18	1.30	26	86
8-65	148.0	303.0	4.46	3.38	28	94
8-60	175.0	359.0	5.69	6.52	30	98
8-55	154.0	316.0	6.30	7.03	32	103
8-50	107.0	219.0	7.89	7.65	33	111
8-45	66.2	135.5	7.07	3.80	36	125
8-40	34.0	69.7		29.68	42	132
8.35	20.7	42.4				
8-30	14.8	30.3				
8-25	11.8	24.2	308.4			
8-20	9.8	20.1				
8-15	10.5	21.5				
8-10	14.1	28.9				
8-5	20.8	42.6				
8-0	14.0	28.7				
		1773.9				

Table 8/9 Leaving loss. Nozzle 6. N = 330

Posn.	Flow density in^3/min	Flowrate q in^3/min		Abs.vel. V_o ft/s	KE $\frac{1}{2}\rho q V_o^2$ ft.lbf/min	Angle V^o	H^o
9-60	39.0	81.0		3.60	0.59	39	116
9-55	95.5	198.0		2.49	0.69	30	120
9-50	123.0	255.0		3.81	2.08	30	128
9-45	122.0	253.0		4.20	2.50	35	137
9-40	80.5	167.0		5.10	2.44	44	154
9-35	46.5	96.5			8.30		
9-30	28.7	59.6					
9-25	22.8	47.4					
9-20	22.0	45.7	457.3				
9-15	25.2	52.4					
9-10	25.4	52.8					
9-5	20.5	42.6					
9-0	14.6	30.3					
		1381.3					

A3.7 Information derived from table 8.

In table 8, totals are given for each traverse of

(a) overall flowrate

(b) flowrate for stations where it has not been possible to measure velocity.

(c) leaving loss for stations where velocity has been measured.

A3.7.1 Check on flowrate at outlet.

The flowrate has been summed over each traverse and the overall flowrate, $\sum q = 16,059 \text{ in}^3/\text{min} \equiv 0.155 \text{ ft}^3/\text{s}$.

cf. flowrate at entry, $Q = 0.1514 \text{ ft}^3/\text{s}$.

Error $= 0.0036 \text{ ft}^3/\text{s} \equiv 2.38\%$.

A3.7.2 Determination of mean overall head.

Although not shown in table 8, the flowrate at each station has been multiplied by the head (h) relative to Datum in Fig.18, and the products summed.

e.g. At station 7-60°, $h = 6.492$ ft

$\therefore \quad q \times h = 320 \times 6.492 = 2070$

Then $\sum qh = 103,227$. Thus for No.6 nozzle, the mean overall head,

$$H = \frac{103,227}{16,059} = \underline{6.428 \text{ ft}}$$

Then, $h_c = 6.428 - 6.175 = 0.253$ ft.

A3.7.3 Estimation of total leaving loss.

Considering stations where velocity has been charted, the sum of recorded leaving losses = 340.16 ft. lbf/min

$$\equiv 5.67 \text{ ft.lbf/s}$$

At stations where velocity is uncharted, the sum of the flowrates = 2219.9 in^3/min. Taking account of the velocity gradient approaching this uncharted region and appreciating that the absolute velocity along each traverse will fall to a minimum then increase again as the relative velocity decreases, the average velocity in this region has been estimated at 4 ft/s. Then unrecorded leaving loss

$$= \frac{1}{2} \times \frac{62.4}{32.2} \times \frac{2212.9}{1728 \times 60} \times 4^2$$

$$= 0.33 \text{ ft.lbf/s.}$$

∴ For nozzle 6, total leaving loss

$$= 5.67 + 0.33 = 6.0 \text{ ft.lbf/s}$$

Corresponding details used in estimating the leaving loss for nozzles 4 to 7 are given in table 9.

Table 9. Estimation of leaving loss.

Nozzle		4	5	6	7
Recorded leaving loss	(ft.lbf/s)	2.59	4.06	5.67	7.17
Estimated V_o, where unrecorded	(ft/s)	3	4	4	4
Σq, where V_o unrecorded	(in^3/min)	2037	2371	2213	2907
Estimated additional leaving loss	(ft.lbf/s)	0.17	0.36	0.33	0.44
Total leaving loss	(ft.lbf/s)	2.76	4.42	6.0	7.61
(Friction + leaving) loss	"	7.97	10.31	12.13	15.77
Friction loss, by difference	"	5.21	5.89	6.13	8.16
<u>Other data</u>					
Mean vel. head, $P_e/\gamma Q$	(ft)	0.544	0.612	0.62	0.64
Mean vel. at outlet, V_o	(ft/s)	5.92	6.28	6.32	6.42

A3.7.4 Estimation of radius ratio.

Radius ratio, m is defined as r_o/r_1. The mean radius at outlet,

$r_o = \frac{\Sigma(q.r)}{\Sigma q}$. The radius r for each position was taken as a grid radius. Similarly the mean radius at inlet was taken as the distance of the centre of the ellipse from the wheel centre, i.e. $r_1 = 3.15$ in.

Then $r_o = \frac{65,570}{16,059} = 4.08$

$\therefore \quad \underline{m} = \frac{4.08}{3.15} = \underline{1.3}$

A3.8 Power balance.

The balance has been based on wheel power as output. The mechanical losses at optimum speed varied over the test series between 2.0 and 2.4 ft.lbf/s and a mean constant value of 2.2 ft.lbf has been selected to obtain mean values of shaft power. Nozzle losses have been included in the balance and friction losses obtained by difference.

Table 10. Power balance.

Nozzle	4		5		6		7	
	Power ft.lbf/s	Fraction	Power ft.lbf/s	Fraction	Power ft.lbf/s	Fraction	Power ft.lbf/s	Fraction
Shaft power, P	22.00	0.664	33.05	0.704	44.20	0.728	55.40	0.730
Mech. losses, P_m	2.20	0.066	2.20	0.047	2.20	0.036	2.20	0.029
Wheel power, $P_o = P + P_m$	24.20	0.730	35.25	0.751	46.40	0.764	57.60	0.759
Nozzle loss, P_n	0.98	0.030	1.39	0.030	2.21	0.036	2.50	0.033
Leaving loss, P_e	2.76	0.083	4.42	0.094	6.00	0.099	7.61	0.100
Friction loss, P_b	5.21	0.157	5.89	0.125	6.13	0.101	8.16	0.108
Input power, P_1	33.15	1.000	46.95	1.000	60.74	1.000	75.87	1.000

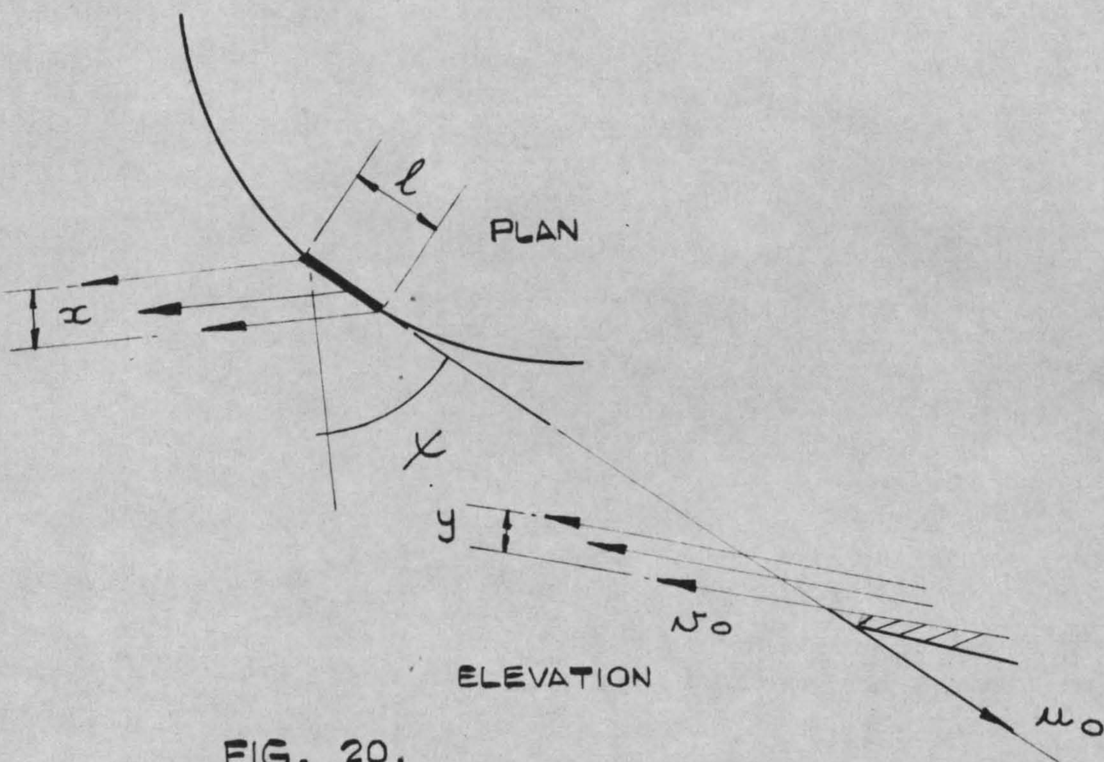

FIG. 20.

A3.9 Relative velocity and energy calculations.

Relative velocities at outlet have been measured directly from velocity diagrams and are represented in contour form for nozzle 6 in chart C.12. Peripheral velocities for each traverse radius are recorded in table 7. The relative energy at each station, $(v_o^2 - u_o^2)$ requires no elaboration.

A3.10 Deviation and profile calculations.

Diagram D.1 gives a plan view of a bucket at outlet with relevant angles shown. α, the deviation from the axial direction, has been obtained directly from velocity diagrams.

A useful basis of comparison of discharge angles is the deviation from the normal at any outlet station, and this is given by ψ. The link angle, ϵ has been measured graphically for each station and recorded in table 7. Then $\psi = \alpha + \epsilon$.

At any outlet station, area of cross-section of water normal to flow = xy i.e. $y \times l \cos\psi = \frac{q}{v_o}$ (see Fig.20)

$$l = \frac{1}{2}'' \quad \therefore \; y = \frac{q}{v_o \, l \cos\psi} = \frac{2q}{v_o \cos\psi} \quad \text{for inch units}$$

$$\therefore \; y = \frac{2}{60 \times 12} \times \frac{q}{v_o \cos\psi} \quad \text{where } q - \text{in}^3/\text{min}, \; v_o - \text{ft/s}$$

$$\text{Profile,} \quad y = \frac{q}{360 \, v_o \cos\psi} \quad \text{in}$$

At station 7-60°, v_o = 16.65 ft/s, $\psi = 37^\circ$

$$\therefore \quad y = \frac{1}{360} \times \frac{320}{16.65 \times 0.799} = \underline{0.067 \text{ in}}$$

Table 11 gives details of relative energy, profile etc. at outlet for nozzle 6.

Table 11/1 and /2 Relative energy, etc. Nozzle 6 $N = 330$

Posn.	Rel. vel. v_o ft/s	Periph. vel. u_o ft/s	Rel. energy $v_o^2 - u_o^2$ $(ft/s)^2$	Deviation ψ °	Profile y in
1-115	13.9	6.48	151.0	44	0.022
1-110	12.7		119.0	41	0.036
1-105	11.8		97.2	40	0.036
1-100	10.8		74.7	35	0.038
1-95	10.4		66.0	38	0.041
1-90	9.0		39.0	28	0.040
1-85	8.2		25.3	28	0.042
1-80	7.6		15.8	28	0.040
1-75	7.1		8.4	25	0.035
2-110	14.5	7.77	150.7	44	0.035
2-105	14.6		153.7	42	0.052
2-100	13.8		131.2	30	0.049
2-95	13.4		120.3	33	0.047
2-90	13.1		112.3	28	0.027
2-85	11.6		75.3	23	0.028
2-80	9.9		38.7	17	0.037
2-75	8.3		9.2	9	0.046
2-70	7.8		1.5	6	0.049
2-65	7.1		-8.9	5	0.050

Table 11/3 Relative energy, etc. Nozzle 6. N = 330

Posn.	Rel.vel. v_o ft/s	Periph.vel. u_o ft/s	Rel. energy $v_o^2 - u_o^2$ $(ft/s)^2$	Deviation $\psi°$	Profile y in
3-105	14.3		120.5	26	0.028
3-100	14.5		126.0	29	0.040
3-95	14.25		119.0	32	0.043
3-90	14.3		120.5	28	0.037
3-85	13.9		109.0	27	0.031
3-80	13.3		93.0	26	0.031
3-75	12.1	9.16	62.5	21	0.034
3-70	10.4		23.0	12	0.036
3-65	9.9		14.0	10	0.033
3-60	8.7		-13.3	4	0.030
3-55	8.3		-15.0	- 4	0.027
3-50	7.3		-30.7	-10	0.028

Table 11/4 Relative energy, etc. Nozzle 6 N = 330

Posn	Rel. vel. v_o ft/s	Periph. vel. u_o ft/s	Rel. energy $v_o^2 - u_o^2$ $(ft/s)^2$	Deviation ψ^o	Profile y in
4-100	13.9		81.0	26	0.021
4-95	14.0		84.0	31	0.041
4-90	13.9		81.0	36	0.047
4-85	14.1		87.0	40	0.050
4-80	13.4		67.5	42	0.049
4-75	13.2	10.6	62.0	39	0.044
4-70	12.7		48.0	37	0.043
4-65	12.5		43.0	31	0.039
4-60	12.0		32.0	24	0.033
4-55	10.7		2.5	19	0.029
4-50	10.0		-12.0	7	0.020
4-45	8.5		-39.7	-9	0.016

Table 11/5 Relative energy, etc. Nozzle 6. N = 330

Posn.	Rel.vel. v_o ft/s	Periph.vel. u_o ft/s	Rel.energy $v_o^2 - u_o^2$ $(ft/s)^2$	Deviation ψ°	Profile y in
5-95	14.0		52	34	0.015
5-90	14.0		52	37	0.044
5-85	14.3		60	41	0.051
5-80	14.4		64	45	0.060
5-75	14.8		74	51	0.069
5-70	14.9	12.0	78	44	0.058
5-65	14.9		78	44	0.052
5-60	15.0		81	43	0.044
5-55	14.9		78	40	0.037
5-50	14.0		52	34	0.030
5-45	12.5		12	26	0.018

Table 11/6 and /7 Relative energy, etc. Nozzle 6. N = 330

Posn.	Rel.vel. v_o ft/s	Periph.vel. u_o ft/s	Rel.energy $v_o^2 - u_o^2$ $(ft/s)^2$	Deviation χ°	Profile y in
6-90	13.9		15	26	0.006
6-85	14.5		32	33	0.035
6-80	14.5		32	39	0.057
6-75	14.9		44	44	0.063
6-70	15.4		59	46	0.069
6-65	15.9	13.35	75	46	0.068
6-60	16.1		81	46	0.060
6-55	15.7		69	46	0.048
6-50	16.1		81	40	0.031
6-45	15.0		47	37	0.025
6-40	12.6		-19	19	0.015
7-80	15.3		25	23	0.016
7-75	15.4		27	30	0.052
7-70	15.6		35	33	0.062
7-65	16.2		53	36	0.067
7-60	16.7	14.45	68	37	0.067
7-55	17.5		97	38	0.055
7-50	17.7		105	39	0.037
7-45	16.8		73	37	0.019

Table 11/8 and /9 Relative energy, etc. Nozzle 6. N = 330

Posn.	Rel. vel. v_o ft/s	Periph. vel. u_o ft/s	Rel. energy $v_o^2 - u_o^2$ $(ft/s)^2$	Deviation χ^o	Profile y in
8-70	15.6		10	10	0.024
8-65	15.7		13	16	0.056
8-60	16.2		29	18	0.065
8-55	16.6	15.26	43	22	0.057
8-50	17.4		70	27	0.039
8-45	16.6		43	35	0.028
9-60	14.9		-18	- 4	0.015
9-55	15.3		- 8	4	0.036
9.50	15.7	15.5	+ 7	8	0.046
9.45	15.4		- 3	13	0.047
9-40	14.4		-33	13	0.033

Appendix 4.

SYSTEMS OF COORDINATES

It is most convenient for measuring purposes to use a Cartesian system of coordinates fixed in space. For the purposes of analysis however it is preferable to study the various quantities relative to a bucket and so conversion to a rotating system of coordinates is required. The two systems of coordinates may thus be defined as follows:-

(a) Fixed system (see diagram D.10)

Coordinates, x - horizontal, radial from shaft centre.

y - horizontal, parallel to projection of shaft.

z - vertical.

(b) Rotating system

Coordinates, x' - radial

y' - parallel to shaft

z' - tangent to periphery

Appendix 5.

CONSTRUCTION OF VELOCITY DIAGRAM AT OUTLET

This construction is shown typically in diagram D.4 which is lettered accordingly.

In the $x_o y_o$ plane a straight line ab is set off at H^o to the y_o axis, then another line ac, of length V_o to scale, is set off at V^o to ab. Then the perpendicular bc represents z_o, ad represents x_o and bd, y_o.

To obtain the coordinates in the $y_o z_o$ plane an arc of radius bc is described about b to the position e such that be is perpendicular to bd. The shaft axis lies at 20^o to the y_o axis hence y_o', z_o'' are set off at 20^o to y_o, z_o. Then (x_o, y_o', z_o'') represents V_o relative to the plane of the wheel.

Turning to the lower diagram, in the plane of the wheel, vector coordinates are (x_o, z_o'') from f to g. Changing the coordinates to the instantaneous position of the bucket, (x_o', z_o') replaces (x_o, z_o'').

To obtain the true shape of the velocity diagram in the plane of the paper, u_o is drawn to scale through f parallel to z_o' and gh parallel to x_o'. V_o is drawn to scale from f to gh. Then fjh represents the velocity diagram at outlet and jh is the relative velocity to scale.

If now y_o' is set off perpendicular to x_o' then α represents the projected angle in the x_o' y_o' plane.

Appendix 6.

CONSTRUCTION OF PARTICLE TRAJECTORY.

A typical step-by-step construction in tracing the trajectory of a particle of ideal fluid across a bucket surface is detailed in the following and shown in diagram D.8. The selected particle in this case is the first to strike the bucket inlet at the top of the ellipse. The surface element chosen to illustrate the method is about halfway across the bucket. The position of the element relative to the bucket surface as a whole is defined by the elevation of the corners with respect to a datum plane. Only three of the four corners can be used to specify fully the position of the plane element. The points (H,4), (J,4) and (J,5) are selected in this case as they form the triangle within which the major part of trajectory will lie. (see D.7)

The projections of the element are set out in the planes x'y', x'z' and z'y'. Note that (H,4 - J,4) is the true length in the x'z' plane and (J,4 - J,5) is the true length in the z'y' plane. The relative velocity components to any scale are now set off in the various planes, da at ε_7, eb at δ_7 and fc at λ_7.

In plane x'z' a perpendicular dg is drawn to intersect (J,4 - H,4) produced. Lines perpendicular to (J,4 - J,5) are now set off at all corners of the element in the z'y' plane and a parallel drawn through f. Also in this plane the true length (J,4 - H,4) - produced to g - is set off between the perpendiculars, thus giving the true shape of the plane element. A perpendicular to (J,4 - H,4) through g meets the parallel through f in 0.

Then 0.1_7 is the projection of the relative velocity vector in the plane of the surface element. Producing this line gives the orthogonal trajectory $1_7.1_8$.

Projecting back gives a', b', c' and with no rotation of the bucket aa', bb', cc' would give the new angle components. Correction for rotation involves motion in the x'z' plane and no movement in the y' direction. The angle of rotation related to trajectory time is calculated as shown in D.8, and the correction is made in the x'z' projection. Normally this has components in both x' and z' directions but in this case the radial component is zero. The correction in the z' direction is shown in the z'y' plane. Entry angle components to the next element are then ε_8, δ_8 and λ_8.

Appendix 7.

A.7 AUXILIARY TESTS

When a jet of liquid impinges tangentially on a curved vane, it tends to spread in directions at right angles to the principal plane of motion as can be seen in photograph P.35. As the liquid spreads its thickness decreases so that a progressively greater proportion is influenced by the boundary layer. The problem is further complicated by relative motion of the fluid filaments due to angular motion of the vane. In an attempt to analyse the nature of spread and how it is associated with friction, a series of tests was initiated using jets of various cross-sections impinging tangentially on one vane curved in two dimensions and on another curved in three dimensions.

A numerical method for use in a digital computer was devised on the basis that the fluid was ideal, with two objects in view. The first aimed to assess the effect of friction from a comparison of experimental and calculated results, the second to predict the spread from associated flow patterns with different dimensions.

It was clear that tests on a static bucket taken from an impulse wheel of high specific speed would have produced results of doubtful comparative value. In order to determine basic relationships, it was decided to use jet and vane shapes which were simple yet related to turbines of the jet type; this also simplified the force analysis. Inspection of Pelton and Turgo wheel buckets reveals that their generally ellipsoidal shapes are made up of sections approximately of the form of circular cylinders and parts of a sphere, and this determined the choice of vane shapes. A nominal radius of curvature of 2 inches was chosen for the vanes, as this was considered a minimum size for the nature of spread to be observed. The turning angle of the vane was restricted to 90° to facilitate measurements at outlet. Typical jet shapes of segmental and rectangular form were obtained from No.5 nozzle ($1\,{}^{1}/_{16}$" diameter). For most of the auxiliary tests a supply head was used equal to the mean inlet relative velocity head in the main tests.

A7.1 Theoretical analysis.

A7.1.1 Dimensional analysis.

The spread of a jet traversing a static vane can be usefully represented by a dimensional analysis comparing jet forces. Let the force of reaction, F_o on the vane at outlet be taken in the mean direction of flow; the total jet potential force, F_1 as experienced for example by a flat plate normal to the jet at inlet, is given by $\rho a V_1^{2}$, where $\underline{a}$ is the area of cross-section of the jet and V_1 is the total jet velocity at the vane. Graph GA.0 gives an additional guide to notation.

Considering, for example, a jet of rectangular cross-section, it can be shown that the force ratio,

$$\frac{F_o}{\rho (HB)\ V_1^{2}} = f\left[(Re), (Fr), \left(\frac{H}{B}\right), \theta \right]$$

where θ = turning angle of the vane.

(Re) is the Reynolds' No. governing frictional effects. (Fr) is the Froude No, $\frac{Hf}{V_1^2}$ governing the wave effect. If R is taken as the radius of curvature of the vane, then the lateral acceleration of jet particles, $f \propto \frac{V_1^2}{R}$

$$\therefore \quad (Fr) = \frac{H}{V_1^2} \cdot \frac{V_1^2}{R} = \frac{H}{R},$$

i.e. <u>independent of the supply head.</u>

$$\therefore \frac{F_o}{\rho (HB) V_1^2} = f_1 \left[(Re), \left(\frac{H}{R}\right), \left(\frac{H}{B}\right), \theta \right]$$

For an ideal fluid, the pattern of flow across the vane is independent of head, and this enabled the computer program to be constructed on a non-dimensional basis. For a real fluid, little change in the pattern of flow should be apparent with a limited change of head and tests at an increased head bore this out.

$\frac{H}{B}$ is termed the "shape factor" for the rectangular jet. For any other jet section, the depth is represented by the hydraulic mean depth, M at inlet, the wetted perimeter being taken as the jet width in contact with the vane. It will be noted that M and H are equivalent for the rectangular section, thus $\frac{M}{R}$ and $\frac{M}{B}$ are taken as general expressions for wave parameter and shape factor respectively.

A7.1.2 <u>Flow analysis across a two-dimensional vane.</u>

The object of the computer program is to estimate the change in

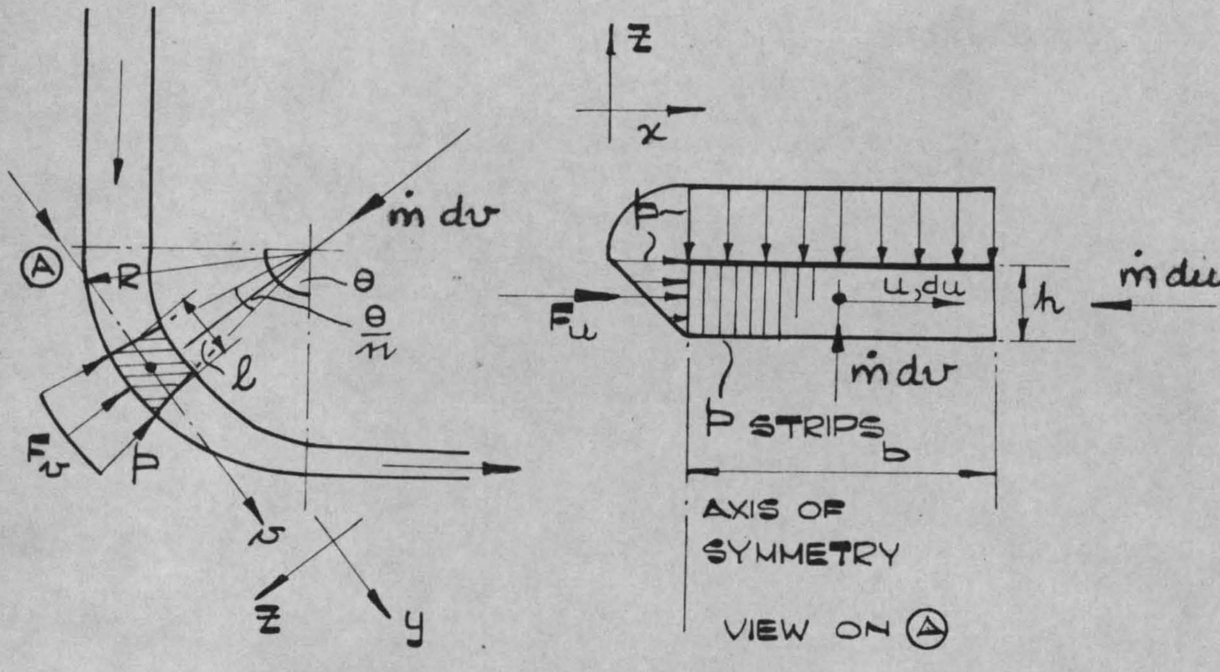

Z
x
ṁ dv
A
R
θ
θ/n
l
Fv
P
v
Z
y
P
Fu
u, du
h
ṁ du
ṁ dv
P STRIPS
b
AXIS OF SYMMETRY
VIEW ON A

FIG. 23.

profile of a jet of liquid, initially rectangular in form, as it crosses a curved vane; also to find the variation in angle of discharge α, relative to the normal, and the force on the trailing edge of the vane.

The program is based on a step-by-step method, involving two distinct series of operations. In the first the angle subtended by the vane is divided into n equal parts, each being characterised by a different control volume. (see Fig.23) The change in velocity of the mass of fluid in the x-direction, du is obtained by force analysis and this leads to the mean value of the velocity component, u. Using equations of linear motion the increase in b is calculated due to the free spread of the section in the xz plane, assuming that the rectangular form of the section is maintained. This provides the new quantitites for repeating the process referred to as a q-operation. When n identical q-operations have been performed on this mass flowrate, the final depth h is identified as the profile peak on the axis of symmetry.

Secondly, the half-section of the jet is divided into p equal strips, all having the same depth. If the boundary of the control volume were now moved from the axis of symmetry one strip to the right, it can readily be seen that the same force analysis would apply to a smaller mass flow, resulting in a wider spreading action. Thus p sets of q-operations are performed on the mass flow which is diminished by equal amounts with each step. The nett result of this subtraction process is that for each of p equal mass flow elements, the profile depth, angle of discharge and force component can be found at outlet.

A7.1.3 Force analysis (2)

The force analysis for a rectangular jet crossing a vane curved in two dimensions is shown in Fig. 23. The elementary control volume takes the form of a near-rectangular prism shown shaded in the figure. The axes of reference x, y, z move with the control volume and are defined as shown.

Flow is based on the following assumptions:-

(a) the fluid is ideal.

(b) the energy of all particles is based on the total head at outlet from the vane.

(c) the total velocities are the same at inlet and outlet, i.e. the change in elevation across the vane can in this way be discounted.

A7.1.4 Program construction (2)

The control volume subtends Θ/n at the centre of curvature. For the purpose of force analysis it is assumed that during any step calculation, v changes in direction but not in magnitude through the control volume. Then the force components in the y-direction will be in balance. In the z-direction, the hydrodynamic force, $F_v = \dot{m} \; dv = p.l.b$

$$\therefore \quad \dot{m} = \frac{p.l.b}{dv} \qquad \ldots (A.1)$$

Applying the cosine formula to the velocity diagram

$$dv = v\sqrt{2(1 - \cos \Theta /n)}$$

It is assumed that the pressure varies linearly across the film thickness. Then the mean pressure across the plane of symmetry = p/2. In the x-direction, $F_u = \frac{p}{2} \cdot h \cdot l = \dot{m}\ du$

$$\therefore \underline{du} = \frac{p}{2} \cdot h \cdot l \cdot \frac{dv}{p.l.b} = \underline{\frac{h}{b} \cdot \frac{dv}{2}}$$

Assuming that the cross-section (h.b) retains its shape and size and moves at a mean lateral velocity $\left(u + \frac{du}{2} \right)$ during the time taken for a particle to cross the vane element, then the distance moved by the centre of gravity, $s = \left(u + \frac{du}{2} \right) \times \frac{l}{v}$. If the section should now collapse about the centre of gravity and fill the space while retaining its rectangular form, the new breadth = b + 2s. Then the new depth, h = cross-section area/new breadth.

For a mean particle, the total energy

$$\propto \frac{V_1^2}{2} = \frac{v^2}{2} + \frac{u^2}{2} + \frac{p/2}{\rho}$$

On a non-dimensional basis, $V_1 = 1$.

Then $1 = v^2 + u^2 + \frac{p}{\rho}$ where v, u and p now represent the corresponding non-dimensional parameters.

But equation (A.1) gives $p = \frac{\dot{m}\ dv}{l.b}$

Also $\dot{m} = \rho.b.h.v$

$$\therefore \frac{p}{\rho} = \frac{b.h.v.dv}{l.b} = \frac{h}{l} . v. dv$$

$\therefore$ correction for v between q-operations involves

$$v = \sqrt{1 - u^2 - \frac{h}{l} . v . dv}$$

It is convenient to calculate the discharge angle, α for each mass element by using the spread for each strip in the final q-operation of the series. It is assumed for any bundle of strips, that the spread for the mass element is obtained by dividing the total spread by the number of strips and thus $ds = 2 s/m$. After accounting for the spread of previous elements, the angle of discharge, $\alpha = \arctan (ds/l)$

For any mass element discharging from the vane, the force ratio,

$$dF = v/V_1 = \cos \alpha$$

Hence the total force ratio, $F = \sum dF$.

The source program, written in ALGOL, and appropriate input data, are given in Appendix 8.

A7.1.5 Force analysis (3)

Some far-reaching assumptions were involved in simplifying the analysis of flow across a two-dimensional vane. Further assumptions would be required in extending the analysis to suit a three-dimensional vane. An attempt to produce a computer program on this basis proved inconclusive, but a force analysis is presented to show how the changing field of force tends to contain the spread.

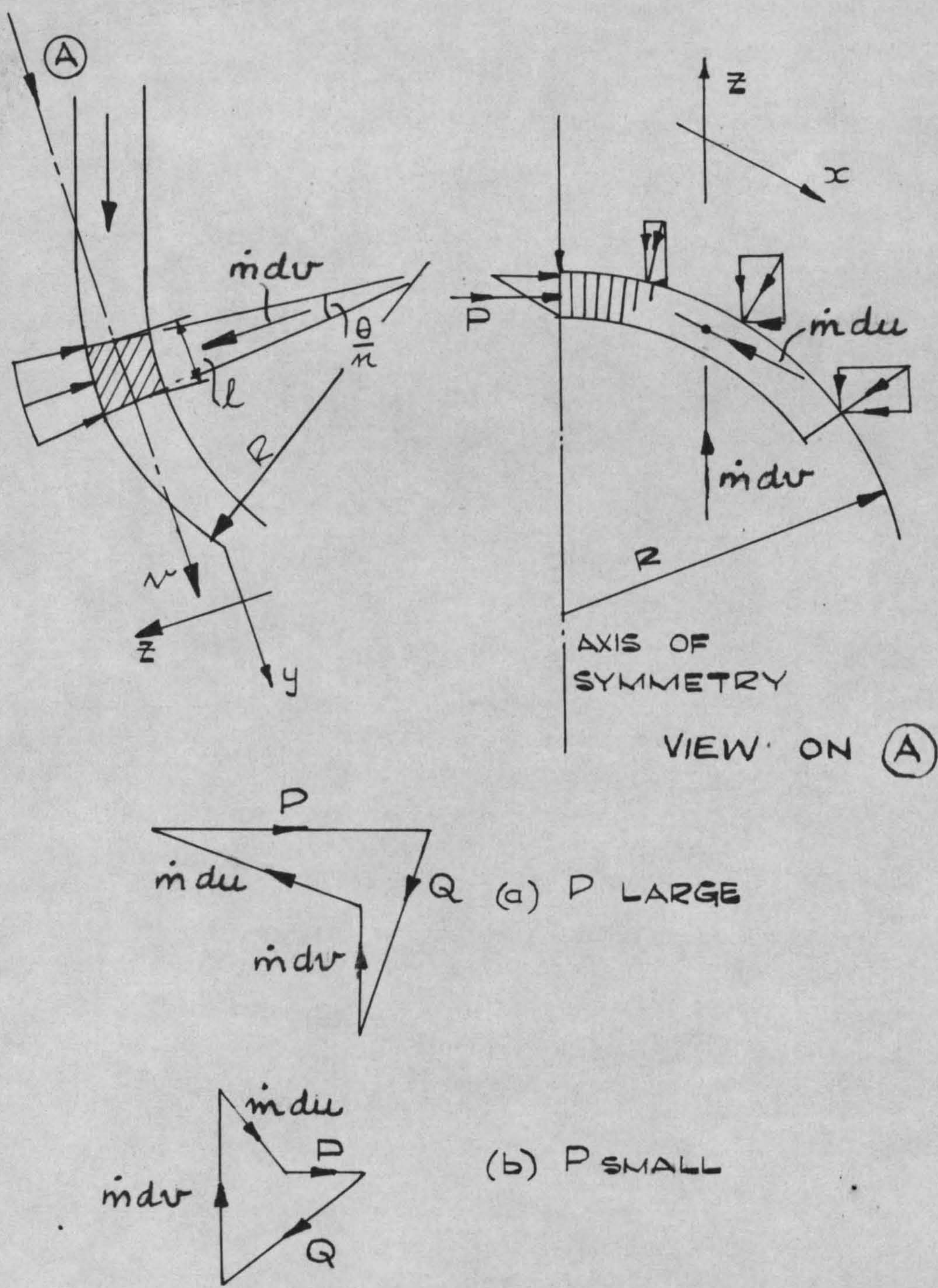
A
ṁdv
θ/n
l
R
v
z
y
z
x
P
ṁdu
ṁdv
R
AXIS OF SYMMETRY
VIEW ON A
P
ṁdu
Q
(a) P LARGE
ṁdv
ṁdu
P
(b) P SMALL
ṁdv
Q

FIG. 24.

Fig.24 shows the body of fluid in the control volume. The jet is tracing a mean path across the surface of the vane in the plane of symmetry parallel to yz. A change in direction is thus impressed on the fluid in planes parallel to the plane of symmetry, but as the pressure force must act normal to the vane surface, the lateral curvature produces an increasing inward component which resists the spreading action. Force Q in the figure represents the integral of the resultant elementary pressure forces exerted by the vane surface on the fluid in the xz plane.

It can be seen that during the early part of the trajectory, when the fluid layer is thick, the force P is large whilst the resisting component is small and this results in a large outward acceleration. Later in the trajectory when the fluid layer is thin and the spread relatively large, the force P is small and the resisting component large, resulting in a deceleration in the x-direction.

A7.2 Test apparatus.

A general arrangement of the test rig is shown in photograph P.30. Water was supplied through a header tank, fitted with a constant-head overflow device and suitable baffling arrangements to the nozzle which was bolted to the base of the tank. The jet emerging from the nozzle impinged on the vane undergoing test and was directed on discharge back to the sump. Suitable devices were assembled to measure the profile, mean velocity and angle of divergence of the jet at discharge.

A7.2.1 Jet shape.

A jet of segmental form was easily obtained by fixing the vane in the required relative position. Then the chord of the segment was formed by the inlet edge of the vane.

A jet approximately of rectangular form could be obtained from a jet of circular section by allowing the inlet edge of the vane to cut off a segmental part of the jet and shaping the nozzle to remove an equal segmental part from the opposite side. As shown in P.32 and P.33, a short length of solid brass of segmental section was fitted to the straight part of the nozzle bore and faired off smoothly to the adjacent internal wall with putty. This proved a good material for the purpose as the profile of the fillet could be readily altered to ensure that the jet section maintained its shape. Also at the low test heads used, the surface of the putty resisted any tendancy to erode.

A7.2.2 Vanes.

The two-dimensional vane was produced from a four inch bore cast iron cylindrical pipe. A quadrant was milled from this pipe thus ensuring a flat surface at inlet which could be set up horizontally. The vane was machined to a knife-edge where it came into contact with the jet at inlet and outlet; this was necessary at outlet to avoid distortion at the ends of the jet. The surface was polished smoothly.

As can be seen in P.38 the three-dimensional vane took the form of a spherical surface and was cut from a brass cistern ball. The shape was made rigid by setting half of the ball in a mould of plaster of paris and allowing this to set prior to cutting. The edges of the vane protruded from the mould sufficiently to avoid external interference with the jet action.

The vanes were mounted about two inches below the outlet surface of the nozzle. Once secured, the position and size of the jet relative to the vane were varied in the following way. As shown in P.34 and P.36, each end of the vane was attached to a length of angle secured to the frame by bolts passing through slots which allowed a limited amount of axial movement. The movement of each angle was controlled by means of a fine screw and measured by a vernier gauge. To obtain the required value of H, the vane position was adjusted until the leading edge just touched the jet surface; the vane was then moved into the jet until the verniers on each side indicated the same required setting, then the supporting angles were clamped in position.

A7.2.3 <u>Profile measurements.</u>

The jet profile at outlet was measured by a pointer on a micrometer head secured to an attachment which moved on rollers along a rigid beam mounted across the jet, as shown in P.28 and P.29. This beam was secured to the same angles as the vane to ensure that the measuring devices retained their position relative to the vane. The micrometer position was then adjusted so that the pointer traced out a line $\frac{1}{16}$" upstream from the outlet edge. The depth of water at any point in a traverse across the jet at outlet could then be obtained by observing the depths of the vane and water surfaces.

A7.2.4 Direction and velocity measurement.

The devices for gauging direction and velocity were combined in a single unit and mounted on a pin on the outside of a disc free to move about the micrometer pointer. These details can be distinguished in P.28 and P.29. The direction device took the form of a plane vane or blade passing through the water film. The direction of the blade could be lined up with the direction of flow by equalising the wave pattern in the wake. A needle attached to the disc moved relative to a fixed protractor thus indicating the angle of spread.

The appliance for measuring velocity took the form of a clockwork wheel mounted on a cantilever bearing with the plane of the wheel parallel to the blade. When a wheel of this type is dipped into a body of liquid moving at uniform velocity and its depth of immersion increased, it is found that the wheel speed increases until the surface makes a tangent with the root diameter of the teeth; further immersion produces a reduction in wheel speed.

The rotational speed of the wheel, which was obtained by using a stroboscope, was calibrated against a jet moving at a range of velocities appropriate to the tests. The jet is seen in P.37 emerging from a sharp-edged orifice of known characteristics, fitted to the side of a tank in which the head could be varied. The calibration curve is linear and is shown in graph GA.13. The velocity on test was thus obtained by varying the depth of immersion of the wheel until the maximum speed was recorded. It was important too for the plane of the wheel to be in line with the direction of flow as a cross component also produced a change in rotational speed.

It will also be noted that the velocity was measured at a point about half an inch downstream from the trailing edge of the vane. In these tests the boundary layer thickness was comparable to the liquid film thickness and the larger the gap the greater was the tendancy for the particle velocities to equalise across the film, with the result that the velocity reading tended closer to the mean.

In the case of the three-dimensional vane, it was further found necessary to allow the measuring devices to swing about the centre of the spherical surface at outlet in order to observe the flow characteristics normal to the surface. This is apparent in P.38.

A7.2.5 <u>Increased head.</u>

To verify that the spreading action of the jet across the vane was independent of head, tests were run with the head increased threefold. The test rig was altered by erecting a standpipe attached directly to the nozzle flange and arranging a suitable overflow. The modified arrangement appears in P.31.

A7.3 <u>Procedure.</u>

The investigations were directed principally towards the spread of a rectangular jet across a two-dimensional vane as it was considered that this was more representative of the action of the Turgo wheel, and the computer program was prepared on this basis. Supporting tests were performed for a range of jet depths on both shapes of vane. The segmental jet was also used with both vanes, firstly, in the form of a "half-jet", typical of the Pelton wheel and secondly, with a lesser depth, a form related more to the Turgo wheel.

For a chosen jet and two-dimensional vane formation, the outlet profile was constructed by measuring film depths at intervals of 0.2 in across the breadth. Velocities and directions were measured at the same increments. For the tests on the three-dimensional vane, angular increments of 5° replaced the linear ones.

The readings and calculated results are shown in full for one jet form together with specimen calculations. The results of all tests are shown in graphical form in graphs GA.1 - GA.9, together with the corresponding results obtained from the computer. The graphs are plotted for one half only of the symmetrical form.

Tests at the increased head were performed using only the rectangular jet of depth 0.6 in, and the results are presented in GA.4 on the same graph as the results pertaining to the standard head.

GA.10 shows the characteristics of flow of a jet of rectangular form on both two-dimensional and three-dimensional vanes to the same scale and gives a graphic picture of the effect of lateral containment.

In GA.11 profile depth has been plotted against velocity and there is clearly some connection between these quantities provided the vane geometry remains constant.

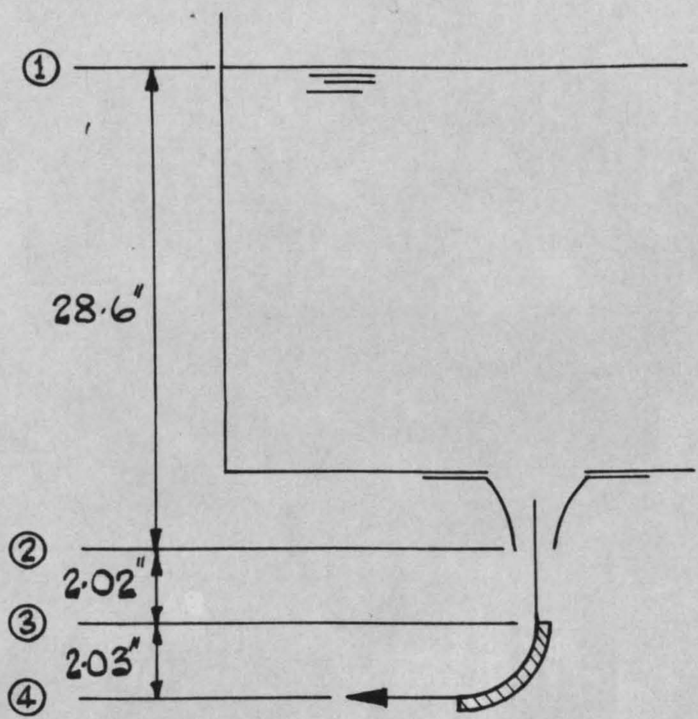

FIG. 25.

For each jet form at outlet, the cross-section was divided into strips of equal width and the total force of reaction found from an integration of the component forces in planes normal to the outlet edge. The flowrate was integrated at outlet in the same way and compared with the incoming flow, thus providing a check on the measured velocities at outlet. Since the integrated flow was in every case within 5% of the flow at inlet, it may be assumed not only that the velocity measuring device was effective but also that the velocity at the point of measurement approximated closely to the mean.

Finally GA.12 shows the inter-relation of friction and spread as they affect the force of reaction on the trailing edge of the vane.

A7.4 Tabulated results and specimen calculations

Head and Velocity

Due to the change in head across the vane, the velocity increases from inlet to outlet, but as in the main tests, the velocity has been considered constant and taken as the ideal value at outlet.

From Fig.25, the total head from the water surface to the vane outlet at (4),

$$H_4 = 32.65 \text{ in}$$

Head loss in nozzle 5

$$= H_2(1 - C_v^{\,2}) = 28.6\,(1 - 0.983^2) = \underline{0.97 \text{ in}}$$

Head available in the form of velocity , $\frac{V_4^2}{2g} = 31.68$ in

and $\underline{V_4 = 156.5 \text{ in/s}}$

This velocity was achieved at outlet positions where the profile was thick and friction effects relatively small.

In the case of the three-dimensional vane, as the spherical radius was slightly larger than the radius of curvature of the two-dimensional vane, the vane level was adjusted to give the same overall head.

Radius, R = 2.03" for 2-dim. vane

and R = 2.22" for 3-dim. vane

For the rectangular section considered, H = 0.5" and mean B = 1.02".

<u>2-dimensional vane</u>

Flow at inlet, $Q_1 = 0.51 \times 0.5 \times 156.5$

$= 39.91 \text{ in}^3/\text{s}$

and at outlet, $Q_o = \sum \text{b.h.v.}$

$= 38.0 \text{ in}^3/\text{s}$

Error $= \frac{1.91}{39.91} = 4.8\%$

Also force at inlet, $F_1 \propto Q V_1$

$= 39.91 \times 156.5$

$= 6246$ inch units

and at outlet, $F_o = \sum d\,F_o = 5191.5$ inch units

$\therefore$ Force ratio, $F = \dfrac{F_o}{F_1} = 0.831$

3-dimensional vane

$Q_1 = 39.91 \; in^3/s$, $\quad Q_o = 39.71 \; in^3/s$

$\therefore$ Error $= \dfrac{0.2}{39.91} = 0.5\%$

$F_1 = 6246$ inch units, $\quad F_o = 5838$ inch units

$\therefore$ Force ratio, $F = 0.935$

Table A7/1

2-dimensional vane. Mid-point = 11.65"

Scale in	Speed in/s	Angle α°	Profile in	Scale in	Speed in/s	Angle α°	Profile in
11.8	156.5	-5°	0.161	11.6	156.5	$+2^\circ$	0.162
12.0	155.8	-10°	0.147	11.4	155.0	$+6^\circ$	0.155
12.2	155.0	-14°	0.136	11.2	155.0	$+12^\circ$	0.148
12.4	155.0	-18°	0.126	11.0	155.0	$+16^\circ$	0.135
12.6	154.0	-21°	0.114	10.8	154.0	$+19^\circ$	0.121
12.8	152.8	-24°	0.102	10.6	152.0	$+22^\circ$	0.110
13.0	150.3	-28°	0.091	10.4	151.0	$+25^\circ$	0.098
13.2	149.7	-31°	0.083	10.2	149.7	$+29^\circ$	0.086
13.4	145.4	-34°	0.078	10.0	146.0	$+33^\circ$	0.078
13.6	143.0	-37°	0.069	9.8	143.0	$+36^\circ$	0.075
13.8	140.0	-40°	0.062	9.6	138.0	$+39^\circ$	0.070
14.0	134.3	-42°	0.055	9.4	132.0	$+42^\circ$	0.060
14.2	123.0	-44°	0.047	9.2	128.3	$+44^\circ$	0.052
14.4	113.0	-	0.041	9.0	118.0	$+46^\circ$	0.046
14.6	87.3	-	0.036	8.8	93.4	-	0.042
14.8	-	-	0.033	8.6	-	-	0.031
15.0	-	-	0.029	8.4	-	-	0.028

Table A7/2

2-dimensional vane, b = 0.2"

Lateral Distance x (in)	0.1	0.3	0.5	0.7	0.9	1.1	1.3	1.5
Mean depth h (in)	0.162	0.151	0.14	0.13	0.117	0.108	0.097	0.087
Area (b.h.) (in^2)	.0324	.0302	.028	.026	.0234	.0216	.0194	.0174
Total linear speed V (in/s)	156.5	156.5	156	155	154	152.5	151	149
Disch. angle α°	3	8.5	12.5	16.5	20	23.5	27	30
$u = V \sin \alpha$	8.15	23.2	33.6	44.0	52.6	60.9	68.5	74.5
$dQ_o = b.h.v.$	5.07	4.67	4.26	3.86	3.37	3.02	2.61	2.25
$dF_o \propto b.h.v^2$	792.0	723.5	649.1	574.5	490.4	422.4	351.2	289.7

Data from GA.3

Table A/7 (continued)

Lateral Distance x (in)	1.7	1.9	2.1	2.3	2.5	2.7	2.9	3.1	3.3
Mean depth h (in)	0.08	0.072	0.065	0.058	0.05	0.044	0.038	0.032	0.027
Area (b.h.) (in^2)	.016	.0144	.013	.0116	.01	.0088	.0076	.0064	.0054
Total linear speed V (in/s)	146	143	138	133	126	116	105	90	73
Disch. angle α°	33.5	36.5	39.2	42	44	46	48	50	52
$u = V \sin \alpha$	80.6	85.2	87.3	89.0	87.7	83.5	78.0	69.0	57.5
$dQ_o = b.h.v.$	1.95	1.66	1.39	1.15	.91	.71	.53	.37	.24
$dF_o \propto b.h.v^2$	237.2	190.4	148.7	113.3	82.1	57.2	37.5	21.4	10.9

Table A7/3

3-dimensional vane.   Mean readings.

Scale β°	Speed in/s	Angle α°	Profile in
0°	156.5	0°	0.205
5°	156	3°	0.209
10°	155	5°	0.199
15°	155	6°	0.186
20°	153	7°	0.175
25°	149	$6\frac{1}{2}^\circ$	0.161
30°	148	5°	0.124
35°	145	4°	0.121
40°	125	-	0.101
45°	-	-	0.071
50°	-	-	0.041

Table A7/4

3-dimensional vane, $b \doteqdot 0.2''$

Lateral Angle β°	$2\frac{1}{2}$	$7\frac{1}{2}$	$12\frac{1}{2}$	$17\frac{1}{2}$	$22\frac{1}{2}$	$27\frac{1}{2}$	$32\frac{1}{2}$	$37\frac{1}{2}$	$42\frac{1}{2}$	$47\frac{1}{2}$	$52\frac{1}{2}$
Mean depth h (in)	0.208	0.202	0.192	0.180	0.165	0.148	0.128	0.105	0.08	0.05	0.02
Area b.h. (in^2)	0.042	0.040	0.038	0.036	0.033	0.030	0.026	0.021	0.016	0.010	0.004
Total linear speed V (in/s)	156.5	156	154	152	149	147	142	132	112	88	43
Disch angle α°	1.7	4	5.6	6.6	6.9	5.8	4.4	3.7	3.4	3.2	3.1
$u = V \sin \alpha$	4.65	10.9	15.0	17.45	17.9	14.85	10.9	8.5	6.65	4.9	2.25
$dQ_o \doteqdot b.h.V$	5.99	5.81	5.47	5.08	4.57	4.07	3.41	2.61	1.70	0.84	0.17
$dF_o \propto b.h.V^2$	937.3	906.8	842.4	771.4	681.3	597.9	483.9	344.8	190.7	74.0	7.1

Data from GA.8

A7.5 Discussion.

(a) Two-dimensional vane.

The results of the tests on the rectangular jet are shown graphically in GA.1 to GA.5. The actual profile at outlet follows a similar pattern to the calculated profile. GA.4 confirms that the wave characteristics are unaffected by the change in head. The thickening of the film is due to the presence of a boundary layer. Assuming however that the boundary layer thickness is related to Reynolds' number, at a specified position on the vane surface, by an expression of the form, $\delta = \frac{\text{constant}}{(Re)^n}$, where $n < 1$, and bearing in mind that these tests were performed at a very low velocity, it would appear that the divergence between the actual and calculated values is approaching a maximum. A substantial increase in head would decrease the film thickness thus reducing the divergence between the profiles.

A discontinuity common to all the profile curves becomes more evident as the shape factor increases. As the jet comes from a circular nozzle, the greater the depth H of the section the further it departs from the rectangular form. The discontinuity comes from the corner of the section which curves in towards the vane at impingement.

A study of the calculated angles of discharge reveals little change with variation of shape factor, whether incurred by altering the depth or breadth. The experimental results follow the calculated ones closely, but the scope of the tests was too limited to assess in detail the connection between angle of spread on the one hand and velocity and profile on the other. In addition the tests were performed without varying the turning angle or radius of curvature of the vane, which might be expected to have a considerable effect on the angle of discharge. This was checked by using suitable input data in conjunction with the computer program.

The jet velocity at any distance from the axis of symmetry seems to be a function mainly of the profile at that point and the thickness of the boundary layer. This is confirmed by the fact that the velocity is maintained over a greater degree of spread when the depth increases.

Experimental results for the segmental jets are shown graphically in GA.6 and GA.7. It will be noted that the profiles are convex outwards. This is probably due to the fact that for any number of strips - as defined in A7.1.2 - of the jet at inlet, the ratio of pressure force : mass flow is greater than in the corresponding rectangular section. This would cause a greater spreading action in the case of the ideal fluid, but friction effects quickly decelerate the initial thin fluid film. The slowing down of the oncoming fluid hinders its complete natural spread thus maintaining the convex profile of the jet. Although the same forces are at work in the rectangular jet, the strips, having relatively greater mass, initially form a thicker layer and the oncoming fluid is able to move at a greater velocity relative to this layer. The decelerating effect is evident from the variation in the u-component of velocity across the outlet profile shown in GA.3

This convex profile implies a relatively thicker fluid layer which has noticeably beneficial effects on the velocity pattern. On a basis of shape factor the segmental jet characteristics in GA.6 may be compared to the rectangular jet characteristics in GA.1. The segmental jet having a greater tendancy to spread has a peak profile of 0.1 in compared with 0.125 in. in the case of the rectangular jet. The velocities at these points are related to the depths and due to the difference in outlet profiles, the rate of change of the jet velocity gradient is lower for the segmental shape than for the rectangular. In fact there is a noticeable degree of consistency between profile and velocity readings in respect of the two-dimensional vane as is demonstrated in GA.11 by a plot of all experimental results on this vane.

Graph GA.12 shows the variation of force ratio with the parameter M/R. As R, B and θ were maintained constant during these tests the parameter may be regarded as representing the inlet depth or shape factor. As the fluid depth increases at outlet so friction effects are of progressively less importance, but so too does the spread of fluid at outlet increase so that a greater proportion of the fluid is discharging at angles widely diverging from the normal. This results in a fall in force ratio with increase in depth, well illustrated by the calculated results using an ideal fluid, where the force ratio $\longrightarrow$ 1 as the depth M $\longrightarrow$ 0. However as the depth of the real fluid decreases, the fluid is affected more and more by friction and this causes a reduction in force ratio. The optimum shape factor will then occur when a balance is reached between these two opposing effects and this is borne out by the results of the tests. This becomes an important criterion when calculating the bucket pitch for a certain jet size.

For larger depths of jet there is very little discrepancy between the calculated and experimental results as shown in GA.12. This is due mainly to the close correspondence between actual and ideal angles of divergence. The poor showing of the segmental jets in this connection is due principally to the low peaks of profile and velocity.

(b) Three-dimensional vane.

It was anticipated that the critical force ratio would occur within the same range of depths as in the two-dimensional case, consequently the number of tests on the rectangular jet form was reduced to three. These are presented in GA.8, and GA.9 shows the graphical test results for the segmental forms.

The most striking feature of the tests on the three-dimensional vane, evident in the photographs, is the pronounced reduction in spread of the jet. The initial lateral acceleration quickly diminishes and reverses in sense and this accounts for the angle of divergence rising to a peak, falling, then levelling off. The outlet profile becomes convex outwards, influenced by this changing pattern of velocities. Relative to the profile range the jet velocity is well maintained. The differences between the rectangular and segmental characteristics, noted in the two-dimensional case, are also present in this case.

The relative effect of the introduction of a third dimension is more evident from a comparison of the characteristics of the same rectangular jet shape on the two vanes, shown in GA.10. The reduction in angle of spread and containment of the jet are quite apparent. However, a feature emerges not previously apparent viz. that the velocity in the case of the three-dimensional vane diminishes rapidly below two-dimensional values despite the fact that the profile depth is greater than in the two-dimensional case. This effect is marked and consistent throughout the tests as can be seen from reference to the curves in GA.11. This reduction in velocity is probably the result of increased turbulence stemming from the reversed lateral motion and consequent eddying of the fluid.

The deterioration in force ratio due to this factor is however far outweighed by the improvement in spreading characteristics, as can be seen in GA.12. The improvement in the force ratio of the segmental jet is due to the rise in the profile peak; while still lower than the corresponding peak from the comparable rectangular jet, it nonetheless appears to lie outwith the boundary layer with a consequent rise in velocity.

As can be seen in GA.11, again in the case of the three-dimensional vane there is a discernible relationship between profile and velocity independent of jet form.

There are many quantities which would have to be systematically varied in tests of this nature in order to obtain a comprehensive picture of the phenomena controlling the flow of fluid in an impulse turbine. Limited though the tests have been it is felt that the information derived has proved useful in assessing the relative importance of the factors involved in this study.

A7.6 Findings

1. The wave pattern of a liquid jet across a static curved vane is unaffected by a change in head.

2. The introduction of lateral curvature reduces the spread of the jet but leads to increased turbulence and friction losses.

3. The optumum jet shape is one for which the combined effects of friction and spread are at a minimum. This is an important factor when deciding on the number of buckets required in an impulse wheel.

4. Within the limitations imposed by test conditions, for either vane configuration there is a direct relationship between profile depth and velocity, independent of the shape of the impinging jet.

Appendix 8.

SOURCE PROGRAM IN ALGOL.

```
'begin'
   'integer'  k;
      k:=  read;
'begin'
'real' B,H,R,theta,  conv,  l,b,h,u,du,v,dv,
      s,ds,x,A,totA,sumA,  F,  dF,  alpha,  thetar,  factor,  area;
   'integer'  m,  n,  j;
   'for'  j:=1'step'  1  'until' k .'do'
'begin'       B:= read;  H:= read;  R:= read;
    theta:= read;  n := read;
    writetext('(''('3c')'DATA')'); print (j, 2, 0) ;
    writetext('(''('c3s')'p'('8s')'x'('11s')'h'('13s')'alpha'('2c')'')');
    x:=  F  := ds:=  0;
    h:=  H;
    b:=  B/2;
    conv:= 3.14159/180;
    thetar:=  theta * conv;
    l  :=  R * thetar/n;
    totA:= H * B/2;
    A:= totA/n;
    factor:= sqrt(2*(1-cos(thetar/n) ) );
    m:= n;


'begin'
   'integer'  p,  q;
'for'  p:=  1  'step'  1  'until'n-1   'do'
   'begin'  u:=du:=0; v:=1;
            sumA:= m * A;
      'for'  q:= 1 'step'  1 'until'  n  'do'
      'begin'  dv:=v* factor;
            area:= sumA/v;
              du:= h/b * dv/2;
                     s:= (u + du/2)  *  l/v ;
                     b:=  b + 2 * s;
                     h:= area/b;
                     u:= u + du;
                     v:= sqrt  (1-u↑2-h/l*v*dv);
```

```
      'end' of inner for;

              x:= x + b/m ;
              ds:= ds + 2*s/m ;
         alpha:= (arctan(ds/1) )/conv;
              dF:=(cos(alpha * conv) )/n;
              F:= F + dF;
         newline (1);
         print (p,3,0);
         space (4) ;
         print (x,2,3);
         space (4) ;
         print (h,1,4);
         space (4);
         print (alpha,2,3);
         m:= m - 1 ;
         h:= H;
         b:= B/2* m/n
      'end' giving final x for each m
    'end';
    writetext ('(''('2c')'F')') ; print (F,2,4);
    'end' ;
  'end' ;
finish : 'end'
```

INPUT DATA

DATA/1

16

1.046,	0.3,	2.03,	88,	100
1.038,	0.4,	2.03,	88,	100
1.02,	0.5,	2.03,	88,	100
1.0,	0.6,	2.03,	88,	100
0.98,	0.7,	2.03,	88,	100
1.0,	0.5,	1.0,	90,	100
1.0,	0.5,	1.5,	90,	100
1.0,	0.5,	2.0,	90,	100
1.0,	0.5,	2.5,	90,	100
1.0,	0.5,	3.0,	90,	100
1.0,	0.5,	2.0,	100,	100
1.0,	0.5,	2.0,	110,	100
1.0,	0.5,	2.0,	120,	100
1.0,	0.5,	2.0,	130,	100
1.0,	0.5,	2.0,	140,	100
1.0,	0.5,	2.0,	150,	100

DATA/2

9

1.0,	0.3,	2.0,	90,	100
1.0,	0.4,	2.0,	90,	100
1.0,	0.5,	2.0,	90,	100
1.0,	0.6,	2.0,	90,	100
1.0,	0.7,	2.0,	90,	100
1.4,	0.4,	2.0,	90,	100
1.2,	0.4,	2.0,	90,	100
0.8,	0.4,	2.0,	90,	100
0.6,	0.4,	2.0,	90,	100

Appendix 9.

REFERENCES.

(1) DOBLE, W.A. "The tangential water wheel", Trans. Am. Inst. Min. Engrs. 1899, 29, p.852.

(2) DURAND, W.F. "The Pelton water wheel", Mech. Engng. 1939, 6, p.447 and 7, p.511..

(3) CREWDSON, E. "Design and performance of a new impulse water-turbine, Proc. I.C.E. 1921, 213, p.396.

(4) EILKEN, H. "Piezoelektrische Messungen an einer Freistrahlturbine", Forschung auf dem gebiete des ingenieurwesens, 1938, 9, No.6, p.287.

(5) LOWY, R. "Efficiency analysis of Pelton wheels", Trans. A.S.M.E., 1944, 66, p.527.

(6) QUICK, R.S. "Problems encountered in the design and operation of impulse turbines", Trans. A.S.M.E. 1940, 62, p.15.

(7) OGUEY, P., MAMIN, M. and BAATARD, F. "Etude theoretique et experimentale de la dispersion du jet dans la turbine Pelton", Bulletin Technique de la Suisse Romande, 1944, No.21, p.265 and No.22, p.281; 1951, No.4, p.37 and No.5, p.53.

(8) SHIPULIN, I.F. "Inclined jet water turbine" Mashgiz, 1956, 19, p.57.

(9) SHIPULIN, I.F. "Working characteristics of an inclined jet turbine based on the energy balance of the working stream". Mashgiz, 1958, 21, p.76.

(10) EDEL, U.Y. "Bucket type water turbines". Mashgiz, 1963.

(11) EDEL, U.Y. "Investigation of flow over the surface of a Pelton wheel bucket with an analysis of flow losses". TRUDY C.K.T.I. Kotloturbstroienie, Wyp.46, 1964, p.41.

(12) GILBERT GILKES & GORDON, LTD. "On the development of water power". 1956, p.58.

GUIDE TO NOTATION AT OUTLET

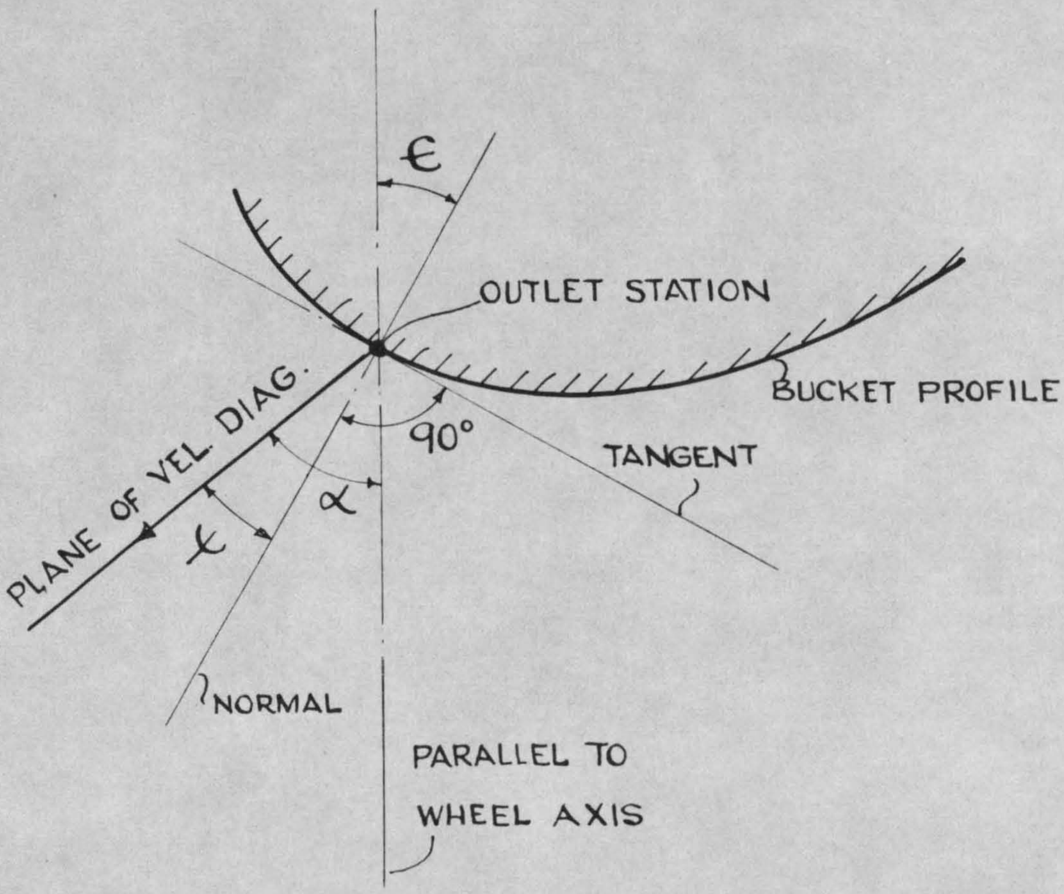

PLAN VIEW OF BUCKET AT OUTLET

$x'y'$ PLANE

D.1.

TYPICAL VELOCITY DIAGRAMS AT OUTLET

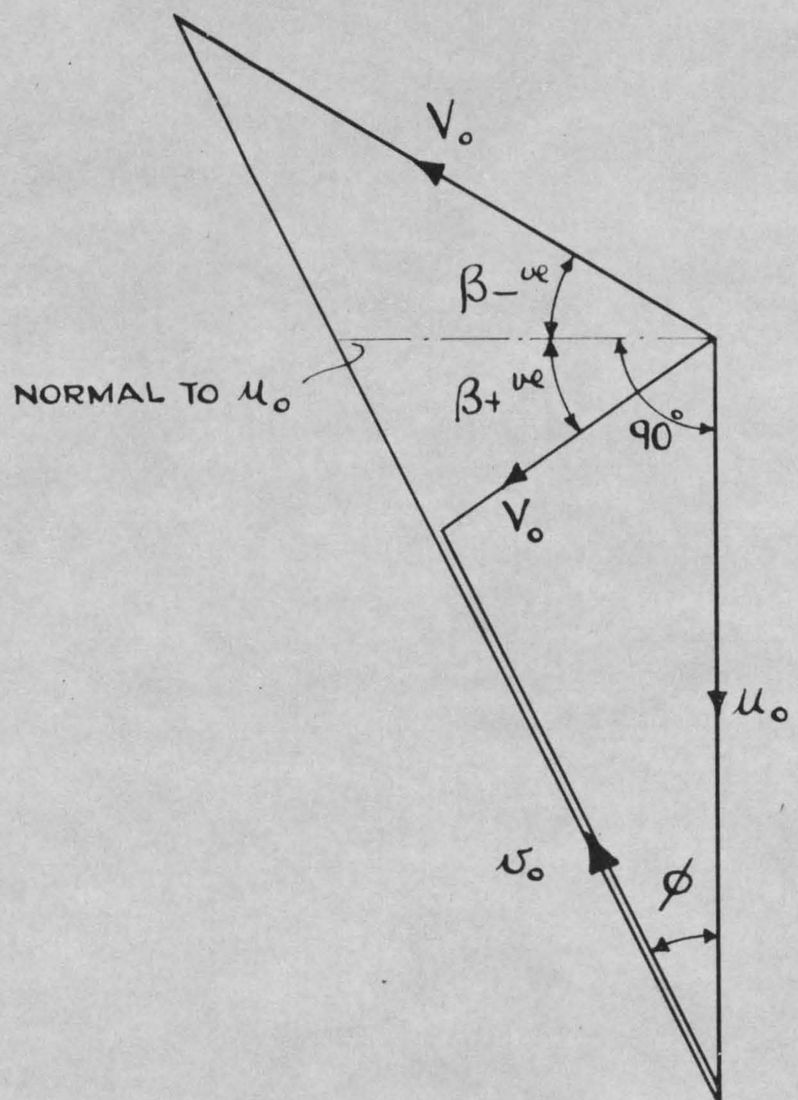

D.2.

$\boxed{6}$

FROM EXPERIMENT	FROM DIAGRAM
$V_o = 6{\cdot}9\,ft/s$, $u_o = 13{\cdot}35\,ft/s$	$v_o = 14{\cdot}9\,ft/s$
$V^\circ = 22^\circ$	$\alpha = 69^\circ$, $\gamma = 44^\circ$
$H^\circ = 75^\circ$	$\beta = 1^\circ$, $\phi = 28^\circ$

$\boxed{6 - 75^\circ}$

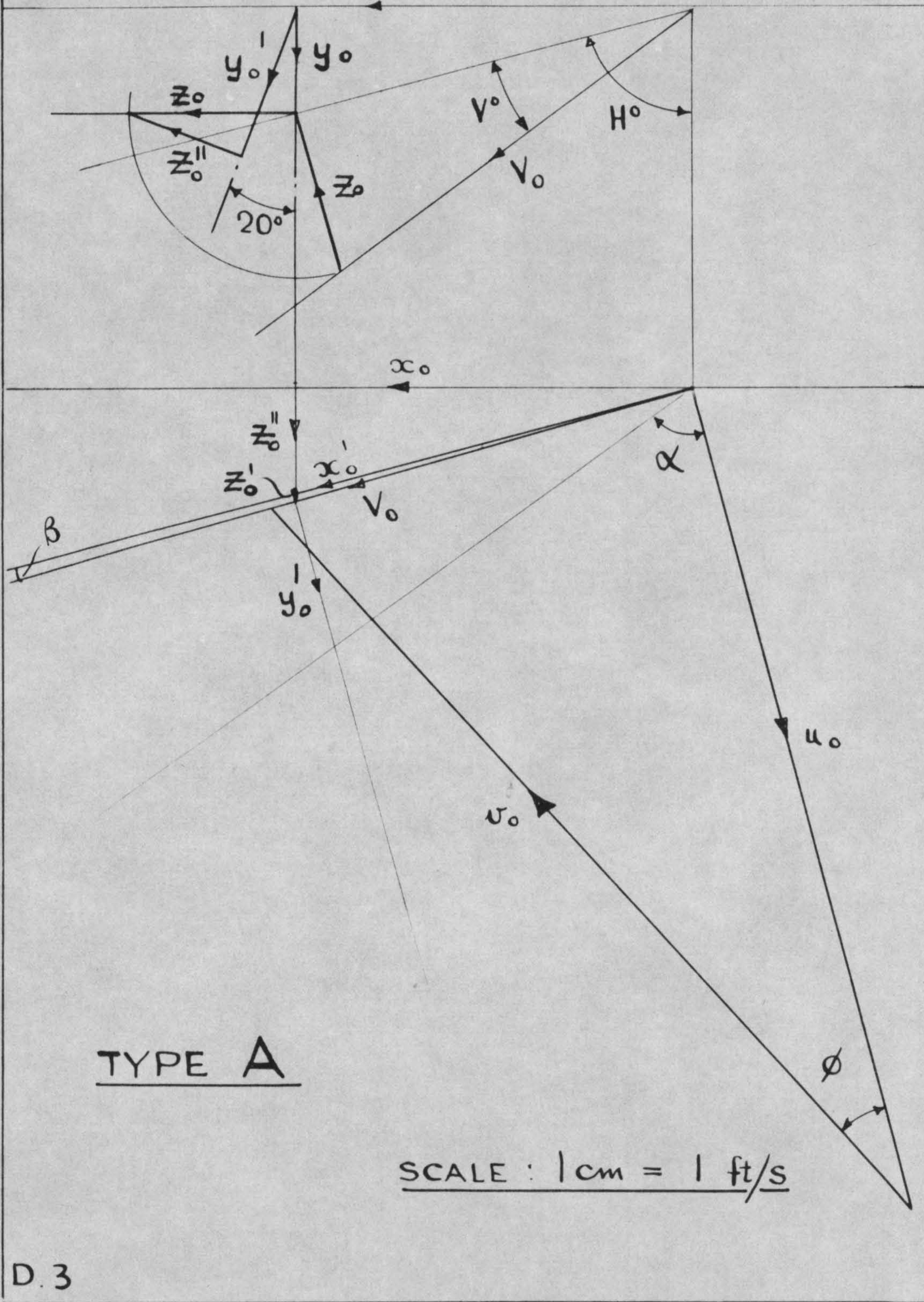

D. 3

6

3- 95°

FROM EXPERIMENT

$V_0 = 7\cdot 3$ ft/s

$u_0 = 9\cdot 16$ ft/s

$V° = -15°$

$H° = 23°$

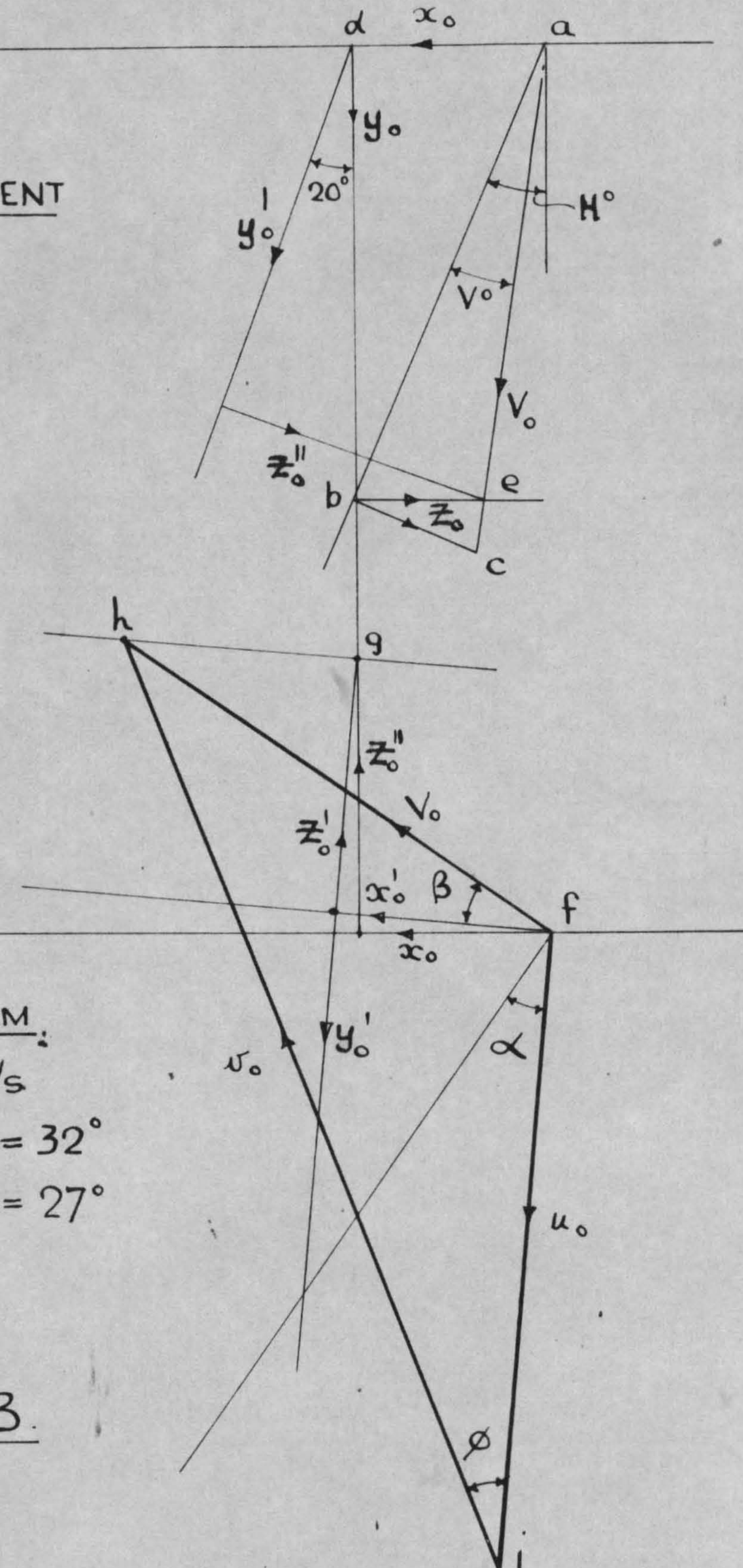

FROM DIAGRAM:

$v_0 = 14\cdot 25$ ft/s

$\alpha = 30°$, $\chi = 32°$

$\beta = -30°$, $\phi = 27°$

TYPE B.

SCALE: 1cm = 1 ft/s.

D.4.

$\boxed{6}$

FROM EXPERIMENT	FROM DIAGRAM
$V_o = 5{\cdot}4\ ft/s,\ u_o = 10{\cdot}6\ ft/s$	$v_o = 10{\cdot}0\ ft/s$
$V^\circ = 47^\circ$	$\alpha = 13^\circ,\ \gamma = 7^\circ$
$H^\circ = -6^\circ$	$\beta = 21^\circ,\ \phi = 30^\circ$

$\boxed{4 - 50^\circ}$

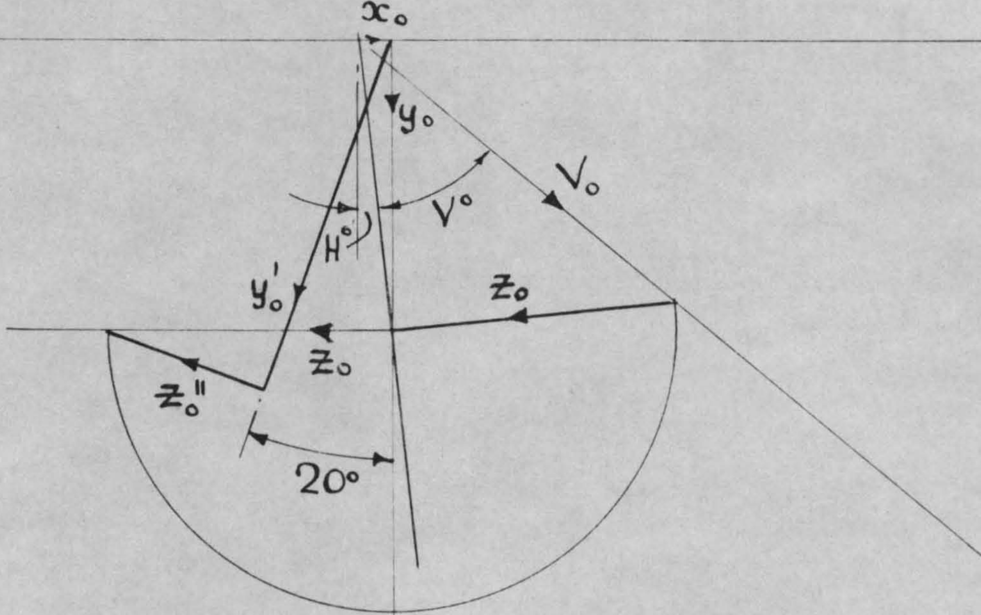

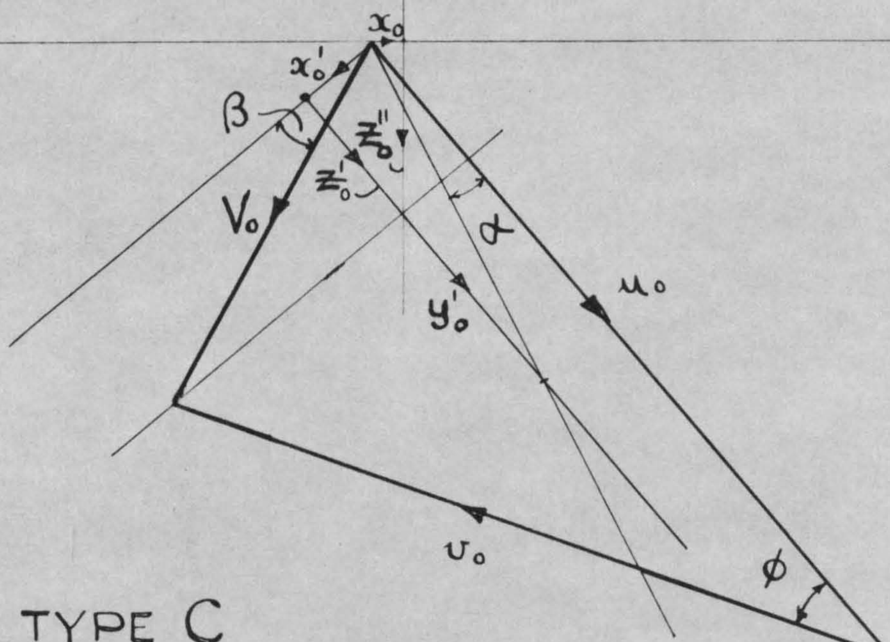

TYPE C

SCALE : 1 cm = 1 ft/s

D.5.

TRAJECTORIES : IDEAL FLUID

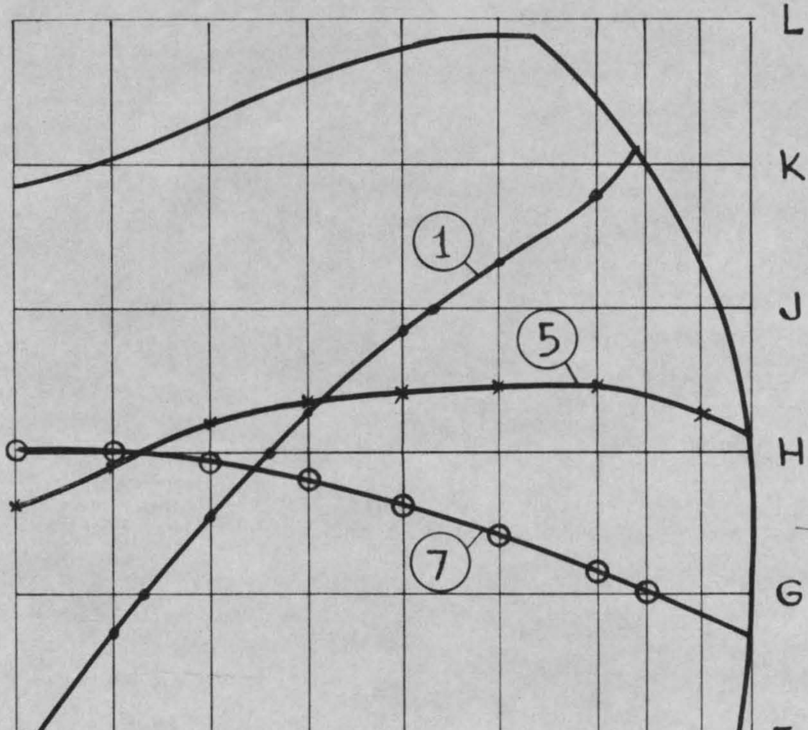

D.9.

MEASURING COORDINATE SYSTEM

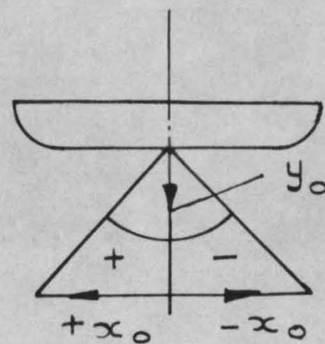

HORIZONTAL PLANE, H°

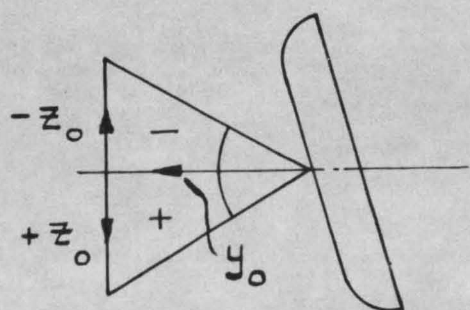

VERTICAL PLANE, V°

DIAGRAM D. 10.

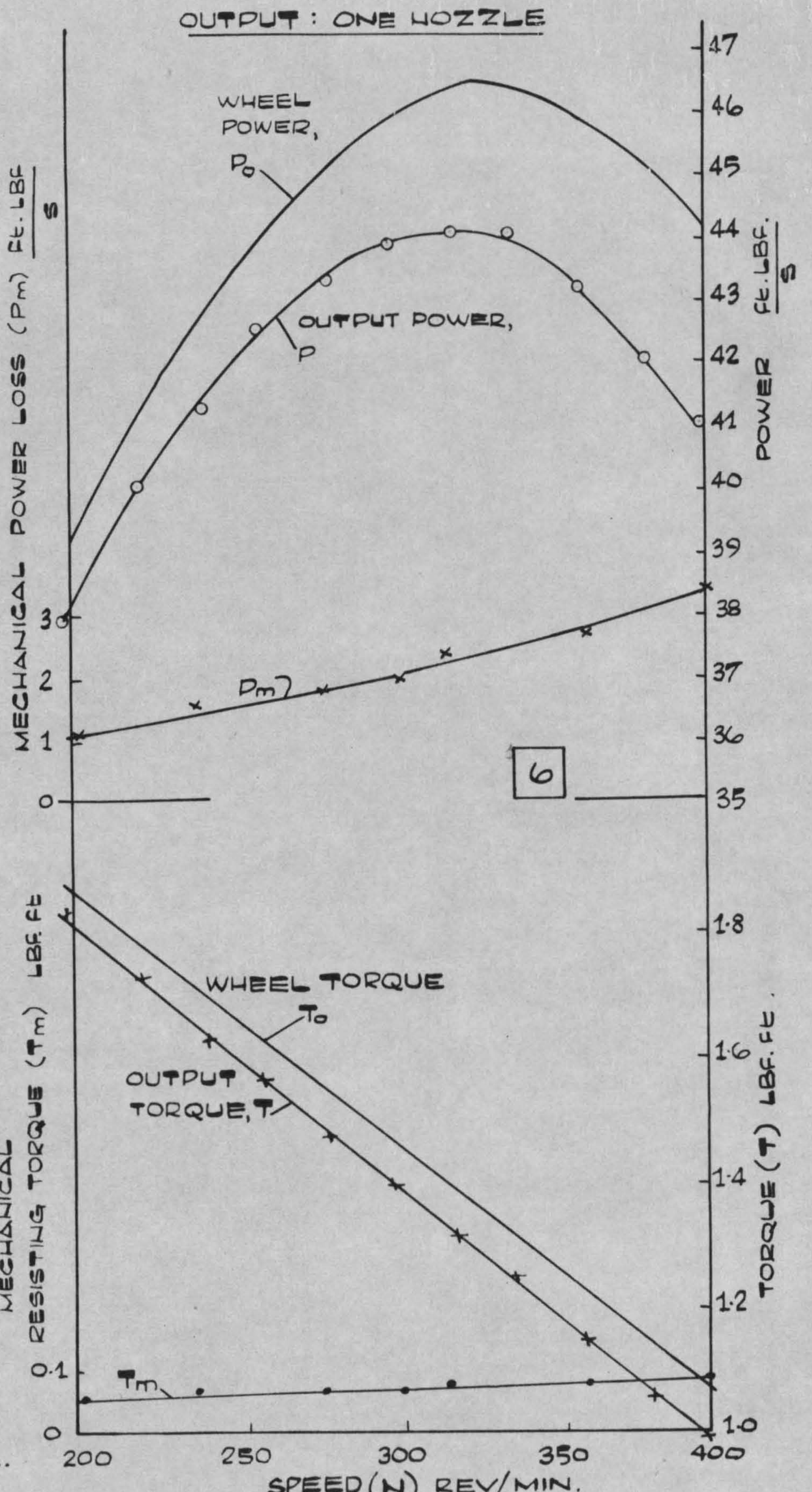

OUTPUT : ONE NOZZLE
WHEEL POWER, P_0
OUTPUT POWER, P
P_m
6
WHEEL TORQUE T_0
OUTPUT TORQUE, T
T_m
MECHANICAL POWER LOSS (P_m) FT. LBF./S
POWER FT. LBF./S
MECHANICAL RESISTING TORQUE (T_m) LBF. FT
TORQUE (T) LBF. FT.
0
1
2
3
0
0.1
47
46
45
44
43
42
41
40
39
38
37
36
35
1.8
1.6
1.4
1.2
1.0
200
250
300
350
400
SPEED (N) REV/MIN.

G.1.

RANGE OF OUTPUT

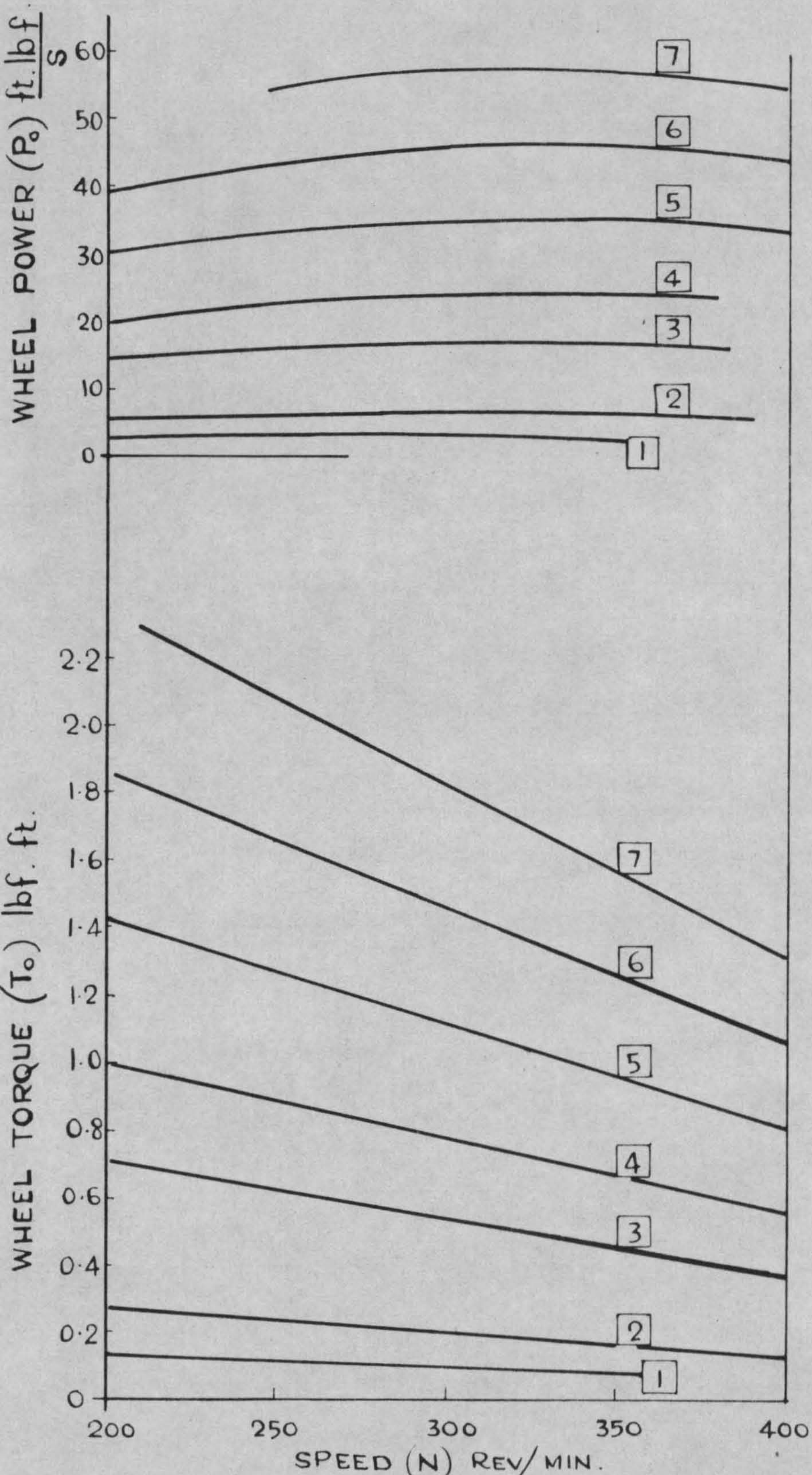

G.2.

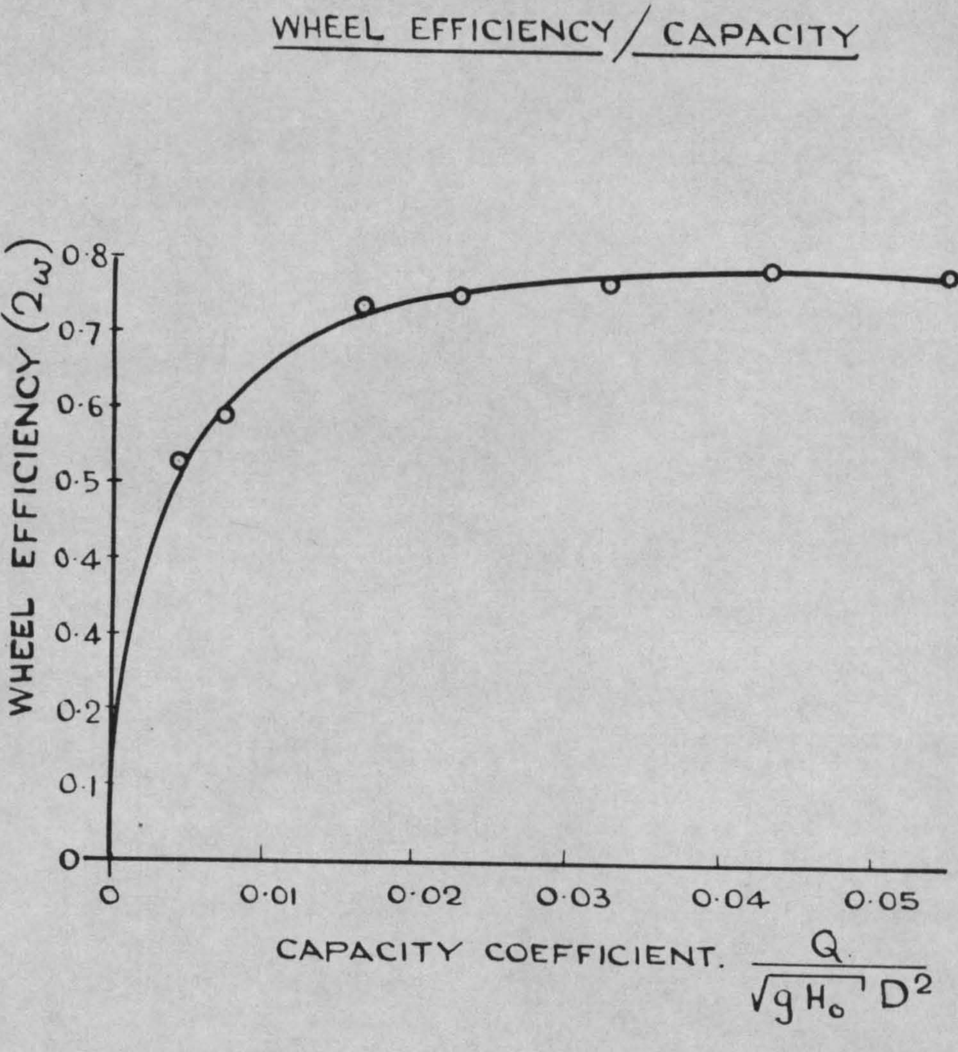
WHEEL EFFICIENCY / CAPACITY
WHEEL EFFICIENCY (2ω)
0·8
0·7
0·6
0·5
0·4
0·4
0·2
0·1
0
0
0·01
0·02
0·03
0·04
0·05
CAPACITY COEFFICIENT. $\frac{Q}{\sqrt{gH_o}\,D^2}$

G.3.

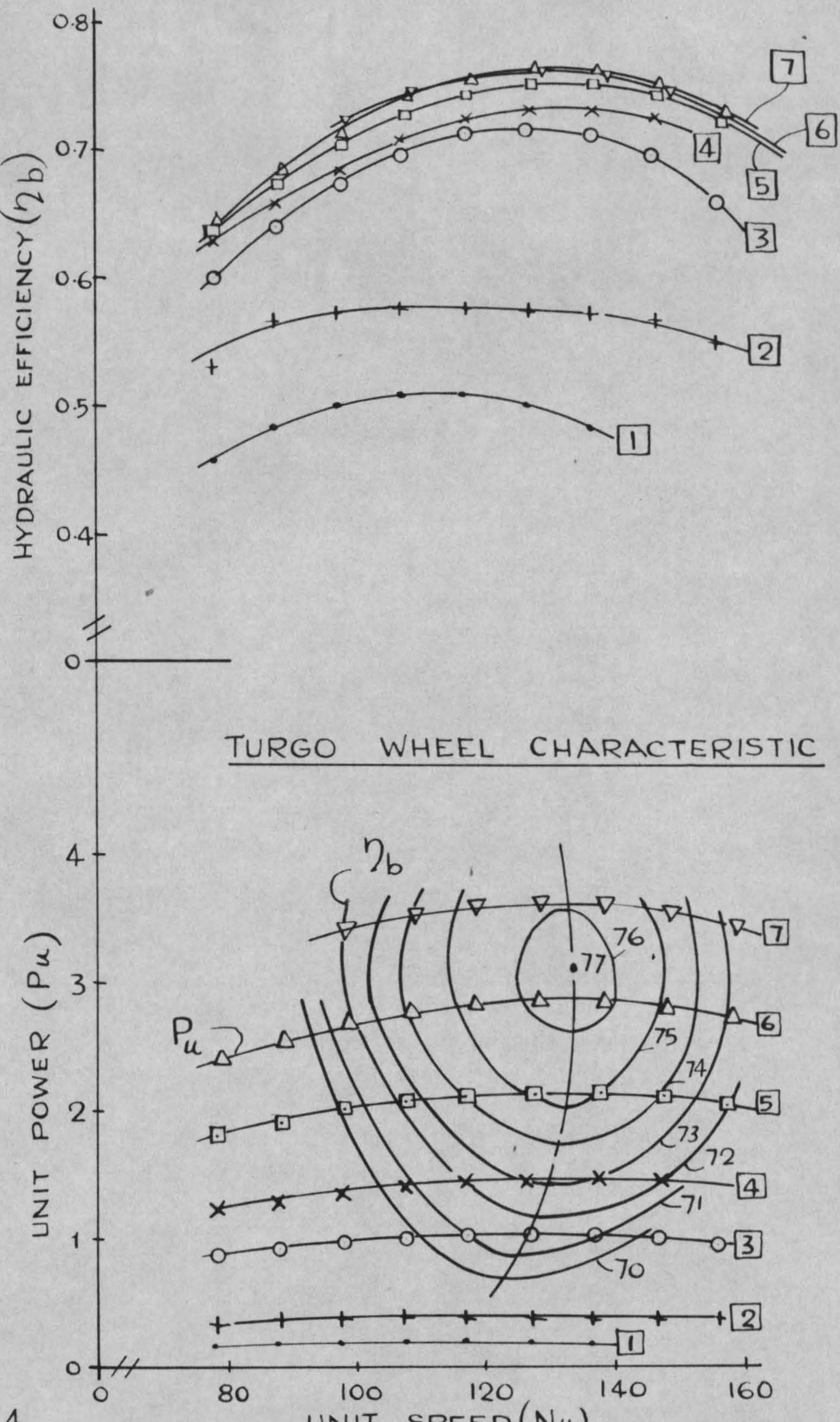

HYDRAULIC EFFICIENCY (η_b)
0.8
0.7
0.6
0.5
0.4
0
1
2
3
4
5
6
7
TURGO WHEEL CHARACTERISTIC
UNIT POWER (Pu)
η_b
Pu
77
76
75
74
73
72
71
70
UNIT SPEED (Nu)
0
80
100
120
140
160

G.4.

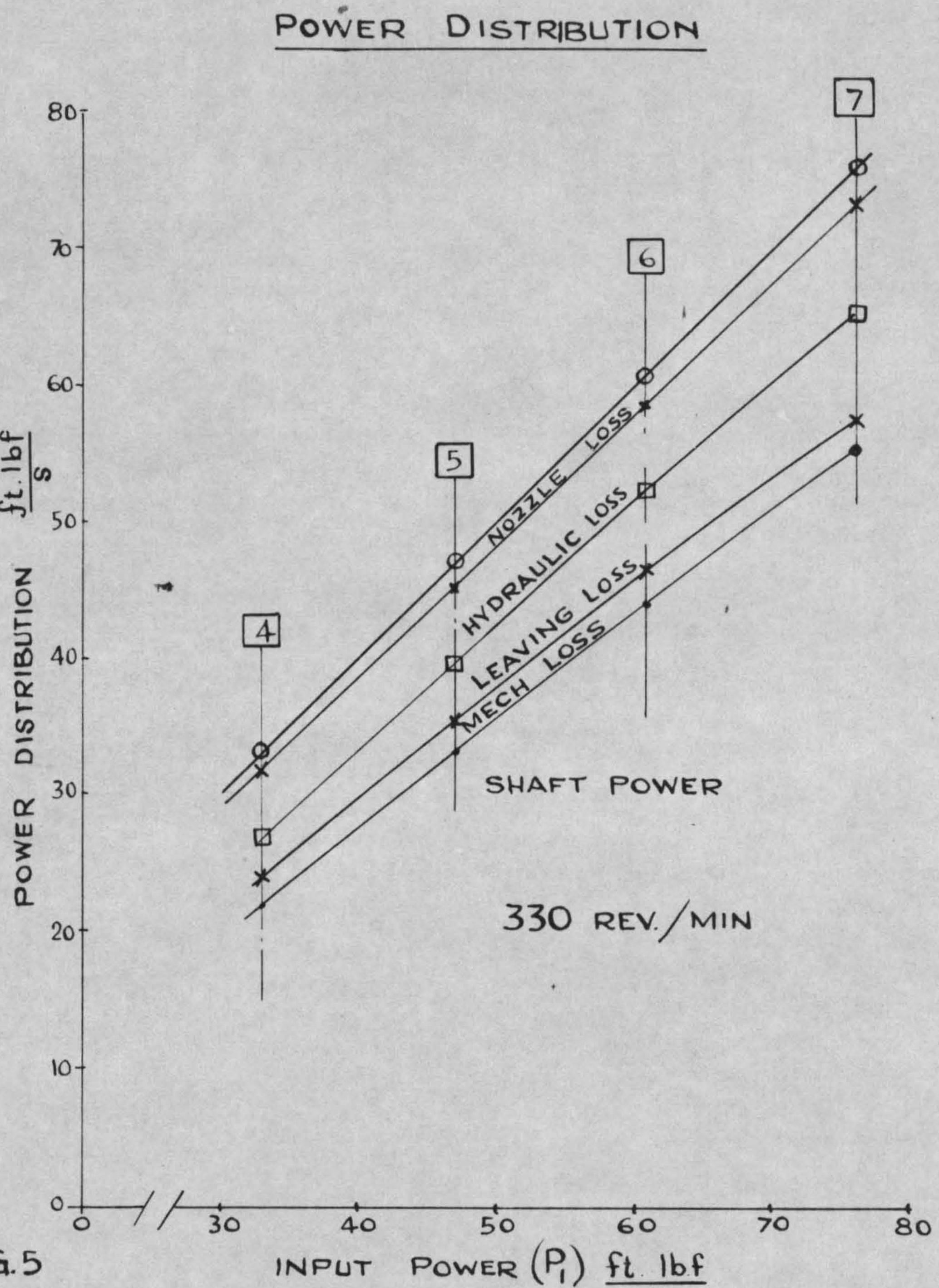
POWER DISTRIBUTION
80
70
60
50
40
30
20
10
0
POWER DISTRIBUTION ft. lbf / s
4
5
6
7
NOZZLE LOSS
HYDRAULIC LOSS
LEAVING LOSS
MECH LOSS
SHAFT POWER
330 REV./MIN
0
30
40
50
60
70
80
INPUT POWER (P1) ft. lbf / s
G.5

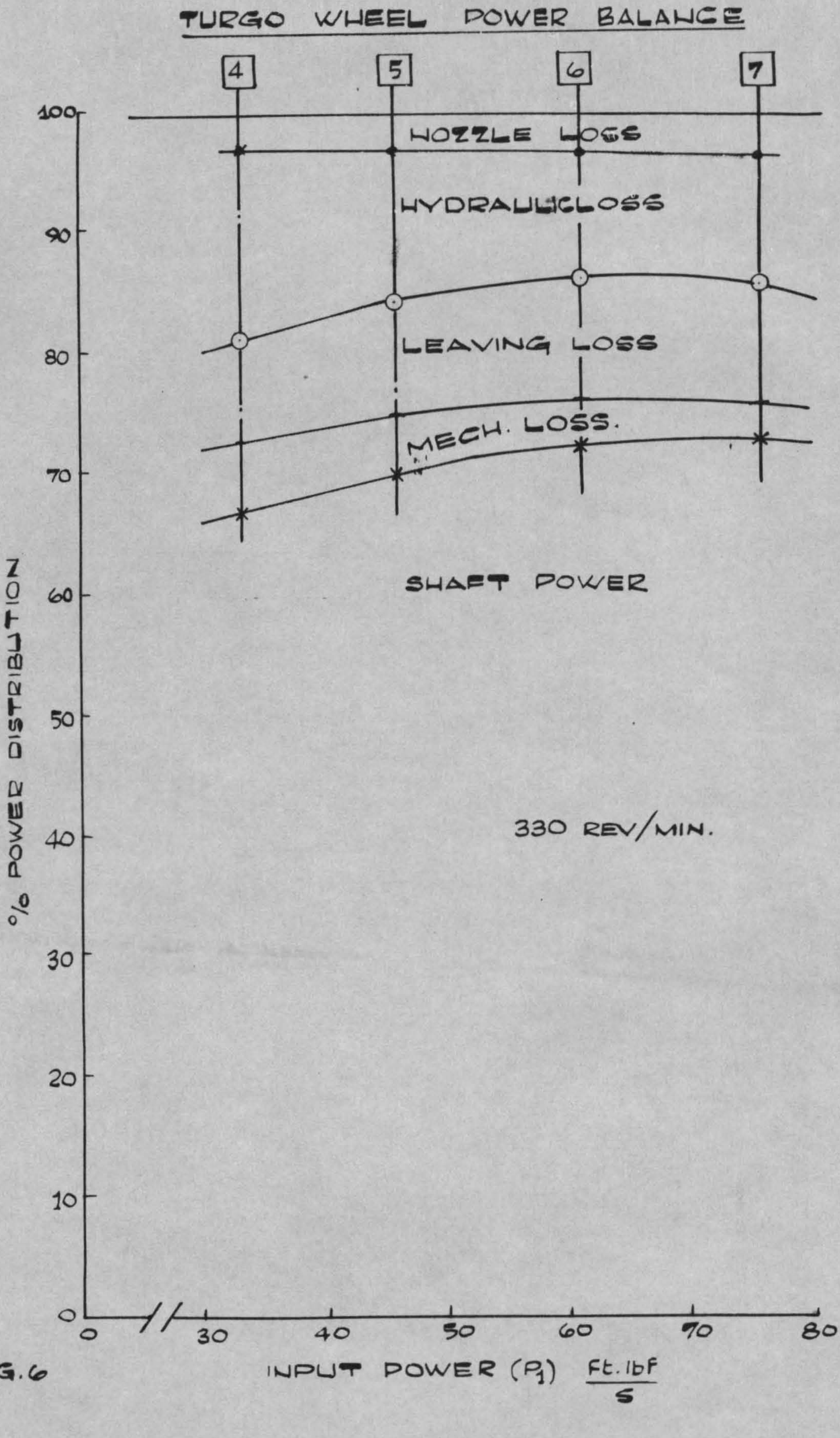
TURGO WHEEL POWER BALANCE
4
5
6
7
NOZZLE LOSS
HYDRAULIC LOSS
LEAVING LOSS
MECH. LOSS.
SHAFT POWER
330 REV/MIN.
% POWER DISTRIBUTION
100
90
80
70
60
50
40
30
20
10
0
0
30
40
50
60
70
80
INPUT POWER (P_1) $\frac{\text{ft.lbf}}{\text{s}}$

G.6

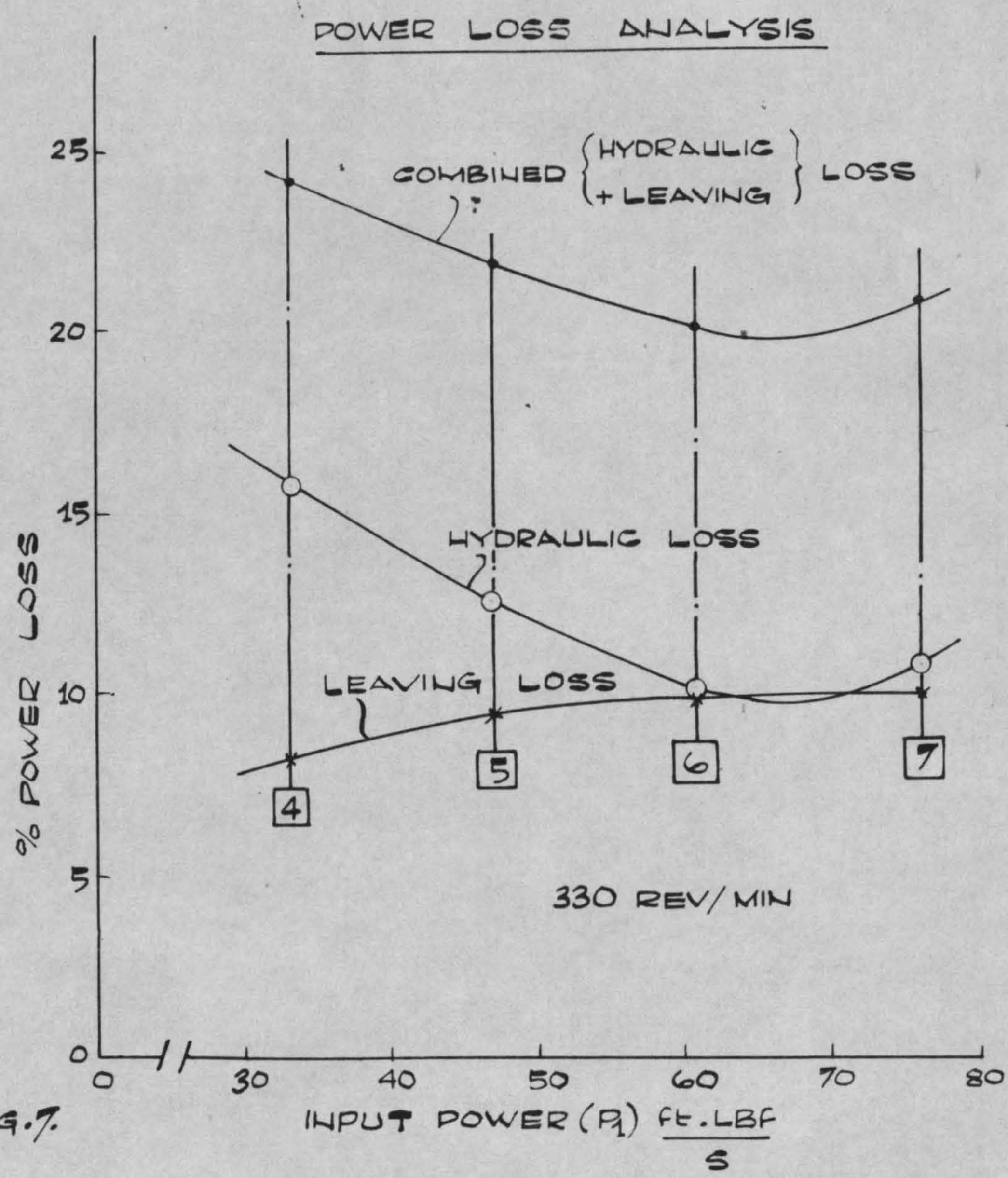

POWER LOSS ANALYSIS
COMBINED (HYDRAULIC + LEAVING) LOSS
HYDRAULIC LOSS
LEAVING LOSS
% POWER LOSS
330 REV/MIN
4
5
6
7
0
5
10
15
20
25
0
30
40
50
60
70
80
INPUT POWER (P_1) ft.LBF/s

G.7.

VARIATION OF RELATIVE ENERGY ACROSS JET AT INLET

6

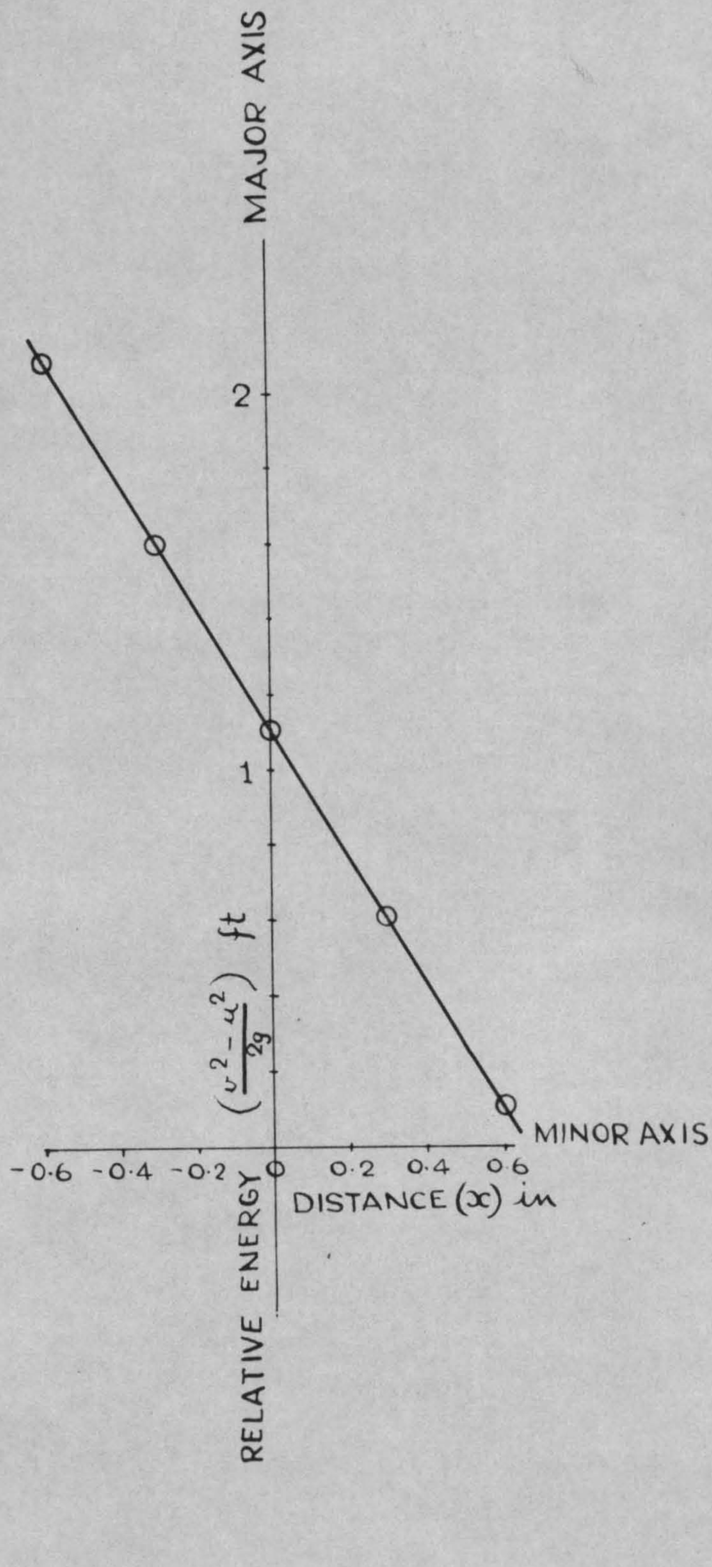

G.8.

RELATIVE ENERGY CONDITION AT INLET.

6

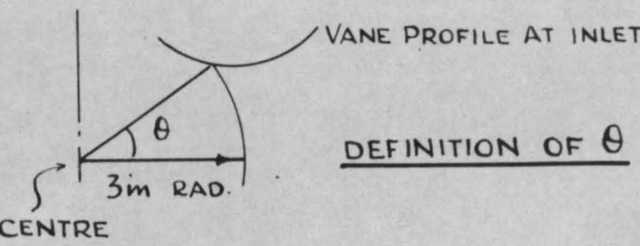

DEFINITION OF θ

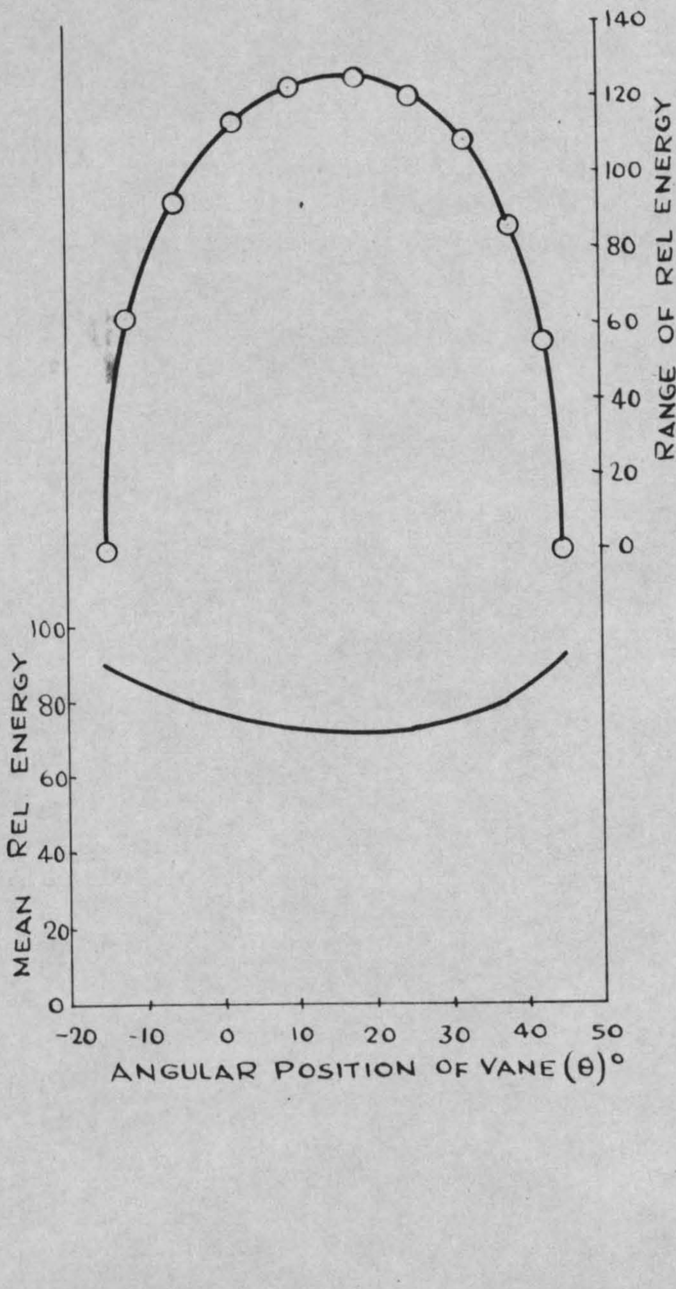

G.9.

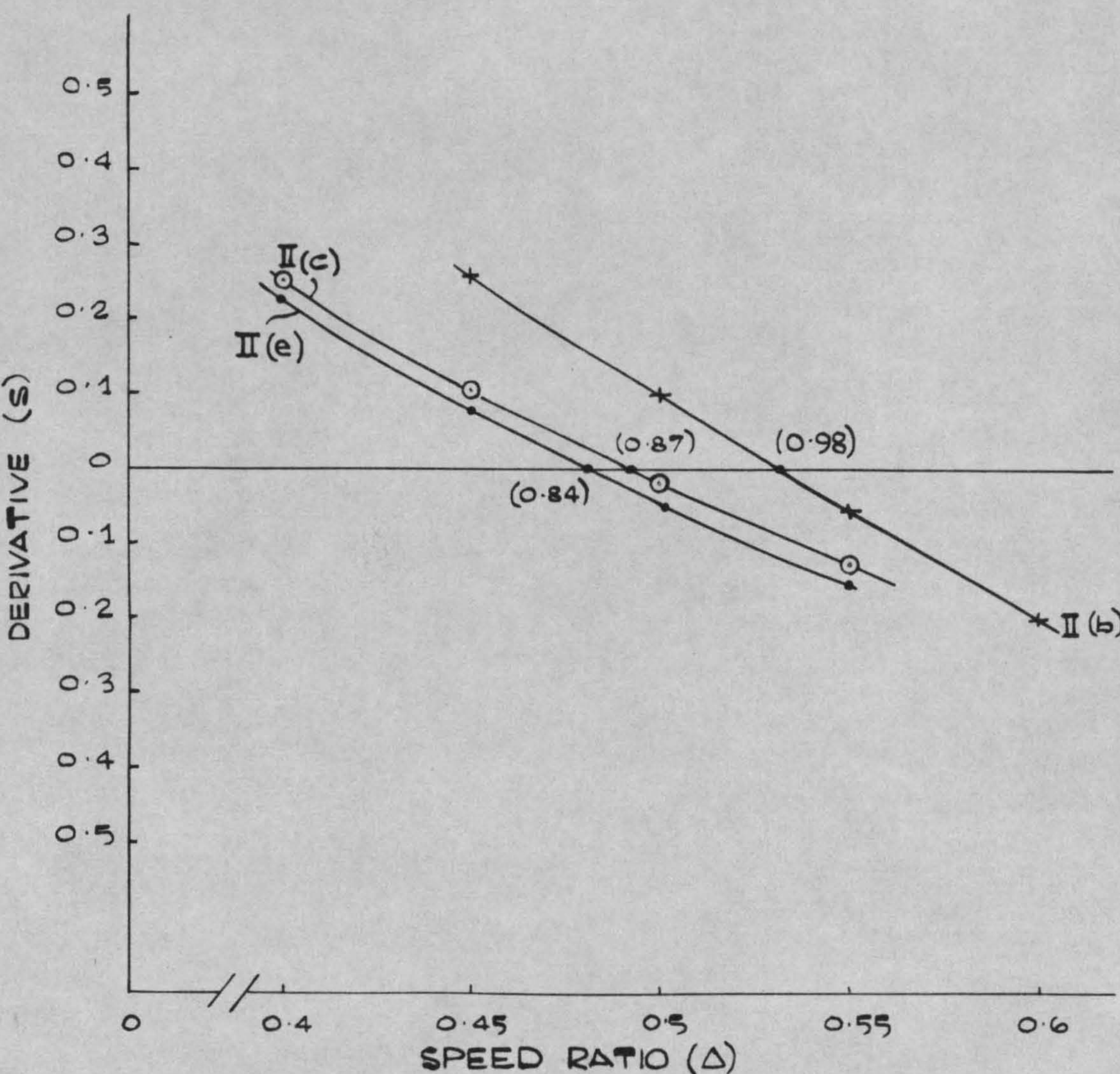
DERIVATIVE (s)
0·5
0·4
0·3
0·2
0·1
0
0·1
0·2
0·3
0·4
0·5
II(c)
II(e)
II(b)
(0·87)
(0·98)
(0·84)
0
0·4
0·45
0·5
0·55
0·6
SPEED RATIO (Δ)

G.10.

GUIDE TO NOTATION

(a) JET OF RECTANGULAR CROSS-SECTION AT INLET

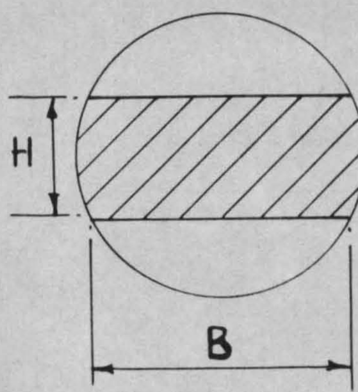

— REPRESENTED BY $\boxed{\cdot 5}$

i.e. $H = 0{\cdot}5$ in

$B = 1$ in (NOMINAL)

(b) JET OF SEGMENTAL CROSS-SECTION AT INLET

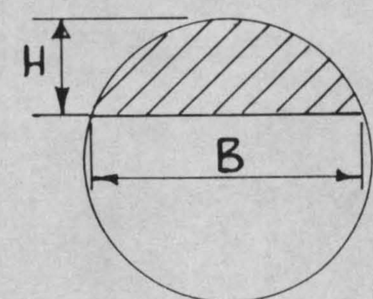

— REPRESENTED BY ·4

i.e. $H = 0{\cdot}4$ in

$B = 1$ in (NOMINAL)

NOTE: $H = 0{\cdot}53$ REPRESENTS "HALF-JET"

— TESTS PERFORMED WITH CONSTANT JET DIA., $d = 1{\cdot}06$ in

— 2-DIMENSIONAL VANE REPRESENTED BY (2)

3-DIMENSIONAL VANE REPRESENTED BY (3)

G.A.O.

2 - DIM. VANE ·3

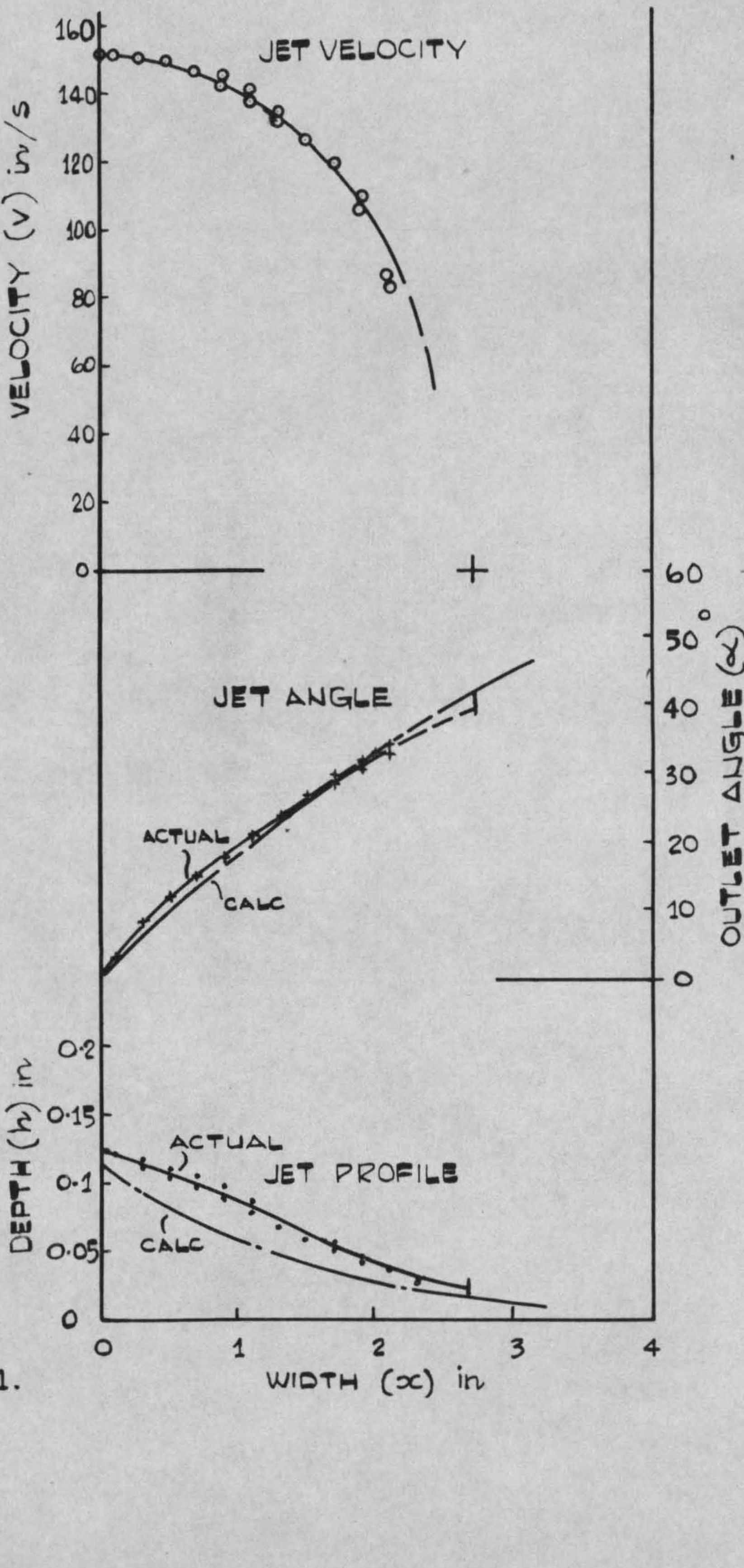

GA.1.

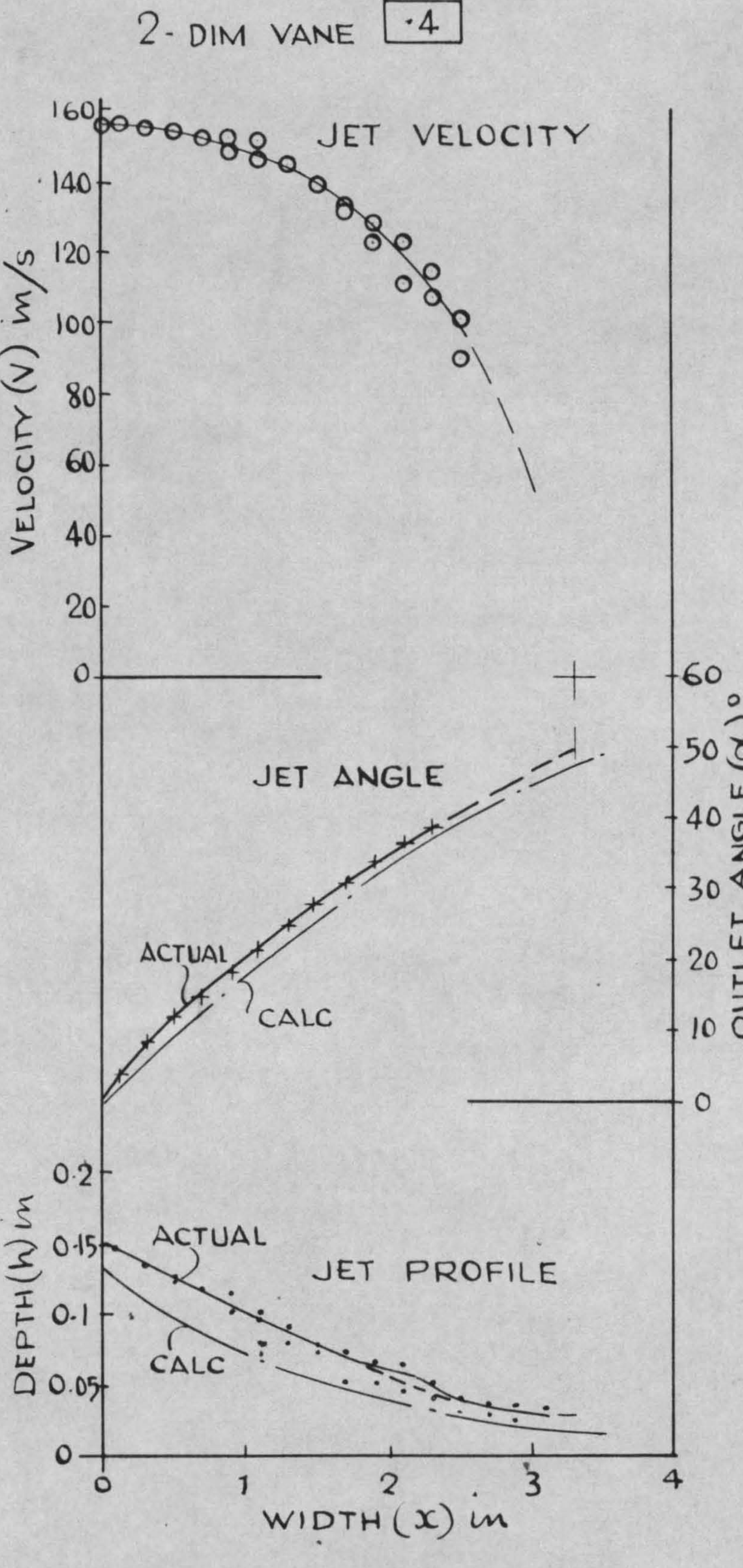
2-DIM VANE ·4
JET VELOCITY
VELOCITY (V) m/s
160
140
120
100
80
60
40
20
0
JET ANGLE
ACTUAL
CALC
OUTLET ANGLE (α)°
60
50
40
30
20
10
0
JET PROFILE
ACTUAL
CALC
DEPTH (h) in
0.2
0.15
0.1
0.05
0
0
1
2
3
4
WIDTH (x) in

GA.2.

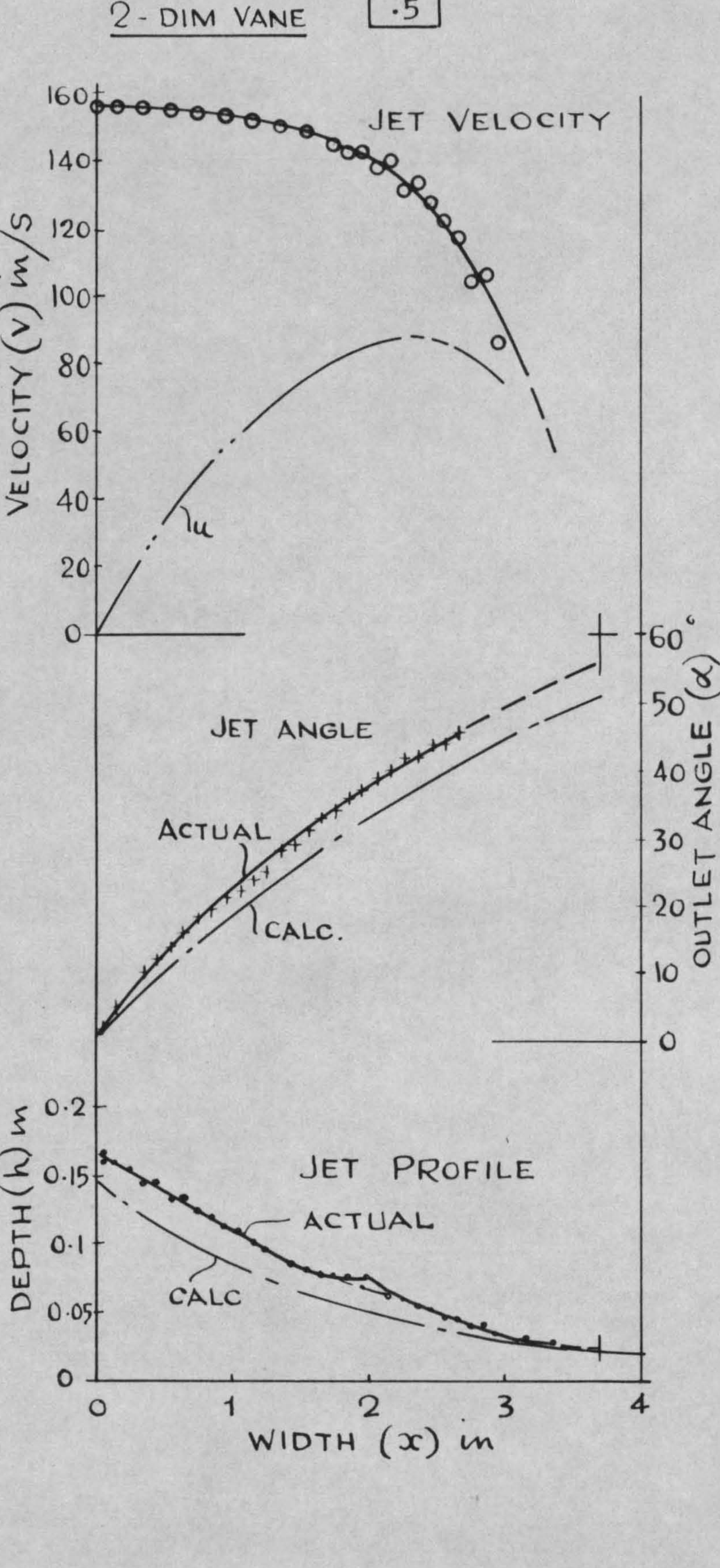
2 - DIM VANE
·5
JET VELOCITY
VELOCITY (V) m/S
160
140
120
100
80
60
40
20
0
u
JET ANGLE
ACTUAL
CALC.
OUTLET ANGLE (α)
60°
50
40
30
20
10
0
DEPTH (h) m
0·2
0·15
0·1
0·05
0
JET PROFILE
ACTUAL
CALC
0
1
2
3
4
WIDTH (x) m

G.A. 3.

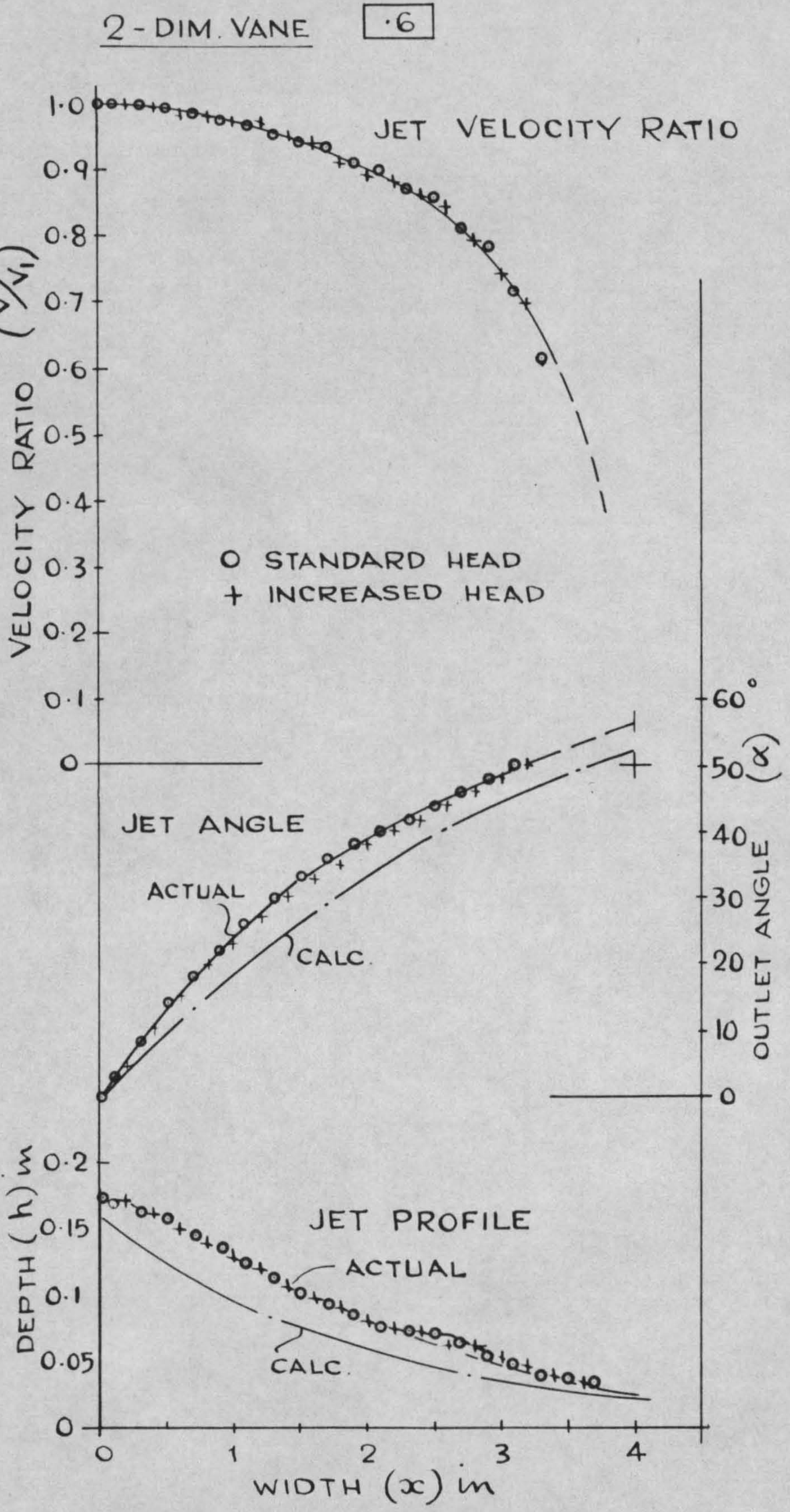

2 - DIM. VANE
·6
JET VELOCITY RATIO
VELOCITY RATIO (V/V1)
1·0
0·9
0·8
0·7
0·6
0·5
0·4
0·3
0·2
0·1
0
O STANDARD HEAD
+ INCREASED HEAD
JET ANGLE
ACTUAL
CALC.
60°
50
40
30
20
10
0
OUTLET ANGLE (α)
JET PROFILE
ACTUAL
CALC.
DEPTH (h) in
0·2
0.15
0.1
0.05
0
0
1
2
3
4
WIDTH (x) in

G.A.4

2-DIM VANE $\boxed{\cdot 7}$

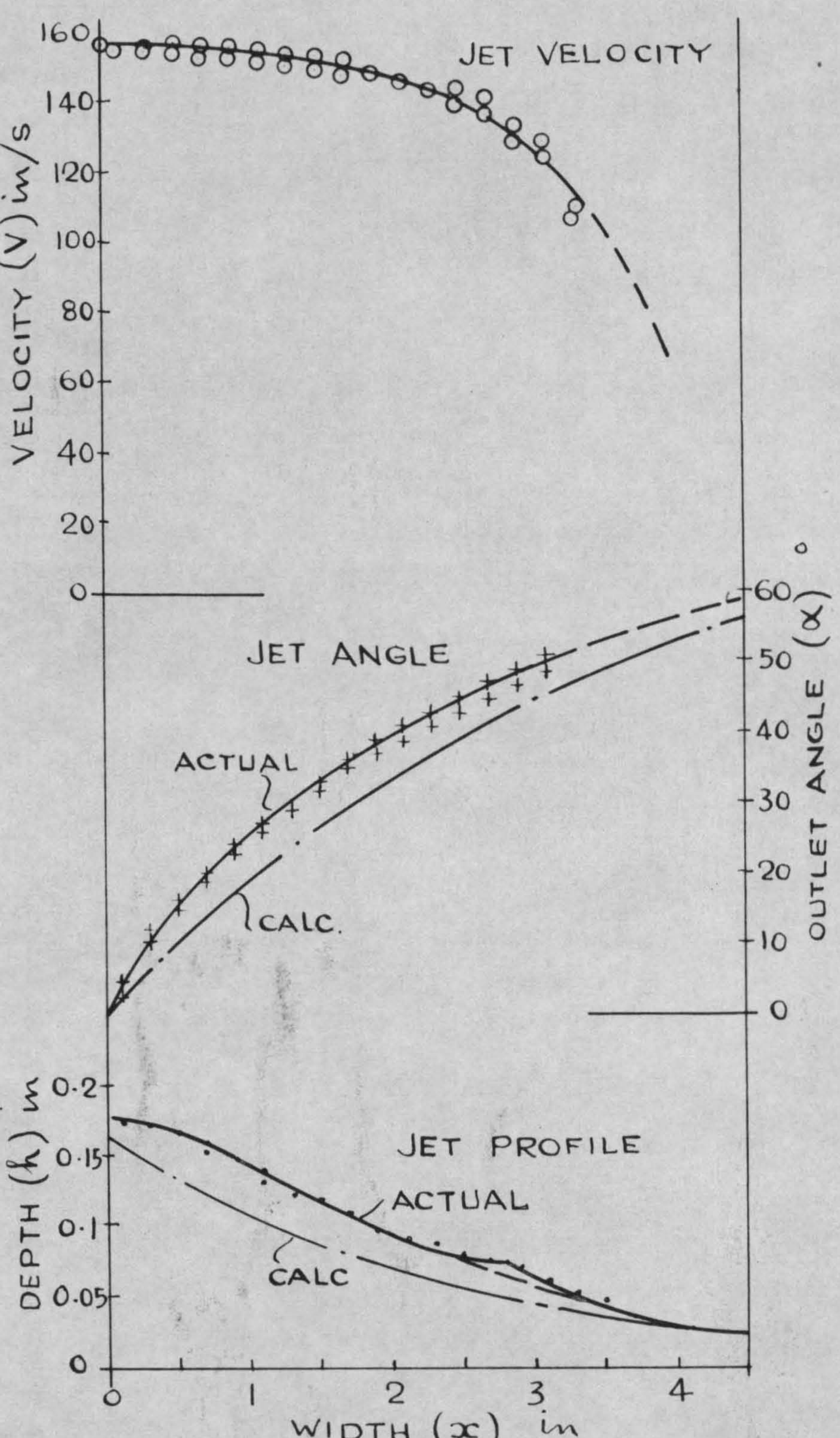

G.A.5.

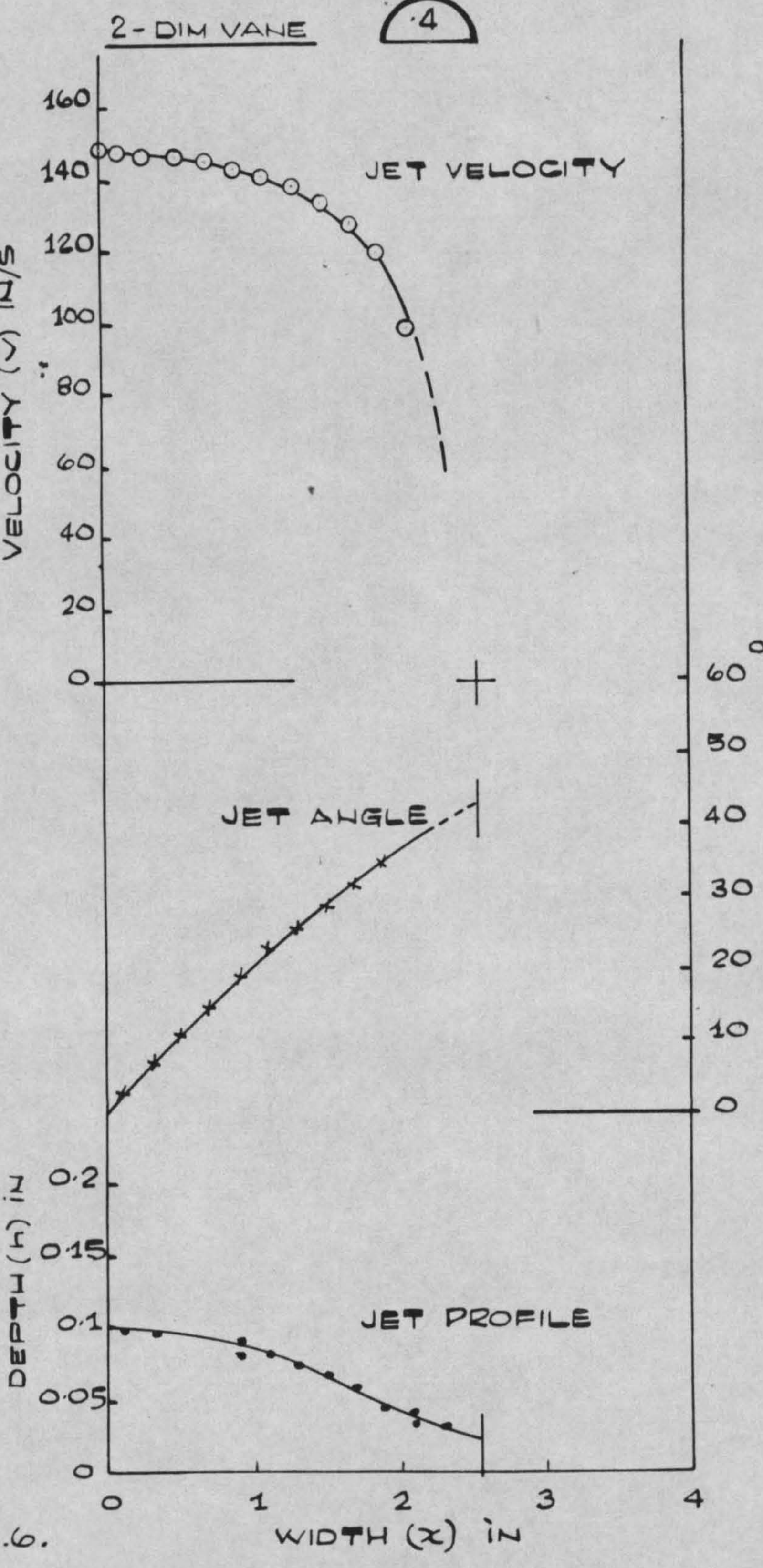
2-DIM VANE
·4
JET VELOCITY
VELOCITY (V) IN/S
160
140
120
100
80
60
40
20
0
JET ANGLE
OUTLET ANGLE (α)
60°
50
40
30
20
10
0
DEPTH (h) IN
0·2
0·15
0·1
0·05
0
JET PROFILE
0
1
2
3
4
WIDTH (x) IN

G.A.6.

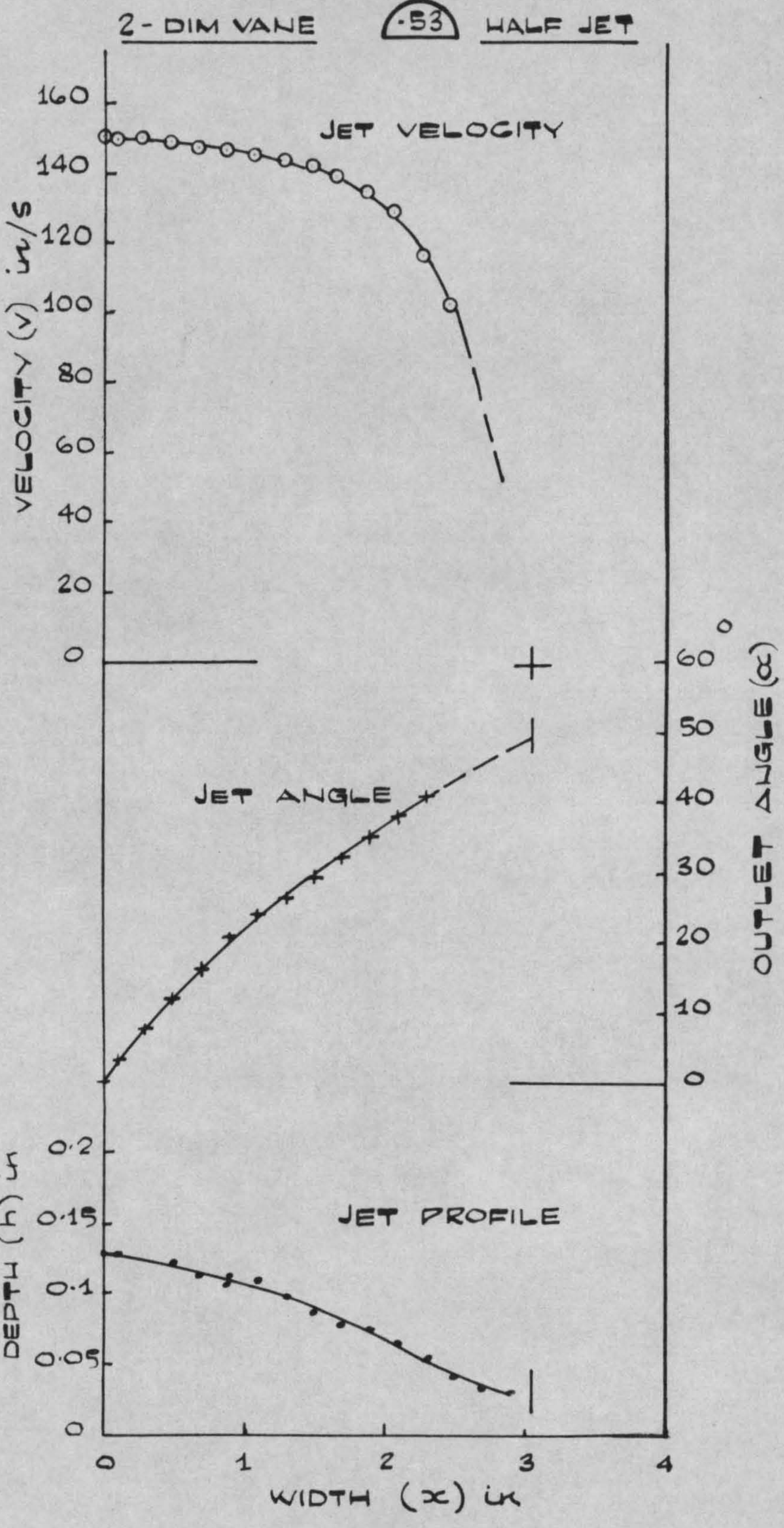
2 - DIM VANE
·53
HALF JET
JET VELOCITY
JET ANGLE
JET PROFILE
VELOCITY (v) in/s
160
140
120
100
80
60
40
20
0
60
50
40
30
20
10
0
OUTLET ANGLE (α) °
DEPTH (h) in
0·2
0·15
0·1
0·05
0
1
2
3
4
WIDTH (x) in

GA.7.

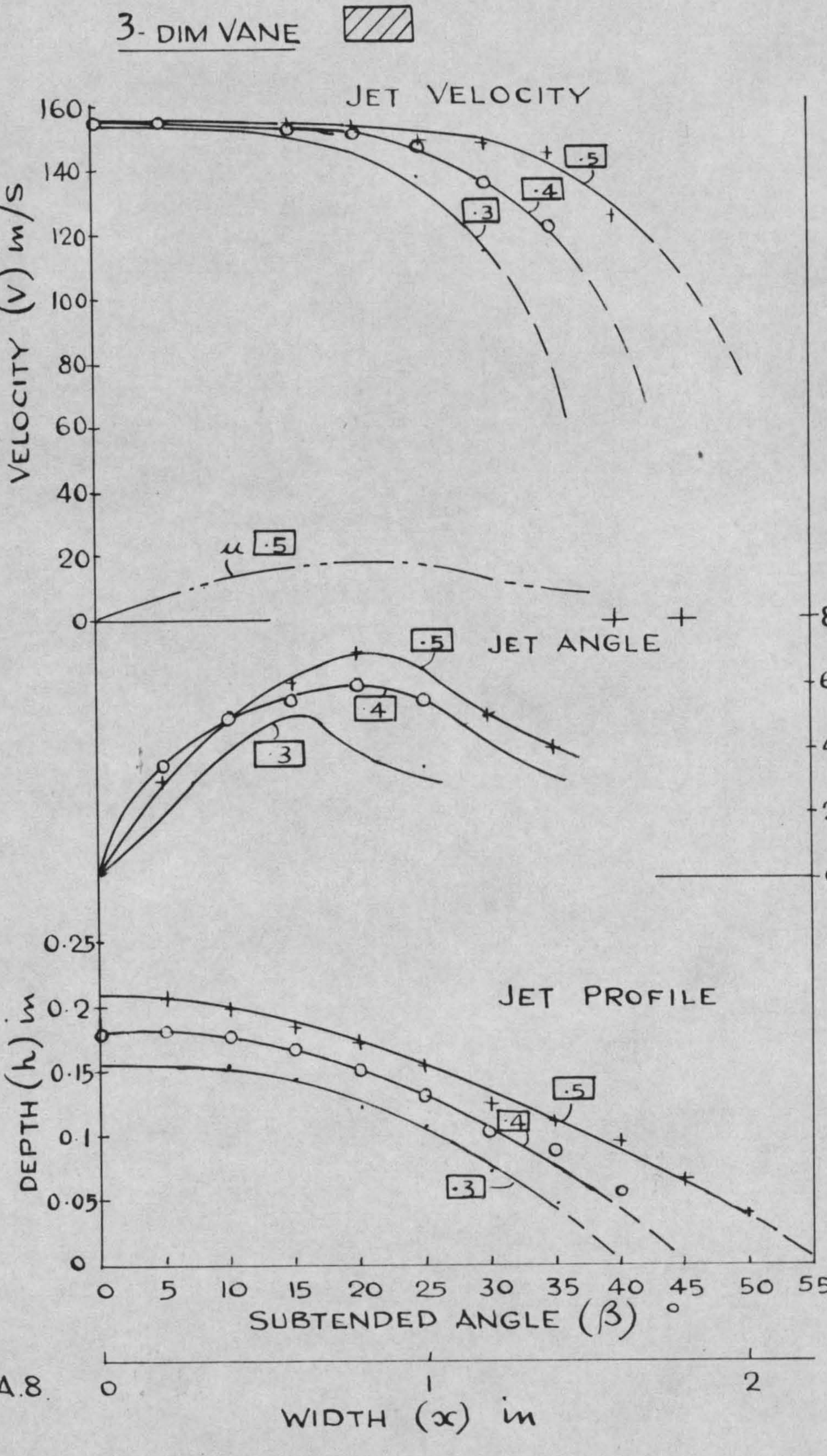
3- DIM VANE
JET VELOCITY
VELOCITY (V) in/S
160
140
120
100
80
60
40
20
0
·5
·4
·3
u ·5
JET ANGLE
OUTLET ANGLE (α) °
8
6
4
2
0
JET PROFILE
DEPTH (h) in
0.25
0.2
0.15
0.1
0.05
0
0 5 10 15 20 25 30 35 40 45 50 55
SUBTENDED ANGLE (β) °
0 1 2
WIDTH (x) in

G.A.8.

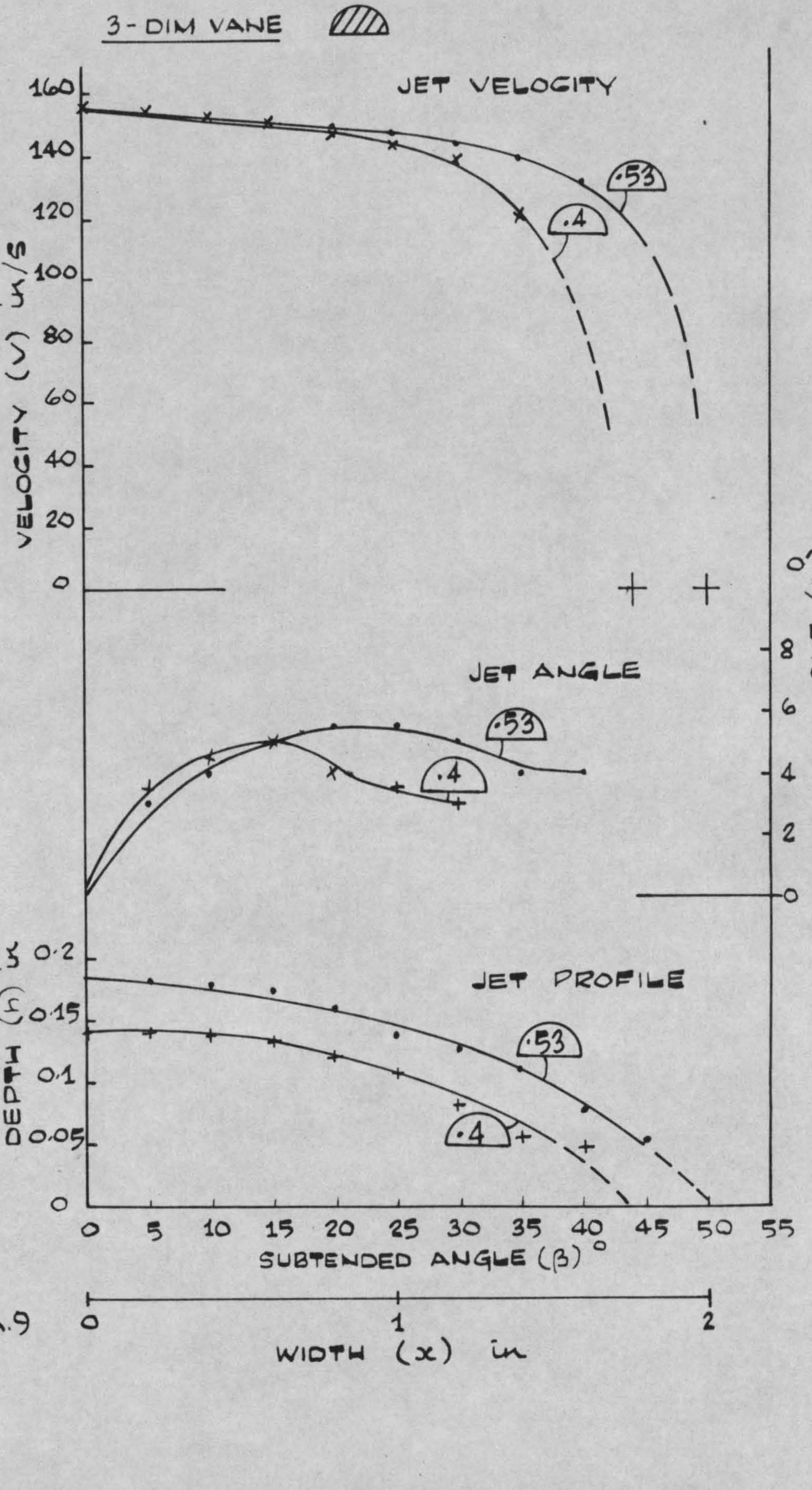
3-DIM VANE
JET VELOCITY
VELOCITY (V) in/s
160
140
120
100
80
60
40
20
0
·53
·4
JET ANGLE
OUTLET ANGLE (α)°
8
6
4
2
0
JET PROFILE
DEPTH (h) in
0·2
0·15
0·1
0·05
0
0
5
10
15
20
25
30
35
40
45
50
55
SUBTENDED ANGLE (β)°
0
1
2
WIDTH (x) in

GA.9

COMPARISON OF DISCHARGE CHARACTERISTICS OF SIMILAR JETS ON 2 AND 3 DIMENSIONAL VANES

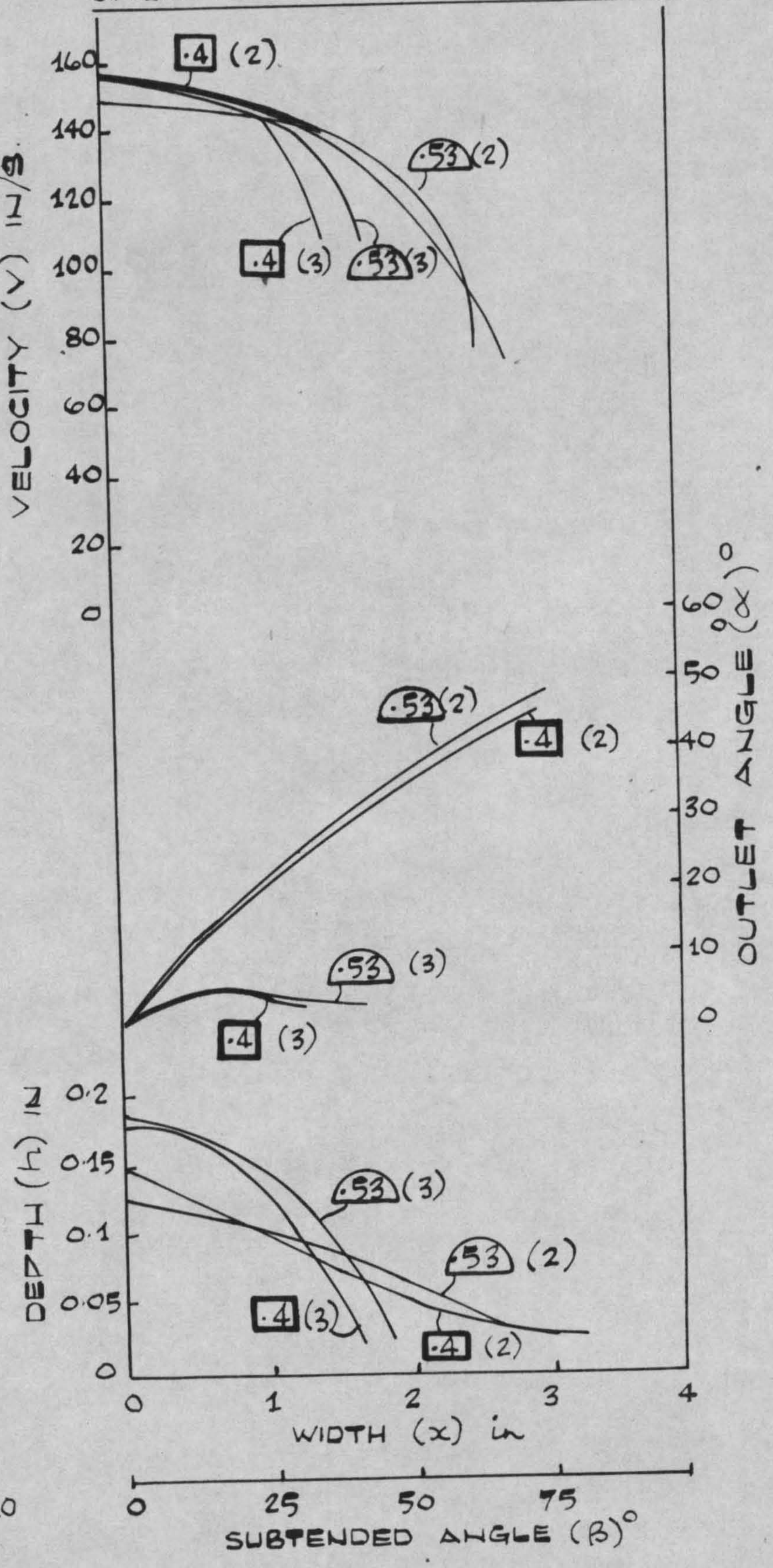

GA.10

VARIATION OF PROFILE DEPTH WITH VELOCITY

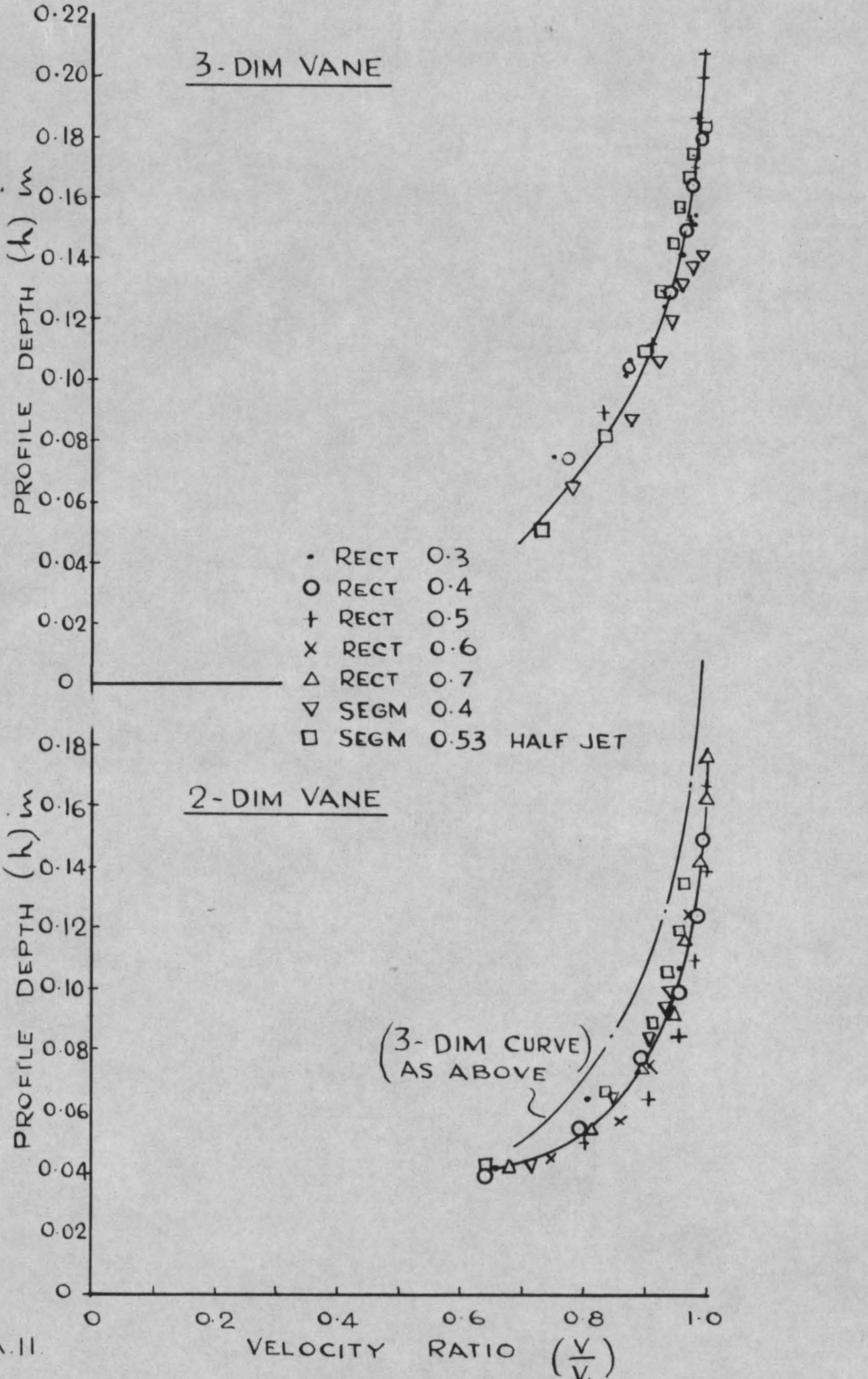

GA.11.

VARIATION OF OUTLET : INLET FORCE RATIO WITH GEOMETRIC PARAMETER

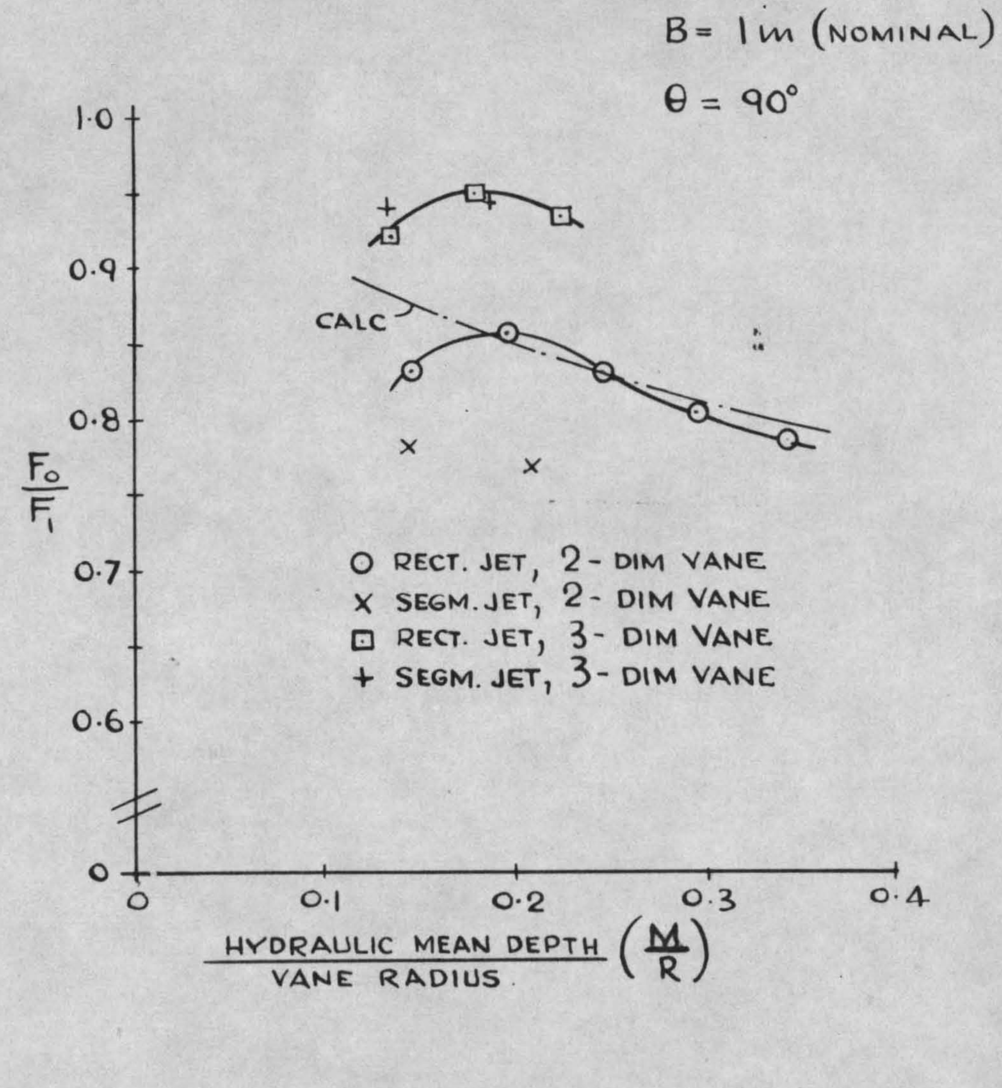

G.A. 12.

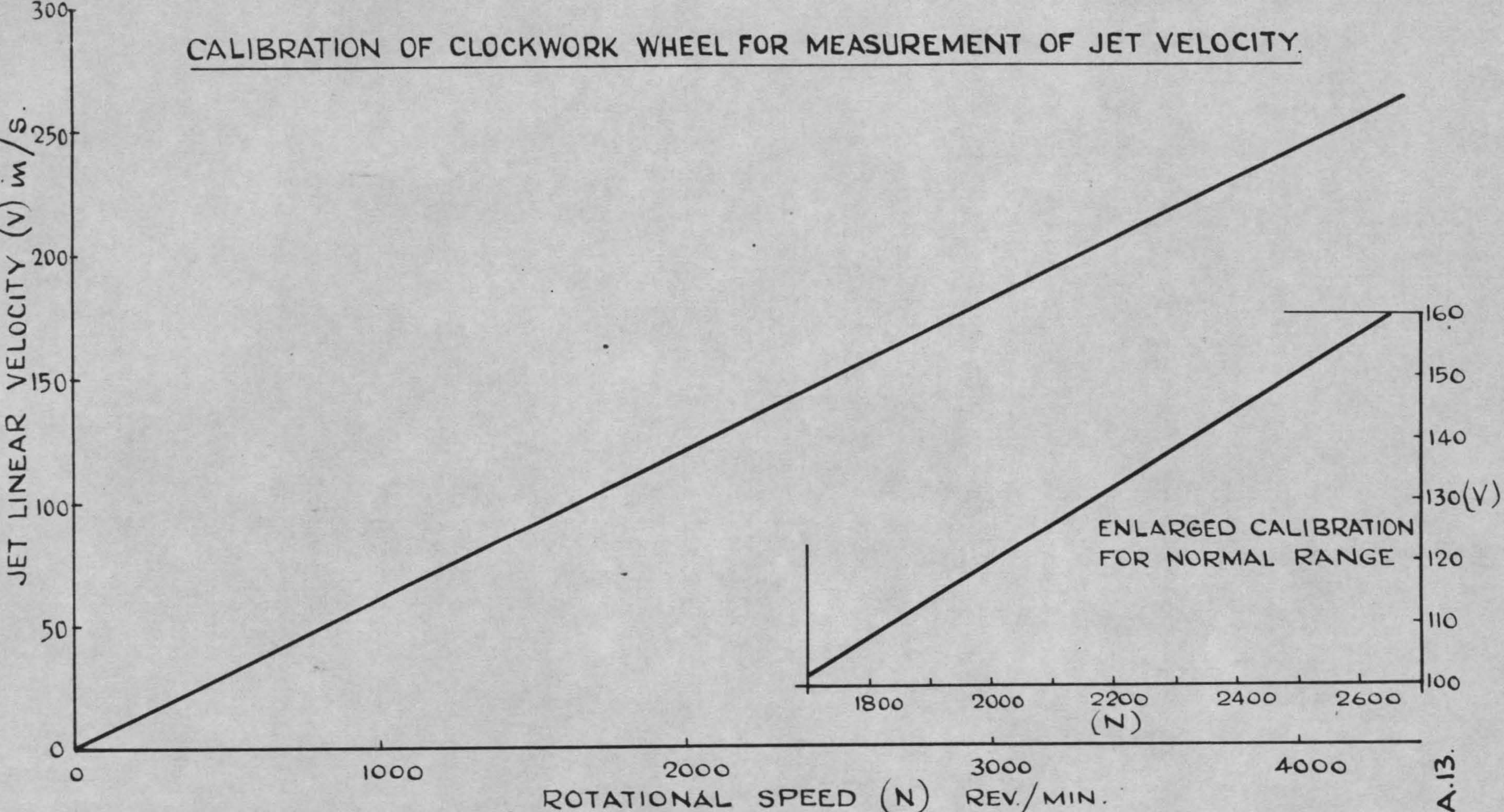
CALIBRATION OF CLOCKWORK WHEEL FOR MEASUREMENT OF JET VELOCITY.
JET LINEAR VELOCITY (V) m/s.
300
250
200
150
100
50
0
0
1000
2000
3000
4000
ROTATIONAL SPEED (N) REV./MIN.
ENLARGED CALIBRATION
FOR NORMAL RANGE
160
150
140
130 (V)
120
110
100
1800
2000
2200
(N)
2400
2600

G.A.13.

COLOUR CODE

FLOW DENSITY

$in^3/min.$

15 - 20	
20 - 30	
30 - 40	
40 - 60	
60 - 80	
80 - 100	
100 - 120	
120 - 140	
140 - 160	
160 - 180	
ABOVE 180	

ABSOLUTE VELOCITY ft/s		RELATIVE VELOCITY ft/s
		LESS THAN 10
LESS THAN 4		10 - 13
4 - 5		13 - 14
5 - 6		14 - 15
6 - 7		15 - 16
7 - 8		16 - 17
8 - 9		17 - 18
ABOVE 9		

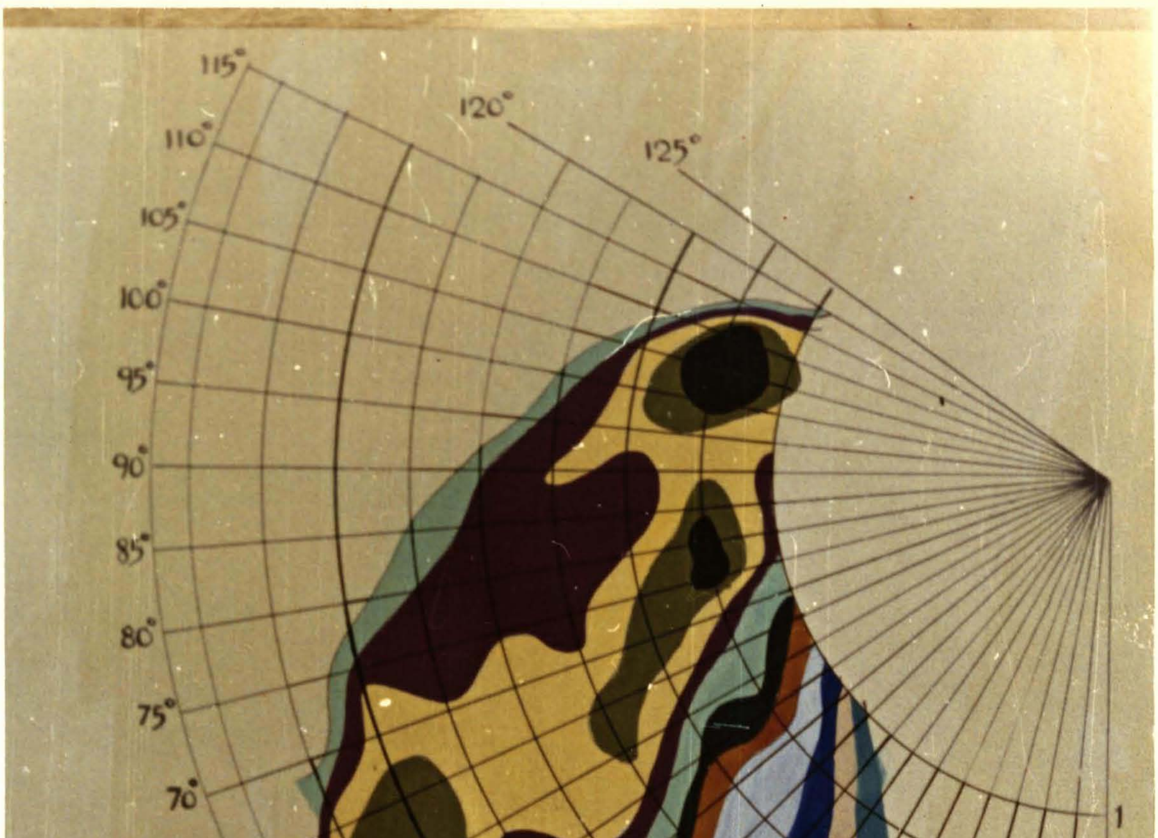
115°
120°
125°
110°
105°
100°
95°
90°
85°
80°
75°
70°
65°
60°
55°
50°
45°
40°
35°
30°
25°
20°
15°
10°
5°
0°
1
2
3
4
5
6
7
8
9
7 FLOW DENSITY
C.1.

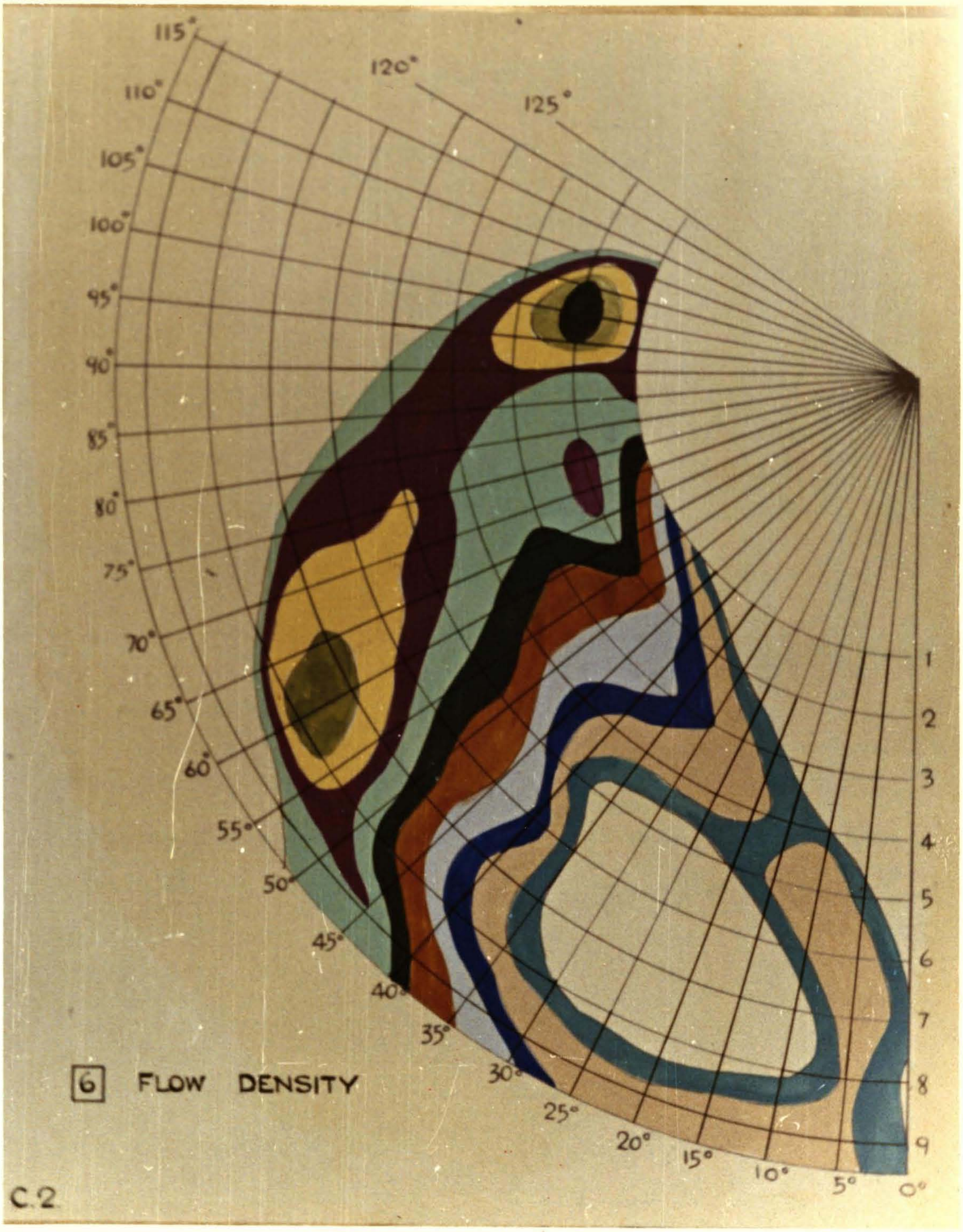

115°
120°
125°
110°
105°
100°
95°
90°
85°
80°
75°
70°
65°
60°
55°
50°
45°
40°
35°
30°
25°
20°
15°
10°
5°
0°
1
2
3
4
5
6
7
8
9
6 FLOW DENSITY
C.2

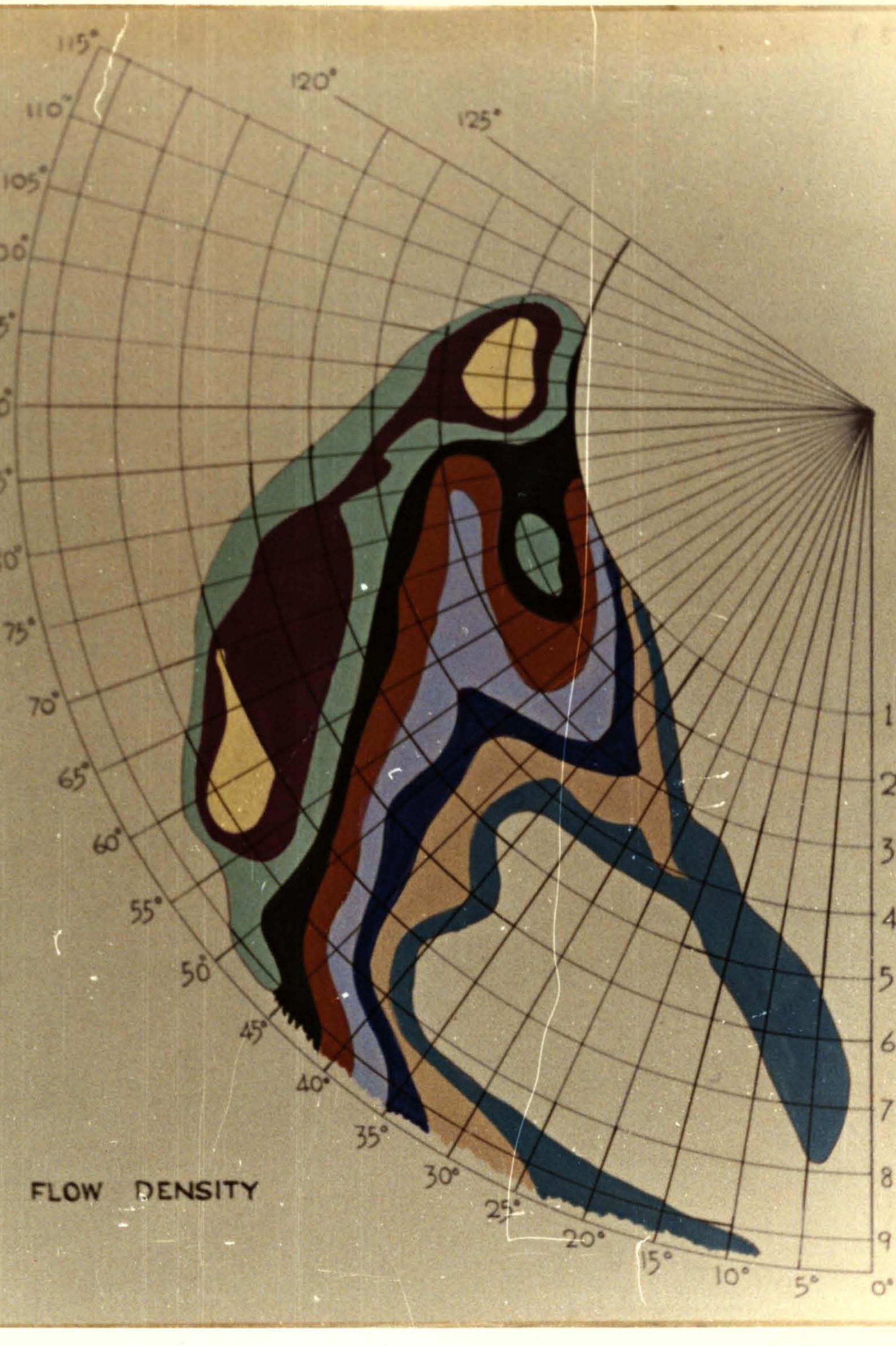

5 FLOW DENSITY

C.3

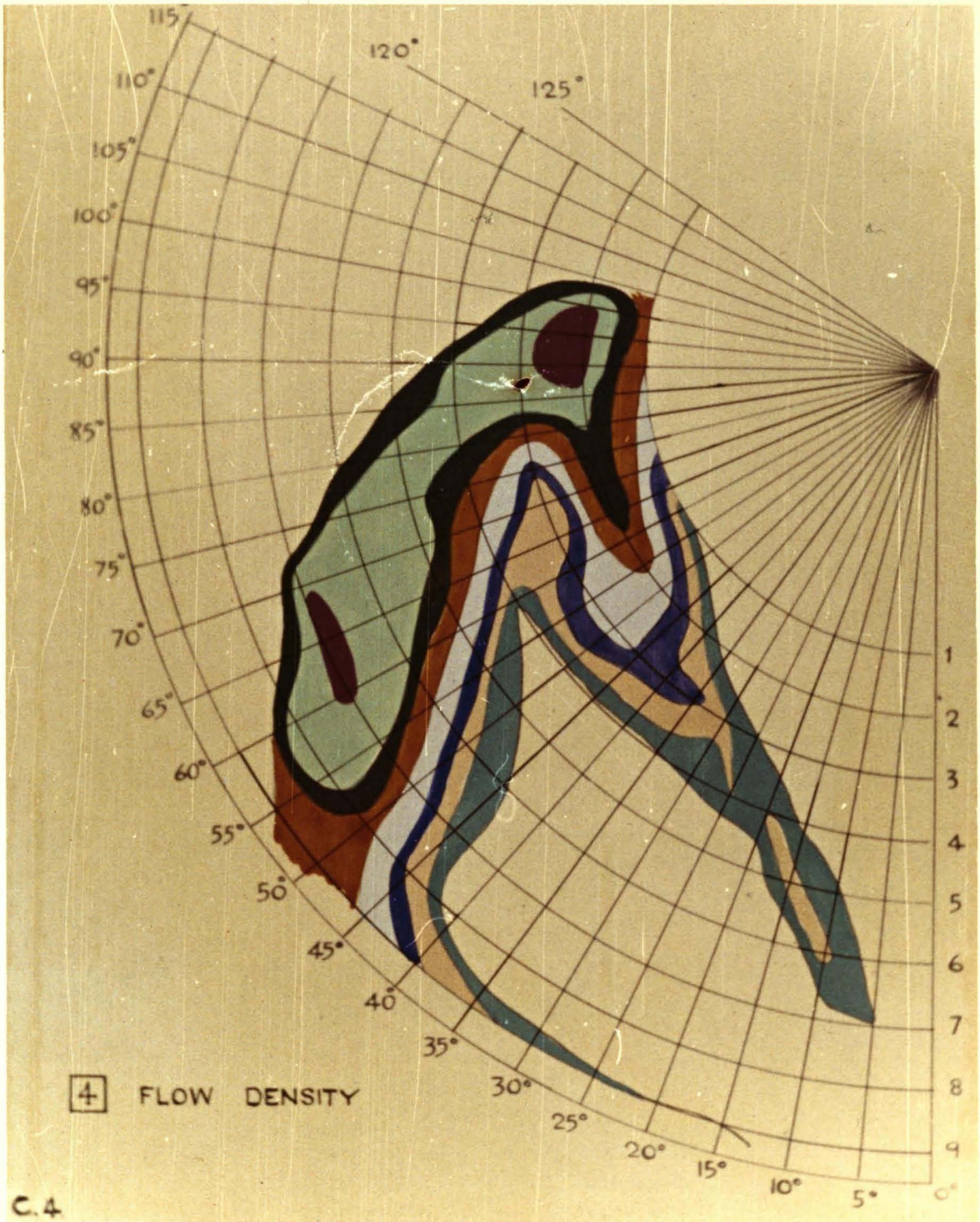

115°
110°
105°
100°
95°
90°
85°
80°
75°
70°
65°
60°
55°
50°
45°
40°
35°
30°
25°
20°
15°
10°
5°
0°
120°
125°
1
2
3
4
5
6
7
8
9
4 FLOW DENSITY
C.4

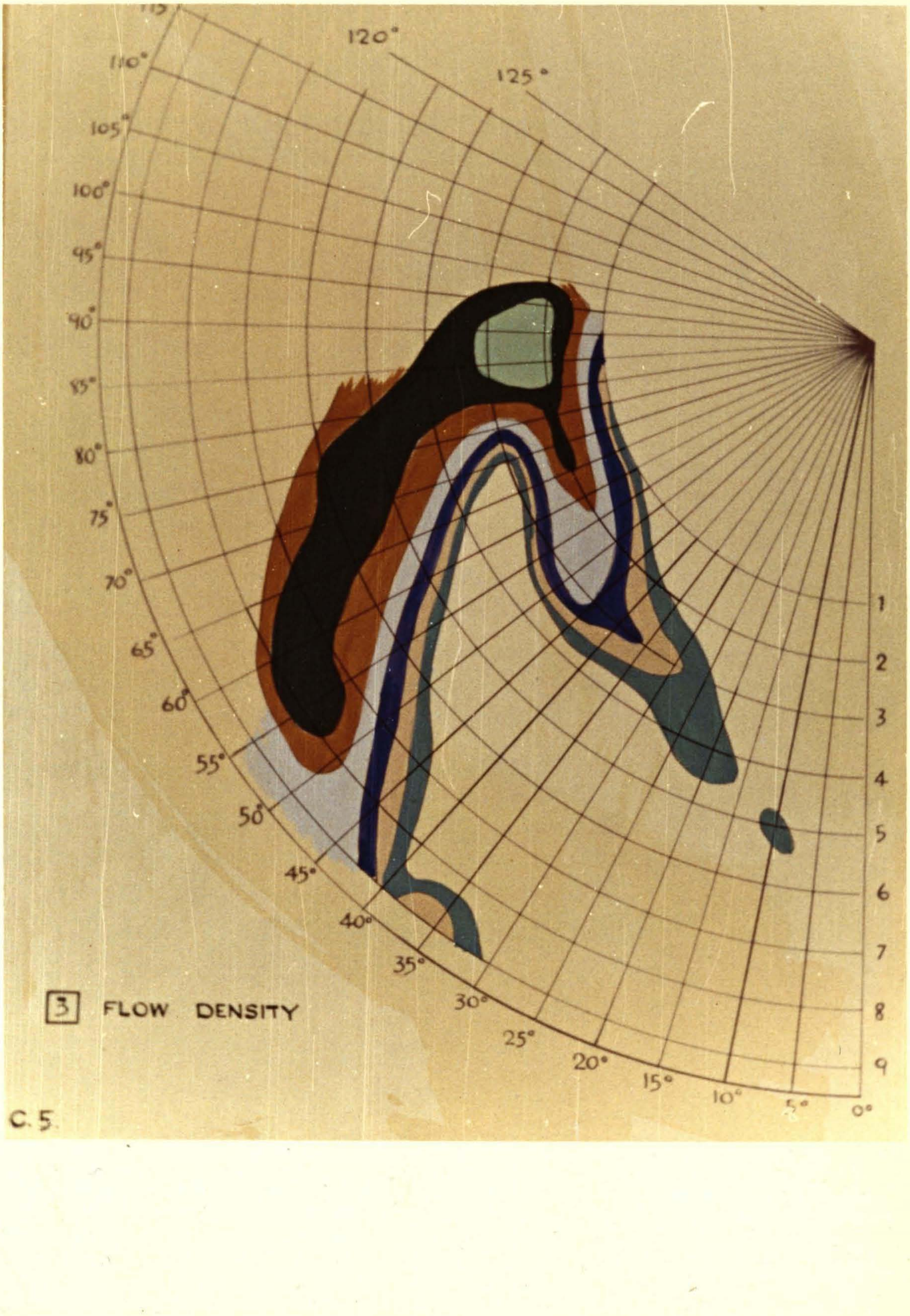
120°
125°
110°
105°
100°
95°
90°
85°
80°
75°
70°
65°
60°
55°
50°
45°
40°
35°
30°
25°
20°
15°
10°
5°
0°
1
2
3
4
5
6
7
8
9
3 FLOW DENSITY

C. 5

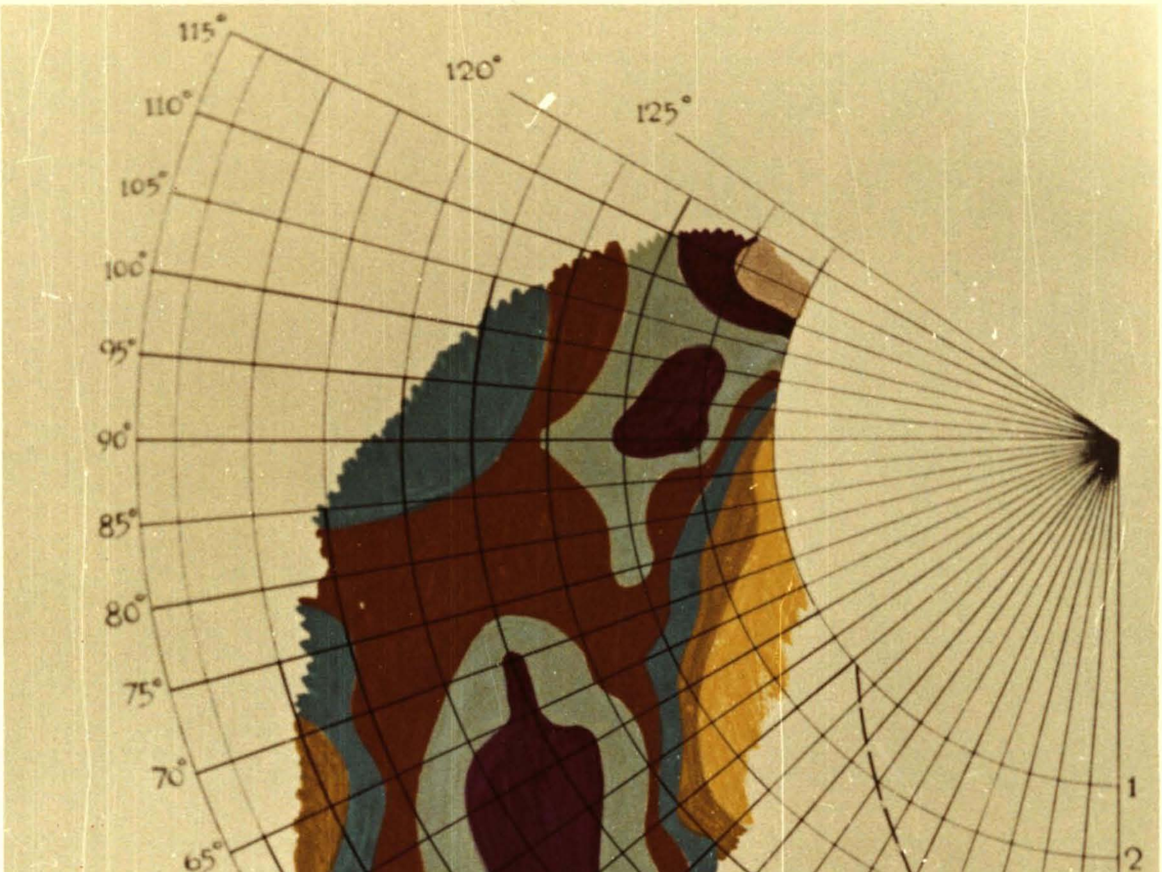
115°
120°
125°
110°
105°
100°
95°
90°
85°
80°
75°
70°
65°
60°
55°
50°
45°
40°
35°
30°
25°
20°
15°
10°
5°
0°
1
2
3
4
5
6
7
8
9
7 ABSOLUTE VELOCITIES
C.6

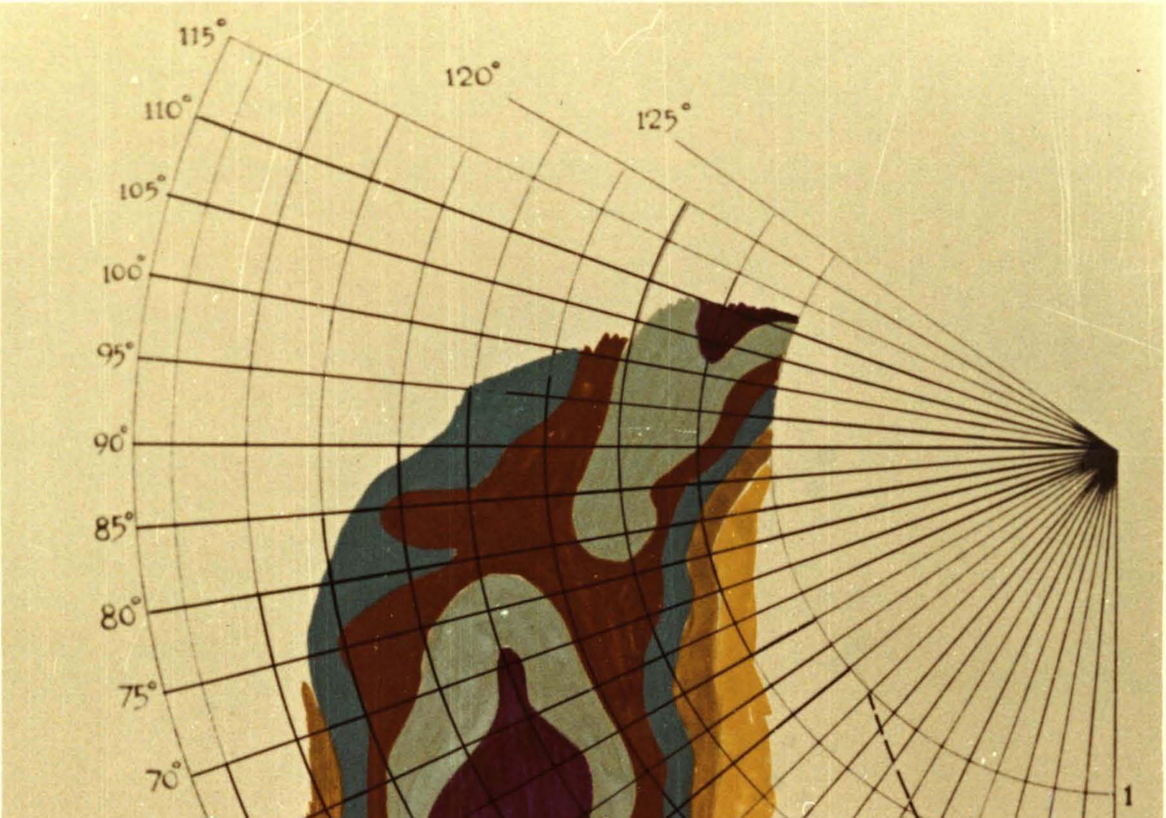

6 ABSOLUTE VELOCITIES

C.7.

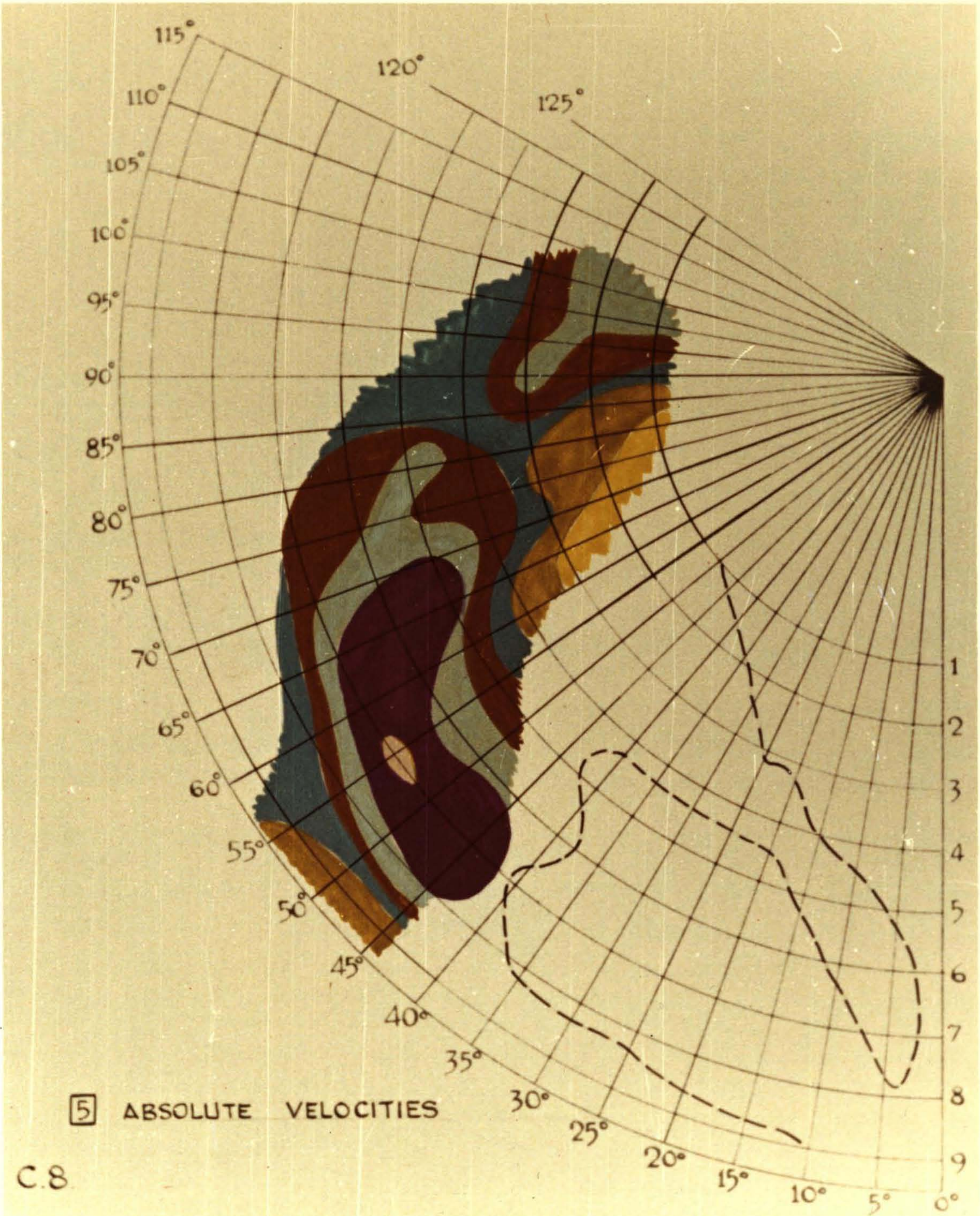
115°
120°
125°
110°
105°
100°
95°
90°
85°
80°
75°
70°
65°
60°
55°
50°
45°
40°
35°
30°
25°
20°
15°
10°
5°
0°
1
2
3
4
5
6
7
8
9
5 ABSOLUTE VELOCITIES
C.8

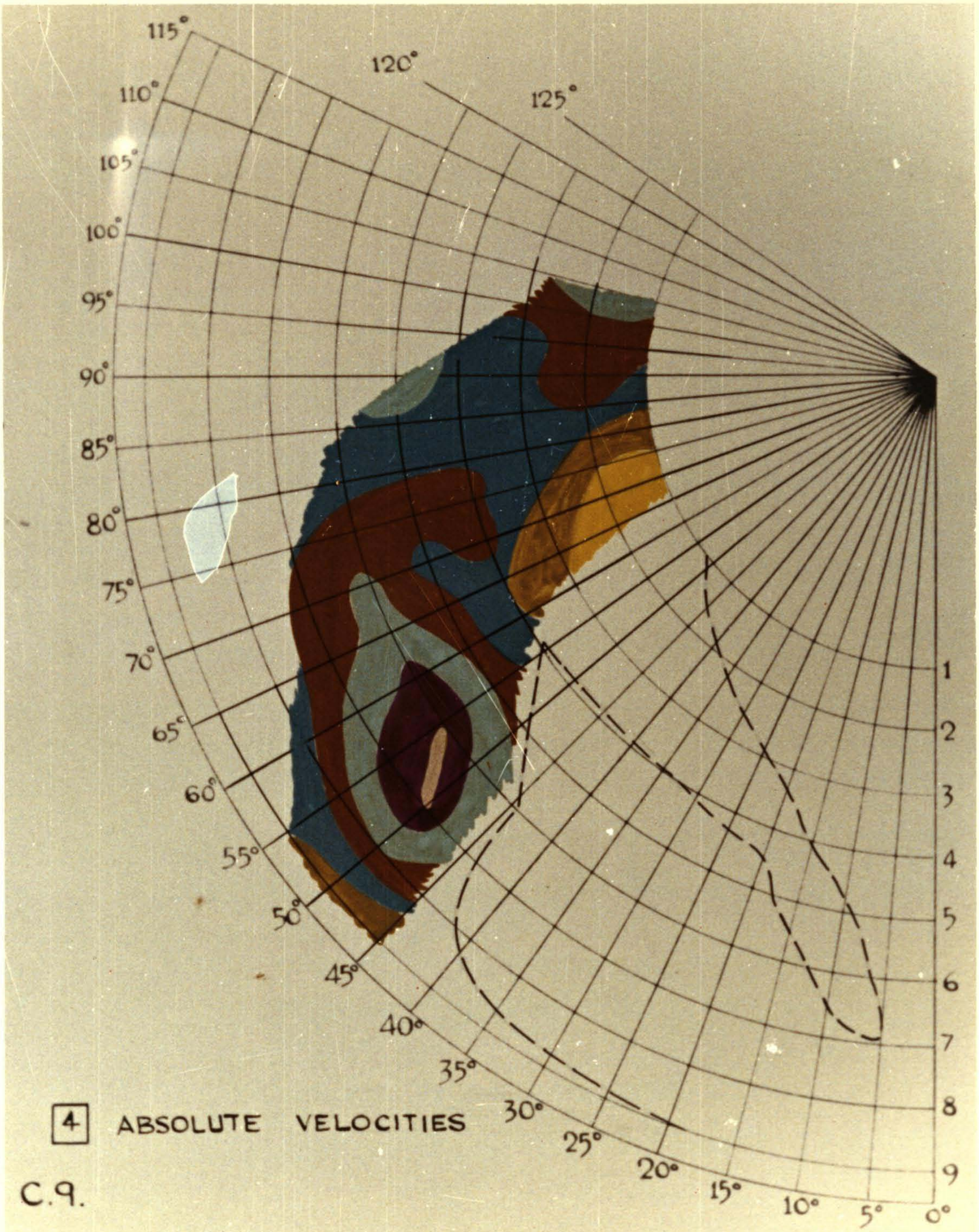

115°
110°
105°
100°
95°
90°
85°
80°
75°
70°
65°
60°
55°
50°
45°
40°
35°
30°
25°
20°
15°
10°
5°
0°
120°
125°
1
2
3
4
5
6
7
8
9
4 ABSOLUTE VELOCITIES
C.9.

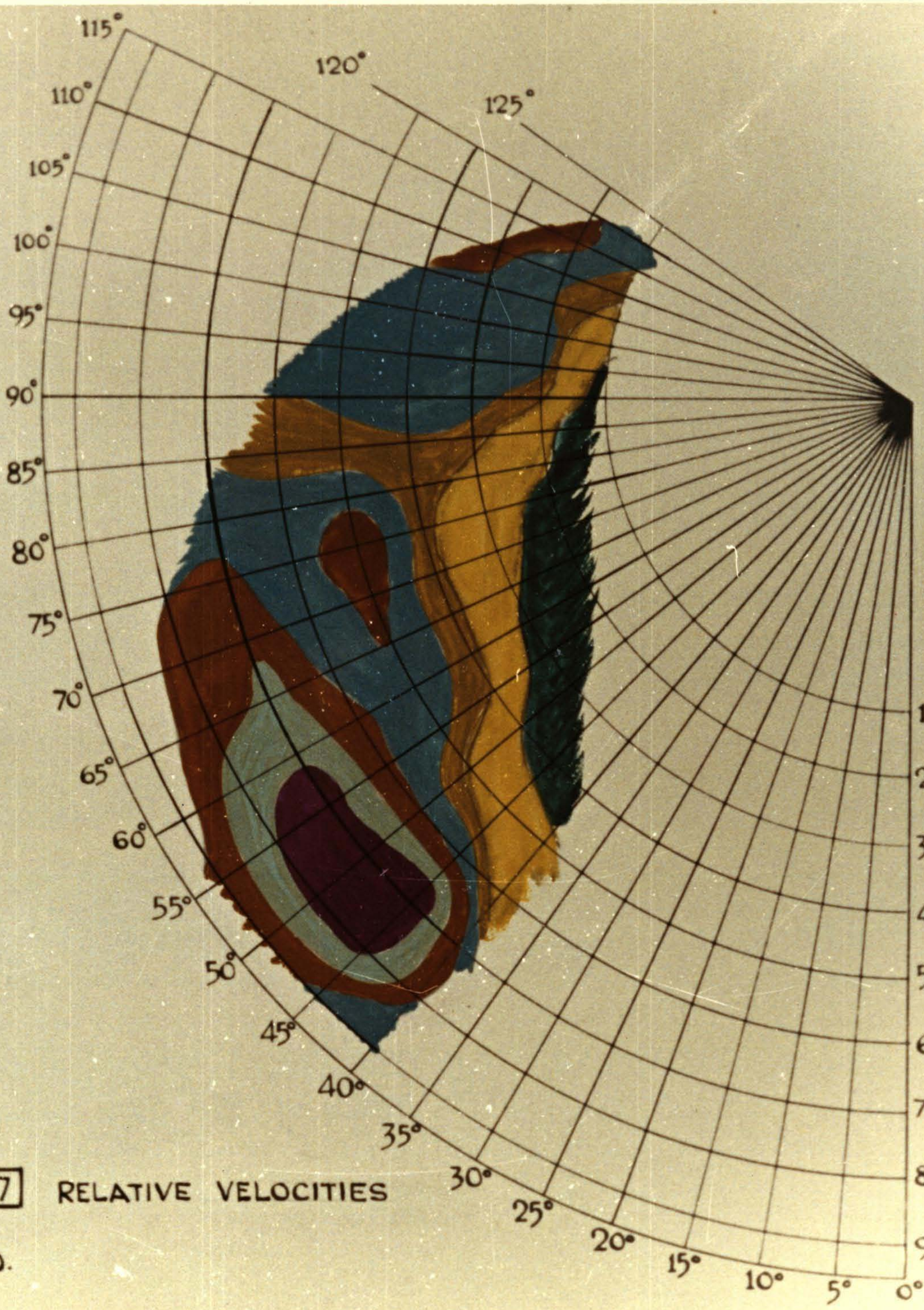

7 RELATIVE VELOCITIES

C.10.

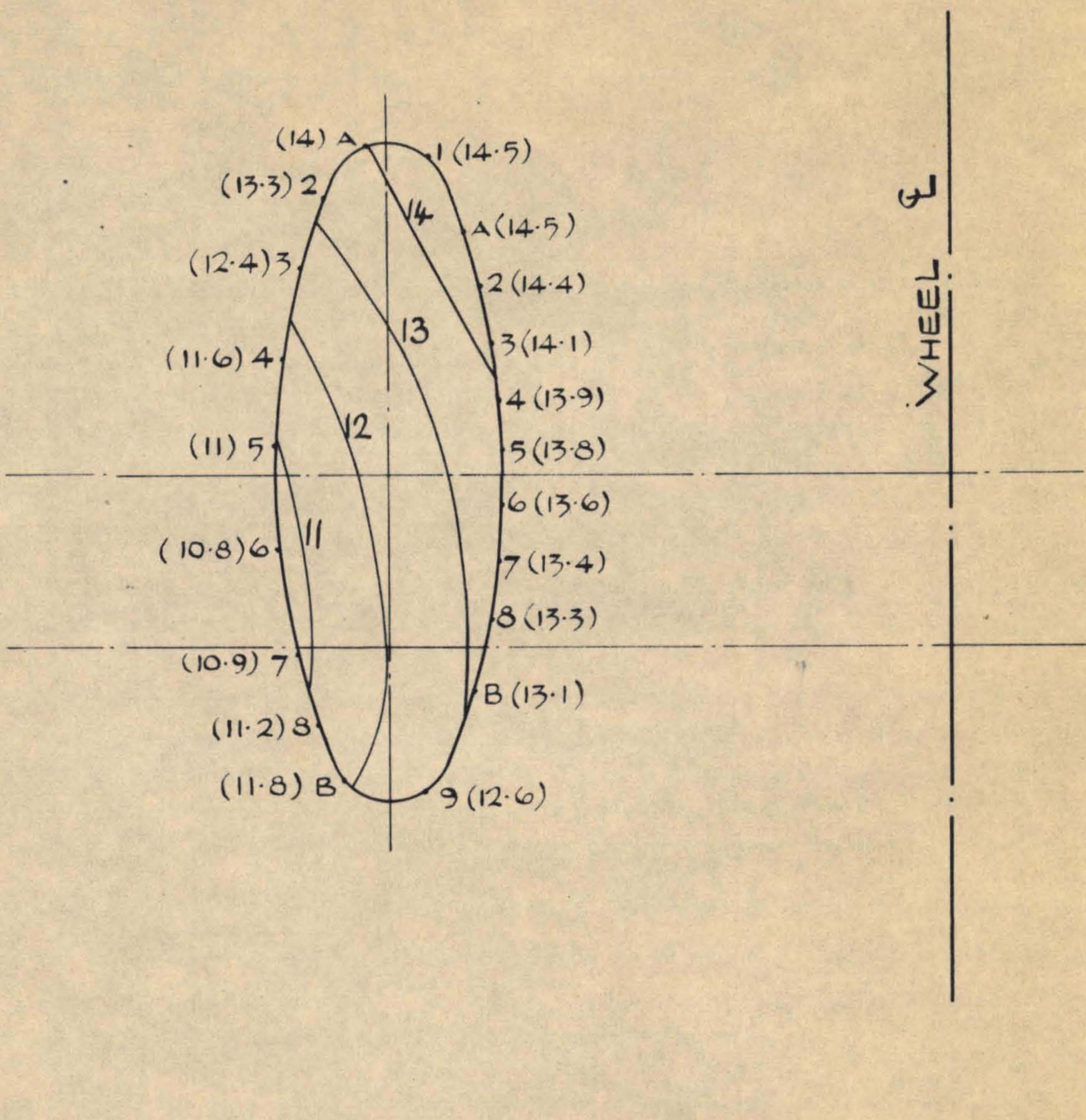

6 DISTRIBUTION OF RELATIVE VELOCITY AT INLET.

C.11

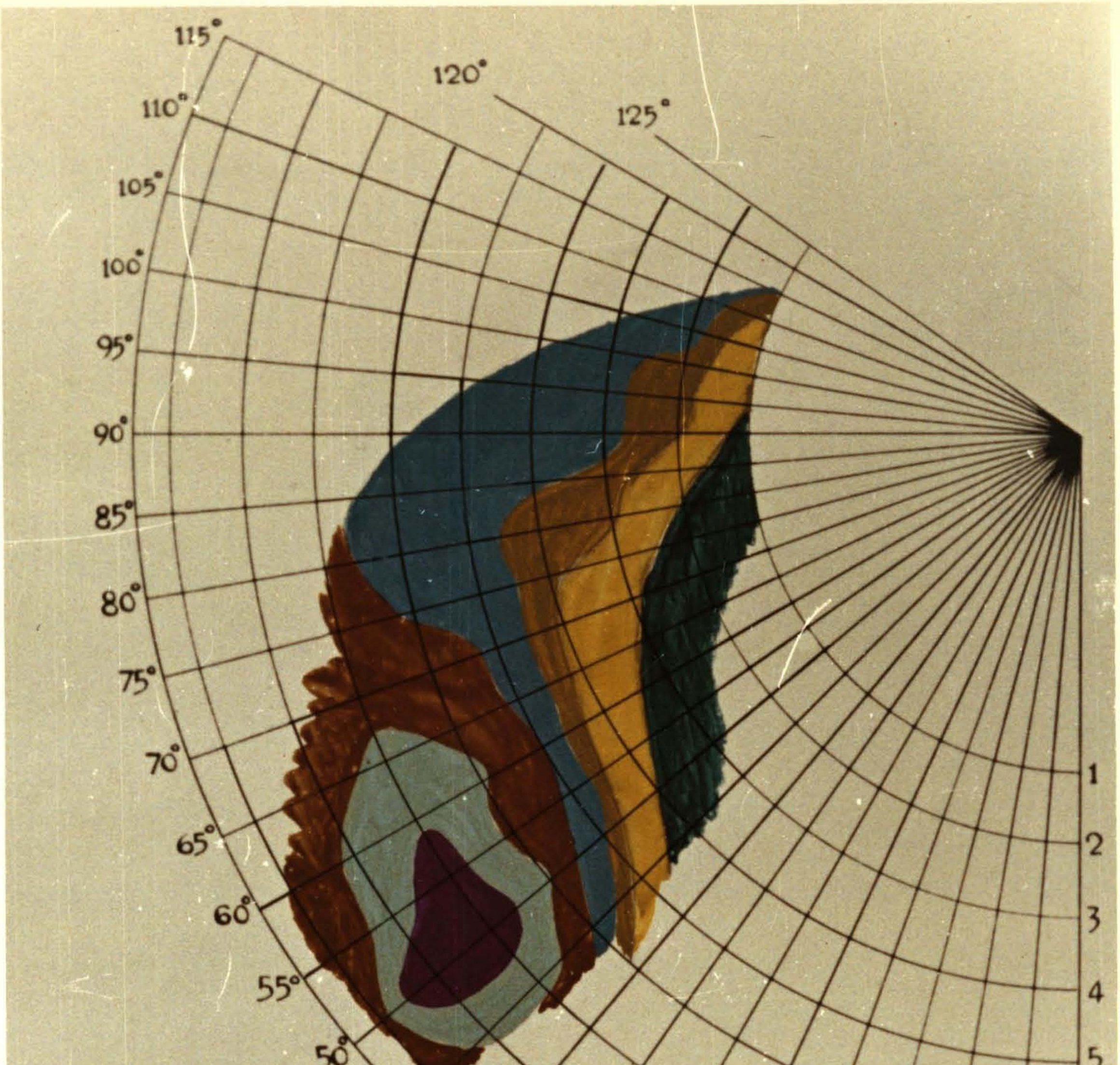

6 RELATIVE VELOCITIES

C.12.

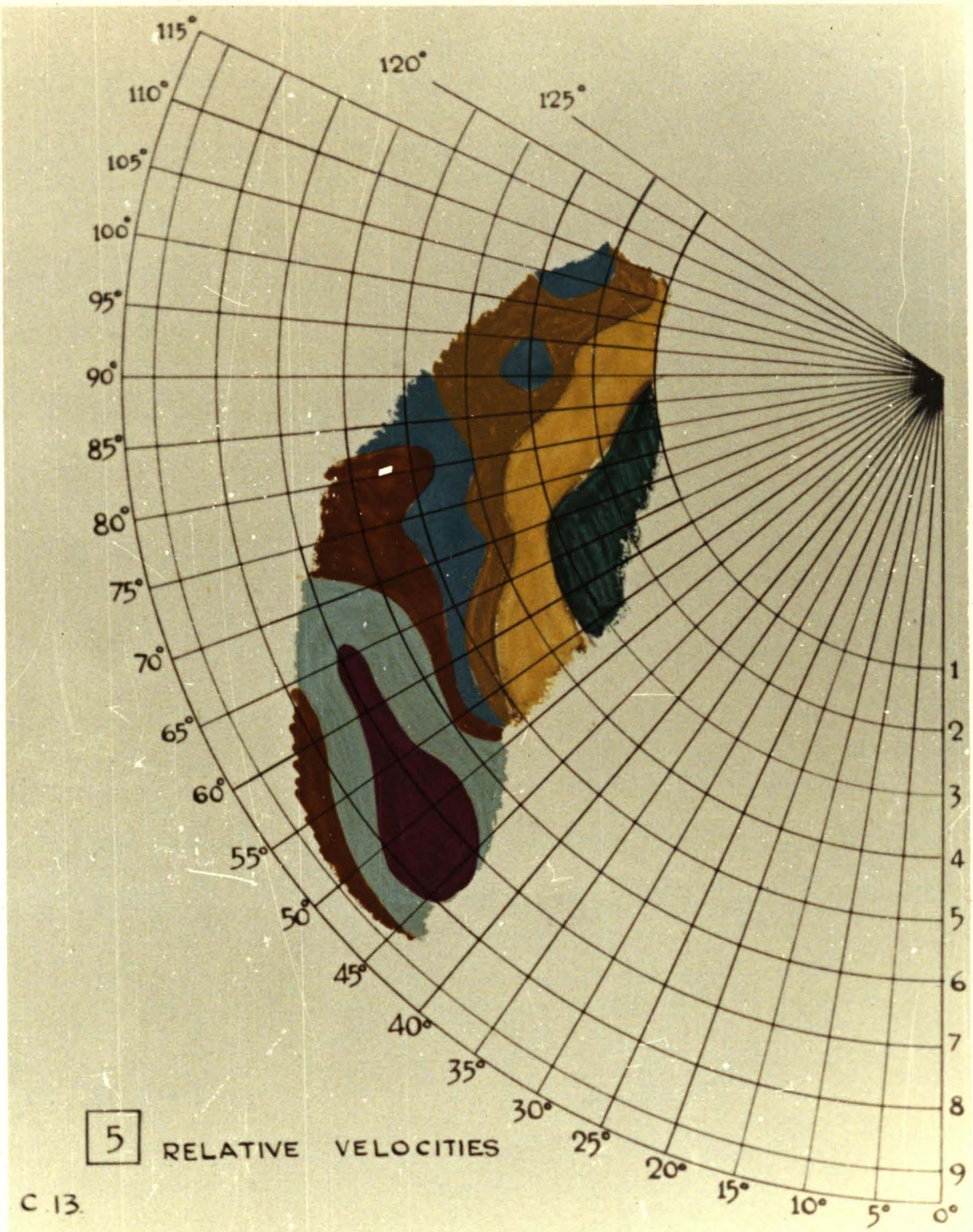
115°
110°
105°
100°
95°
90°
85°
80°
75°
70°
65°
60°
55°
50°
45°
40°
35°
30°
25°
20°
15°
10°
5°
0°
120°
125°
1
2
3
4
5
6
7
8
9
5
RELATIVE VELOCITIES
C 13.

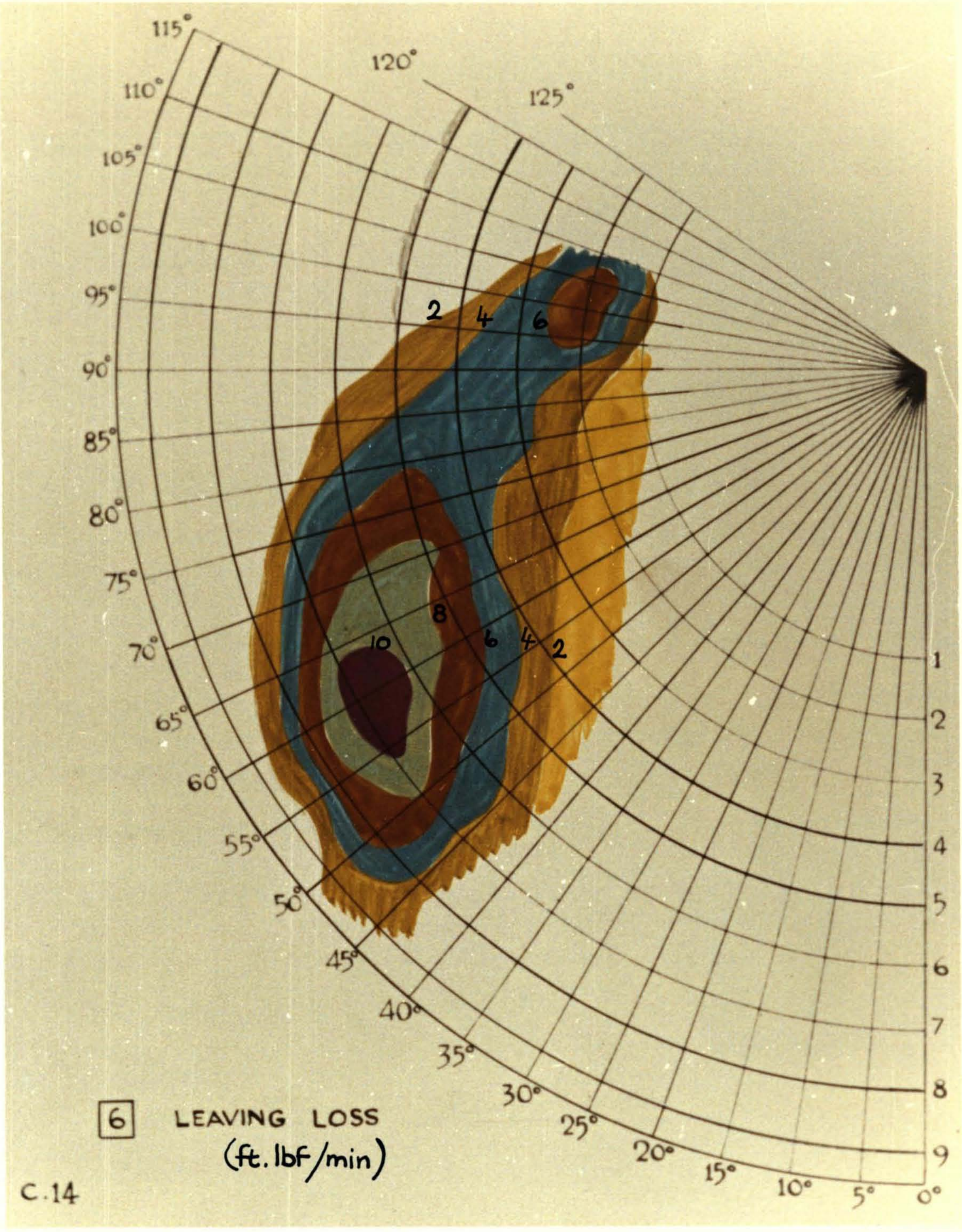

6 LEAVING LOSS
(ft. lbF/min)

C.14

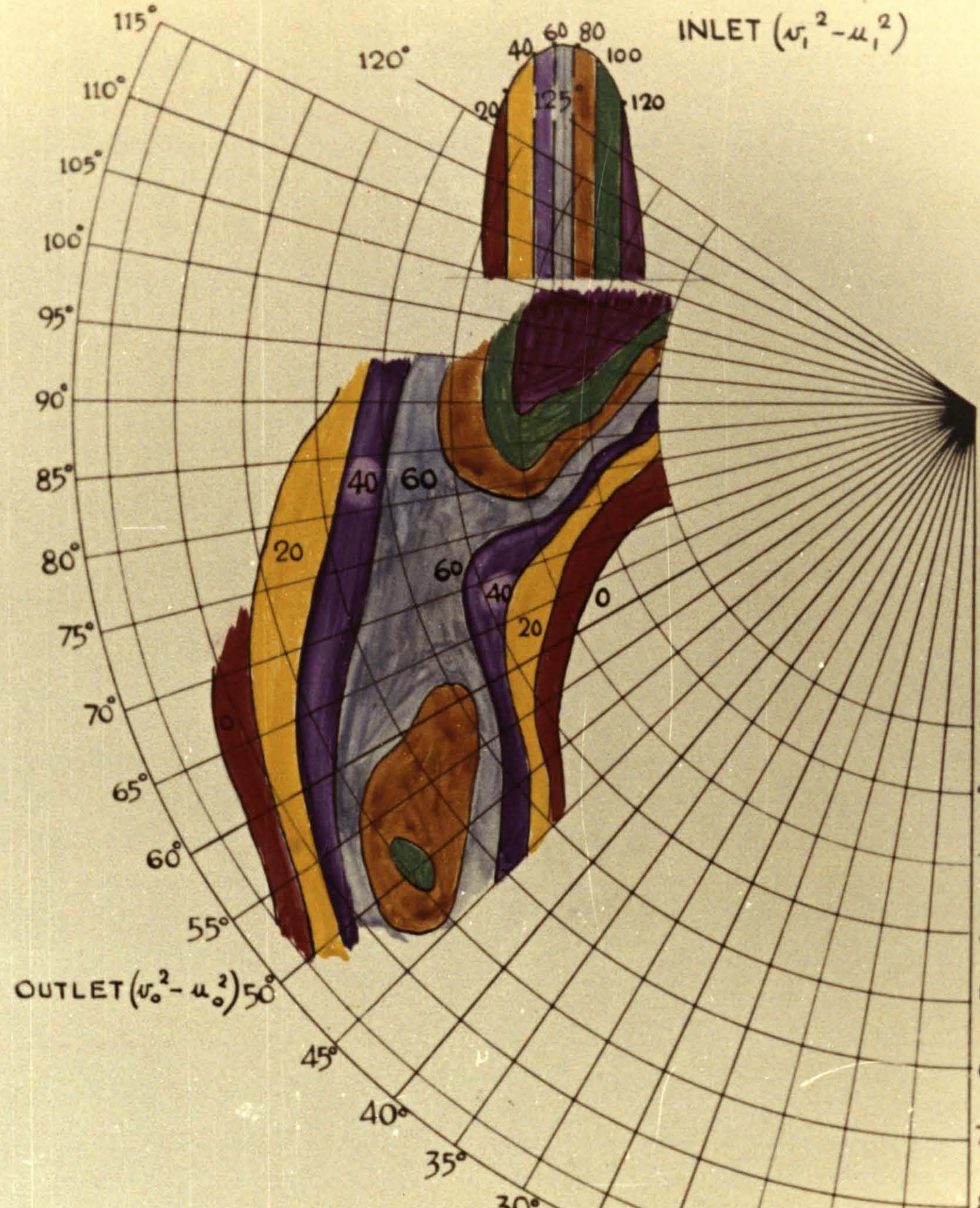

6 RELATIVE ENERGY $(v^2 - u^2)$ $(ft/s)^2$

C.15.

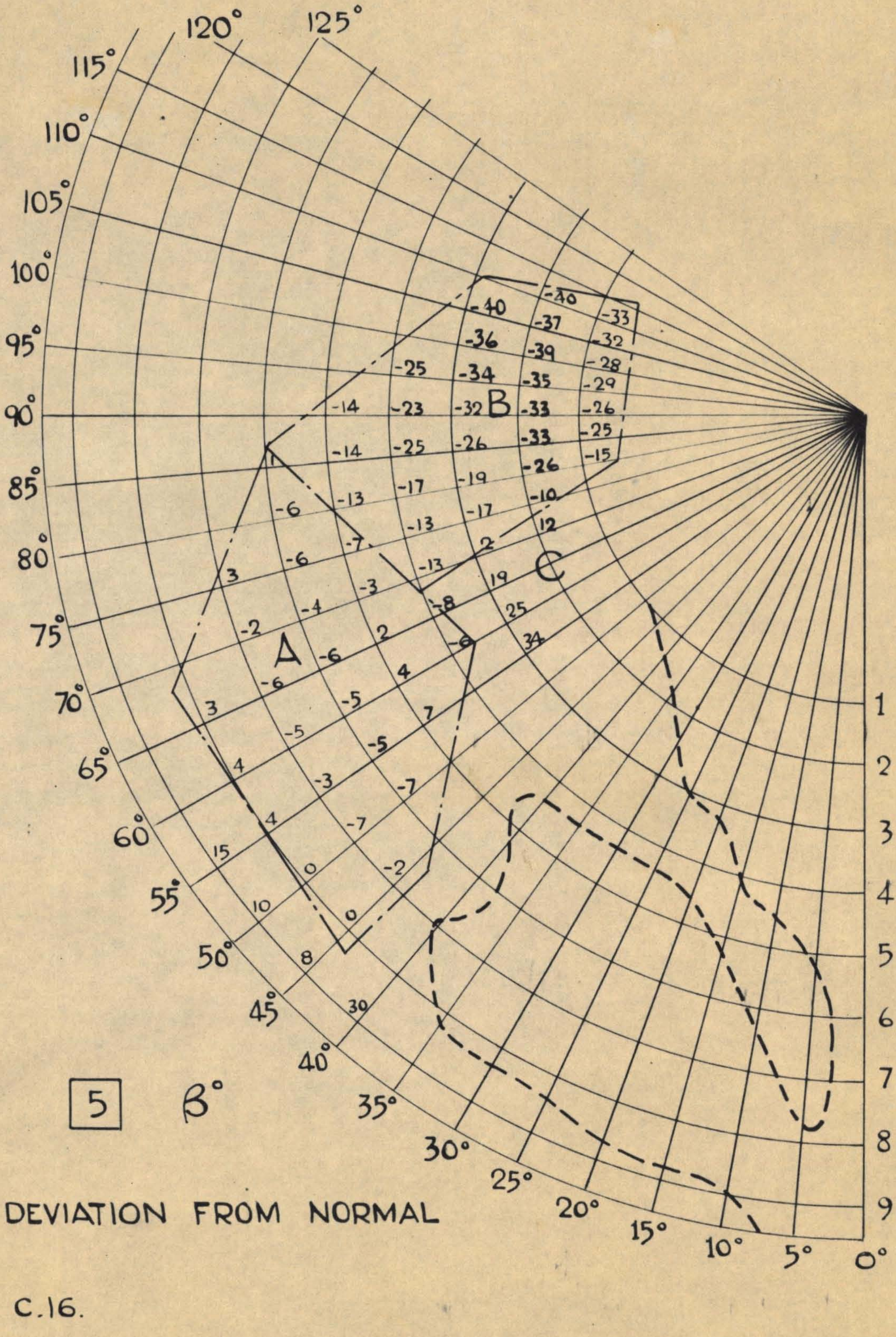

DEVIATION FROM NORMAL

C.16.

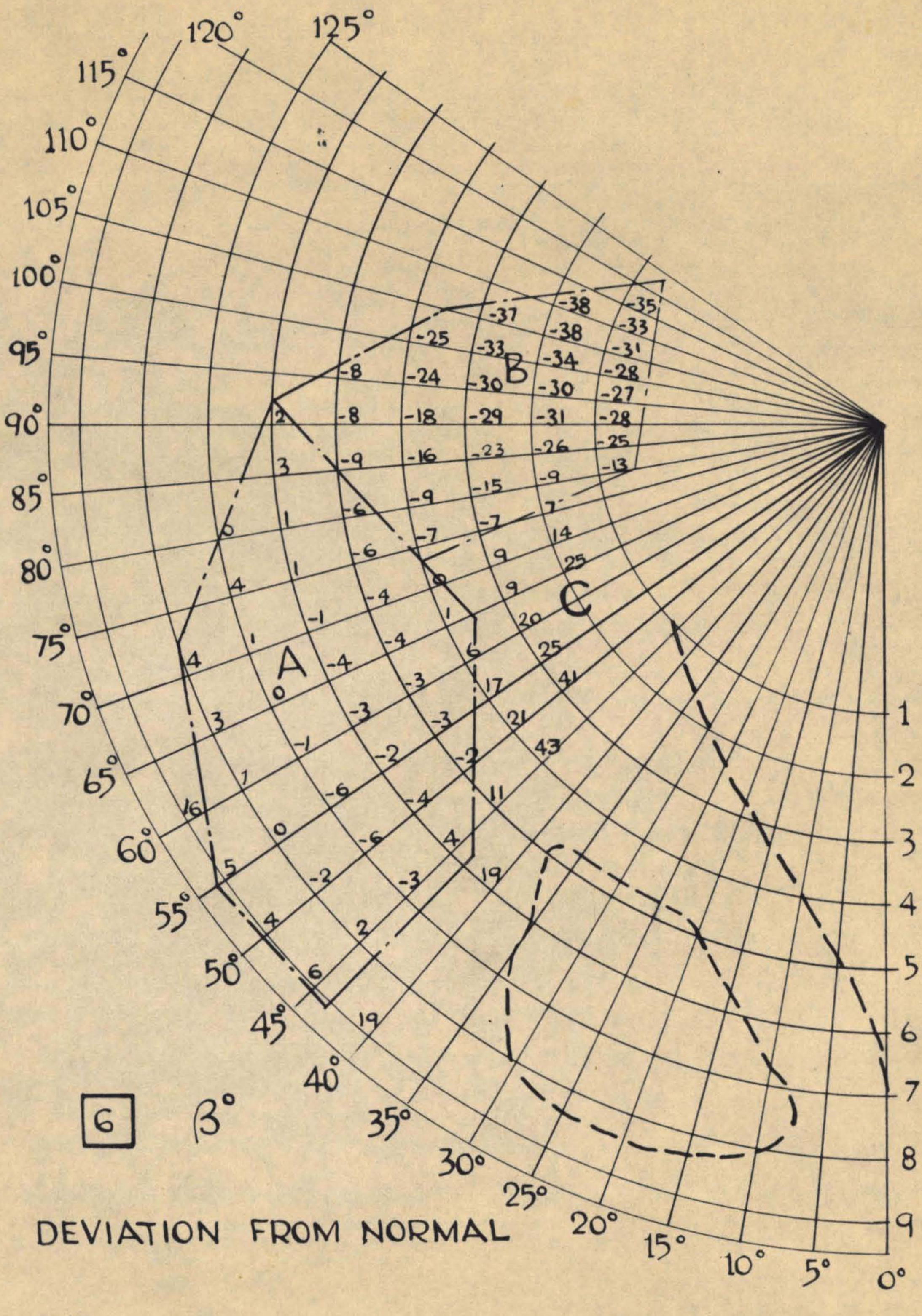

$\boxed{6}$ β°

DEVIATION FROM NORMAL

C.17

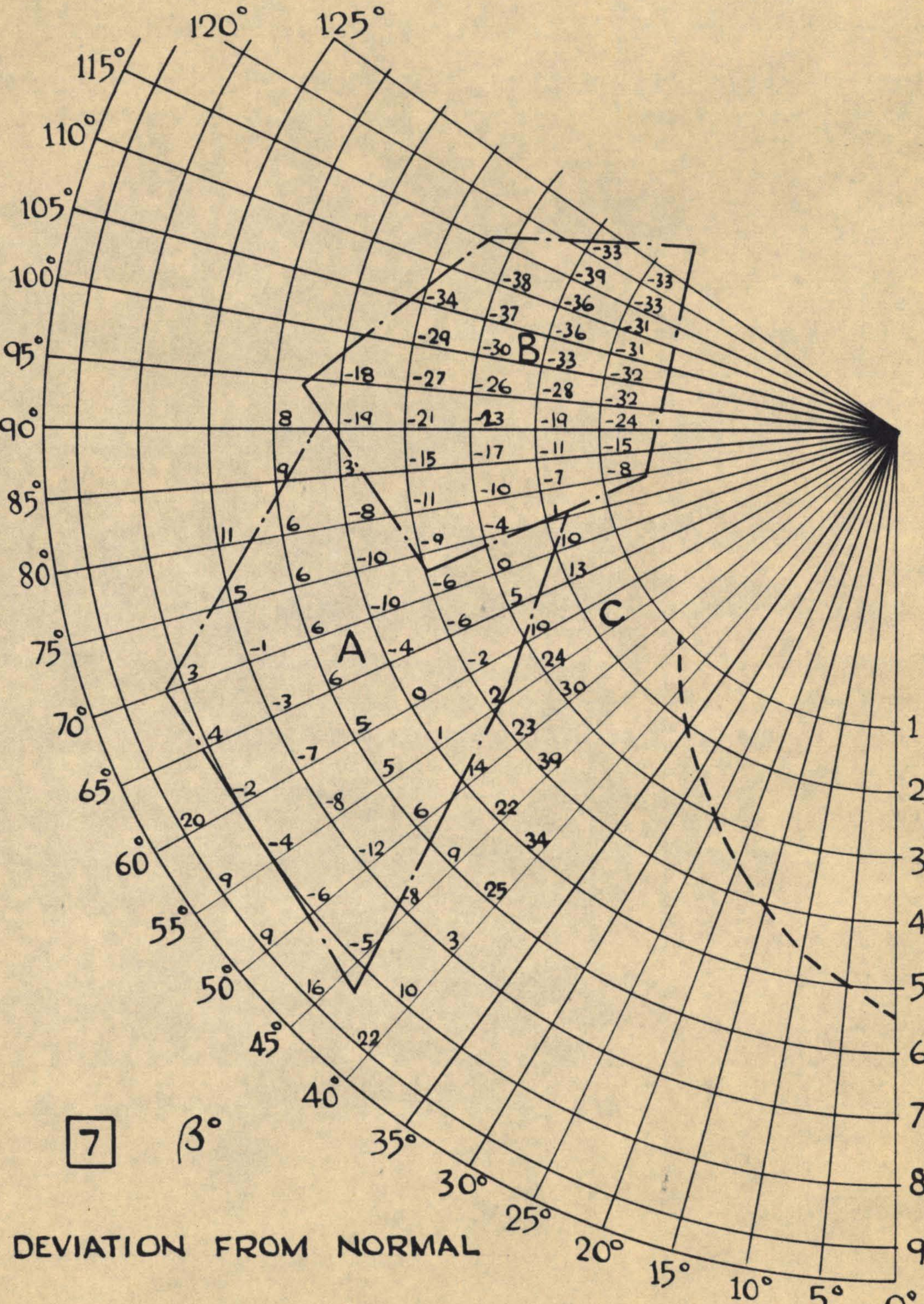

7 β°

DEVIATION FROM NORMAL

C. 18.

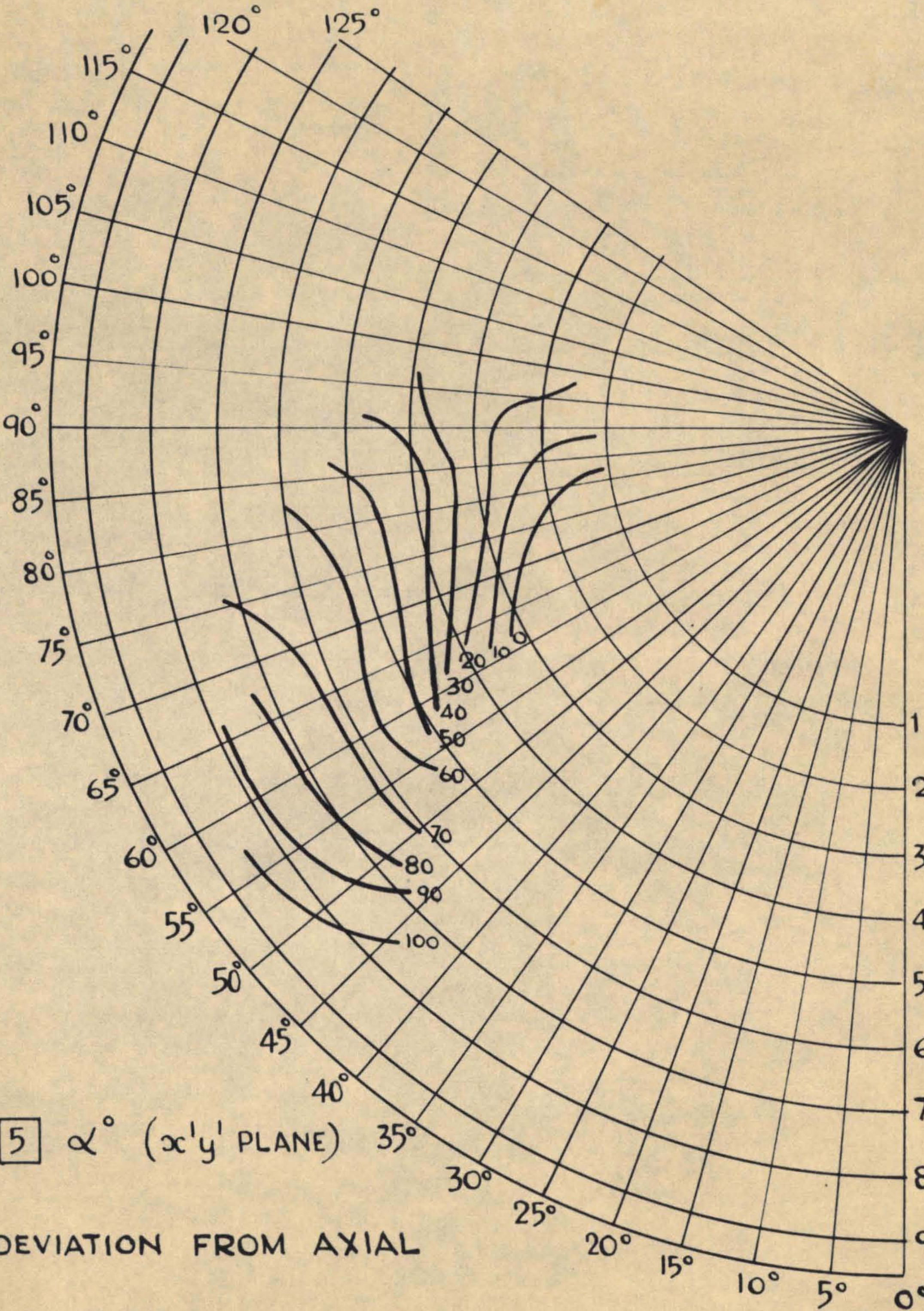

5 α° ($x'y'$ PLANE)

DEVIATION FROM AXIAL

C.19

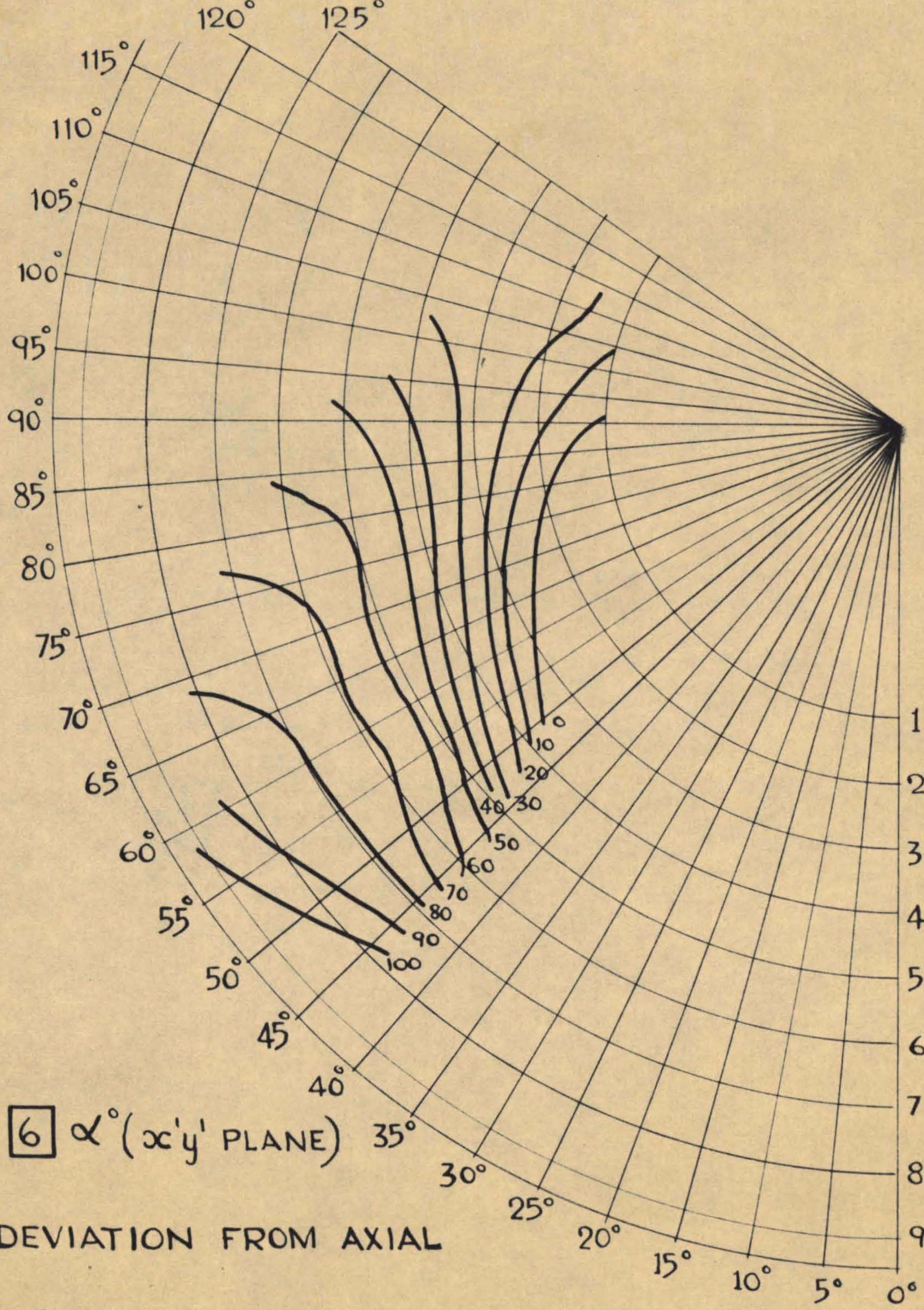

$\boxed{6}$ α° ($x'y'$ PLANE)

DEVIATION FROM AXIAL

C. 20.

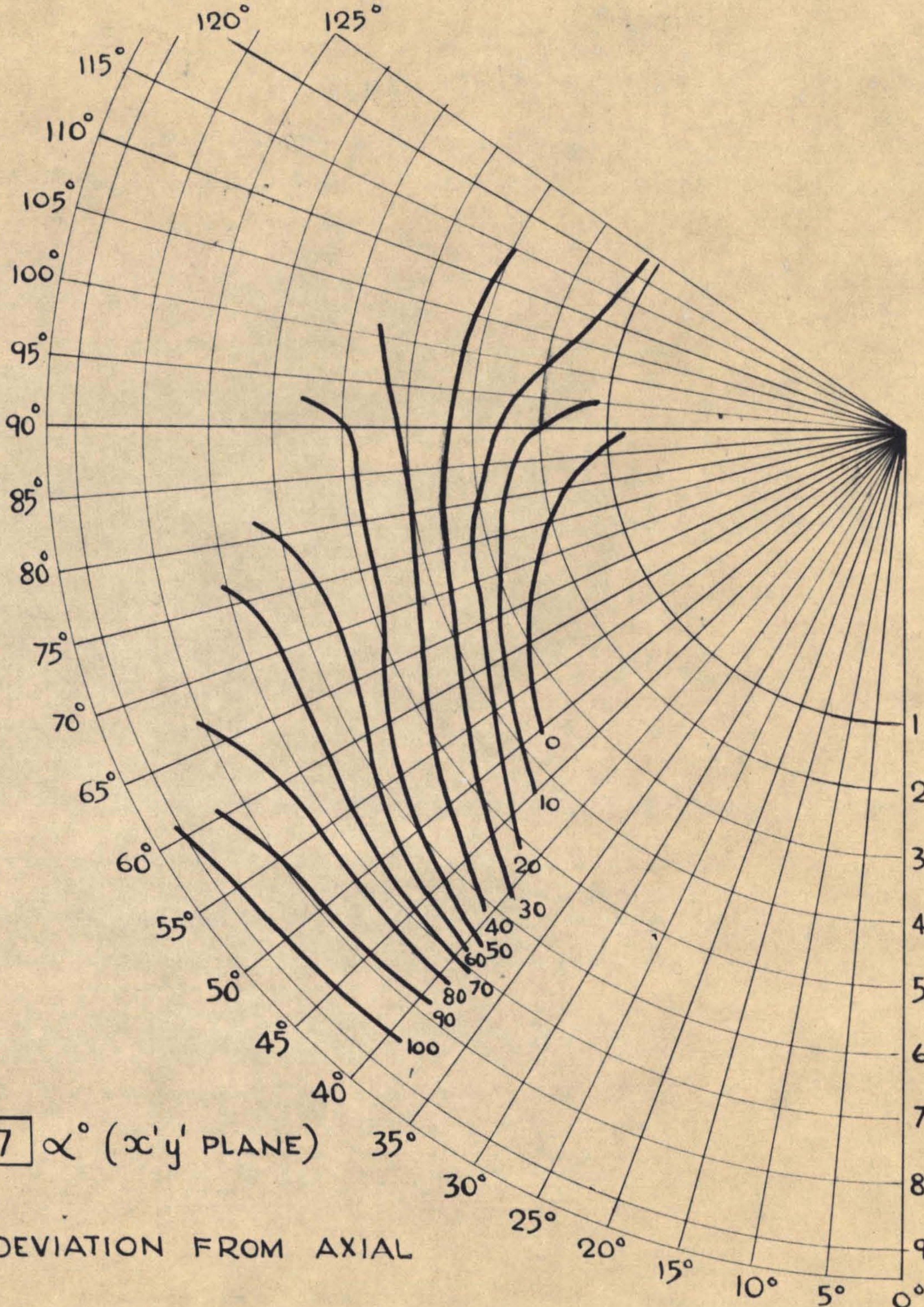

7 α° ($x'y'$ PLANE)

DEVIATION FROM AXIAL

C.21.

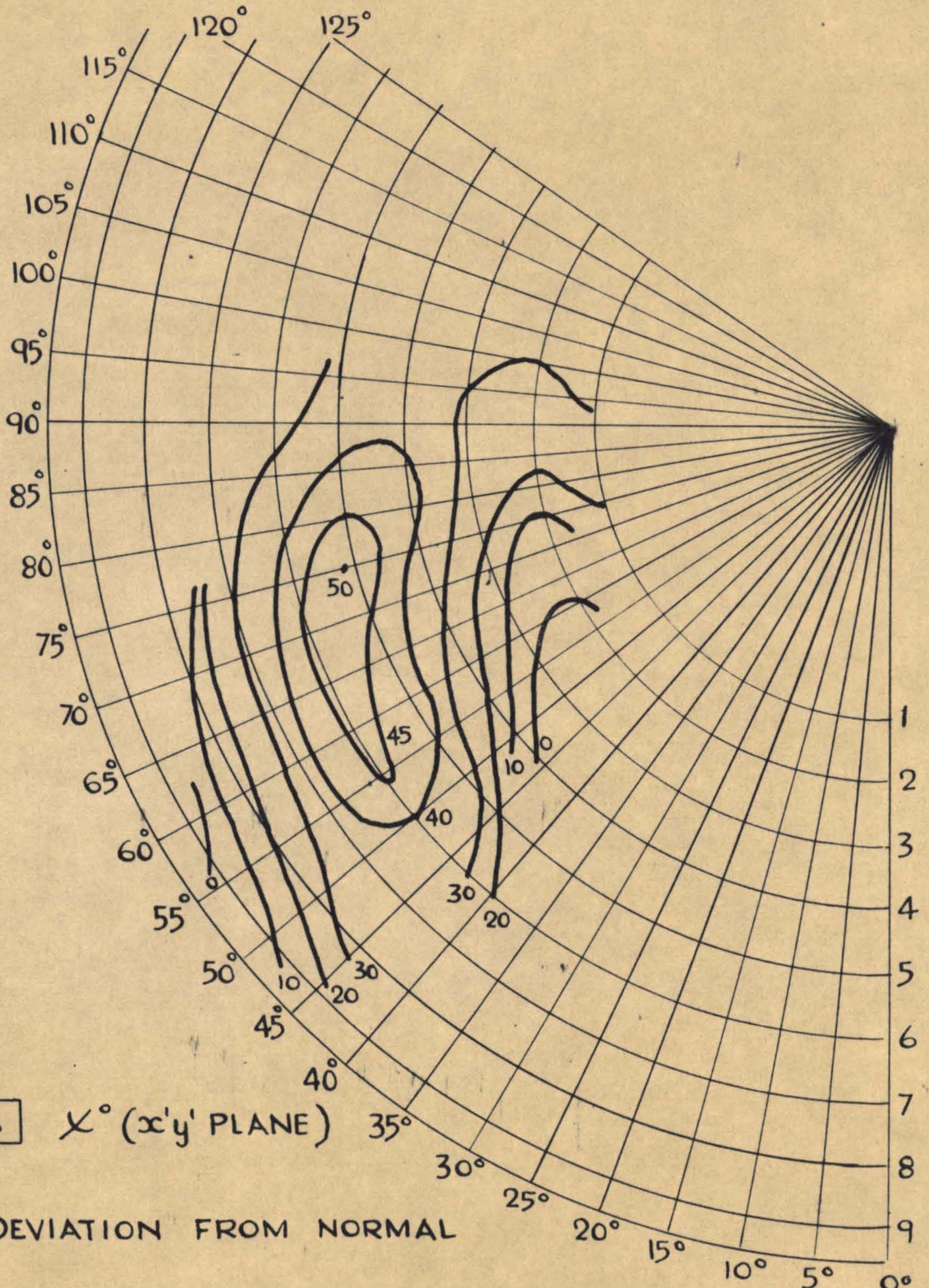

6 $\chi°$ ($x'y'$ PLANE)

DEVIATION FROM NORMAL

C.22.

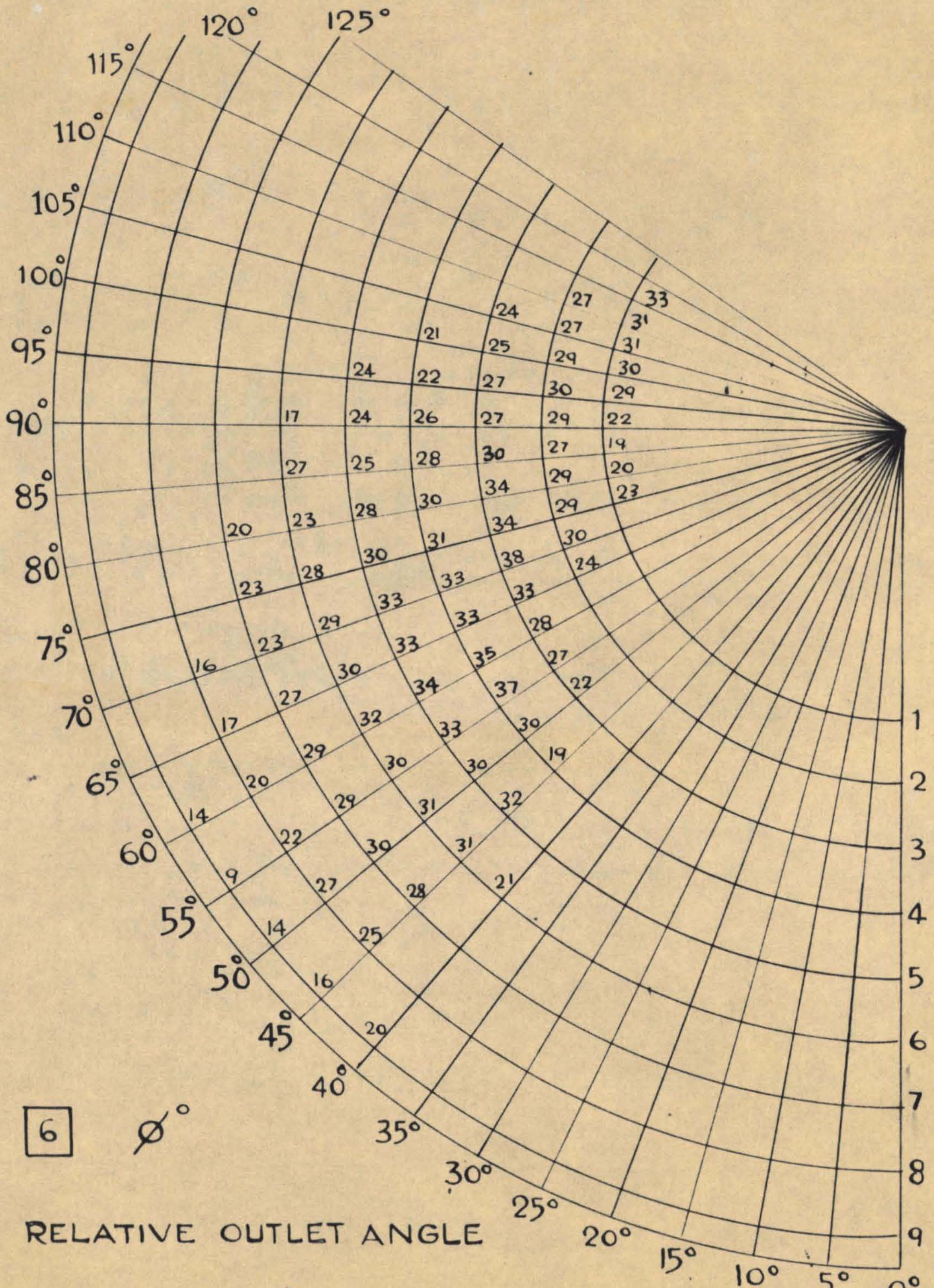

6 ϕ°

RELATIVE OUTLET ANGLE

C.23

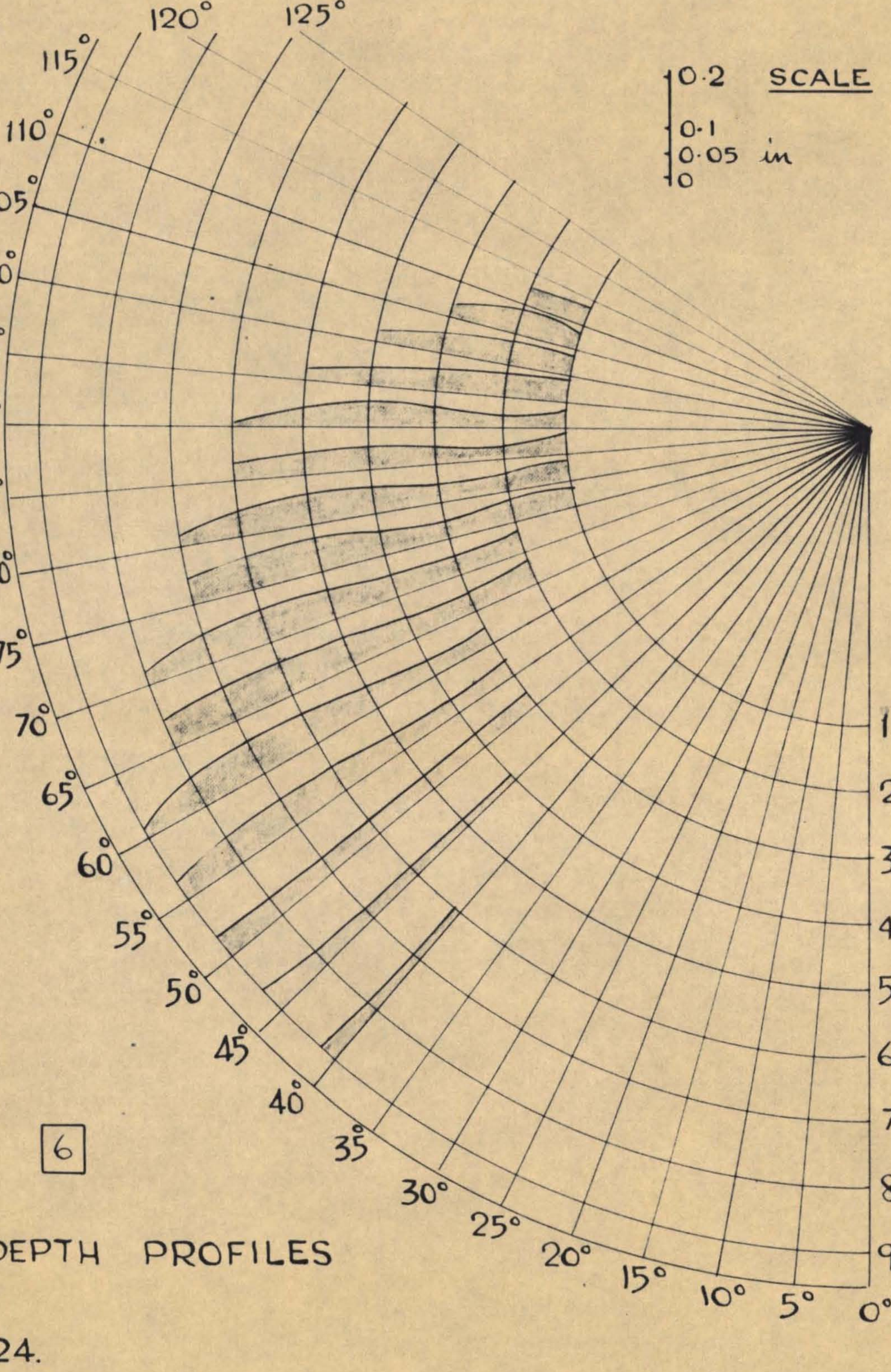

6

DEPTH PROFILES

C.24.

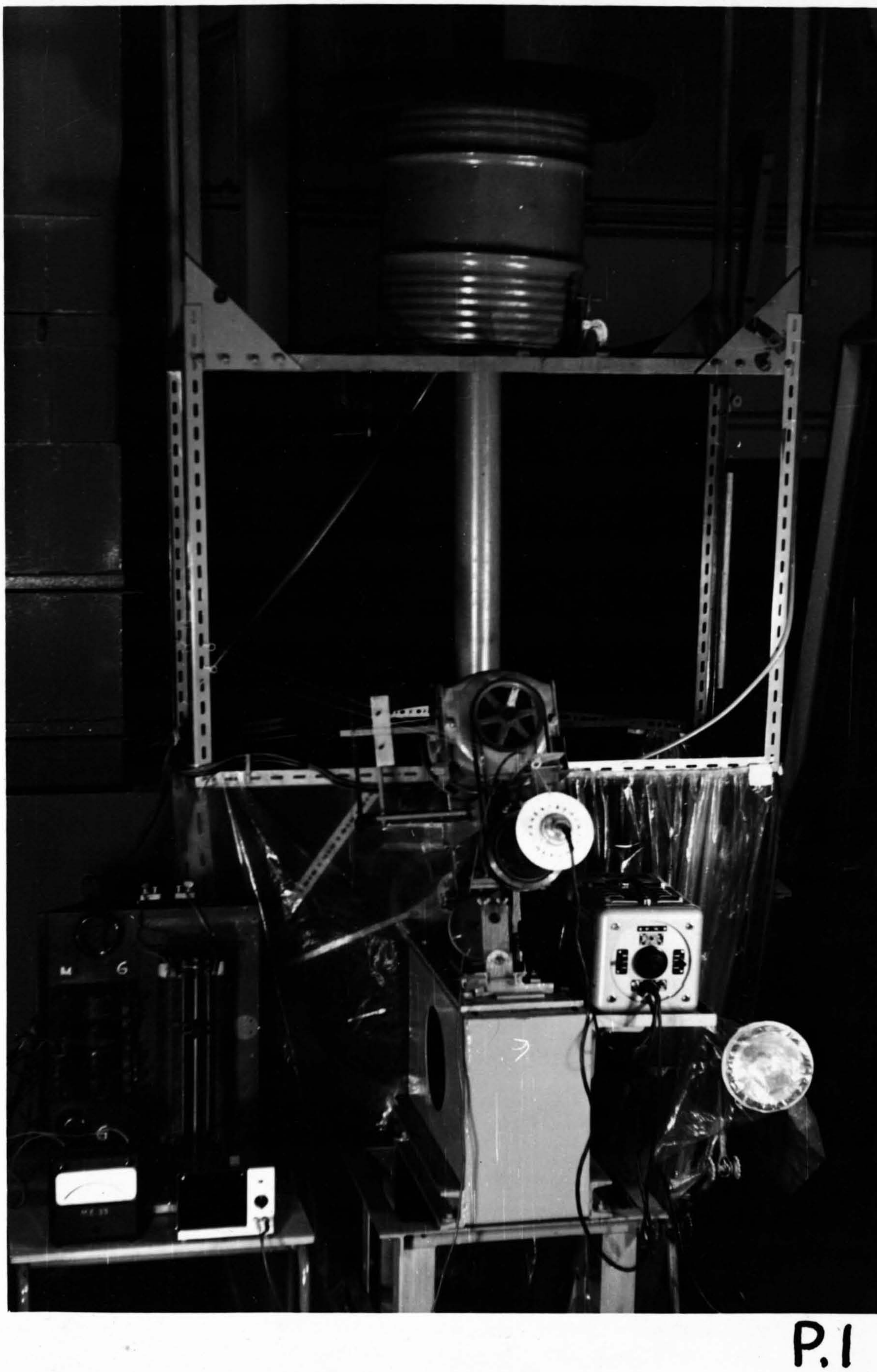

P.1

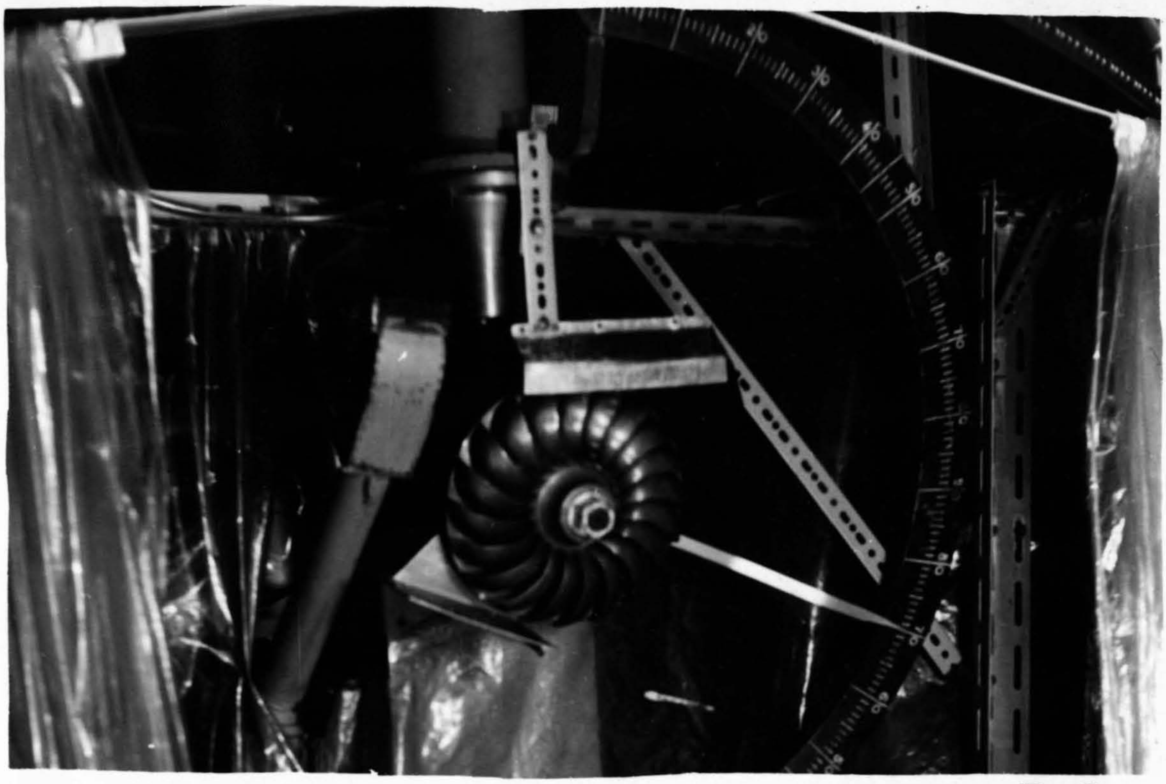

P.2

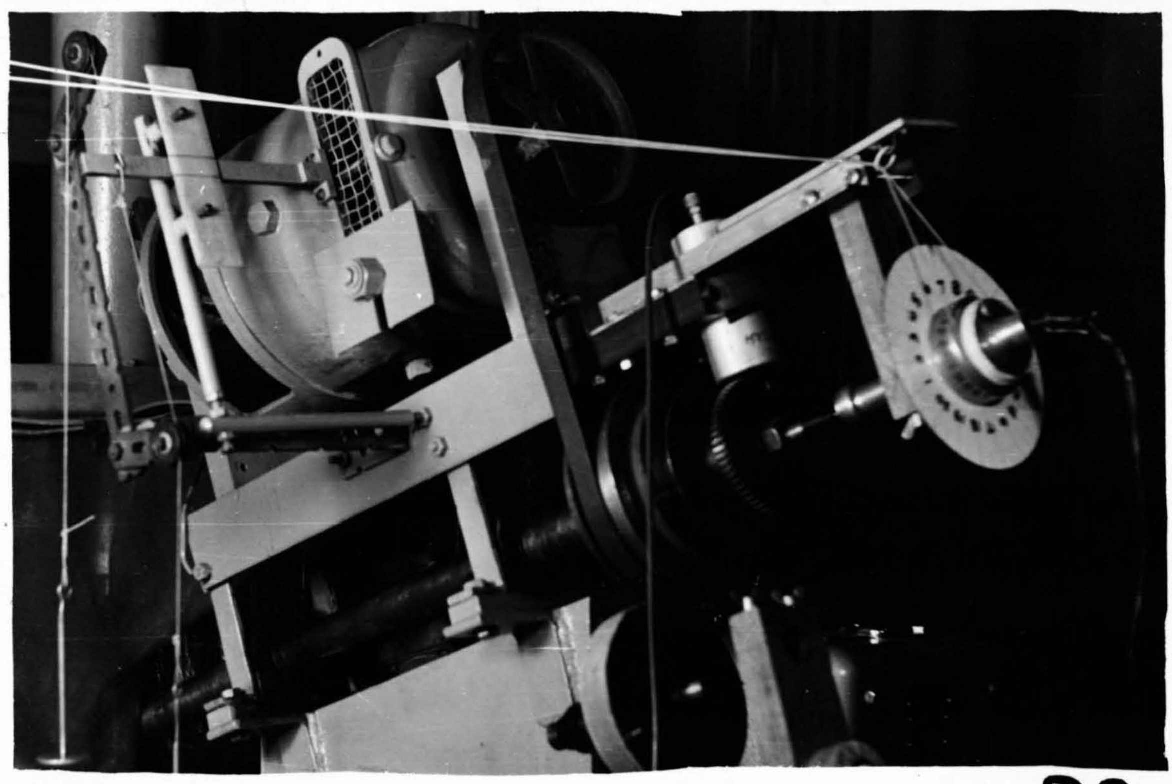

P.3

P.4

P.5

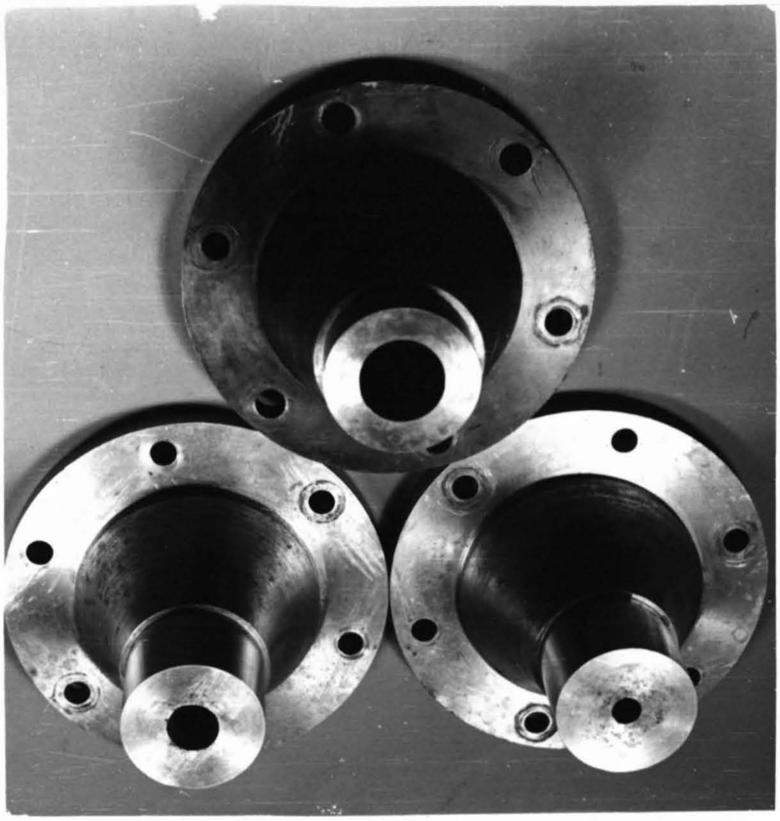

P.6

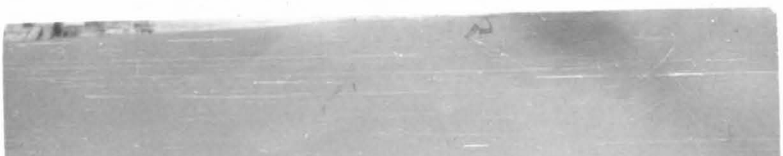

P.7

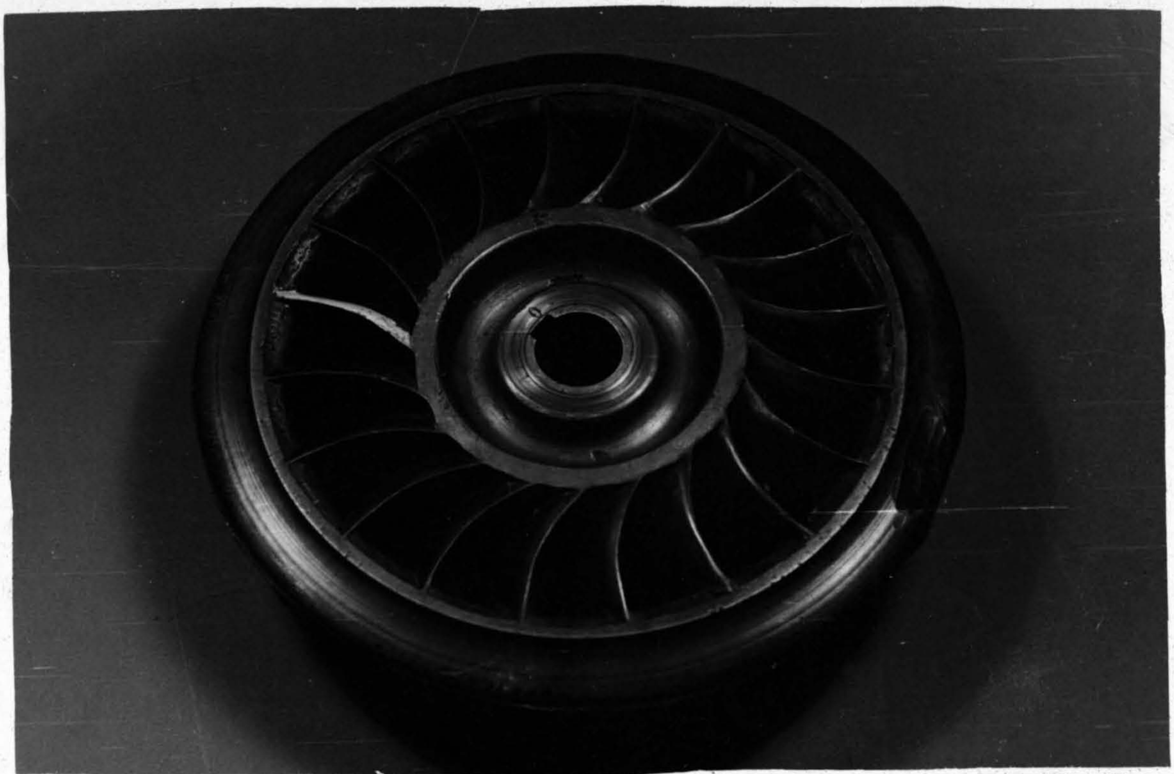

P.8

P.9

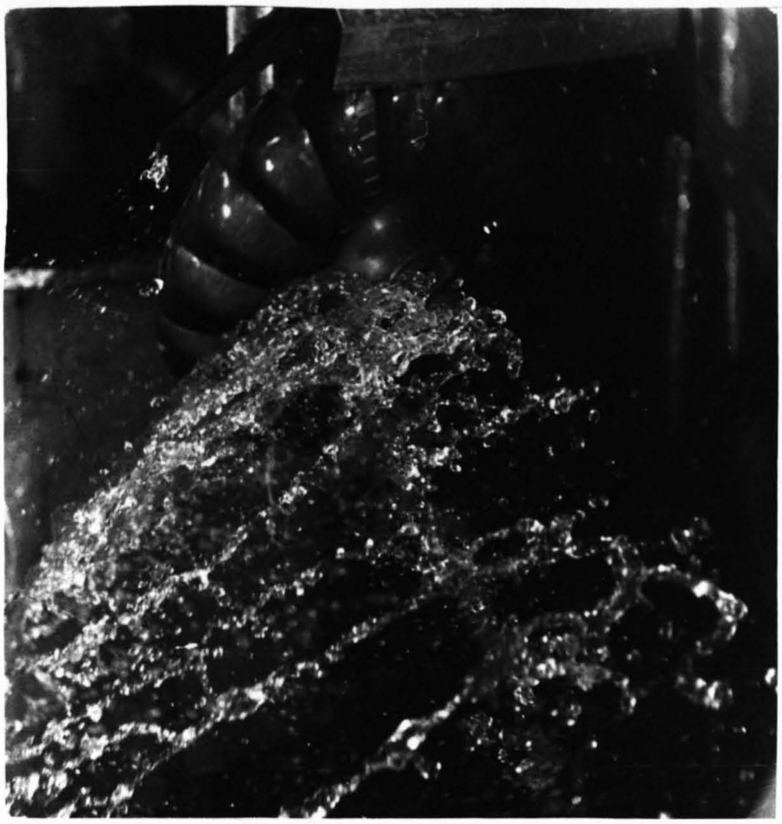

P.11

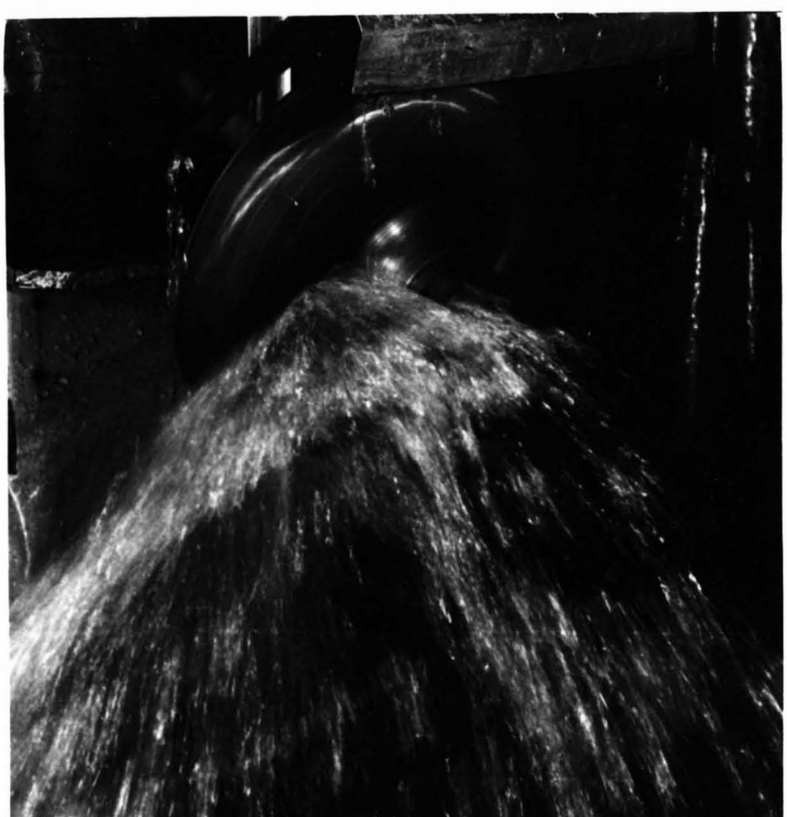

P.10


P.13


P.12

P.14

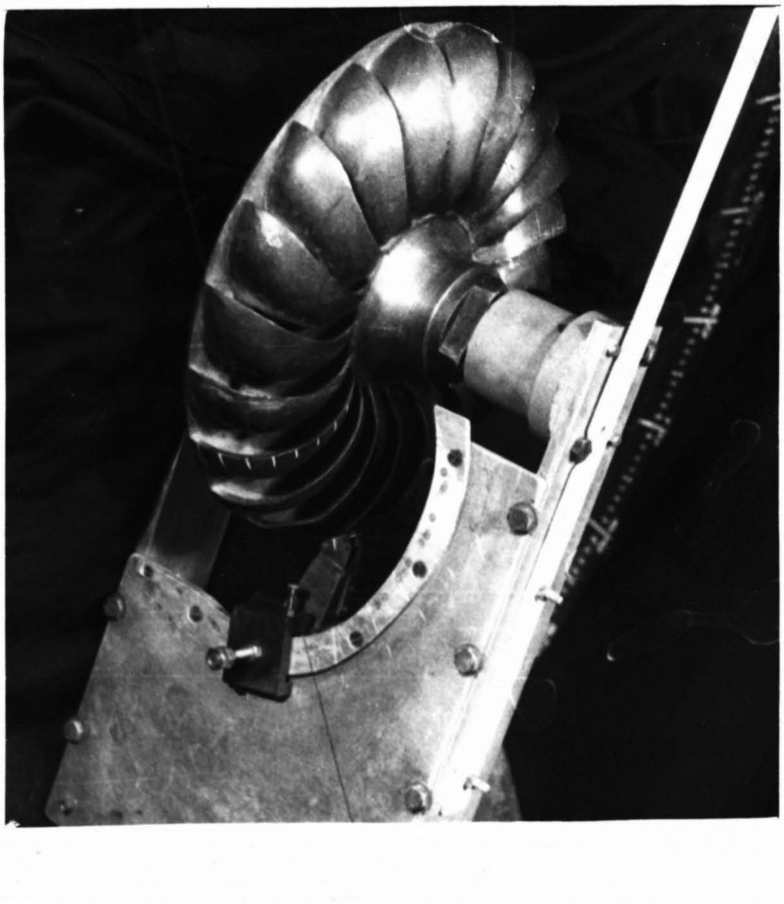

P.15

P.16

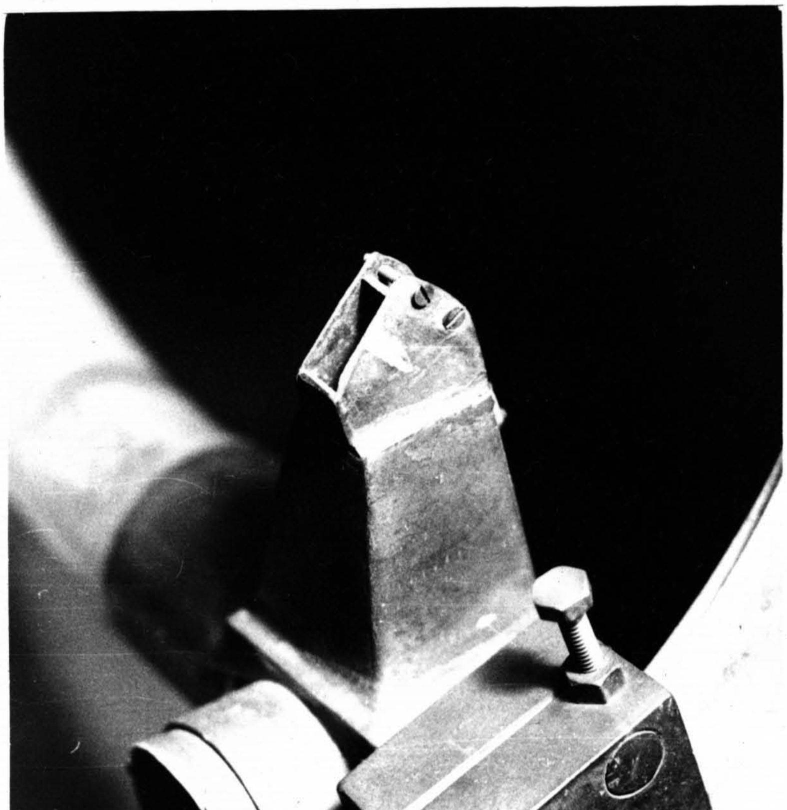

P.17

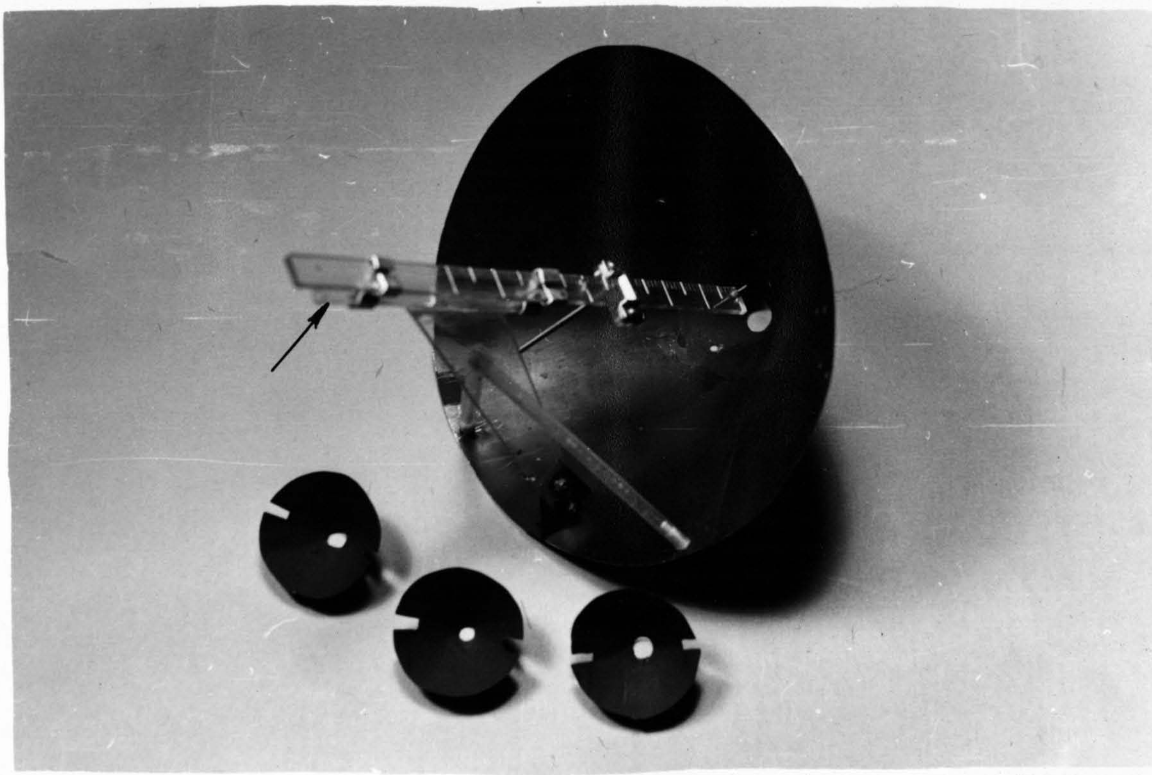

P.18

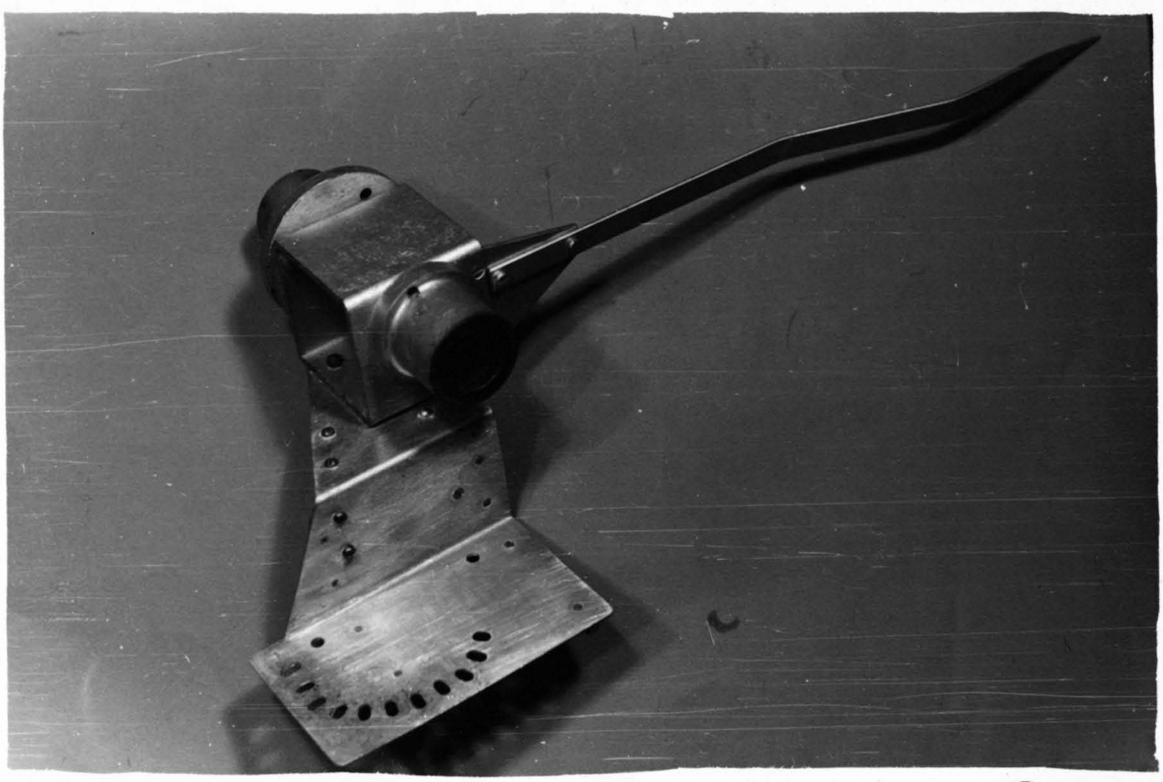

P.19

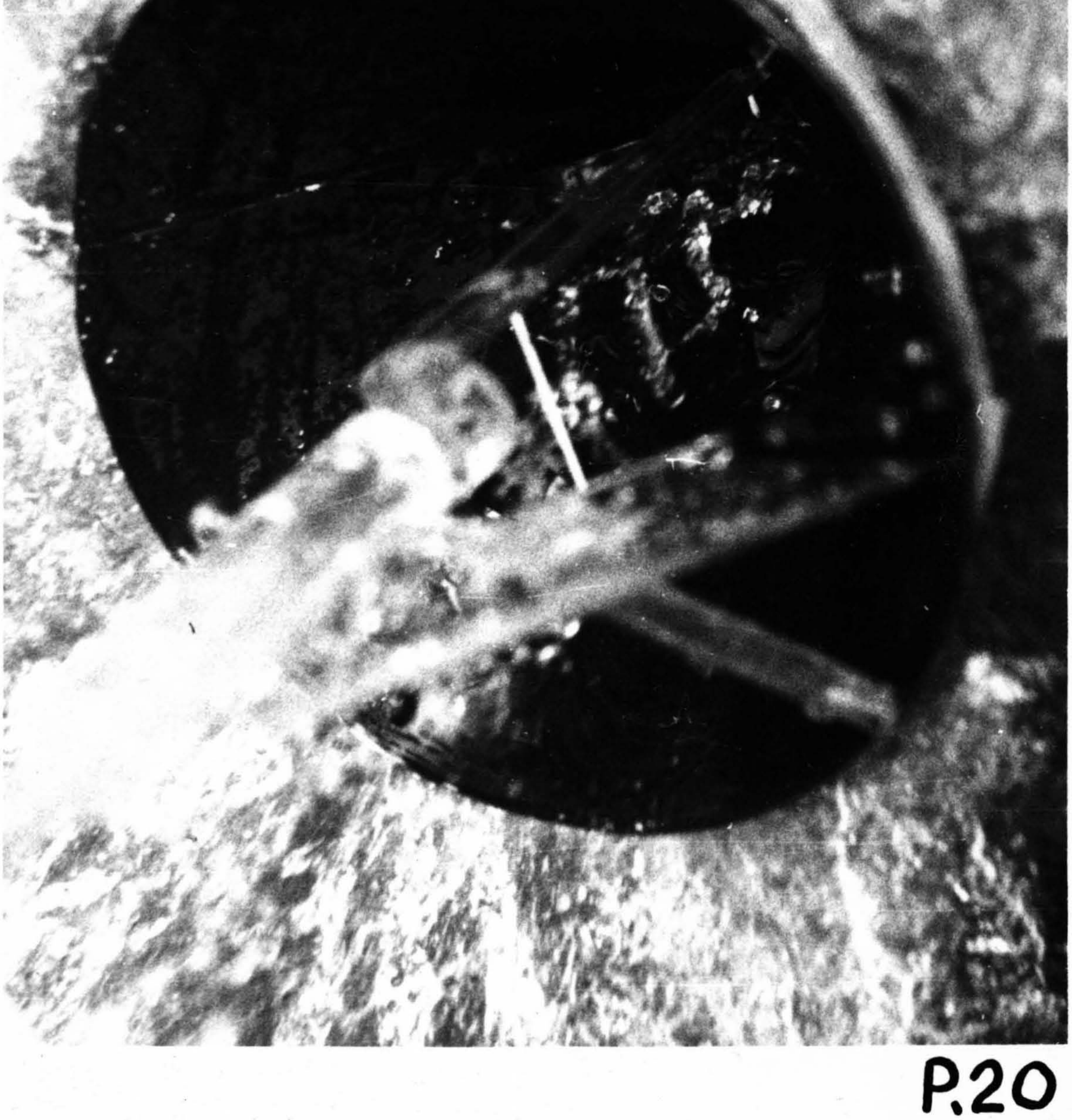

P.20

P.21

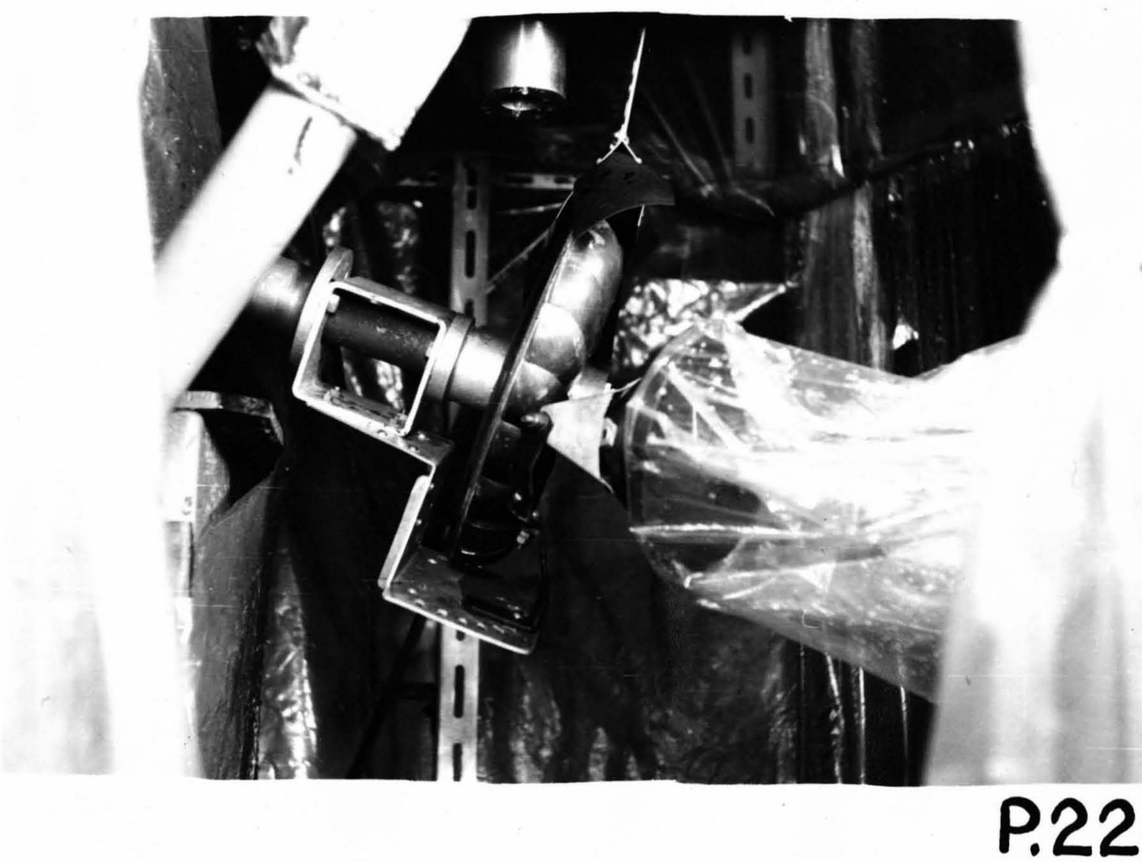

P.22

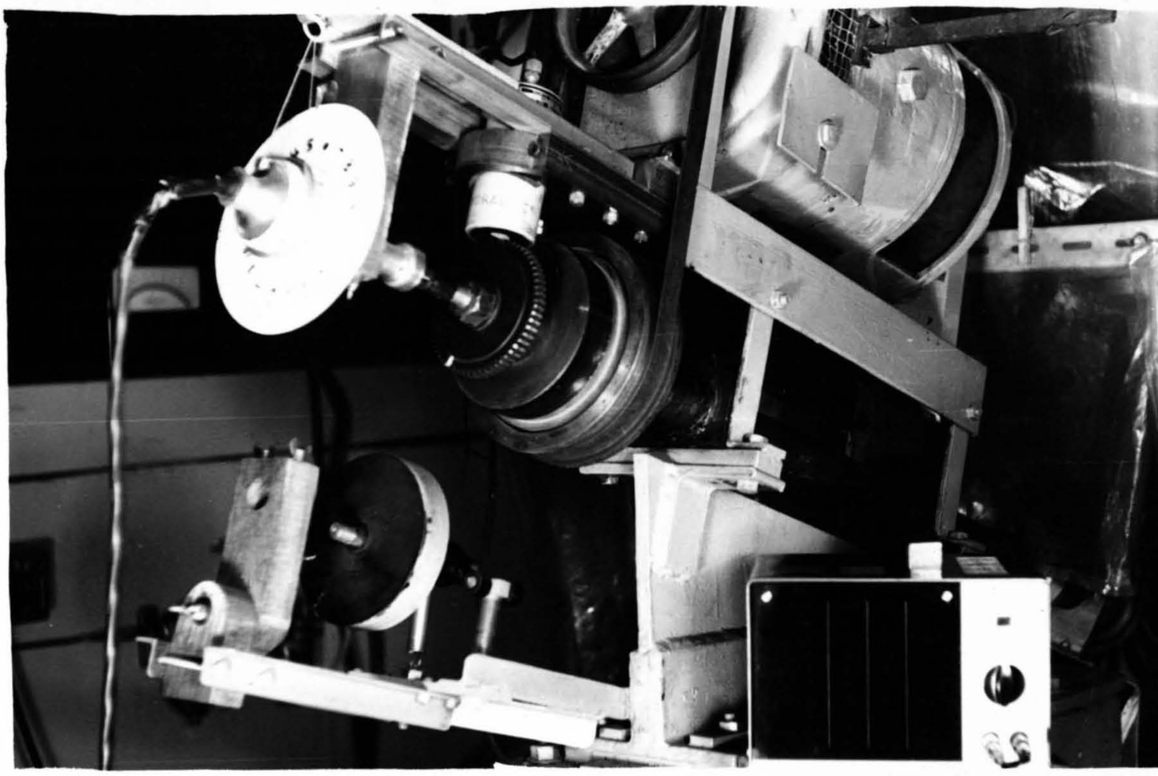
P.23

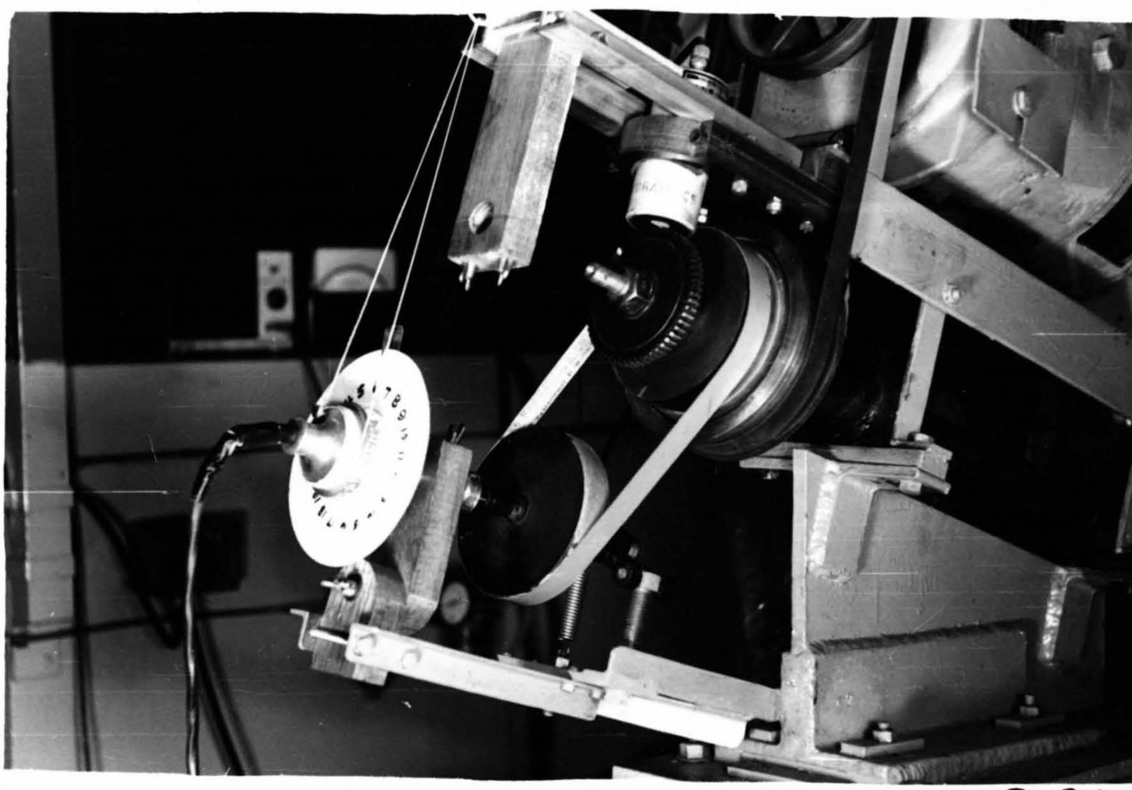
P.24

P.25

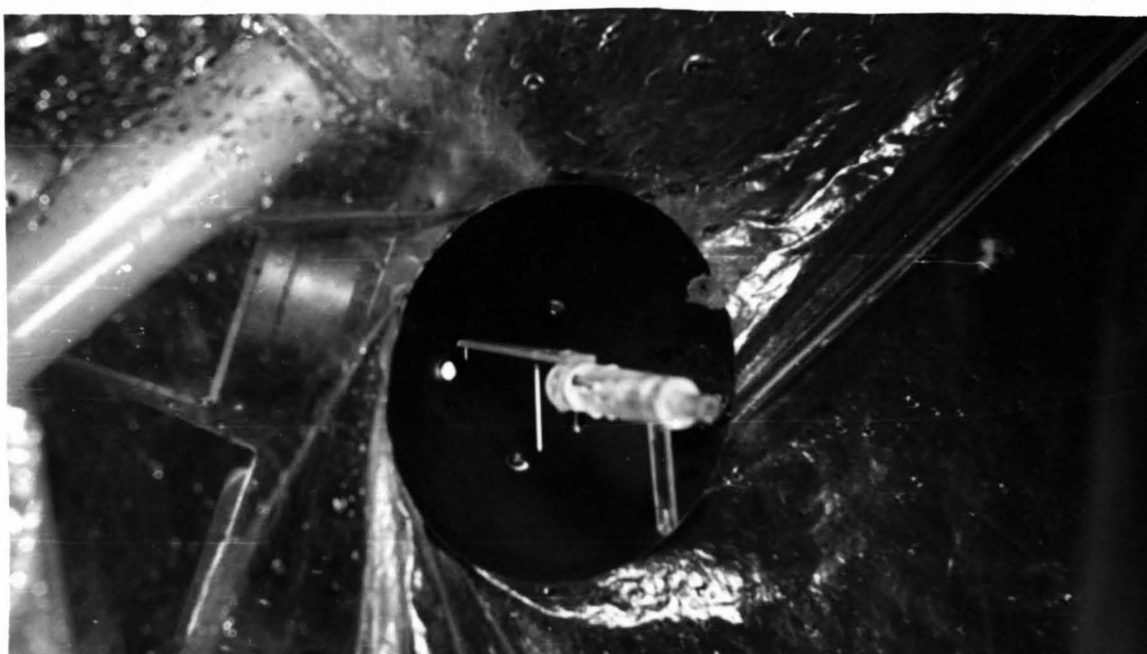

P.26

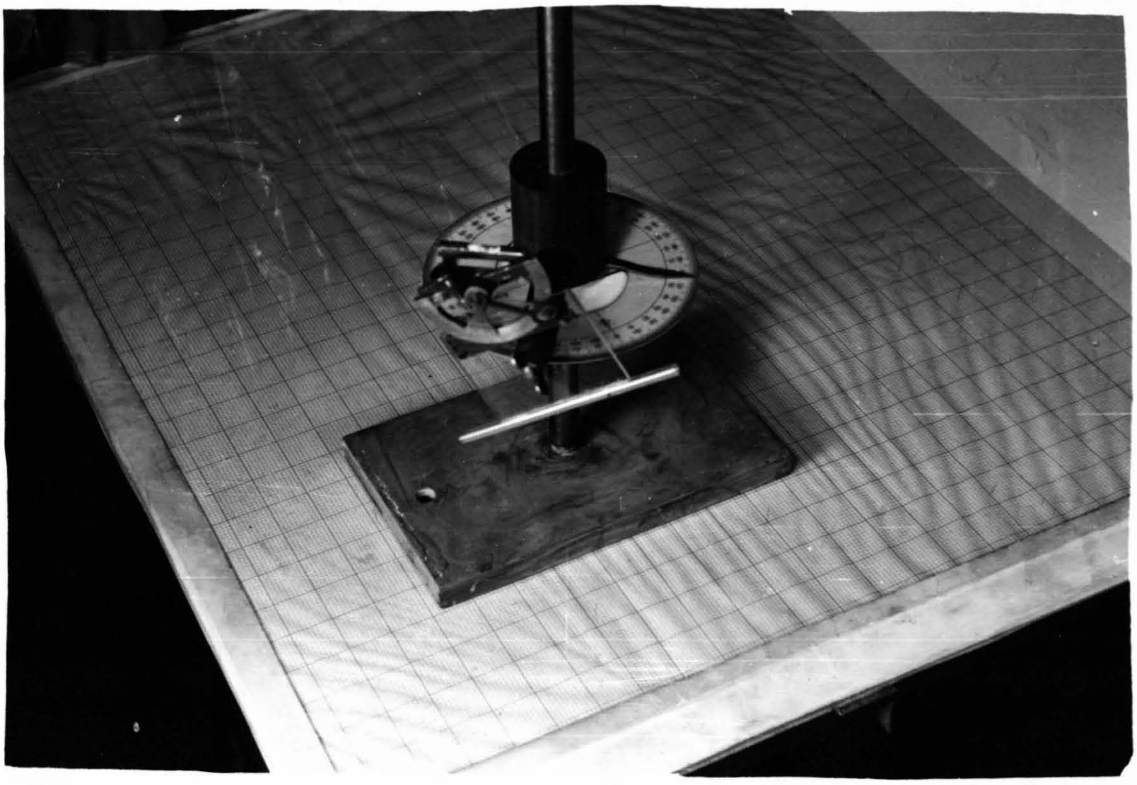

P.27

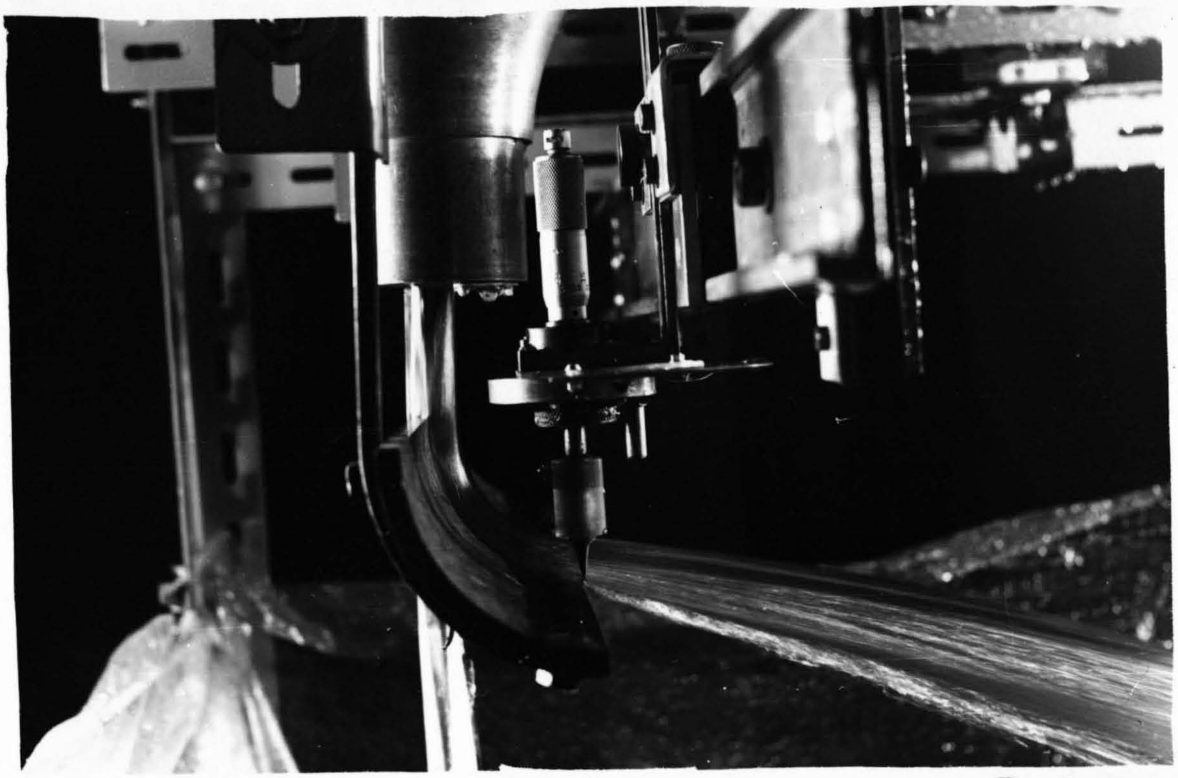

P.28

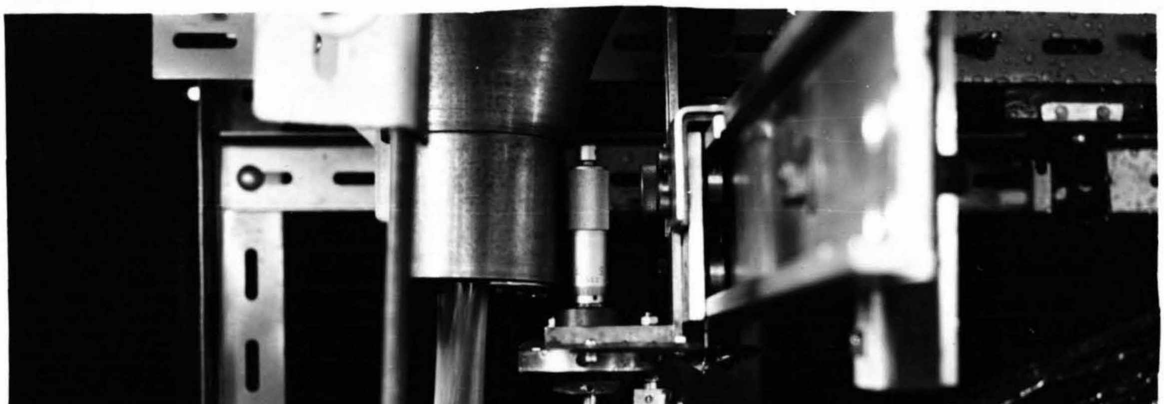

P.29

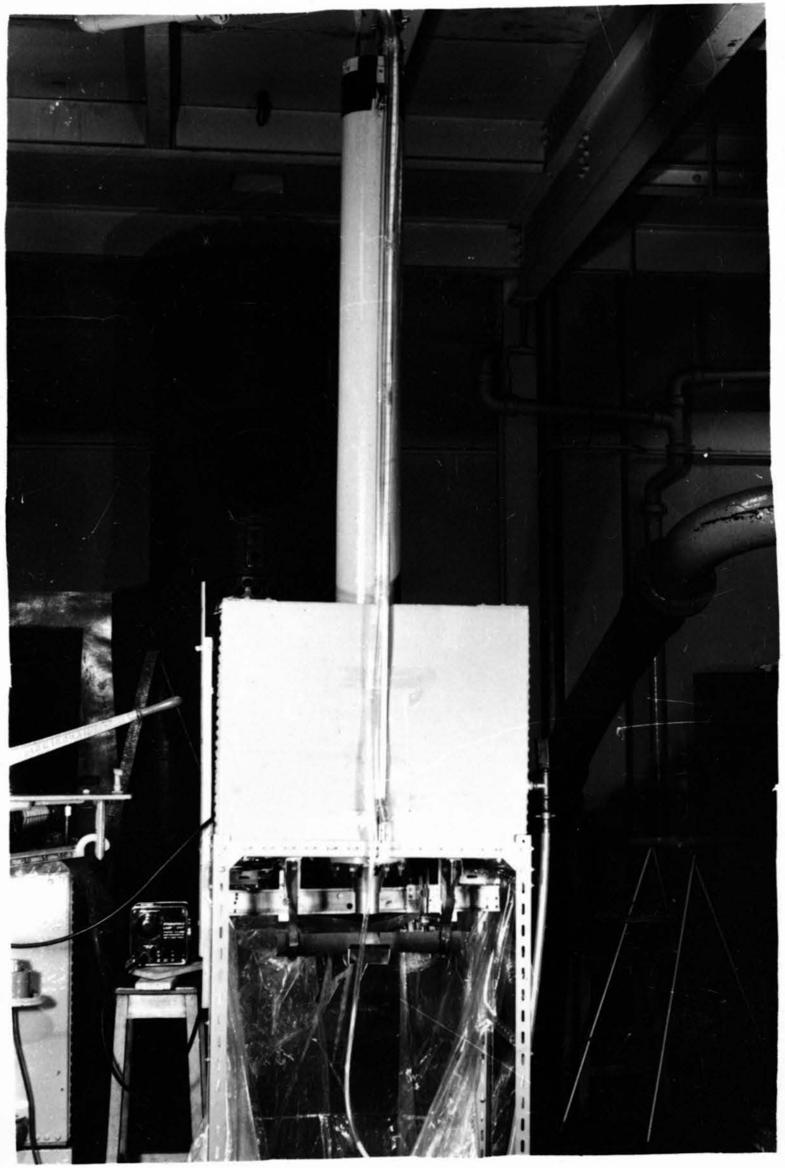

P.31

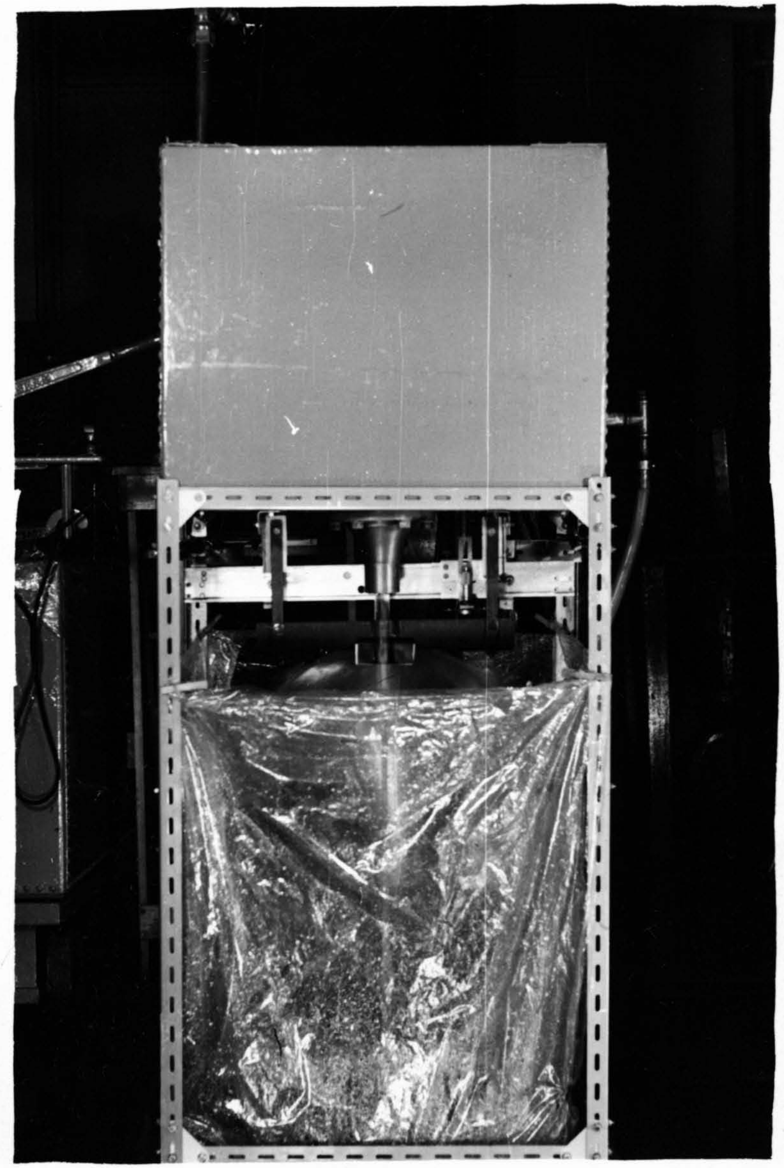

P.30

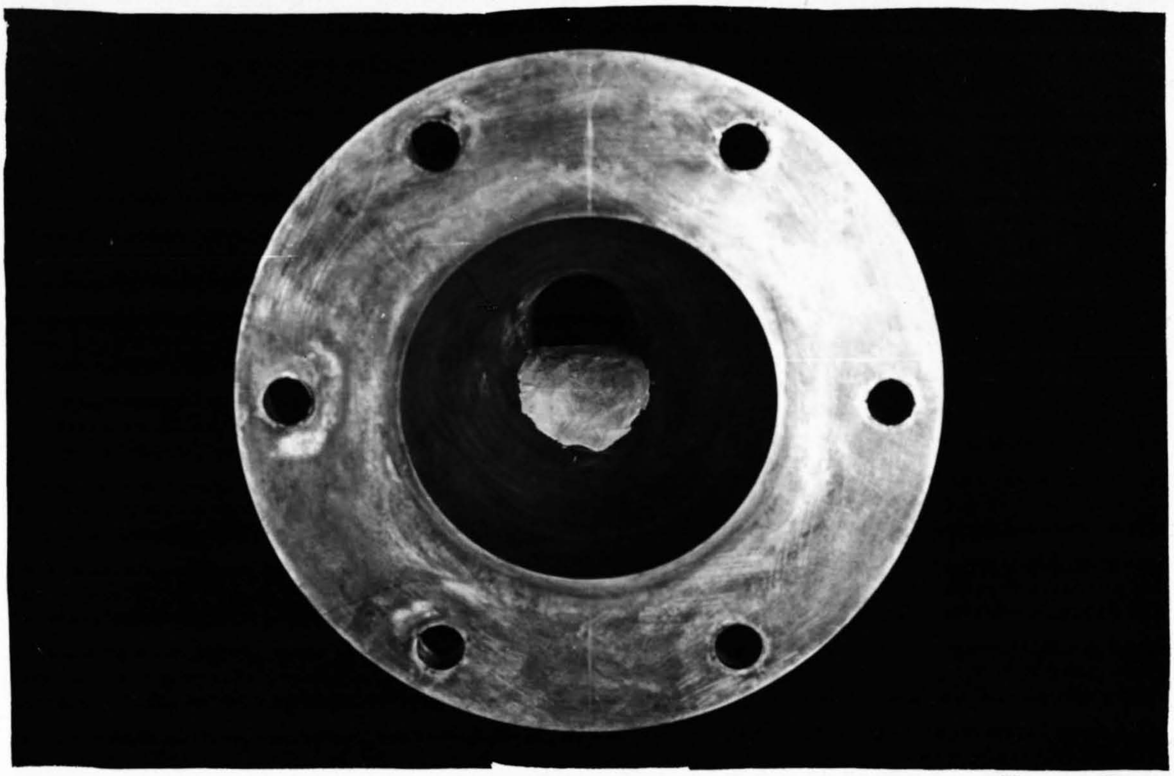

P.32

P.33

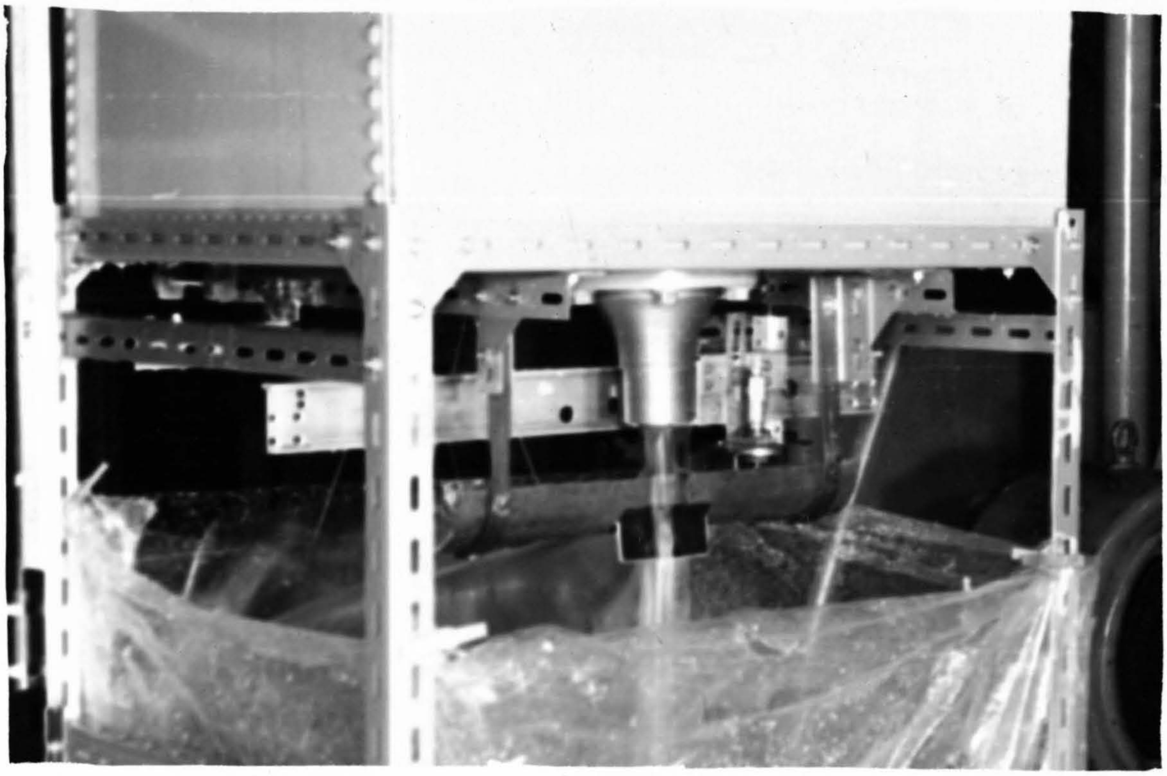

P.34

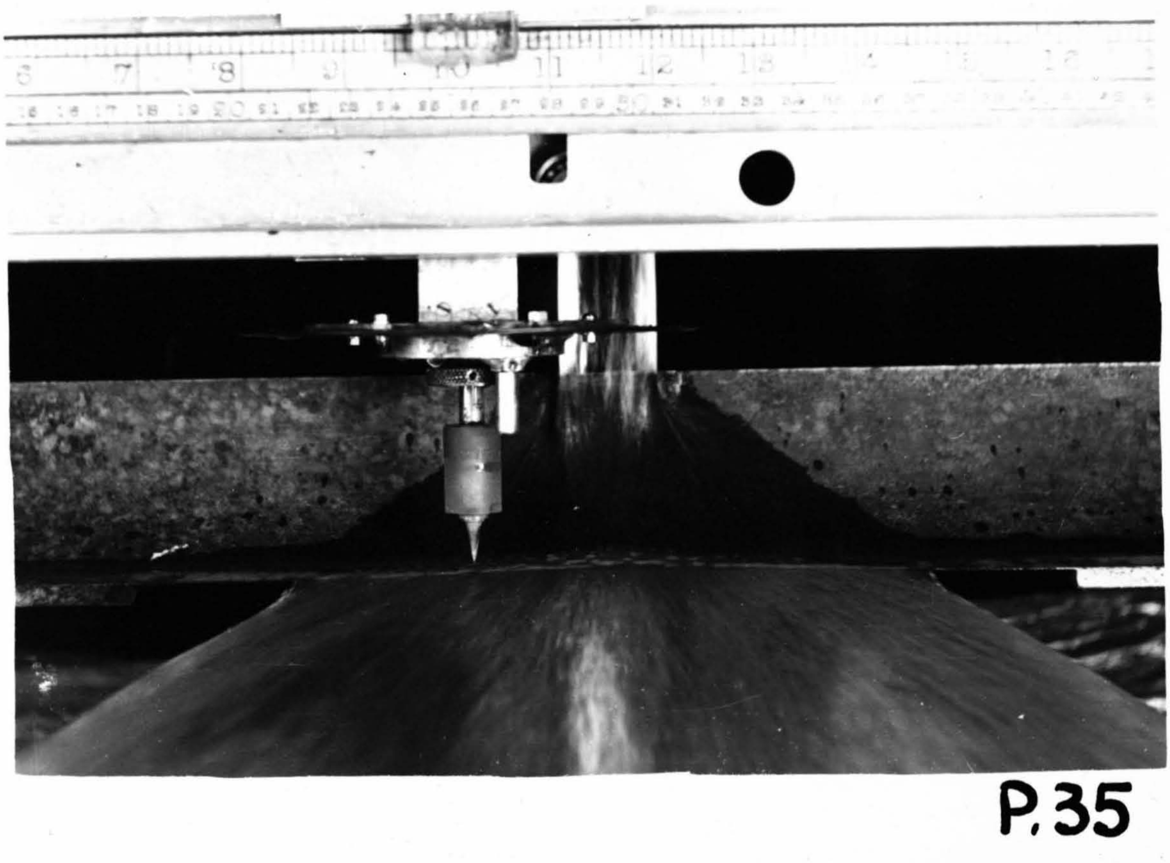

P.35

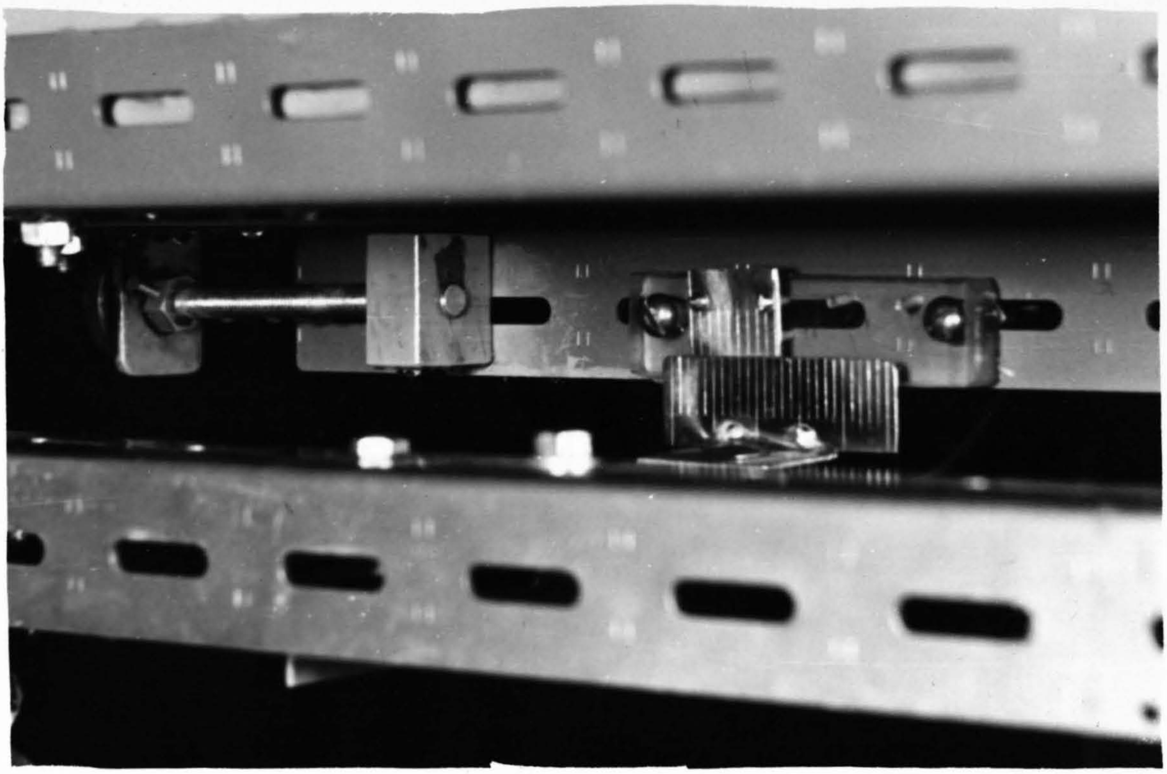

P.36

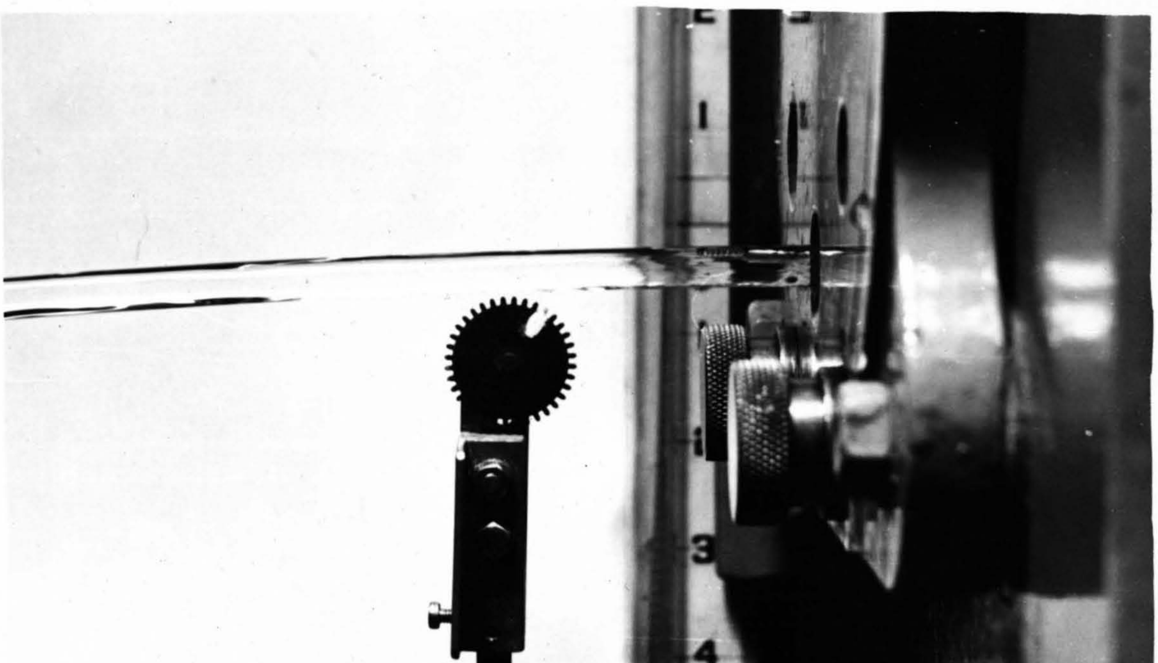

P.37

P.38

P.39

ANALYSIS OF VELOCITY COMPONENTS

AT INLET NOZZLE 6

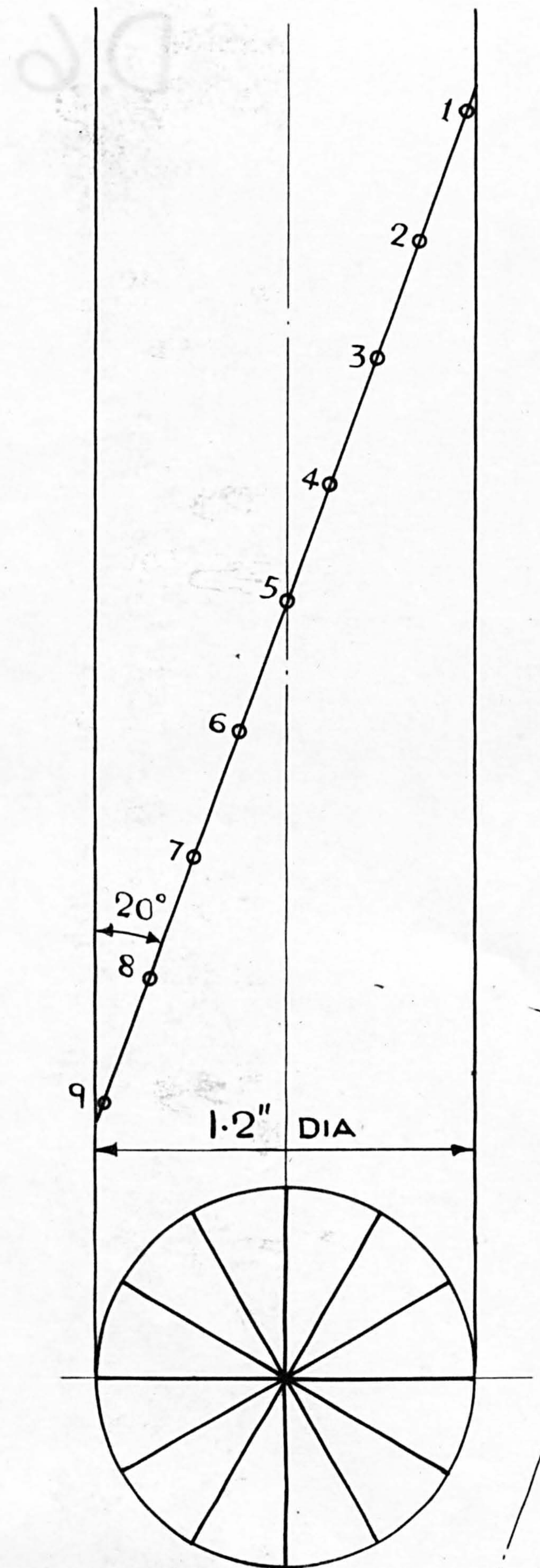

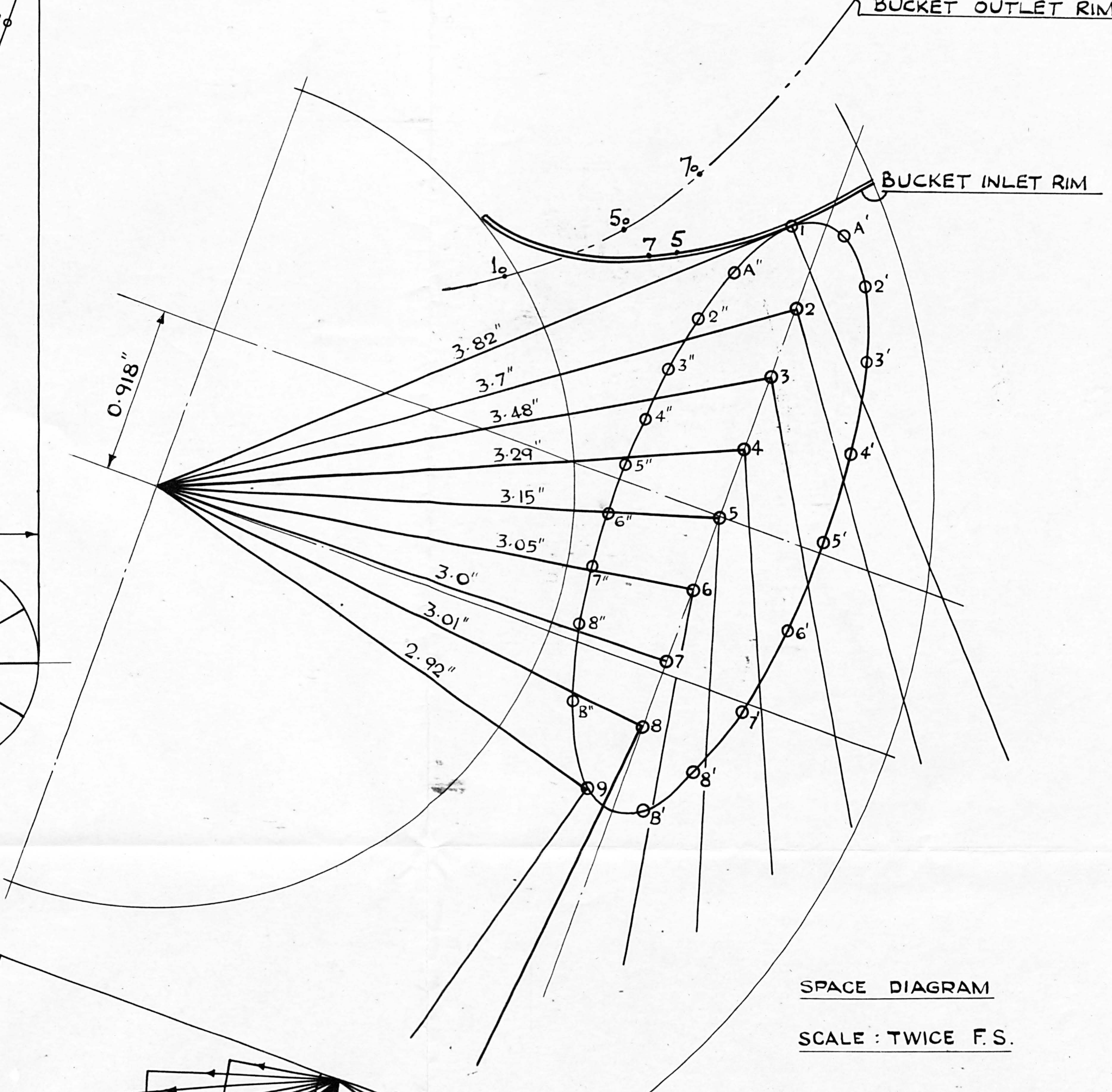

SPACE DIAGRAM

SCALE : TWICE F.S.

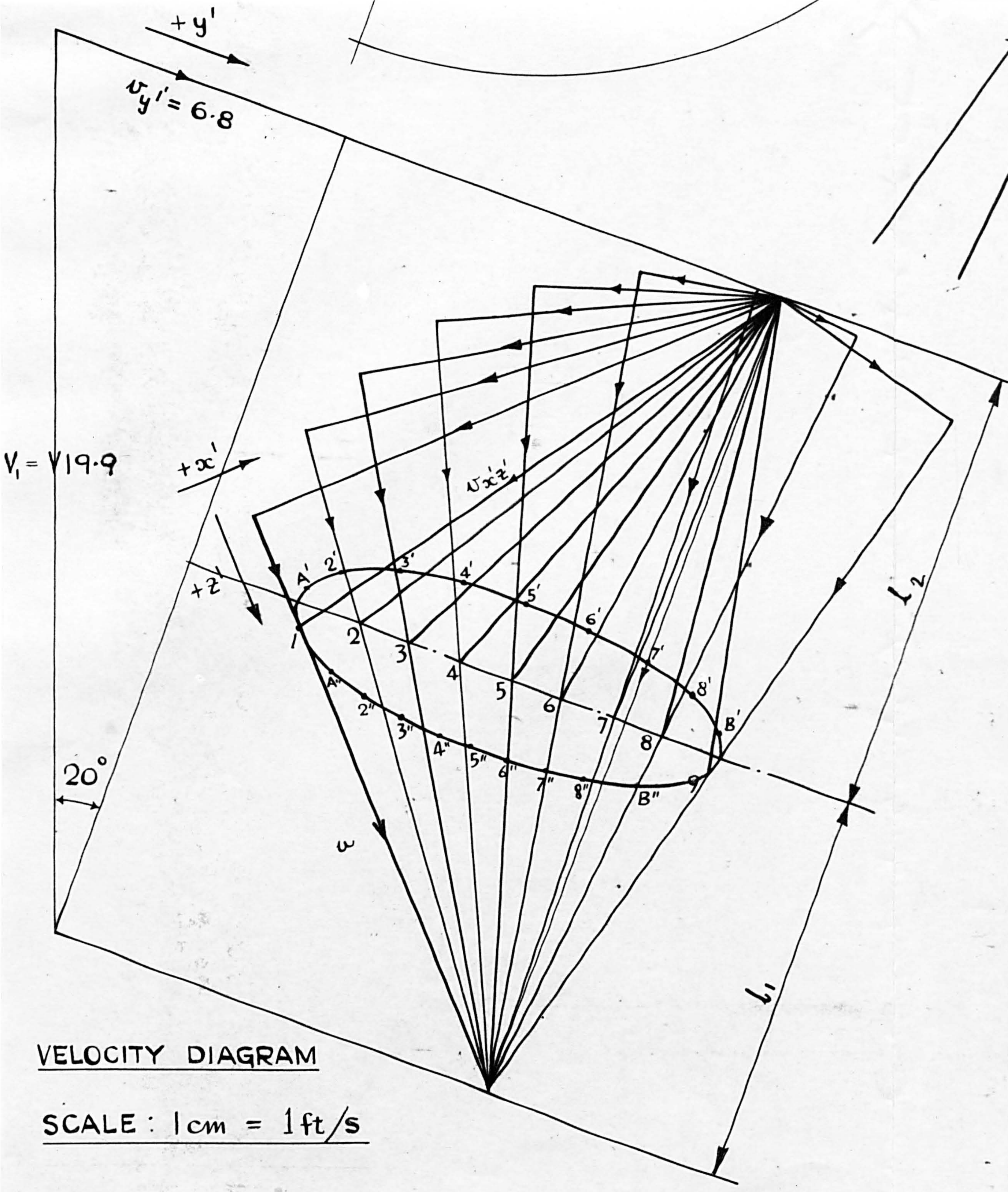

VELOCITY DIAGRAM

SCALE : 1cm = 1ft/s

	1	2	3	4	5	6	7	8	9
$v_{x'}$	−12·55	−10·85	−9·45	−7·6	−5·45	−3·15	−0·5	+1·9	+4·65
$v_{z'}$	2·65	4·4	6·0	7·5	8·65	9·5	9·9	9·75	9·5
$v_{x'z'}$	12·85	11·75	11·15	10·6	10·25	10·0	9·9	9·95	10·6
v	14·54	13·58	13·06	12·6	12·3	12·09	12·01	12·05	12·6
$\delta = \tan^{-1}\frac{y'}{x'}$	151·5	148	144·2	138·2	128·7	114·8	94·2	74·4	55·6
$\lambda = \tan^{-1}\frac{y'}{z'}$	68·7	57	48·5	42·2	38·2	35·6	34·5	35	35·6
$\varepsilon = \tan^{-1}\frac{z'}{x'}$	168	158	147·6	135·4	122·2	108·3	93	79	64

D.6

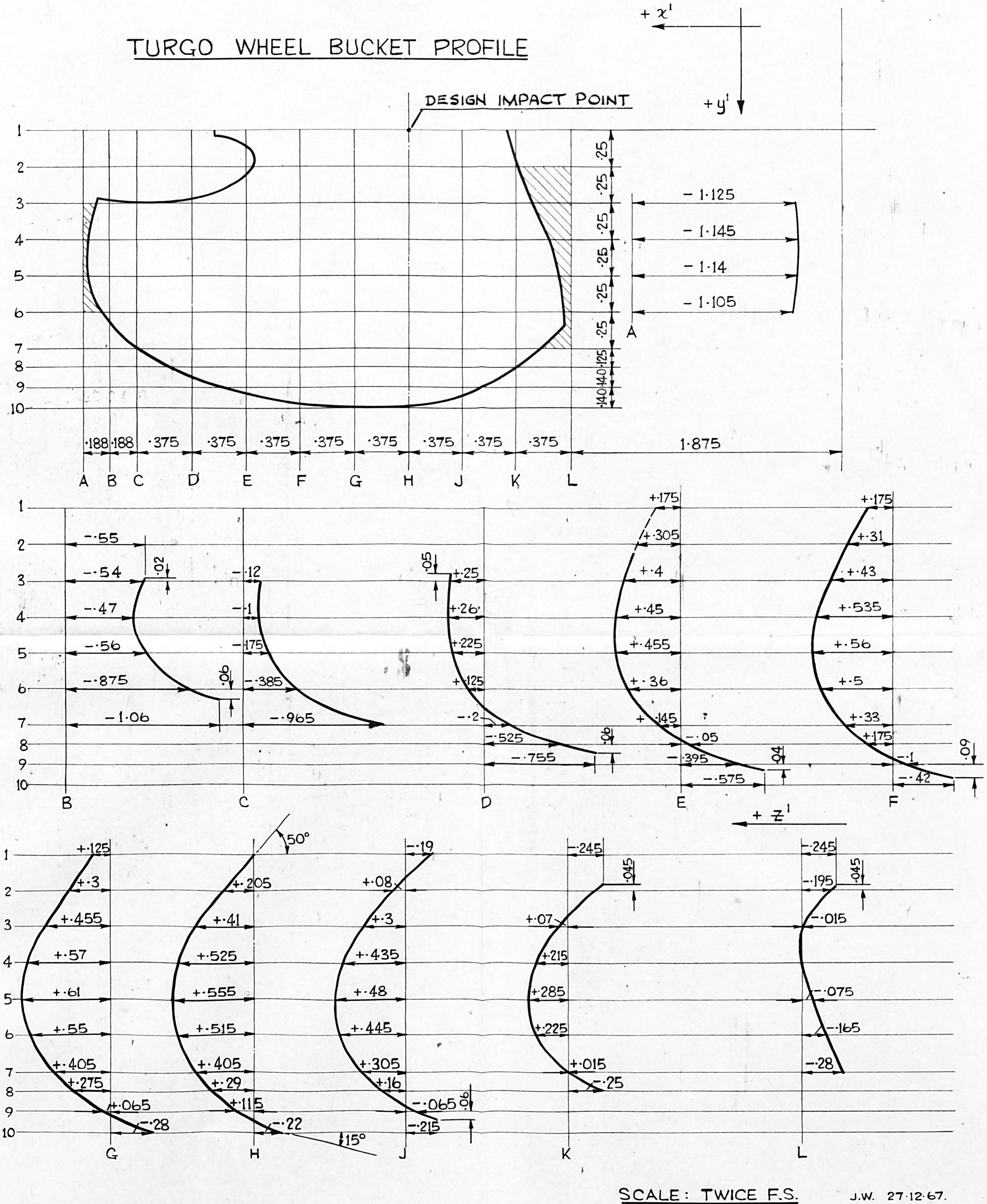

TURGO WHEEL BUCKET PROFILE
DESIGN IMPACT POINT
+ x'
+ y'
+ z'
A B C D E F G H J K L
- 1·125
- 1·145
- 1·14
- 1·105
·188 ·188 ·375 ·375 ·375 ·375 ·375 ·375 ·375 ·375
1·875
50°
15°
SCALE: TWICE F.S.
J.W. 27·12·67.

D.7

PARTICLE TRAJECTORY : TYPICAL CONSTRUCTION.

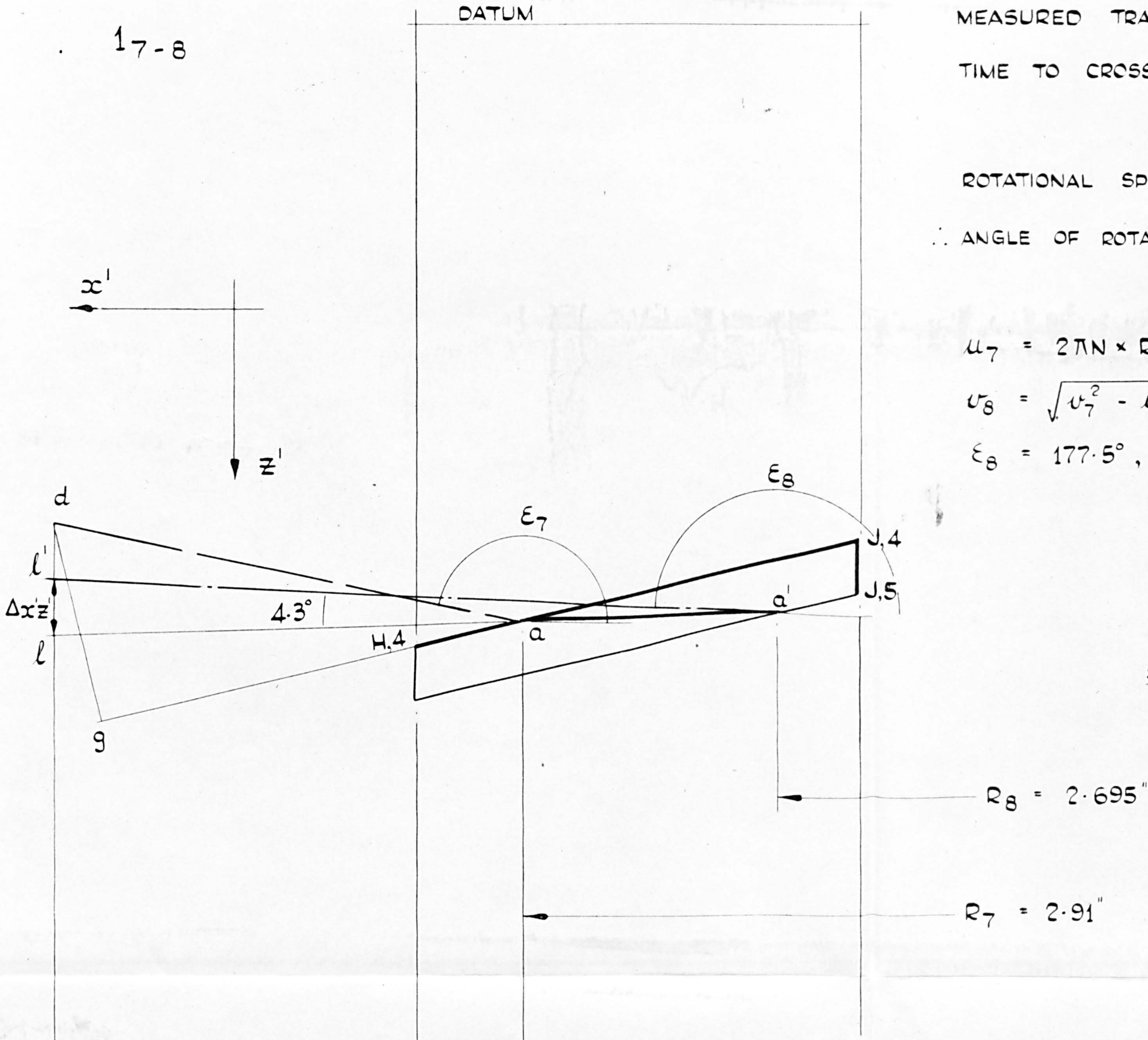

MEASURED TRAJECTORY ACROSS ELEMENT, l = 0·33"

TIME TO CROSS, $t = \frac{l}{v_7} = \frac{0 \cdot 33}{12} \times \frac{1}{12 \cdot 7}$

$= 0 \cdot 002165$ SEC.

ROTATIONAL SPEED, N = 330 REV/MIN.

$\therefore$ ANGLE OF ROTATION $= \frac{330}{60} \times 360 \times 0 \cdot 002165$

$= 4 \cdot 3°$

$u_7 = 2\pi N \times R_7 = 8 \cdot 38$ FT./S, $u_8 = 7 \cdot 75$ FT./S

$v_8 = \sqrt{v_7^2 - u_7^2 + u_8^2} = 12 \cdot 3$ FT./S

$\varepsilon_8 = 177 \cdot 5°$, $\delta_8 = 130°$, $\lambda_8 = 88°$

SCALE : TEN TIMES F.S.

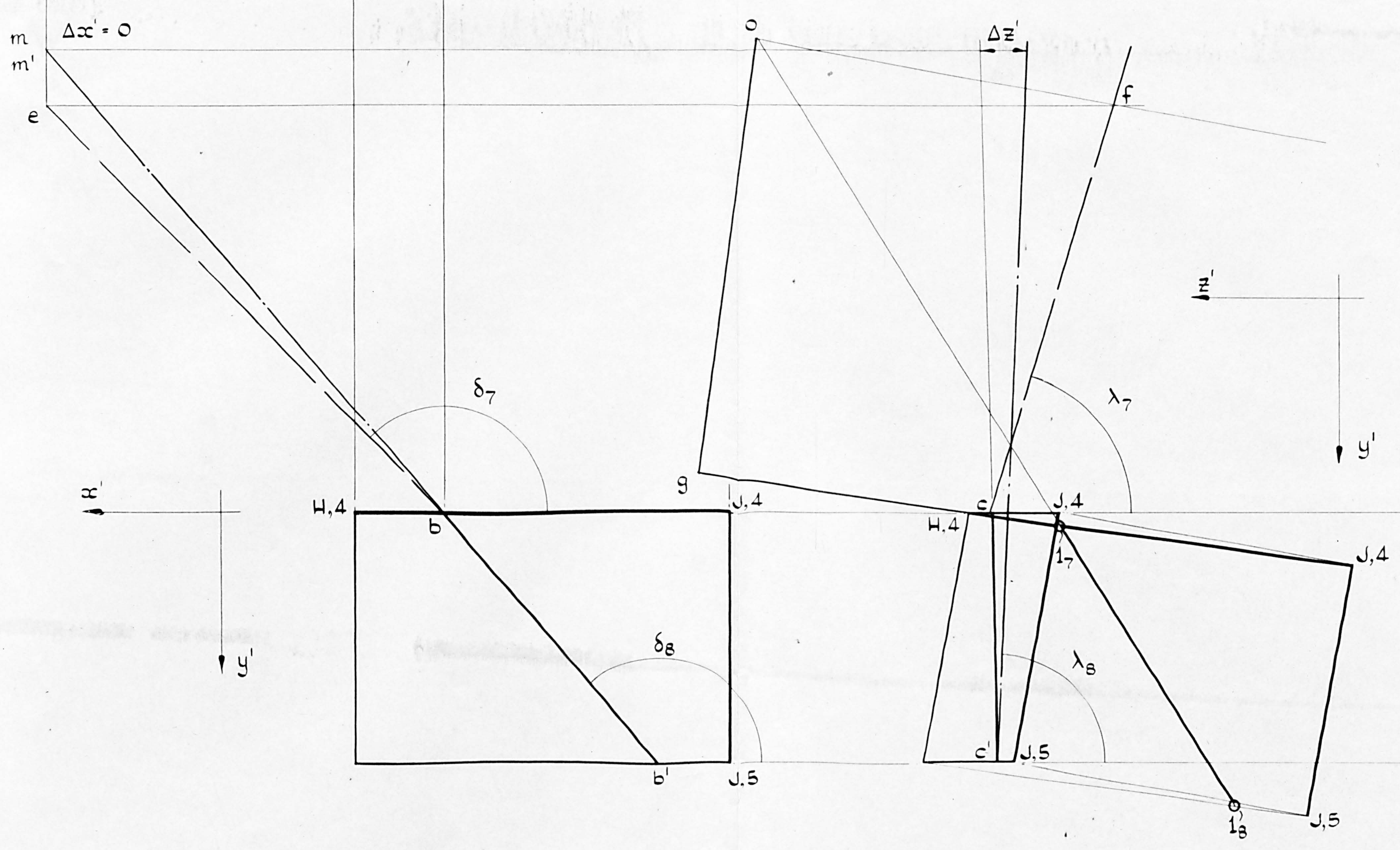

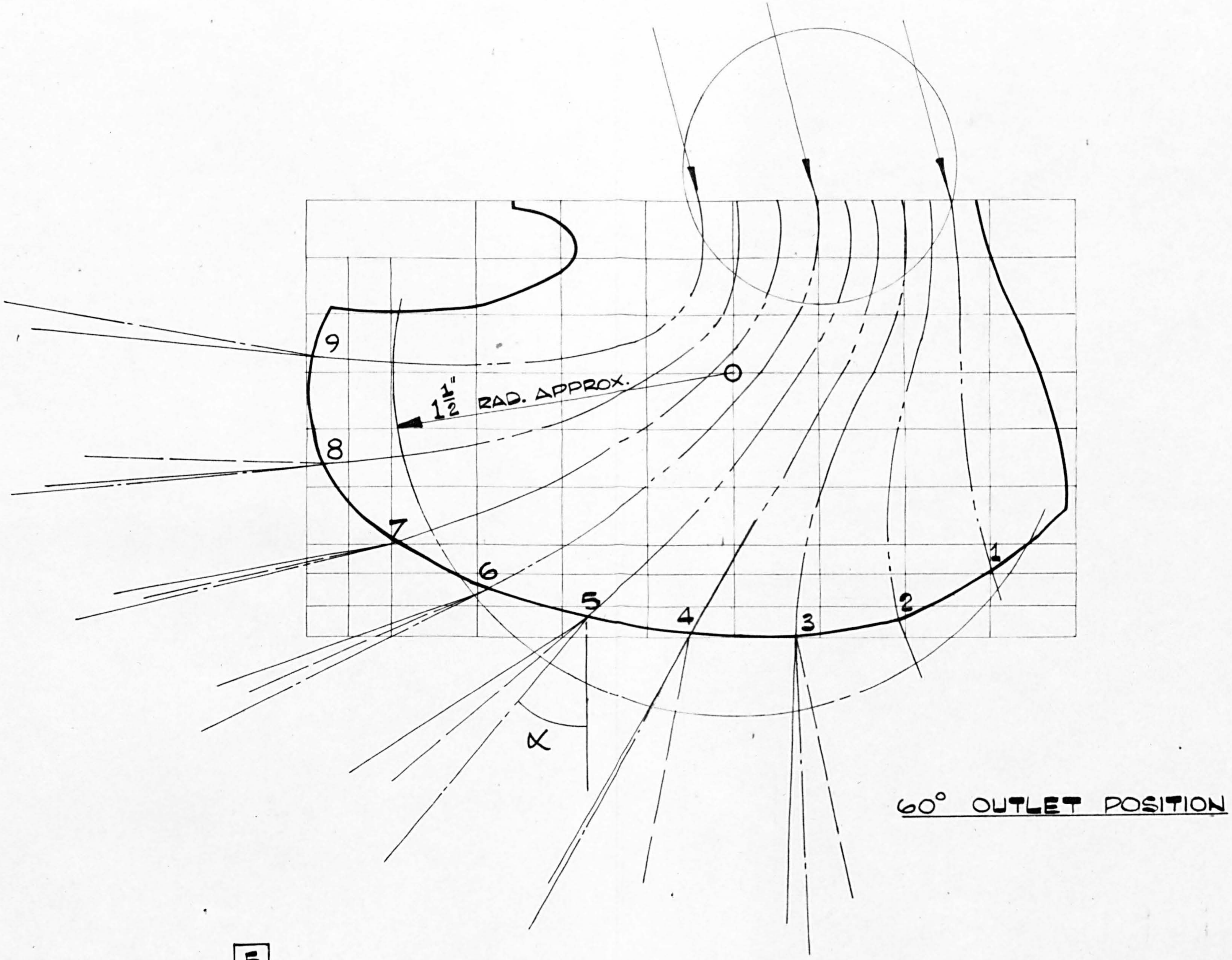

5

6

7

PROBABLE FLOW PATTERN

D.11.